

A Thesis Submitted for the Degree of PhD at the University of Warwick

Permanent WRAP URL:

<http://wrap.warwick.ac.uk/167030>

Copyright and reuse:

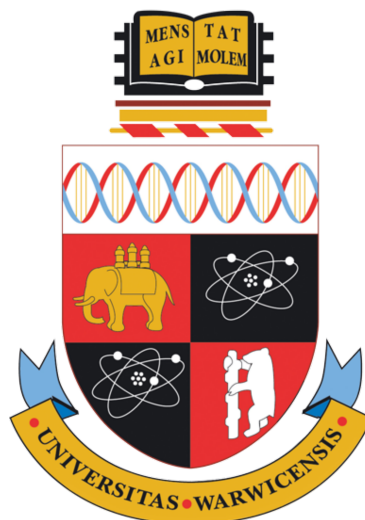
This thesis is made available online and is protected by original copyright.

Please scroll down to view the document itself.

Please refer to the repository record for this item for information to help you to cite it.

Our policy information is available from the repository home page.

For more information, please contact the WRAP Team at: wrap@warwick.ac.uk



**Towards a deeper understanding of the
photodynamics of UV filters for sunscreen
applications, using ultrafast spectroscopy and
complementary analytical techniques**

by

Emily Louisa Holt

Thesis

Submitted to the University of Warwick

in partial fulfilment of the requirements

for admission to the degree of

Doctor of Philosophy in Analytical Science

Molecular Analytical Science Centre for Doctoral Training

November 2021

Contents

Acknowledgements	iii
List of Figures	v
List of Tables	xix
Abbreviations	xxii
Declarations	xxv
Abstract	xxvii
Chapter 1 Introduction	1
1.1 Quantum mechanics for spectroscopy	2
1.1.1 Quantum nature of light	2
1.1.1.1 Wave-particle duality	3
1.1.1.2 Wavefunctions and the Schrödinger equation	3
1.1.1.3 Franck-Condon principle	5
1.2 Light-induced molecular processes	7
1.2.1 Absorption	8
1.2.2 Deactivation of excited states	9
1.2.2.1 Intramolecular non-radiative processes	9
1.2.2.2 Conical intersections	10
1.2.2.3 Excited-state intramolecular proton transfer	11
1.2.2.4 Intramolecular radiative processes	11
1.2.2.5 Intermolecular processes	12
1.3 Experimental	13
1.3.1 Generation of ultrafast laser pulses	13
1.3.1.1 Pump pulse generation	16
1.3.1.2 White-light continuum (WLC) generation	17

1.3.2	Transient absorption spectroscopy	18
1.3.3	Analysis of transient absorption data	24
1.3.3.1	Global kinetic fitting model	25
1.3.3.2	Chirp correction	27
1.3.4	Time-resolved ion yield	29
1.3.5	UV-Visible spectroscopy	30
1.3.6	Fluorescence spectroscopy	31
1.3.6.1	In solution	31
1.3.6.2	In vacuum	32
1.3.7	Computational methods	34
1.3.7.1	Basis sets and functionals	34
1.3.7.2	Density functional theory	35
1.3.7.3	Modelling solvent environments	36
1.4	Photoprotection	37
1.4.1	Solar radiation	37
1.4.2	Ultraviolet filters	38
1.4.2.1	Nature-inspired UV filters	40
1.4.2.2	Antioxidant potential and endocrine disruption	42
1.4.3	Sunscreen formulations	44
1.4.4	How effective is your sunscreen?	45
1.4.4.1	Metrics	45
1.4.4.2	Ideal sunscreen formulation	46
1.5	Summary	48
Chapter 2 Insights into the photoprotection mechanism of the UV filter homosalate		69
Chapter 3 Towards symmetry driven and nature inspired UV filter design		102
Chapter 4 Determining the photostability of avobenzone in sunscreen formulation models using ultrafast spectroscopy		121
Chapter 5 Conclusions and outlook		149
Appendices		157
A1	Coding	157
A2	Declaration of contributions	162
A3	Bibliography	163

Acknowledgements

Where do I begin? It feels almost surreal being in a position to write these acknowledgements. There are so many people that I would like to take this opportunity to thank, who have all played their part in this thesis being realised.

Firstly, I am indebted to my supervisor, Vas, for all the help, support, guidance and expertise that you have given me throughout these past four-and-a-bit years. Thank you for keeping me on track, for your enduring dedication to your craft (it doesn't go unnoticed) and your belief that I could get to the end; I will always be so grateful.

Doing a PhD in collaboration with industry has afforded me opportunities that I never would have dreamed of (like meeting Monty the koala, who makes an appearance on page 1), as such I am grateful to Lubrizol for taking on my project. Thank you to my supervisors at Lubrizol: Laurent, your enthusiasm was infectious and the way you were so passionate about this work was truly wonderful, we were so sad to see you go. Juan, thank you for your advice and for the opportunity to visit you in Barcelona.

Next, I must thank the Stavros group, past and present (in no particular order): Konstantina, Georgia, Nat, Mitch, Jack, Matt, Mick, Daniel, Tosin, Sofia, Abbie, Adam, Neil, Philip and Martin. It's been a joy to work with you all, both as colleagues and friends. The regular pilgrimages to the shop, the fifth floor for a hot beverage, group meetings (with or without parsnips) and the Friday trips to Café Library and/or the pub definitely helped me through this PhD! Special mentions are extended to Mitch, thank you for helping me in the beginning and training me in the art of ultrafast. Also to Jack, thanks for all your help in the lab — it was never anything that being proper Northern and a bit of Greatest Showman soundtrack couldn't fix!

My PhD experience has certainly been enhanced by being a part of the MAS CDT; I will always be extremely grateful to everyone involved in deciding to accept me on to the course and giving me the opportunity to follow my dream of “doing something more applied”. Thank you also to Naomi, Eleanor and Christina for all

your help with my queries over the years. The MAS base at Senate House has always been a happy, supportive place to come and that is in no small part thanks to all the fantastic people that I've had the pleasure of meeting there. Special thanks go to the MAS 2016 cohort, thank you for your friendship, and the D&D nights in lockdown.

I have been truly blessed to have the unwavering love and support of my family. To my wonderful mum and dad, Beverley and David, thank you for giving me all the opportunities that you did, to make sure that I had the best chance to succeed and thrive in the big wide world. I am truly so grateful for your passion for giving me (and the girls) the best education you could, and for all the sacrifices that you've made over the years to make this happen. You are the most incredible parents. To my sisters Lucy and Sophie and big brother Russ, thank you for all the banter. You're the best siblings anyone could ever ask for. I also thank my grandparents: Nanna and Grandad at Chantlers, Grandad at Barrow and Nanna at Burnley. Thank you to you all for always believing in me, I hope that I've been able to make you all proud.

On the note of education, there are several teachers that hold a special place in my heart. Thank you to you all for the knowledge you've shared with me.

To Jean, my 93-year-old friend and former neighbour in Kenilworth, thank you for the fun afternoons and evenings with you having tea and biscuits. To "Kitty", my feline friend who followed me into my flat after coming home from the lab or office, you brought me so much joy and always made me smile, even though you weren't my cat!

Having the opportunity to play bassoon and clarinet throughout my time at Warwick has been so special to me. I have met so many amazing people over the years through music here and has most definitely enhanced my University experience. Thank you also to the Warwick Music Centre for always supporting my music-making.

Thank you to all the friends who I've been rubbish at keeping in touch with, I appreciate you all (and your patience!) so much.

Finally, to my other half, Andy. At the time of writing these acknowledgements, we've only been in the "new home" for six weeks, but thank you for the six years (so far!) of always being there, through the good times and the bad. Thank you for making me cry whilst I'm laughing and laugh whilst I'm crying. And, of course, thank you for all the proof-reading (with or without pizza) and for all "standing around like piffy" you've done over the years. I couldn't have done this without you.

List of Figures

- 1.1 Two-dimensional representation of the electronic ground state (S_0) and first electronic excited state (S_1) PESs and the corresponding vibrational wavefunctions. The purple arrow represents the most likely absorption transition, with the green arrow the most likely emission, according to the Franck-Condon principle. 6
- 1.2 A summary of the main photophysical processes that can occur following photoexcitation of a sample, in the form of a Jablonski diagram. Singlet states are denoted S_i , the lowest energy triplet state is denoted T_1 . Vibrational modes are denoted by ν_n . Radiative processes are denoted by the solid lines: absorption in purple, fluorescence in green and phosphorescence in red. Non-radiative processes are denoted by the wavy lines: internal conversion ($S_i \rightarrow S_j$) in dark red, intersystem crossing ($S_i \rightarrow T_j$) in light blue and vibrational relaxation in orange. The timescales for each process²⁷ are also given.²⁸ 8
- 1.3 Schematics (not to scale) of the laser table components used to generate the ultrafast pulses required for the spectroscopy data presented in this thesis. Thereafter, the optical path of the pump and probe pulses to the respective TEAS tables is also shown. 14
- 1.4 Schematic (not to scale) of the probe pulse WLC generation setup in WCUS. The white light is generated, then collimated using the curved mirrors shown (labelled C, $f = 10$ cm) and focused into the sample. The pump is shown to indicate how both the pump and probe arrive at the sample. Post sample, the intensity of the WLC is monitored by the spectrometer. An example of the WLC spectrum generated between 320 – 720 nm is shown, as measured after a proportion of the excess 800 nm light is removed using a colour compensating filter, to avoid saturation of the spectrometer’s detector. 17

1.5	Full schematic (not to scale) of the optics used in the TEAS setup in Laboratory E0.19 at the Department of Chemistry at the University of Warwick, which was used for data acquisition in Chapters 2 and 3. The beamlines that are depicted as solid lines were used during experiments, the other beamline that appears faded is the harmonic generation capability, which was not implemented for the results in this thesis.	19
1.6	Full schematic (not to scale) of the optics used in the TEAS setup in the Warwick Centre for Ultrafast Spectroscopy (WCUS), which was used for data acquisition in 2 and 4. The beamline that appears faded is the harmonic generation capability, which was not implemented for the results in this thesis. The WLC continuum generation for this setup is shown in more detail in Fig. 1.4 and is thus not replicated here.	20
1.7	Simplified schematic of the flow-through sample cell that is used to heat the sample to skin surface temperature in ultrafast TEAS experiments in Chapter 4. A very similar cell was used in Chapters 2 and 3, except that there is no heating component. Pulse 1 passes through the unpumped sample and the transmitted light intensity (I_0) is recorded. Then, Pulse 2 (a UV pump pulse) photoexcites the sample. Finally, Pulse 3 is the probe pulse for the pumped sample. Pulses 2 and 3 arrive at the sample cell with a predefined time delay between them ($0 \leq \Delta t \leq 2.5$ ns). The sample at this point is replenished between each pump-probe pair of measurements via recirculation. . .	21
1.8	Diagram of possible contributions to a transient absorption spectrum for a given time delay: ⁵⁹ excited-state absorption (ESA, red dashed line), photoproduct absorption (PP, light green dotted line), ground state bleach (GSB, yellow dashed line), and stimulated emission (SE, blue dotted line). The transient (black solid line) is the sum (convolution) of these contributions. ²⁸	23

1.9	Solvent response of methanol, following photoexcitation at 350 nm at high power (1.5 mW). Top row: Selected wavelength transients (IRFs) before chirp correction (left), where the effect of group velocity dispersion (GVD) due to white light probe interaction with the CaF ₂ window at the sample can be clearly observed. (Right) The same transients after chirp correction using the KOALA package. ¹⁰⁹ All wavelengths are now closely aligned in time. Bottom row: False colour heat maps, showing solvent transients for all wavelengths between -0.2 and 0.8 ps before chirp correction (left) and after chirp correction (right) using the KOALA package ¹⁰⁹ . In this thesis, heat maps have been chirp corrected for display purposes only, as the effect is accounted for during the fitting process, described in Section 1.3.3.1.	29
1.10	Simplified Jablonski diagrams to show the differences between excitation spectra (as carried out in LIF experiments) and emission spectra, as implemented in solution and in DFL experiments. The dotted line in the excitation spectrum diagram represents that fact that emission can occur in states other than $\nu = 0$ in the gas phase.	33
1.11	Example of the arrangement of the atom-centred spheres (in blue) in the COSMO implicit solvent model, in this instance for homosalate in ethanol.	36
1.12	List of selected organic UV filters that have been approved by the EU and the FDA in the United States (with the exception of DHHT, which is not FDA approved). The structures of key sunscreen functional groups are highlighted in the structures: salicylates (pink), cinnamate (blue) and benzophenone (green). λ_{\max} is the peak of absorption and ε is the absorption coefficient of the filter at λ_{\max} , as reported by Shaath. ¹⁹⁹	39
1.13	Structures of sinapic acid, sinapoyl malate (the ester found in plant leaves), and the four structures investigated by both Liu <i>et al.</i> and Dean <i>et al.</i> : ^{135,222} methyl sinapate (MS), isopropyl sinapate (IS), sinapoyl methyl lactate (SML) and sinapoyl dimethyl malate (SDM), with the groups added to the sinapate ester moiety shown in blue for reference. ²⁸	41

1.14	(a) Expected absorbance profiles of sunscreens with SPF 50+ (black line), SPF 30 satisfying UVA protection requirements (red line) and SPF 30 that does not satisfy UVA protection criteria (blue line), as calculated <i>in silico</i> using a sunscreen simulator. ³⁰⁸ (b) Corresponding transmission profiles for sunscreens with SPF 50+ (black line), SPF 30 satisfying UVA protection requirements (red line), and SPF 30 sunscreen that does not satisfy these requirements (blue line), calculated <i>in silico</i> using a sunscreen simulator. ³⁰⁸ The critical wavelength (370 nm), the wavelength at which more than 10% of the protection should be offered by the formulation, is indicated by the dashed line in both figures. In addition, the regions referred to as UVA (320 – 400 nm) and UVB (290 – 320 nm) are indicated. ²⁸	47
2.1	Normalised UV-visible spectra of homosalate (HMS) in acetonitrile (blue line), ethanol (black line) and cyclohexane (red line), with molecular structure of HMS (<i>enol</i> form) inset. The dashed line indicates the presence of an intramolecular hydrogen bond.	71
2.2	(a) A representation of the different energy levels of HMS (conformer 1) in vacuum in the <i>enol</i> (left) and <i>keto</i> (right) form, as predicted using the PBE0/cc-pVTZ level of theory. In (a), the red arrow represents the absorption of a photon, the blue arrow represents fluorescence, and the green arrow represents phosphorescence. The dotted lines in blue and orange between the S ₀ and S ₁ states are indicative of the linear interpolation of internal coordinates calculated for HMS in vacuum at the PBE0/cc-pVTZ level of theory, shown in further detail in (b) alongside the predicted structures of HMS at selected steps. These calculations suggest that, when in the ground state, conformer 1 of HMS exists in the <i>enol</i> form, whereas in the first excited singlet state (S ₁) HMS converts to the <i>keto</i> state in an energetically barrierless process.	74
2.3	TR-IY magic angle transients for HMS photoexcited at (a) 305 nm, (b) 320 nm and (c) 335 nm, the S ₁ (<i>v</i> = 0) origin of HMS, with a 200 nm probe. Black circles are experimental points, while the red curves correspond to kinetic fits (discussed in S1.2 in the ESI), from which the time constants shown inset are extracted. The baseline for all plots is zero within the signal-to-noise ratio of our measurements. . .	75

2.4	(a) LIF spectrum of vaporised HMS upon photoexcitation in the 29806 – 32787 cm ⁻¹ energy region, with Gaussian curves (FWHM = 500 cm ⁻¹) demonstrating the regions photoexcited in the TR-IY measurements with $\lambda_{\text{pump}} = 335$ nm (red), 320 nm (blue) and 305 nm (green). (b) The same LIF spectrum in more detail, with the inset showing the peak and energy corresponding to the S ₁ ($v = 0$) origin of HMS.	76
2.5	(a)–(c): False colour heat maps showing all transient absorption spectra (TAS) of homosalate (HMS) in acetonitrile (ACN) ($\lambda_{\text{pump}} = 306$ nm), ethanol (EtOH) ($\lambda_{\text{pump}} = 307$ nm) and cyclohexane (CHX) ($\lambda_{\text{pump}} = 309$ nm) respectively. In these plots, the time delay axis is shown as a linear scale until 10 ps and as a logarithmic scale thereafter. (d)–(f): TAS at selected pump-probe time delays for HMS in ACN, EtOH and CHX respectively. These plots are attained by taking vertical slices through the false colour heat maps at the given time delay and are presented on the same $m\Delta\text{OD}$ scale as the corresponding false colour heat map. (g)–(i): Kinetic fits of the transient data at 340 nm (black), 450 nm (red) and 550 nm (blue) for HMS in ACN, EtOH and CHX respectively. The circles denote the raw data at each wavelength and the solid line is the fit attained using the parallel model described in the main text. In each case, the time delay axis is presented on a logarithmic scale. False colour heat maps containing residuals for every datapoint can be found in the ESI (Fig. S12).	77
2.S1	Power dependence study for HMS in vacuum photoexcited at $\lambda_{\text{pump}} = 305$ nm at $\Delta t = 0$ ps. Black circles correspond to data points which are an average of four consecutive scans; the error bars on each data point correspond to two standard deviations from this average. The red line denotes the line of best fit attained by linear least squares regression.	88
2.S2	Gaussian fit (red line) to the Xe TR-IY transients at $\lambda_{\text{pump}} = 330$ nm (black dotted line). The FWHM of the fitting curve presented provides us with the pump-probe beam cross-correlation width of ~ 170 fs, which we quote as our IRF.	88
2.S3	(a) Dispersed fluorescence spectrum of HMS. (b) Fitted transient (black dotted line, with line of best fit shown in red) to extract the fluorescence lifetime of HMS at origin.	89

2.S4	Selected transients for solvent-only time-zero IRFs at given probe wavelengths, plotted using black dashed lines (pump wavelengths were kept the same as for TEAS measurements for each solution): (a) ethanol at 330 nm, IRF \sim 65 fs (b) cyclohexane at 320 nm, IRF \sim 55 fs and (c) acetonitrile at 330 nm, IRF \sim 80 fs. These IRFs have been extracted from a Gaussian fit function, with the line of best fit shown in red.	89
2.S5	Power dependency study for HMS in ethanol for key features at $\Delta t = 1$ ps at the following probe wavelengths: (a) 340 nm (b) 450 nm and (c) 530 nm. Explanation of the derivation of the error bars is given in the text in Section S1.2.3.	90
2.S6	Power dependency study for ethylhexyl salicylate (octisalate) in ethanol for key features at $\Delta t = 1$ ps at the following probe wavelengths: (a) 340 nm (b) 450 nm and (c) 530 nm. Explanation of the derivation of the error bars is given in the text in Section S1.2.3.	90
2.S7	(a) UV-visible spectra taken of three $\sim 20 \mu\text{M}$ solutions of HMS in cyclohexane (pink line), ethanol (blue line) and acetonitrile (green line), with the standard solution, $\sim 0.5 \mu\text{M}$ 1,4-diphenyl-1,3-butadiene (DPB) in cyclohexane, shown in black. (b) Averaged fluorescence spectra, attained from averaging five separate scans, which were integrated and the values substituted into Eq. S5.	91
2.S8	Structure and relative energies (relative to conformer 1 in the S_0 state, the lowest energy structure/state) of the two lowest energy conformers of HMS in both the S_0 and S_1 states. The ground state energies were calculated by relaxing the geometry of both conformers at the PBE/cc-pVTZ level of theory and then conducting a single point energy calculation on each at the PBE0/cc-pVTZ level of theory. The excited state energies were calculated by relaxing each conformer with respect to the S_1 state at the PBE0/cc-pVTZ level of theory.	91
2.S9	S_0 , S_1 , and S_2 energies of HMS in specific steps between the <i>enol</i> and <i>keto</i> forms. These steps were generated through a linear interpolation of internal coordinates (LIIC). This figure is an expansion upon Fig. 2b in the main text to demonstrate the lack of intersection between the S_1 and S_2 states over the examined reaction coordinate. As the second conformer does not yield a stable <i>keto</i> structure in the S_1 state, it is not possible to study a LIIC along its respective proton transfer coordinate.	92

2.S10	Lorentzian fits (dashed lines) to the first four peaks of the LIF spectrum of HMS (raw data presented as a grey solid line). These Lorentzian fits return Γ values of 0.84 cm^{-1} for the peak centred at 29833.4 cm^{-1} ($S_1(v = 0)$ origin of HMS, red dashed line), 0.88 cm^{-1} for the peak at 29859.2 cm^{-1} (blue dashed line), 0.92 cm^{-1} for the peak at 29878.6 cm^{-1} (pink dashed line) and 0.97 cm^{-1} for the peak at 29885.5 cm^{-1} (green dashed line).	92
2.S11	S_0 energy of <i>enol</i> form along the rotation coordinate between conformer 1 and conformer 2. This was generated by fixing the dihedral angle shown at 10 degree increments between 0 and 180 degrees and relaxing all other internal coordinates in the ground state at the PBE/cc-pVTZ level of theory. This is an upper bound to the energy barrier between the two conformers.	93
2.S12	False colour heat maps showing the residuals attained from the parallel fitting procedure (compared to raw data) for HMS in (a) acetonitrile, (b) cyclohexane and (c) ethanol, and for EHS in (d) acetonitrile, (e) cyclohexane and (f) ethanol.	93
2.S13	Kinetic fits of the transient data at 340 nm (black), 450 nm (red) and 550 nm (blue) for HMS in (a) acetonitrile, (b) ethanol and (c) cyclohexane. The circles represent the raw data and the solid line is the fit attained using the sequential model described in Section 2.2.1.	94
2.S14	Normalised emission spectra with solvent baseline subtraction of HMS in cyclohexane, ethanol and acetonitrile. Excitation was carried out at the respective peak maxima of each solution: $305 \leq \lambda_{\text{pump}} \leq 310 \text{ nm}$. The slit width was 2.5 nm. The slight discrepancy in the spectra at $\sim 330 \text{ nm}$ is due to Stokes Raman scattering effects that could not be fully subtracted from the fluorescence spectra. ¹⁰ All three solutions display an emission peak at 450 nm. We note, however, the presence of a smaller peak at 350 nm in polar solvents, a phenomenon that has also been observed in the molecular analogue methyl salicylate, although the cause of this dual fluorescence remains uncertain. ¹¹ . . .	94
2.S15	(a) UV-visible absorption spectra of EHS in three different solvents, with the molecular structure of EHS inset. TAS of $\sim 10 \text{ mM}$ solutions of EHS in (b) ethanol ($\lambda_{\text{max}} = 307 \text{ nm}$), (c) cyclohexane ($\lambda_{\text{max}} = 309 \text{ nm}$) and (d) acetonitrile ($\lambda_{\text{max}} = 305 \text{ nm}$).	95

2.S16	TAS at selected pump-probe time delays for EHS in (a) acetonitrile, (b) ethanol and (c) cyclohexane. These plots are attained by taking vertical slices through the false colour heat maps at the given time delay.	95
2.S17	Kinetic fits of the transient data at 340 nm (black), 450 nm (red) and 550 nm (blue) for EHS in acetonitrile, ethanol and cyclohexane respectively, fitted using: (a)–(c) a parallel model, the same as that used for HMS (described in the manuscript) and (d)–(f) a sequential model, as described in section S2.2.1. The circles denote the raw data at each wavelength and the solid line is the fit attained. In each case, the time delay axis is presented on a logarithmic scale.	96
2.S18	(a) TAS of HMS in cyclohexane ($\lambda_{\text{pump}} = 309$ nm) taken at $\Delta t = 2$ ns (black) and $\Delta t = 3$ ns (red), attained using the TEAS setup characterised by Woolley <i>et al.</i> ⁸ Inset is a zoom-in of the data between 350 and 500 nm to more clearly display the long-lived positive signal. (b) TAS of EHS in cyclohexane ($\lambda_{\text{pump}} = 309$ nm) taken at $\Delta t = 2$ ns (black) and $\Delta t = 3$ ns (red). Inset is a zoom-in of the data between 350 and 500 nm to more clearly display the long-lived positive signal.	96
3.1	(a) The geometric structures of diethyl sinapate (DES) and ethyl sinapate (ES), demonstrating the symmetrical functionalization of DES compared to its precursor ES. (b) Schematic illustrating the dynamical processes involved in the photoisomerization of ES. Following photoexcitation with a UV photon (represented by the purple arrow), to the first electronically excited (S_1) state (green curve), <i>trans</i> -ES undergoes three processes during its subsequent relaxation to the electronic ground (S_0) state (black curve). Each process is indicated by a labelled arrow: k_{geo} represents the rate of the geometry rearrangement; k_{evo} is the rate of evolution in the electronic excited state, such as vibrational cooling, along with solvent rearrangement; and k_{iso} is the rate for the photoisomerization. At the S_1/S_0 conical intersection, where the green and black curves meet, there are two possible pathways: relaxation to the S_0 state of the <i>trans</i> - or <i>cis</i> -ES species, represented by the solid black and dashed black arrows respectively.	104

3.2	(a) Transient absorption spectrum (TAS) of DES in C12–15 alkyl benzoate deposited on a synthetic skin mimic, VITRO-CORNEUM [®] (VC/AB) photoexcited at 335 nm, shown as a false colour map, with the intensity scale representing a change in normalized optical density (ΔOD). The time-delay is plotted linearly from -0.5 to 10 ps then as a log scale from 10 to 100 ps. (b) Evolution associated difference spectra (EADS) from the sequential global fit of the TAS of DES in VC/AB photoexcited at 335 nm. Zoomed-in plots showing only k_4 and k_5 for this system can be found in Supplementary Fig. 6a. (c) Selected TAS at specific Δt highlighting the absorption at 380 nm (8 ps, green) and incomplete ground state bleach recovery (2 ns, orange).	105
3.3	UV/visible spectra of DES in C12–15 alkyl benzoate (AB), at varying durations of irradiation at 335 nm and replicating solar intensity. The downwards arrow (in black) denotes the observed 3.3% decrease in absorbance after 7200 s of irradiation.	106
3.4	Endocrine disruption activity of DES, as determined by assays on several cell lines, for the alpha oestrogen receptor ER α (circle) as either an agonist (magenta) or antagonist (blue), and for the xenobiotic receptor PXR (square) as either an agonist (green) or antagonist (orange). The activity of ER α is regulated by the steroid and oestrogen sex hormone 17 β -estradiol (E2). A known agonist for PXR is SR 12813.	106
3.5	The determination of the antiradical activity of DES has been determined via 2,2-diphenyl-1-picrylhydrazyl (DPPH) assay. These tests involve adding DES solution in ethanol at different concentration to homogeneous DPPH solution. The EC $_{50}$, <i>i.e.</i> the amount of DES needed to reduce the initial number of DPPH free radicals by half, is provided by the crossing point of % DPPH (blue) and % reduced DPPH (green), which occurs at 32.7 nmol.	106
3.6	Preparation of DES. DES synthesized through Knoevenagel condensation of syringaldehyde and diethyl malonate.	109

3.S1	(a) Transient absorption spectrum (TAS) of DES in AB photoexcited at 335 nm, shown as a false colourmap, with the intensity scale representing change in normalized optical density (ΔOD). The time-delay is plotted linearly from -0.5 to 10 ps then as a log scale from 10 to 100 ps. (b) Evolution associated difference spectra from the sequential global fit of the TAS of DES in AB photoexcited at 335 nm. (c) Selected TAS at specific Δt highlighting the absorption at 380 nm (8 ps, blue) and incomplete ground state bleach recovery (2 ns, orange).	112
3.S2	(a) TAS of DES in EtOH photoexcited at 336 nm, shown as a false colourmap, with the intensity scale representing change in normalized optical density (ΔOD). The time-delay is plotted linearly from -0.5 to 10 ps then as a log scale from 10 to 100 ps. (b) Evolution associated difference spectra from the sequential global fit of the TAS of DES in EtOH photoexcited at 336 nm. (c) Selected TAS at specific Δt highlighting the absorption at 380 nm (8 ps, blue) and evidence of a long-lived photoproduct (2 ns, orange).	112
3.S3	(a) TAS of DES in cyclohexane photoexcited at 325 nm, shown as a false colourmap, with the intensity scale representing change in normalized optical density (ΔOD). The time-delay is plotted linearly from -0.5 to 10 ps then as a log scale from 10 to 100 ps. (b) Evolution associated difference spectra from the sequential global fit of the TAS of DES in cyclohexane photoexcited at 325 nm. (c) Selected TAS at specific Δt highlighting the absorption at 380 nm (8 ps, blue) and lack of a photoproduct (2 ns, orange).	113
3.S4	Ultraviolet/visible spectra of diethyl 2-(4-hydroxy-3,5-dimethoxybenzylidene)malonate (DES, $\sim 1\mu\text{M}$) in, C12–15 alkyl benzoate (magenta), ethanol (blue) and cyclohexane (green). We note the cut off in absorption of DES in alkyl benzoate below 300 nm, as the absorption of alkyl benzoate saturates the spectrometer	113
3.S5	False colourmap of the transient absorption spectra of DES in (a) AB on the surface of VITRO-CORNEUM [®] (VC) and (b) AB, showing the initial blue shifting of the excited state absorption.	114
3.S6	Zoomed-in plots of EADS k_4 and k_5 for DES in (a) VC/AB, (b) AB and (c) ethanol.	114
3.S7	Solvent-only responses. TAS of (a) VC/AB and (b) AB at 1 ps.	115

3.S8	Selected transients for solvent-only time-zero responses of (a) VC/AB (380 nm), (b) AB (380 nm), (c) ethanol (310 nm) and (d) cyclohexane (360 nm). The probe wavelength was chosen which showed the most Gaussian-like response. The solid line represents the fitted to the experimental data with a Gaussian function. The extracted full width half maxima are: (a) 80 fs, (b) 80 fs, (c) 80 fs and (d) 90 fs. These values are used as our IRFs in the corresponding global fits.	115
3.S9	Residuals from the global fit of DES in (a) VC/AB, (b) AB, (c) ethanol and (d) cyclohexane.	116
3.S10	(a) TAS at 20 ps overlaid on the EADS associated with k_4 , and (b) TAS at 2 ns overlaid with the EADS associated with k_5 . Note normalisation is based on the largest amplitude feature.	117
3.S11	UV/visible spectra of DES in (a) ethanol and (b) cyclohexane at varying durations of irradiation at 336 and 325 nm respectively at solar intensity. The percentage reduction in the UVA λ_{\max} was 3.1% and 1.6% respectively.	117
3.S12	UV/visible spectra of DES (red), ES (black) and avobenzone (blue, Avo) in ethanol. The calculated critical wavelengths are DES = 364 nm, ES = 352 nm and Avo = 378 nm, marked by the vertical line in the corresponding colour.	118
4.1	Normalised UV-visible spectra of $5 \mu\text{g mL}^{-1}$ ($\sim 16 \mu\text{M}$) solution of avobenzone in ethanol taken before and after one hour of irradiation (solid and dotted lines, respectively), using a xenon lamp at solar irradiance ($\sim 1000 \text{ W m}^{-2}$). Inset are the molecular structures of the <i>chelated enol</i> and <i>diketo</i> tautomers of avobenzone that give rise to the spectral peaks at $\sim 350 \text{ nm}$ and $\sim 270 \text{ nm}$, respectively.	123

4.2	(Left-hand column) Two-dimensional colour maps showing all transient absorption spectra (TAS) of ~ 10 mM avobenzene photoexcited at ~ 350 nm, with sample cell temperature set to 35 °C, in (a) ethanol, (b) cyclohexane, (c) diisopropyl adipate (DIA) and (d) lauryl lactate (LL). The region between 340 – 355 nm has been omitted due to oversaturation from the pump pulse. Zoomed-in false colour maps of the wavelength region > 400 nm can be found in the ESI (Fig S9). (Middle column) TAS at selected pump-probe time delays for avobenzene in (e) ethanol, (f) cyclohexane, (g) DIA and (h) LL. These plots are attained by taking vertical slices through the colour maps at the given time delay and are presented using the same $m\Delta OD$ scale as the corresponding colour map, with the same wavelength region omitted. (Right-hand column) Lineouts to show spectral features at specific probe wavelengths in (i) ethanol, (j) cyclohexane, (k) DIA and (l) LL. The features at 360 nm and 375 nm are ground-state bleach features, 395 nm and 415 nm are excited-state absorption features, and 470 nm is stimulated emission. The circles denote the raw datapoints and the solid line in each case is the fit attained using a parallel model (time constants from fitting are presented in Table 1). The time delay axis is presented on a logarithmic scale. Time delays prior to 0.1 ps are presented on a linear scale in the SI (Fig. S6 for ethanol and cyclohexane, Fig. S7 for DIA and LL).	125
4.3	UV-visible absorption spectra of low-concentration avobenzene, EHMC and octocrylene mixtures ($\sim 4 \mu\text{g mL}^{-1}$ of avobenzene, $\sim 10 \mu\text{g mL}^{-1}$ EHMC and $\sim 13 \mu\text{g mL}^{-1}$ octocrylene; 3:7.5:10 ratio), taken following irradiation using a solar simulator at regular intervals between 0 and 2 hours, in the following emollients: (a) diisopropyl adipate (DIA) and (b) lauryl lactate (LL). The molecular structure of the emollients is inset on the respective graphs. The spectra at each time point were measured three times consecutively, then averaged to attain the presented data. This was repeated twice on different days with new sample made with the same bulk ingredients, with similar results. . .	128
4.S1	Instrument response functions in (a) ethanol (378 nm probe) and (b) cyclohexane (381 nm probe), when pumped at 350 nm, through 25 μm path length, without heating. The full-width half maximum was calculated to be ~ 140 fs in (a) and ~ 80 fs in (b).	136

4.S2	(Left) False colour heat maps showing all transient absorption spectra (TAS) of ~ 10 mM avobenzene photoexcited at approximately 350 nm in (a) ethanol and (b) cyclohexane with no heat applied. (Right) TAS at selected pump-probe time delays for avobenzene in (c) ethanol and (d) cyclohexane with no heat applied. These (right) plots are attained by taking vertical slices through the corresponding false colour heat maps at the given time delay and are presented using the same scale as the corresponding heat map. The region between 340 and 355 nm has been removed due to the pump laser pulse interfering with the data.	136
4.S3	False colour heat maps (not chirp corrected) showing all transient absorption spectra (TAS) of ~ 1 mM avobenzene photoexcited at around 350 nm (a) in ethanol with no heat applied; (b) in ethanol with the sample cell heated to 35°C; (c) in cyclohexane with no heat applied and (d) in cyclohexane with the sample cell heated to 35°C. The region between 340 and 355 nm has been removed due to the pump laser pulse interfering with the data.	137
4.S4	Decay associated spectra (DAS) for heated ~ 10 mM avobenzene solutions in (a) ethanol, (b) cyclohexane, (c) DIA and (d) LL, following photoexcitation at ~ 350 nm. These were obtained by using a parallel global kinetic fit model. The associated time constants can be found in Table 1 of the main manuscript. The values in the 340 – 355 nm region have been linearly interpolated.	137
4.S5	Lineouts to show spectral features at specific probe wavelengths for ~ 10 mM avobenzene in (a) cyclohexane and (b) ethanol with no heat applied. The circles denote the raw datapoints and the solid line in each case is the fit attained using a parallel kinetic model (time constants resulting from this fitting are shown in Table S3). The features at 360 nm and 375 nm are ground-state bleach features, 395 nm and 415 nm are excited-state absorption features and 470 nm is stimulated emission (see main manuscript for further details and discussion). The time delay axis is presented on a logarithmic scale. Time delays prior to 0.1 ps are presented on a linear scale in Fig. S6.	138

4.S6	Lineouts prior to 1 ps showing spectral features at specific probe wavelengths for avobenzene photoexcited at around 350 nm (a) in ethanol with no heat applied; (b) in ethanol with the sample cell heated to 35°C; (c) in cyclohexane with no heat applied and (d) in cyclohexane with the sample cell heated to 35°C. The circles denote the raw datapoints and the solid line in each case is the fit attained using a parallel kinetic model.	139
4.S7	Lineouts prior to 1 ps showing spectral features at specific probe wavelengths for 10 mM avobenzene photoexcited at around 350 nm and heated to ~ 35°C in (a) diisopropyl adipate (DIA) and (b) lauryl lactate (LL). The circles denote the raw datapoints and the solid line in each case is the fit attained using a parallel model.	140
4.S8	Lineouts to show offset feature at (a), (b) 550 nm and (c), (d) 600 nm for ~ 10 mM avobenzene in (red) ethanol and (black) cyclohexane photoexcited at 350 nm under heating to ~ 35°C (solid lines) and at room temperature (dotted lines). The circles denote the raw datapoints and the solid/dotted line in each case is the fit attained using a parallel model. The inset figure at 600 nm is a zoom-in of the data between the $m\Delta OD$ values of 0 and 0.3. The time delay axis is presented on a logarithmic scale.	141
4.S9	False colour heat maps showing all transient absorption spectra (TAS) of ~ 10 mM avobenzene photoexcited at approximately 350 nm heated to 35°C in (a) ethanol, (b) cyclohexane, (c) diisopropyl adipate (DIA) and (d) lauryl lactate (LL), between the probe wavelengths of 400 – 720 nm. The $m\Delta OD$ scale is 10-fold reduced compared to those presented in Fig. 2 in the main manuscript, to highlight the weaker features.	142
2.S10	False colour heat maps showing the residuals attained from the parallel fitting procedure of 10 mM avobenzene, photoexcited at approximately 350 nm and heated to 35°C in (a) ethanol, (b) cyclohexane, (c) diisopropyl adipate (DIA) and (d) lauryl lactate (LL).	142

List of Tables

2.1	Extracted transient electronic absorption spectroscopy (TEAS) time constants for three homosalate solutions, following photoexcitation at their respective absorption maxima, obtained via global fitting techniques using a parallel model. ⁴⁵ Whilst the error for τ_1 is given by half the instrument response in each solvent (Fig. S4), the errors presented for τ_2 to τ_4 are those provided by the fitting software package; the quality of the fits can be gauged from the corresponding kinetic fits (Fig. 5) and residuals (Fig. S12).	77
2.S1	This table shows the difference in energies of conformer 1 and conformer 2 ($E_2 - E_1$) in the gas-phase. Both conformers were relaxed at the PBE/cc-pVTZ level of theory. Following this, the single point energies of these structures were calculated using PBE/cc-pVTZ and PBE0/cc-pVTZ, as well as the post Hartree-Fock method MP2/cc-pVDZ.	97
2.S2	Calculated singlet and triplet excited state vertical energies from the optimised ground state geometry of the <i>enol</i> form of HMS in cyclohexane using TD-DFT at the PBE0/cc-pvtz level of theory. . .	98
2.S3	Calculated singlet and triplet excited state vertical energies from the optimised ground state geometry of the <i>keto</i> form of HMS in cyclohexane using TD-DFT at the PBE0/cc-pvtz level of theory. . .	99
2.S4	Extracted transient electronic absorption spectroscopy time constants for HMS solutions upon photoexcitation at λ_{\max} , obtained via global fitting techniques using a sequential model. ³ Whilst the error for τ_1 is given by half the instrument response in each solvent (Fig. S4), the errors presented for τ_2 to τ_4 are those provided by the fitting software package; the quality of the fits can be gauged from the corresponding residuals (Fig. S12) and kinetic fits (Fig. S13).	100

2.S5	Extracted transient electronic absorption spectroscopy time constants for EHS solutions upon photoexcitation at λ_{max} , obtained via global fitting techniques using a parallel model. ³ Whilst the error for τ_1 is given by half the instrument response in each solvent (Fig. S4), the errors presented for τ_2 to τ_4 are those provided by the fitting software package; the quality of the fits can be gauged from the corresponding residuals (Fig. S12) and kinetic fits (Fig. S17).	100
2.S6	Extracted transient electronic absorption spectroscopy time constants for EHS solutions upon photoexcitation at λ_{max} , obtained via global fitting techniques using a sequential model. ³ Whilst the error for τ_1 is given by half the instrument response in each solvent (Fig. S4), the errors presented for τ_2 to τ_4 are those provided by the fitting software package; the quality of the fits can be gauged from the corresponding kinetic fits (Fig. S17).	100
3.1	Summary of rate constants. Rate-constants (k_n) resulting from the sequential global fit of the TAS of DES in VC/AB shown in Fig. 3.2a. The errors are quoted to 2σ . Rate-constants for DES in AB, ethanol and cyclohexane can be found in Supplementary Table 1.	106
3.2	Antioxidant potentials. EC_{50} (nmol) and [antioxidant]/[DPPH] values for DES, ES and several commercially available antioxidants.	107
3.S1	Rate-constants (k_n) resulting from the sequential global fit of the TAS of DES in VC/AB, AB, ethanol and cyclohexane shown in Supplementary Figures 2, 3 and 4 respectively. The errors are quoted to 2σ	118
4.1	Extracted TEAS time constants for four ~ 10 mM avobenzone solutions, following photoexcitation at ~ 350 nm and heating the sample to ~ 35 ° C, obtained by using a parallel global kinetic fit model. ⁴⁷ The error presented for τ_1 is the estimated instrument response (presented in Fig. S1 in the ESI for ethanol and cyclohexane); the errors presented for $\tau_{2,3}$ are those provided by the fitting software package. The quality of the fits is demonstrated in Fig. 2 and in the residual plots in Fig. S10 (ESI). The time constants for the room temperature TEAS measurements in ethanol and cyclohexane can be found in Table S3 of the ESI.	126

4.2	Summary of the SPF and UVA-PF percentage changes attained for Samples 1 to 5 before and after irradiation at $\sim 550 \text{ W/m}^2$ over the 300–800 nm wavelength range for 3.6 hours. Values are an average of results from 3 different samples, which are in turn an average of readings from 3 different points on the sample plate. The negative values for percentage change denote a reduction in that parameter, with the errors equalling the standard deviation of the percentage changes. Sample numbers refer to the blend composition detailed in Table S1 (ESI).	128
4.S1	Breakdown of the ingredients in the oil phases, per 25 g batch, tested for SPF and UVA-PF performance following irradiation.	143
4.S2	Amount of oil phase sample deposited onto each plate, along with amount after application and calculated final coverage for each PMMA plate analysed.	144
4.S3	Extracted TEAS time constants for two unheated $\sim 10 \text{ mM}$ avobenzene solutions, following photoexcitation at $\sim 350 \text{ nm}$, obtained by using a parallel global kinetic fit model. The error presented for τ_1 is the estimated instrument response (presented in Fig. S1); the errors presented for $\tau_{2,3}$ are those provided by the software package. The quality of the fit is demonstrated in Fig. S5.	145
4.S4	Predicted singlet and triplet excited state vertical excitation energies (in nm) for the optimised ground-state geometry of avobenzene in its <i>chelated enol</i> and <i>diketo</i> forms. The energies, and state characters indicated in brackets, were calculated using TD-DFT at the PBE0/6-311++g** level of theory. The optimised ground-state structure, calculated using DFT using the methods detailed in the main manuscript, is also shown.	146
4.S5	Calculated ΔSCF values for the optimised ground-state geometries of avobenzene (<i>chelated enol</i> and <i>diketo</i> forms), calculated using DFT at the PBE0/6-311++g** level of theory. To model the triplet state, the ground state geometry was used with the multiplicity set to 3.	147

Abbreviations

ACN	Acetonitrile
BBO	β -Barium borate
CCD	Charge-coupled device
(cc-)pVDZ	Correlation-consistent polarised valence double zeta
CHX	Cyclohexane
CI	Conical intersection
cm	Centimetres
COSMO	Conductor-like screening model
CPA	Chirped pulse amplification
DES	Diethyl sinapate
DFL	Dispersed fluorescence
DFT	Density functional theory
DIA	Diisopropyl adipate
DIS	Diisopropyl sebacate
DNA	Deoxyribonucleic acid
DPPH	2,2-diphenyl-1-picrylhydrazyl
EC ₅₀	Half maximal effective concentration
EDC	Endocrine disrupting chemical
EHMC	2-ethylhexyl-4-methoxycinnamate
EHS	Ethylhexyl salicylate (octisalate)
ER α	Estrogen receptor alpha

ESA	Excited-state absorption
ESI	Electronic supplementary information
ESIPT	Excited-state intramolecular proton transfer
EtOH	Ethanol
eV	Electronvolt
FDA	Food and Drug Administration
fs	Femtosecond
FWHM	Full width half maximum
GSB	Ground-state bleach
GVD	Group velocity dispersion
HMS	Homosalate
Hz	Hertz
IC	Internal conversion
IR	Infrared
IRF	Instrument response function
ISC	Intersystem crossing
IVET	Intermolecular vibrational energy transfer
IVR	Intramolecular vibrational redistribution
KOALA	Kinetics observed after light absorption
LIF	Laser induced fluorescence
LL	Lauryl lactate
NMR	Nuclear magnetic resonance
ns	Nanosecond
OD	Optical density
OPA	Optical parametric amplifier
PBE	Perdew–Burke–Ernzerhof
PES	Potential energy surface

ps	Picosecond
PXR	Pregnane X receptor
ROS	Reactive oxygen species
SCF	Self-consistent field
SPF	Sun protection factor
TAS	Transient absorption spectrum/spectra
TD-DFT	Time dependent density functional theory
TEAS	Transient electronic absorption spectroscopy
TR-IY	Time-resolved ion yield
UV	Ultraviolet
UVR	Ultraviolet radiation
UV-Vis	Ultraviolet-Visible
WCUS	Warwick Centre for Ultrafast Spectroscopy
WLC	White light continuum

Declarations

This thesis is submitted to the University of Warwick in support of my application for the degree of Doctor of Philosophy and has not been submitted for any previous application for a degree at any institution. It takes the form of a thesis by publication, where Chapters 2, 3 and 4 are comprised of published articles; full references are given below.

- **Emily L. Holt**, Konstantina M. Krokidi, Matthew A. P. Turner, Piyush Mishra, Timothy S. Zwier, Natércia das Neves Rodrigues and Vasilios G. Stavros, Insights into the photoprotection mechanism of the UV filter homosalate, *Physical Chemistry Chemical Physics*, 2020, **22**, 15509–15519.
- Michael D. Horbury, **Emily L. Holt**, Louis M. M. Mouterde, Patrick Balaguer, Juan Cebrián, Laurent Blasco, Florent Allais and Vasilios G. Stavros, Towards symmetry driven and nature inspired UV filter design, *Nature Communications*, 2019, **10**, 4748.
- **Emily L. Holt**, Natércia das Neves Rodrigues, Juan Cebrián and Vasilios G. Stavros, Determining the photostability of avobenzone in sunscreen formulation models using ultrafast spectroscopy, *Physical Chemistry Chemical Physics*, 2021, **23**, 24439–24448.

The work presented, including the acquisition and analysis of data, was carried out by the author except in the cases outlined below:

- In Chapter 2, the time-resolved gas-phase spectroscopy was conducted by K. M. Krokidi with assistance from N. d. N. Rodrigues. The frequency-resolved gas-phase data was collated by P. Mishra in the laboratory of T. S. Zwier. The

computational aspects of the manuscript were performed predominantly by M. A. P. Turner, with contributions from the author and K. M. Krokidi. The manuscript was written with contributions from K. M. Krokidi, M. A. P. Turner and N. d. N. Rodrigues.

- In Chapter 3, the molecule studied was synthesised by L. M. M. Mouterde and F. Allais. Endocrine disruption measurements and assays to measure antioxidant activity were performed by P. Balaguer, L. M. M. Mouterde and F. Allais. The author and M. D. Horbury contributed equally to the collection of the ultrafast spectroscopy data and subsequent analysis. M. D. Horbury was the main contributor to the writing of the manuscript. These declarations are made in accordance with those in the published article.
- In Chapter 4, the making and SPF/UVA-PF testing of the oil phase samples was conducted by N. d. N. Rodrigues, with guidance from J. Cebrián.

As this is a thesis by publication, further details of author contributions are provided in Appendix A2.

Parts of the introduction to this thesis have been previously published by the author in the following:

- **Emily L. Holt** and Vasilios G. Stavros, Applications of ultrafast spectroscopy to sunscreen development, from first principles to complex mixtures, *International Reviews in Physical Chemistry*, 2019, **38(2)**, 242–285.

Abstract

Sunscreen formulations have been developed to provide an artificial barrier against the adverse health implications of overexposure to solar ultraviolet (UV) radiation. The work contained within this thesis employs a combination of time-resolved (ultrafast) and steady-state spectroscopy, alongside other complementary experimental and computational techniques, to identify molecular relaxation pathways in current and candidate UV filters following photoexcitation. The nature of these pathways are, in turn, insightful for assessing a filter's suitability for sunscreen use. Increasing existing knowledge on sunscreen filters has been made necessary due to efficacy and environmental concerns with the current, approved options.

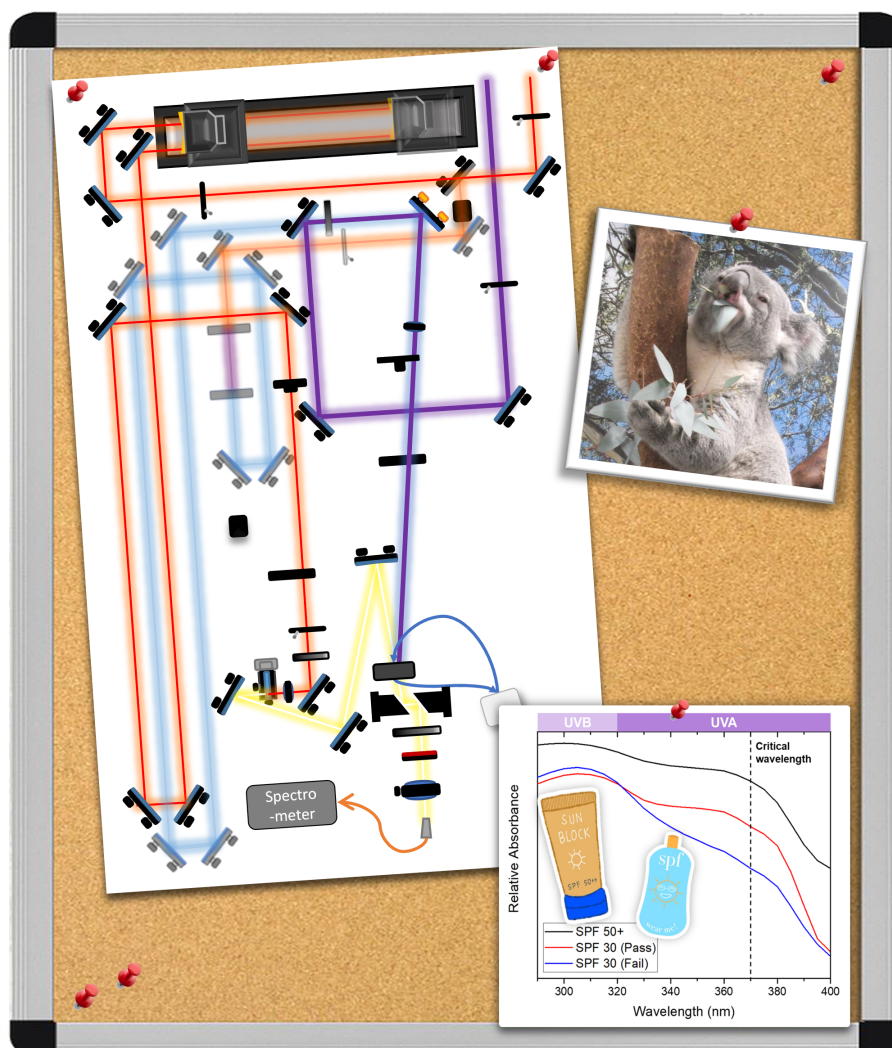
Chapter 2 details the photoprotection mechanism of homosalate (HMS), a worldwide-approved UVB (290 – 320 nm) filter in the salicylate family of molecules. Experiments and supporting calculations, both in vacuum and in solution, conclude that HMS undergoes ultrafast excited-state intramolecular proton transfer upon photoexcitation of an *enol* tautomer. Then, once in the *keto* tautomer, excess energy is largely dissipated non-radiatively and the original (ground-state) *enol* tautomer is returned, which is favourable from a photophysical viewpoint.

The remainder of the thesis focuses upon UVA (320 – 400 nm) filters. In Chapter 3, the merits of selective molecular design are explored: specifically, a nature-inspired sinapate compound was symmetrically functionalised to have equivalent *cis* and *trans* isomers. This maintains the beneficial photophysical properties of the UV filters found in plant leaves, whilst simultaneously alleviating adverse effects that can be induced by *cis-trans* photoisomerisation, as seen in related cinnamates.

Thereafter, Chapter 4 uses the widely used UVA filter avobenzene as a case study to link ultrafast spectroscopy results to industry-standard *in vitro* sun protection factor values, via the observation of the recovery of ground-state bleach spectral features. Together, Chapters 3 and 4 then advance to mimicking the application of sunscreen formulations to the skin surface. This was attained using a synthetic skin mimic (Chapter 3) and a heated sample interaction region to model skin surface temperature (Chapter 4). Cosmetics grade emollients were used as solvents in both cases, to model a completed sunscreen blend more closely.

Chapter 1

Introduction



Parts of this Chapter are based upon a previous publication:
E. L. Holt and V. G. Stavros, *Int. Rev. Phys. Chem.*, 2019, **38(2)**, 243–285.

1.1 Quantum mechanics for spectroscopy

All forms of spectroscopy facilitate the observation of interactions between light (encompassed by the electromagnetic spectrum) and matter (atoms and molecules). Between them, they share several principles that govern the intensity of spectral features and the linewidths observed.¹ The underlying commonalities of the techniques used in this thesis will be outlined in the sections to follow.

1.1.1 Quantum nature of light

Quantum theory, the idea that energy can be subdivided into finite *quanta* (amounts), is essential for fully understanding the behaviours of atoms and molecules, as the subatomic particles from which they are consisted cannot be entirely governed by the classical mechanics laws proposed by Isaac Newton in the seventeenth century.^{2,3} The realisation over time was that the classical laws relating to forces acting on very small particles, and their subsequent motion, were not valid.⁴ The first steps towards explanations for the behaviours of these tiny particles, quantum mechanics, were measurements on black bodies, so-called as they are objects that can uniformly absorb all frequencies of electromagnetic radiation.⁵ These objects, in turn, emit black-body radiation, which is determined by the temperature of the body at thermodynamic equilibrium. One relevant example of a black body (albeit not an ideal black body) for this thesis is the Sun, which has an equilibrium temperature of 5778 K.⁶ In 1900, following observations on black body emitters, Max Planck was the first to postulate that the energies of “electromagnetic oscillators” are limited to discrete values. This became known as the quantisation of energy, with the permitted energies governed by the following formula:

$$E = nh\nu, n \in \mathbb{Z} \tag{1.1}$$

where E is the energy of the system, h is Planck’s constant (6.62608×10^{-34} J s), ν is the frequency of the “oscillator”, finally $n \in \mathbb{Z}$ denotes that n is an integer. It is however noted that, in his seminal work of 1900,⁷ Planck did not state the relation in Equation 1.1 explicitly.⁸ Using these “quantum” assumptions, Planck also derived the expression for the emission of black body radiation, known as the Planck’s law (or the Planck distribution), given in Equation 1.2. There are several equivalent textbook definitions of this law, depending on whether the law is given in terms of frequency, wavelength or angular frequency; furthermore, variables such as ν are given by c/λ instead. The form given here (Equation 1.2) is for the calculation of the total irradiance I of a black body at a temperature T , as a function of wavelength λ .

$$I(\lambda, T) = \int \frac{2\pi hc^2}{\lambda^5} \left(\frac{1}{e^{\frac{hc}{\lambda k_B T}} - 1} \right) d\lambda \quad (1.2)$$

Once again, h is Planck's constant, k_B is Boltzmann's constant ($1.38066 \times 10^{-23} \text{ J K}^{-1}$) with c denoting the speed of light through a given medium. Outside of atmospheric interference, the measured solar spectrum is very similar to that predicted for an ideal black body by Planck's law.

1.1.1.1 Wave-particle duality

Following on from the observations made by Planck that energy can be quantised, Einstein discovered the photoelectric effect: the notion that electromagnetic radiation, which thus far had only been considered as a transverse wave, also had particle-like properties. These particles, from their original name of *light quanta*, eventually became known as *photons*.⁹ The photoelectric effect was observed from the conditions needed to eject electrons from the atoms of a metal; specifically, an energetic threshold needed to be surpassed for electrons to be ejected. Moreover, the kinetic energy of the ejected electrons had a linear dependence on the frequency of the incident light, but was independent of the intensity of the light.¹⁰ Thereafter, the relation governing the wave-like characteristics of particles was made by de Broglie. The eponymous de Broglie wavelength relates the momentum p of any particle to a wavelength λ : $\lambda = \frac{h}{p}$.¹¹ Many experiments since this discovery, such as the Davisson-Germer experiment, have confirmed de Broglie's theory.¹² As such, it became clear that the assumptions of classical mechanics were invalid at the atomic level.

1.1.1.2 Wavefunctions and the Schrödinger equation

It is from the concept of wave-particle duality that the notions of quantum mechanics were formed. Light propagation can be described by a quantum mechanical function, with the properties of a classical wave, which upon detection collapses as its particle nature is revealed.¹³ Quantum mechanics relies on these *wavefunctions*, most commonly denoted by Ψ , which are mathematical functions that contain all the information that it is possible to know about the position and motion of the particle being described.¹⁴ The general form of the Schrödinger equation (Equation 1.3), penned by Erwin Schrödinger in 1926,¹⁵ is proposed to be able to determine the wavefunction for any given system, as a function of electron position, \mathbf{r} and nuclear position, \mathbf{R} .

$$\hat{H}\Psi(\mathbf{r}, \mathbf{R}) = E\Psi(\mathbf{r}, \mathbf{R}) \quad (1.3)$$

In this time-independent form, the Schrödinger equation defines an eigenvalue problem, with Ψ being the eigenfunction of \hat{H} with corresponding eigenvalues E , the latter denoting the possible measured values of the energy of the system. \hat{H} is the so-called *Hamiltonian operator* that carries out operations on the wavefunction. The Hamiltonian is commonly expressed as the sum of operators corresponding to the total kinetic (\hat{T}) and potential energies (\hat{V}) of the system. \hat{T} accounts for the sum of kinetic energy contributions from the nuclei and electrons, with \hat{V} governed by nuclear-nuclear, electron-electron and nuclear-electron interactions, including Coulombic interactions. The expression for \hat{H} is shown in its general form for N particles in Equation 1.4. The variable m denotes the mass of the particle.

$$\hat{H} = \underbrace{-\frac{\hbar^2}{2} \sum_{i=1}^N \frac{1}{m_i} \nabla_i^2}_{\hat{T}_n} + \underbrace{V(\mathbf{r}_1, \mathbf{r}_2, \dots, \mathbf{r}_N, t)}_{\hat{V}} \quad (1.4)$$

For completeness, the Laplace operator (or Laplacian) of particle i , denoted by ∇_i^2 , is defined below.

$$\nabla_i^2 = \frac{\partial^2}{\partial x_i^2} + \frac{\partial^2}{\partial y_i^2} + \frac{\partial^2}{\partial z_i^2}$$

There is also a time-dependent version of the Schrödinger equation, which models the evolution of the wavefunction over time, shown in Equation 1.5.

$$\hat{H} |\Psi\rangle = i\hbar \frac{\partial |\Psi\rangle}{\partial t} \quad (1.5)$$

The constant \hbar is known as the reduced Planck's constant and is equivalent to $\frac{h}{2\pi}$. Analogously to vectors in a Euclidean space, $|\Psi\rangle$ can be written as a linear combination of basis state vectors ψ_1 and ψ_2 for example: $|\Psi\rangle = c_1 |\psi_1\rangle + c_2 |\psi_2\rangle$ with $c_1, c_2 \in \mathbb{C}$. This expression can also be generalised into n dimensions. The term *linear combination* will recur throughout this thesis and this is the formal definition (I feel obliged to include one as a former mathematician).

Definition 1.1.1 (Linear combination). *The vector \mathbf{v} in a vector space V is a linear combination of the vectors $\mathbf{u}_1, \mathbf{u}_2, \dots, \mathbf{u}_n$, if there exists scalars a_1, a_2, \dots, a_n in a field K such that $\mathbf{v} = \sum_{i=1}^n a_i \mathbf{u}_i$.*

It is noted, however, that the Hamiltonian can be simplified by assuming the Born-Oppenheimer approximation, which will become relevant in the computational calculations section of this thesis (Section 1.3.7). This approximation states that, as protons and neutrons are so much larger than an electron (by a factor of ~ 1800), that

nuclei can be assumed to be stationary when electrons move relatively to them.¹⁶ In turn, this ensures that the wavefunctions can be decoupled into nuclear and electronic coordinates, *i.e.* $\Psi(\mathbf{r}, \mathbf{R}) \Rightarrow \Psi(\mathbf{r}) \circ \Psi(\mathbf{R})$. Under this assumption, the Hamiltonian of the system is equivalent to the sum of the Hamiltonians for each individual particle.

Further useful information can be attained from the wavefunction: for example, the square of the wavefunction ($\Psi^*\Psi$) is proportional to the probability of finding a particle (*e.g.* a photon or electron) in a particular region of space. This probability density is known as the Born interpretation of a wavefunction, named after German physicist and mathematician Max Born. The atomic orbitals[†], or one-electron wavefunctions, could be pictured as bounded regions of space at which an electron around a nucleus can be predicted to be found with a given probability. Although, it is impossible to define the momentum and the location of a particle simultaneously, according to Heisenberg's uncertainty principle,¹⁷ quantitatively represented by the relation in Equation 1.6.^{18,19}

$$\Delta p \Delta x \geq \frac{\hbar}{2} \quad (1.6)$$

In this Equation, Δp and Δx are the uncertainties in linear momentum and position respectively. In addition, there is an analogous version with the relationship between the uncertainties between energy (E) and time (t), which is given by Equation 1.7.²⁰

$$\Delta E \Delta t \geq \frac{\hbar}{2} \quad (1.7)$$

This will be returned to later in this thesis during the discussion of ultrafast pulse generation in Section 1.3.1.

1.1.1.3 Franck-Condon principle

The Franck-Condon principle is so-called following its postulation by J. Franck and E. Condon in the 1920s.^{21,22} The rule designates the intensity of a vibronic transition stating that, following the absorption of a photon, the subsequent transition will be more likely to occur where there is the greatest overlap between vibrational wavefunctions. This is represented in diagram form in Fig. 1.1. A vibronic transition is nominally determined, due to changes in vibrational and electronic energy levels of a molecule occurring simultaneously. When discussing the Franck-Condon region in the presented papers, this refers to the potential energy surface (PES) that is reached

[†]These can be described as a combination of four quantum numbers: the principle quantum number n ; the orbital angular momentum (azimuthal) quantum number $l = n - 1$, denoting whether the orbitals is s, p etc.; the magnetic quantum number ($m_l = -l, -l + 1, \dots, l - 1, l$); finally the spin quantum number $m_s = \pm \frac{1}{2}$

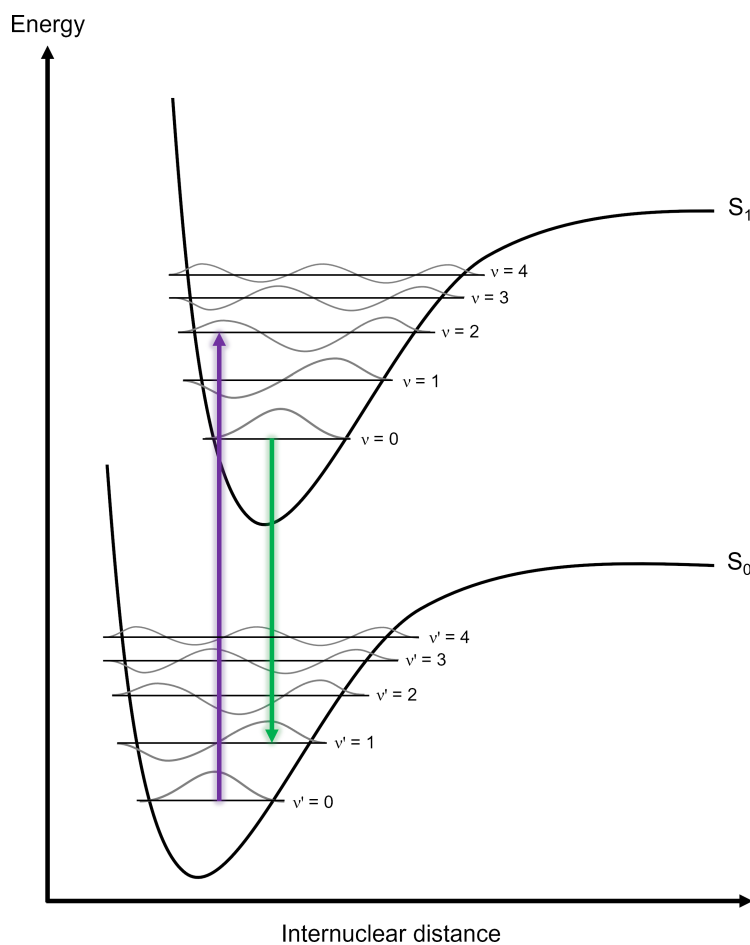


Figure 1.1: Two-dimensional representation of the electronic ground state (S_0) and first electronic excited state (S_1) PESs and the corresponding vibrational wavefunctions. The purple arrow represents the most likely absorption transition, with the green arrow the most likely emission, according to the Franck-Condon principle.

following the vertical transition from the ground state, induced by the incoming photon. Commonly, this references a transition from the ground vibrational state ($\nu' = 0$) from the S_0 to a vibrational level ($\nu = n$) of the S_1 . The rule also applies to relaxation, where vertical transitions are most favourable. The principle is also applicable to molecules dissolved in liquids, which are the model systems detailed within this thesis.²³

The Franck-Condon principle can also be defined quantitatively, known as a Franck-Condon factor, which is defined in Equation 1.8. In this equation, $\psi_{\nu'}$ and ψ_{ν}

are wavefunctions of vibrational levels in the ground and excited states respectively.

$$S_{\nu',\nu}^2 = \left| \int \psi_{\nu'}^* \psi_{\nu} d\tau \right|^2 \quad (1.8)$$

This quantitative form is derived from the expression for the transition dipole moment, which is given by the expression in Equation 1.9. In this equation, μ is the electronic dipole moment operator, ψ_i is the initial wavefunction and ψ_f^* is the complex conjugate of the final wavefunction.

$$\mu_{fi} = \int \psi_f^* \mu \psi_i d\tau \quad (1.9)$$

A transition dipole moment is induced during an electronic transition (due to electron displacement) and persists only for the lifetime of the transition. The probability of a transition occurring is proportional to this value, governed by the relation $P \propto |\mu_{fi}|^2$. These expressions both assume the Born-Oppenheimer approximation.

More details on potential energy surfaces A system of N atoms can be defined uniquely by $3N$ Cartesian or spherical coordinates for each atom, with the PES a representation of the total energy of the N -atom system as a function of the location of the atoms within a molecule.²⁴ As only the relative positions of each atom in the molecule are required to define a PES, the number of coordinates is reduced to $3N - 6$ (equivalent to the number of vibrational degrees of freedom in the molecule) by removing the need to define the overall translation and rotation of the system, each removing three degrees of freedom.²⁵

In order to define a PES, where energy is defined as a function of internuclear distance, the Born-Oppenheimer approximation is implemented to assume the nuclei are fixed. This approximation also ensures that a separate PES can be defined for each electronic state. Although in reality PESs are multi-dimensional, these are often depicted two-dimensionally along one key reaction coordinate (see Fig 1.1 for an example).

1.2 Light-induced molecular processes

The Grothuss-Draper law states that only light that is absorbed by a chemical entity can induce photochemical change, with the Stark-Einstein law stating that, in general, for every photon absorbed, one molecule is excited. With the quantum mechanical fundamentals established, the photochemical and photophysical changes

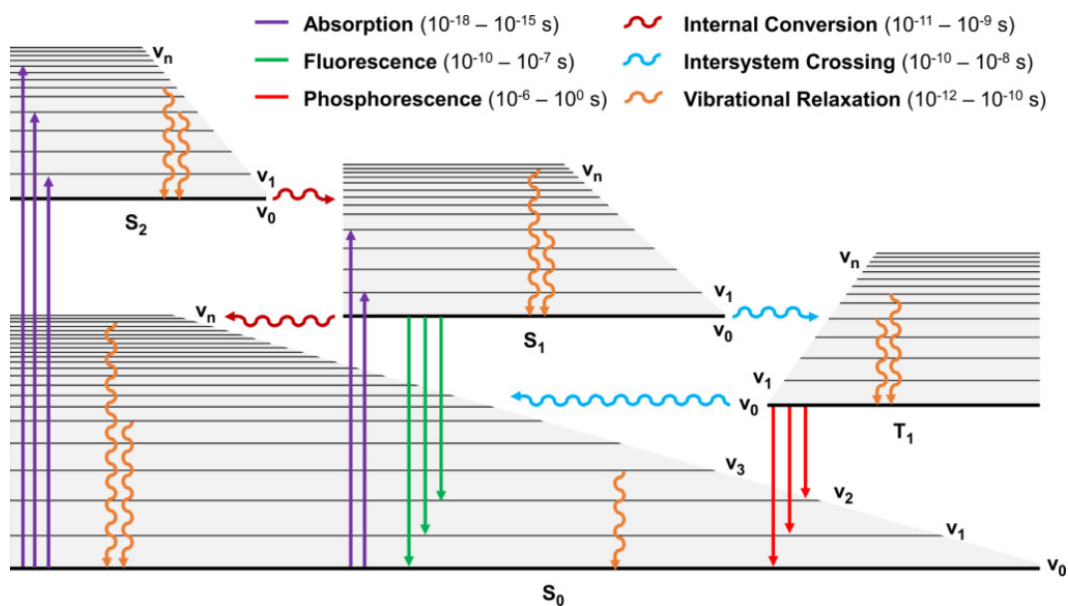


Figure 1.2: A summary of the main photophysical processes that can occur following photoexcitation of a sample, in the form of a Jablonski diagram. Singlet states are denoted S_i , the lowest energy triplet state is denoted T_1 . Vibrational modes are denoted by ν_n . Radiative processes are denoted by the solid lines: absorption in purple, fluorescence in green and phosphorescence in red. Non-radiative processes are denoted by the wavy lines: internal conversion ($S_i \rightarrow S_j$) in dark red, intersystem crossing ($S_i \rightarrow T_j$) in light blue and vibrational relaxation in orange. The timescales for each process²⁷ are also given.²⁸

that are induced as consequences of these laws are explored; Fig. 1.2 summarises the intramolecular processes that can occur following photoexcitation. It is noted that exceptions to the Stark-Einstein law (such as two-photon absorption and non-linear optical processes) can occur upon intense irradiation from certain light sources, such as lasers; examples of these multiphoton effects²⁶ and are addressed in the Experimental section of this thesis.

1.2.1 Absorption

An electronic, vibrational or rotational transition is induced upon the absorption of an incident photon, with the transitions induced being wavelength dependent. The Franck-Condon principle, as earlier described in Section 1.1, determines the most probable electronic transition upon molecular absorption of radiation. Specifically, in this thesis, UV photons need to be absorbed by the chromophores to be suitable for use as a sunscreen filter. The magnitude of an absorption feature is governed by the Beer-Lambert law, which states that the absorbance, A at wavelength λ is

proportional to the molar absorption coefficient (ε) of a substance at λ , the path length (l) of the sample in centimetres and the concentration (c) of the sample.²⁹ It is given in Equation 1.10. This equation also shows the logarithmic dependence on the recorded absorption between the intensity of the incident light (I_0) and the transmitted light (I_t).

$$A(\lambda) = \varepsilon(\lambda)lc = \log_{10} \left(\frac{I_0(\lambda)}{I_t(\lambda)} \right) \quad (1.10)$$

In general, the electronic transitions of interest in this thesis are governed by selection rules. Assuming a non-zero transition dipole moment (defined in Equation 1.9), several selection rules must also be satisfied for absorption to take place. The first selection rule states that there should be no change in the spin state of the molecule from the ground to excited state: the spin multiplicity should remain at $2S + 1$. Secondly, the angular momentum of the system must also be conserved; as a photon possesses an angular momentum (l) of ± 1 , it follows that, for the system, $\Delta l = 0$.

1.2.2 Deactivation of excited states

Following the absorption of a photon, the photoexcited molecule has excess energy that can be dissipated via a number of possible photophysical pathways, to return to equilibrium. These are indicated in Fig. 1.2 and are individually explored in more detail below.

1.2.2.1 Intramolecular non-radiative processes

Non-radiative processes are those that do not result in the emission of a photon upon relaxation. Several intramolecular processes of this type are possible, and are indicated by the wavy lines in the Jablonski diagram in Fig. 1.2. Processes that emit a photon are termed *radiative* processes; these are denoted by the straight arrows in Fig. 1.2 and will be described in a later section (Section 1.2.2.4).

The first of these intramolecular non-radiative processes, *internal conversion* (IC), is an electronic transition that does not result in a change of spin state, nor the emission of a photon. If, however, the spin multiplicity of the electronic states changes during the transition, typically from singlet to triplet or vice versa, this is known as *intersystem crossing* (ISC). Both ISC and IC are dependent on the energy gap and the coupling of vibrational modes between the two states: in general, the smaller the energy gap between the two states, the faster the rate of the process occurring. However, ISC is technically *spin forbidden* and occurs over very long

timescales ($> \mu\text{s}$). These pathways can be more commonly accessed when a molecule is cryogenically cooled (as the effect of oxygen quenching is minimised and the number of vibrational modes decreases), or when a heavy-atom functional group is added, due to an increase in spin-orbit coupling. In addition, El Sayed’s rule states that ISC is also more likely to proceed if the state characters between the two spin states are different from one another (*e.g.* $^1n\pi^* \rightarrow ^3\pi\pi^*$).³⁰

Intramolecular vibrational redistribution (IVR) is the process responsible for vibrational energy being transferred across vibrational modes that are isoenergetic or lower in energy than the original, within the same electronic state of a molecule. In general, the larger the molecule, the faster that IVR can occur, owing to the larger number of vibrational modes to which the energy can be redistributed. The relations between transition rate (Γ) to the accessible density of states (ρ) and the vibrational state coupling (V_{if}) are a consequence of Fermi’s golden rule, which is reproduced in Equation 1.11.³¹

$$\Gamma_{i \rightarrow f} = \frac{2\pi}{\hbar} \rho |V_{if}|^2 \quad (1.11)$$

The comparatively larger energy gap between the S_1 and S_0 states relative to higher-lying states ($S_{n-1} \leftarrow S_n$), ensures that the rate of IC and IVR progresses more slowly as relaxation occurs, no matter which state is initially populated. The much increased rate of IC and IVR in higher-lying states forms the basis for Kasha’s rule of fluorescence (discussed in more detail in Section 1.2.2.4).

1.2.2.2 Conical intersections

A conical intersection (CI) is a set of molecular coordinates whereby there is a degeneracy (an “intersection”) between two or more potential energy surfaces (PESs) of a molecule. It follows that CIs occur at points where the PESs involved are isoenergetic and that the nuclear geometries of these states will be the same at these points along the PES.^{32–38} At a CI, the $3N$ -dimensional PES for a molecule of N nuclei, is reduced to a $3N - 8$ -dimensional subspace of a $3N - 6$ -dimensional space of vibrational modes.³⁹§ The name arises from the topography of the converging PESs resembling two cones, with the crossing point represented at the meeting point of their respective vertices. CIs can have a crucial role in the relaxation transitions from excited to ground electronic states of molecules. There is experimental evidence (particularly from femtosecond spectroscopy) of a “seam” that connects the PESs of excited molecules to their ground state,²⁴ and it is via this route that IC can

§For a diatomic or linear polyatomic molecule, the dimensionality becomes a $3N - 7$ -dimensional subspace of a $3N - 5$ -dimensional space, due to there being one fewer rotational degrees of freedom, although the occurrence of a CI in a linear molecule is rare.⁴⁰

occur. Furthermore, in the region of a CI, the Born-Oppenheimer approximation is no longer a valid assumption. As a result, CIs facilitate non-adiabatic processes, such as photoisomerisation and photodissociation.^{41,42} It is noted here that ISC progresses via an alternative singlet-triplet crossing.⁴³

1.2.2.3 Excited-state intramolecular proton transfer

Often, a photochemical change will accompany the photophysical decay processes outlined above, which can result in the formation of a new molecular species or a reaction intermediate. For example, in Chapter 2 during the study of the salicylate family of UVB filters, it was found that the photoexcited molecules undergo excited-state intramolecular proton transfer (ESIPT) following photoexcitation. Thereafter, the S_1 state of the tautomer could dissipate its excited-state energy in a branched manner. ESIPT mechanisms also form part of a branched decay mechanism for avobenzene, the subject of Chapter 4. ESIPT takes place in aromatic compounds with proton donor and acceptor groups in the *ortho* position, and can be briefly described as a process whereby photoexcited molecules relax via tautomerisation (forming two species that readily interconvert) by the transfer of protons.⁴⁴ There are several excellent reviews on ESIPT, which include descriptions of molecules that undergo this process.⁴⁴⁻⁴⁷

1.2.2.4 Intramolecular radiative processes

Radiative decay processes, which can be considered to be the reverse process to absorption, involve the emission of a photon and are governed by the same selection rules as absorption. There are two types of radiative decay: emission originating from a singlet state, *fluorescence*, and from a triplet state, *phosphorescence*, represented in Fig. 1.2 by the solid green and red arrows, respectively. Phosphorescence is technically *spin forbidden* and therefore unlikely to occur, however the likelihood is increased in molecules that contain a heavy atom, or upon cryogenic cooling due to the increase in proportion of molecules relaxing via ISC. An example of such effects is discussed in the Results and Discussion section of Chapter 2.^{48,49} If phosphorescence does proceed, the timescales are far longer than those for fluorescence (as shown in Fig. 1.2), as the transition is not kinetically favourable.

The energy of the emitted photon will correspond to the difference in energy between the original (most commonly $S_1(\nu = 0)$ for fluorescence)⁵⁰ and final, lower energy state ($S_0(\nu > n)$), according to Kasha's rule, with the frequency of the emitted photon governed by the expression $E = h\nu$. The difference between the peaks of

absorption and emission is known as Stokes shift, and its observation arises from the fact that vibrationally driven processes are completed faster than competing radiative pathways, thus reducing the energy gap between the emissive state and the initially populated state.

The proportion of photoexcited molecules that fluoresce can be quantified; this value is known as quantum yield (Φ_F). Although one way of determining quantum yield experimentally is given in Chapter 2, it can also be determined via the rates of competing photophysical processes, according to the relation in Equation 1.12.⁵¹

$$\Phi_F = \frac{k_F}{k_F + k_{ISC} + k_{IC}} \quad (1.12)$$

This can be particularly useful to verify experimentally determined quantum yields, if reliable rate constants for each process are known.

1.2.2.5 Intermolecular processes

A molecule may also dissipate some of its excess vibrational energy as heat to surrounding molecules by colliding with one another, for example a chromophore in solution could dissipate its vibrational energy to the solvent, known as *intermolecular vibrational energy transfer* (IVET). This results in the “vibrational cooling” of the donor molecule. Of course, such an energy transfer would not be possible in the gas phase experiments presented in this thesis, as the sample molecules are isolated.

Further to these inelastic collisions between molecules, electronic excited states of a donor molecule (also known as a sensitizer) can transfer their excess energy to an acceptor (also known as a quencher), which facilitates the donor to decay to a lower electronic excited state. The acceptor, in turn, is promoted to a higher excited state. The donor-acceptor pairings are relevant for sunscreen applications: for example, the UVB filter 2-ethylhexyl-4-methoxycinnamate (EHMC) increases the rate of degradation of avobenzone⁵² (the subject of Chapter 4) via triplet state energy transfer, which in turn induces photolysis and photoisomerisation in the cinnamate.^{53,54} It is for this reason that the combination of EHMC and avobenzone should not be used. The photostability of avobenzone is improved when it is combined with octocrylene, a UVB absorber in its own right, which acts as a triplet quencher.⁵⁵ As a result, intermolecular energy transfer should be considered carefully for optimum photostability and UV protective coverage.²⁸ Intermolecular distances of < 10 nm are required for donor-acceptor pairings to interact via singlet-singlet energy transfer, reducing to < 1 nm for triplet-triplet energy transfer.⁵⁶

1.3 Experimental

In this section, experimental and instrumentation details surplus to the Methods provided in the published papers in later Chapters will be detailed, beginning with ultrafast spectroscopy. Ultrafast techniques in both the gas and condensed phases can offer a crucial insight into the mechanism of action of both current and potential UV filters upon photoexcitation, which in turn can contribute to the determination of their effectiveness. In this thesis, particular emphasis is placed upon the use of transient electronic absorption spectroscopy (TEAS) for the investigation of sunscreens, with its specifics in the solution-phase discussed further in Section 1.3.2. Two TEAS setups were used to gather the ultrafast spectroscopy data presented in this thesis; this was necessary as one of the setups facilitated observation of time delays beyond 2 ns. As such, the commonalities and differences between the setups are outlined in this section.

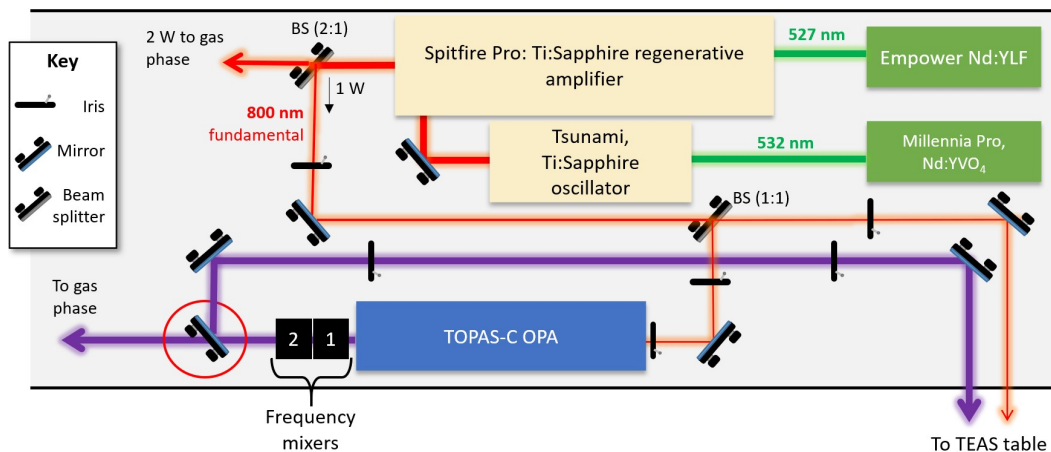
1.3.1 Generation of ultrafast laser pulses

The word “laser” is an acronym for light amplification by stimulated emission of radiation. Since the first laser was successfully built in 1960, laser technology has progressed significantly; an in-depth appraisal of the history of laser development can be found elsewhere.^{57,58} This section specifically details the lasers that generate ultrafast pulses in our two laser laboratories.

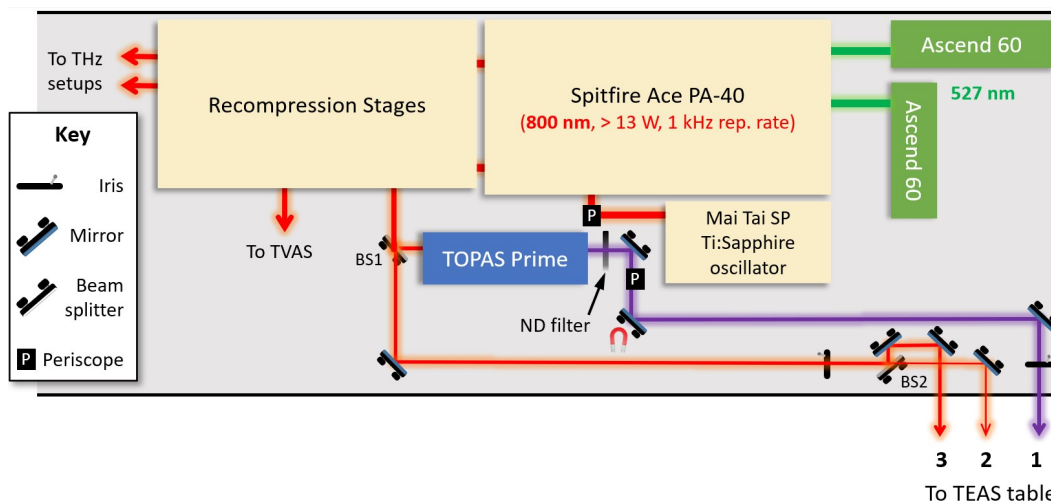
Following on from the discussion of Heisenberg’s uncertainty principle in Section 1.1.1.2, the derived relation between the energy-time uncertainties of a system, given in Equation 1.7, has implications for the widths of ultrafast laser pulses that can be attained, namely, a shorter pulse duration (Δt) implies a larger spectral bandwidth ($\Delta\nu$).⁵⁹ For Gaussian-profiled pulses as generated in our laboratories, the relation, assuming the pulses are transform limited, is defined in Equation 1.13.⁶⁰

$$\Delta t \Delta \nu = 0.441 \tag{1.13}$$

This relationship means that a shorter pulse in time results in a compromise for the narrowness of the spectral bandwidth. The resulting broader pulses coherently excite more vibrational levels within the system being studied, limiting spectral selectivity.⁵⁹ The ultrafast laser pulses generated in the Laboratory E0.19 in the Department of Chemistry, using the setup shown in Fig. 1.3a are shared between the TEAS and gas-phase time-resolved ion yield (TR-IY) setups, the latter is to be discussed further in Section 1.3.4. In the Warwick Centre for Ultrafast Spectroscopy



(a) Laser table layout in Laboratory E0.19 in the Department of Chemistry at the University of Warwick, for the generation of ultrafast laser pulses. The circled mirror is removed when the TOPAS-C OPA is needed for the generation of the pump pulses in the gas phase.



(b) Laser table layout in the Warwick Centre for Ultrafast Spectroscopy (WCUS) at the University of Warwick. The ultrafast pulses are generated and then guided towards the spectroscopy setup needed.

Figure 1.3: Schematics (not to scale) of the laser table components used to generate the ultrafast pulses required for the spectroscopy data presented in this thesis. Thereafter, the optical path of the pump and probe pulses to the respective TEAS tables is also shown.

(WCUS), the generated pulses are shared equally between four optical tables, as depicted in Fig. 1.3b. To clarify, in addition to TEAS, there are three ultrafast experiments that are possible to perform in WCUS, with each having their own optical table, these are: transient vibrational absorption spectroscopy (TVAS), optical pump terahertz probe (OPTP) spectroscopy, and terahertz pump, terahertz

probe spectroscopy (TPTP). The origins of their beamlines are indicated by the three arrows arising from the recompression stages in Fig. 1.3b; these beams then follow a series of optics to their individual optical tables. TVAS implements a pump range of $\sim 235 \text{ nm} - 10 \text{ }\mu\text{m}$ and probe range of $1\text{-}15 \text{ }\mu\text{m}$, with variable temporal pump pulse duration between $\sim 50 \text{ fs} - \sim 1 \text{ ps}$, made possible by an optical grating. The publication by Coxon *et al.*⁶¹ provides a more-detailed description of the specifics of the TVAS setup. OPTP offers a pump range of between $\sim 235 \text{ nm}$ and $15 \text{ }\mu\text{m}$. The specificities of this setup are outlined in more detail by Monti *et al.*,⁶² with several reviews of instrumentation and applications of this technique available in recent reviews.^{63,64} Finally, the THz pump, THz probe (TPTP) experiment also follows the evolution of the far-infrared evolution of a sample like OPTP, but in this case photoexcitation is also induced by a THz laser pulse, with examples of experimental setups and applications of the technique available elsewhere.^{65,66}

The specific lasers used to generate the pulses differ between the two laboratories, the type of lasers used are equivalent. Therefore, the action of these lasers will be broadly described, with any differences between the two laboratories discussed in more detail where appropriate. Both laboratories generate a fundamental 800 nm pulse train to split between the different experiments, using Ti:Sapphire oscillators, seeded by green lasers. Both the Ascend 60 and Empower lasers (Spectra-Physics) are four-level, Q-switched neodymium-doped yttrium lithium fluoride (Nd:YLF) lasers, and the Millenia Pro is a continuous wave, four-level laser that contains a neodymium-doped yttrium orthovanadate (Nd:YVO₄) crystal; their emission is frequency-doubled to the required 527 nm and 532 nm wavelengths, respectively. For example, the Millenia laser is diode pumped and uses a lithium triborate crystal (LiB₃O₅) to attain frequency doubling. A *Millenia*-type laser is contained within a pump chamber in the Mai Tai SP, which is also a Nd:YVO₄ diode pumped, continuous wave source that is frequency doubled to 532 nm .⁶⁷ The green lasers subsequently photoexcite the Ti:Sapphire laser mediums.

The Ti:Sapphire oscillators are examples of mode-locked lasers. Mode-locking facilitates the generation of ultrashort laser pulses, on the order of femtoseconds or picoseconds, and results from a forced coherence between the axial modes present within a laser cavity.⁶⁸ These modes summatively combine to create a series of very narrow (in time) light pulses, with the electric field vector of these pulses equalling the sum of the electric field vectors for each mode. The peak amplitudes of the laser pulses are separated in time by the relation $t = \frac{2L}{c}$, where L is the length of the laser cavity, and c is the speed of light through the cavity. The central wavelength of the Ti:Sapphire oscillators is 800 nm , with a bandwidth of around $40\text{--}60 \text{ nm}$. However,

the pulses generated after mode locking, despite being short, are not of the required energy. As a result, a further amplification stage is required, known as chirped pulse amplification (CPA). CPA is a necessary step in generating high energy femtosecond laser pulses used in pump-probe techniques, including those implemented in this thesis. It is worth noting that Strickland and Mourou, who discovered CPA, were awarded the 2018 Nobel Prize for Physics for this discovery.^{69,70} In short, CPA is achieved by receiving a short pulse, then a pair of gratings stretch the incoming pulse in time (by a factor of ~ 1000), to significantly reduce its peak power. Then, the pulse can be reamplified and compressed using a second grating pair, creating the short and powerful laser pulses required.

In the setup within the Department of Chemistry, this amplification takes place in the Spitfire XP regenerative amplifier (Spectra-Physics), which has a 800 nm, 3 W output with a pulse FWHM of ~ 40 fs and repetition rate of 1 kHz. In WCUS, the same process occurs in the commercially available dual-Ascend pumped Spitfire Ace PA-40 regenerative amplifier, seeded by a Mai Tai SP oscillator. The differences are that the power of the laser pulses is 13 W, however this amount of power is necessary to ensure that all four laser tables available for use in WCUS, as described earlier, can operate.

1.3.1.1 Pump pulse generation

Once the 800 nm ultrafast seed pulses have been generated, a proportion (as indicated in Fig. 1.3), is directed to an optical parametric amplifier (OPA, TOPAS-C or TOPAS Prime) via beamsplitters to be converted into the required probe wavelength. These OPAs use a combination of second order non-linear optical processes, such as sum and difference frequency generation and second harmonic generation, which can generate a wide range of wavelengths. A detailed insight of these processes can be found in the publication by Cerullo and De Silvestri.⁷¹ In this thesis, the range of wavelengths used was 305–350 nm.

It is noted that, for the TR-IY setup used for the *in vacuo* studies in Chapter 2, two TOPAS-C OPAs can be used to generate both the pump and probe pulses. Furthermore, in Chapter 2, the 200 nm probe pulses were generated by third harmonic generation from the 800 nm seed pulses, using a combination of Type I and Type II β -barium borate (BBO, β -BaB₂O₄) non-linear optical crystals.⁷² Two BBO crystals are also installed in the TEAS setups, to generate 400 nm or 267 nm pump pulses, however this capability was not utilised for the studies in this thesis.

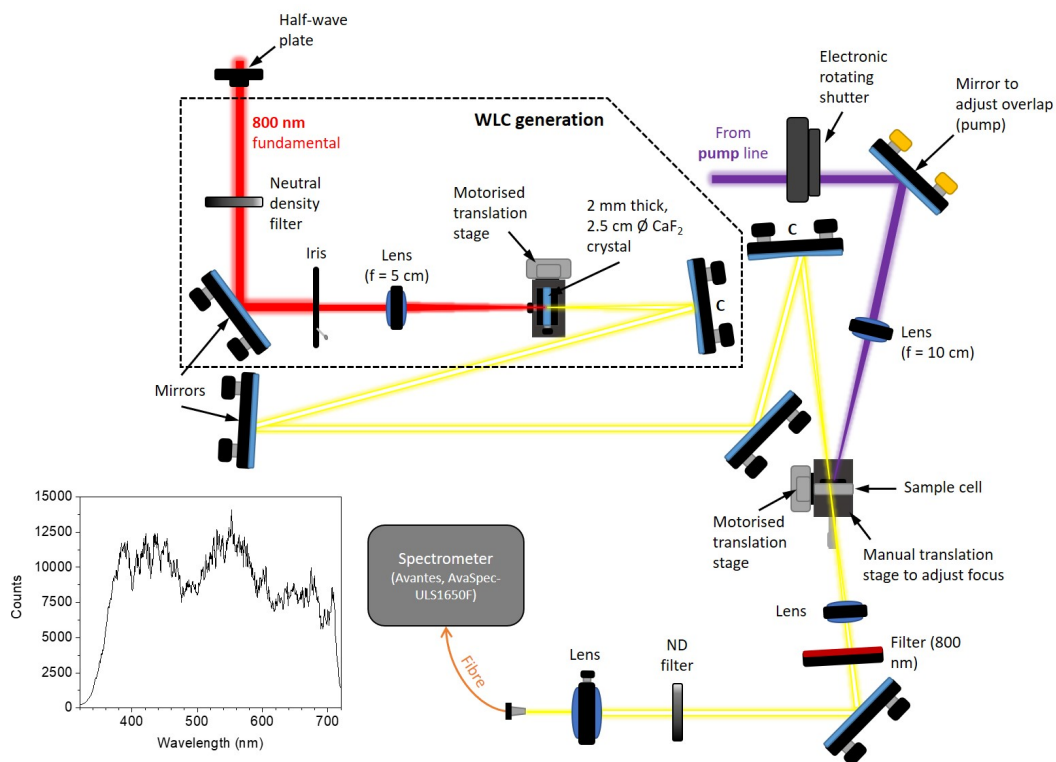


Figure 1.4: Schematic (not to scale) of the probe pulse WLC generation setup in WCUS. The white light is generated, then collimated using the curved mirrors shown (labelled C, $f = 10$ cm) and focused into the sample. The pump is shown to indicate how both the pump and probe arrive at the sample. Post sample, the intensity of the WLC is monitored by the spectrometer. An example of the WLC spectrum generated between 320 – 720 nm is shown, as measured after a proportion of the excess 800 nm light is removed using a colour compensating filter, to avoid saturation of the spectrometer’s detector.

1.3.1.2 White-light continuum (WLC) generation

For the TEAS measurements presented in this thesis, the probe pulse was a white-light supercontinuum, which in general spanned the range 320 – 720 nm. The experimental setup used to generate this spectrum in WCUS, alongside an example of the spectrum generated, is shown in Fig. 1.4.

Prior to the generation of the continuum, the beam needs to be at the correct polarisation, power and profile. A half-wave ($\lambda/2$) plate can change the polarisation of linearly polarised light and is therefore a key optic in this regard. The polarisation of the fundamental 800 nm beam is changed to ensure that the relative polarisations of the pump and probe is “magic-angle” (54.7°) and therefore rotational (anisotropy) effects are not detected.⁷³ The graduated neutral density (ND) filter and size of

the iris can be optimised to attain the laser pulse conditions for the desired WLC profile, which was generated by focusing 800 nm pulses into a crystal of CaF_2 . Other materials can also be used to generate different wavelength profiles, such as BaF_2 ,⁷⁴ sapphire (Al_2O_3),^{75,76} and other transparent media.^{77–80} The continuum should be tailored to the wavelengths of the spectral features you wish to observe, however, in general the wider the probe spectrum, the more spectral signatures you can resolve simultaneously, which in turn can assist greatly with the assignment of a relaxation mechanism.⁷⁶ As an example, there are cases where isomeric photoproducts were not detected in the case of natural sunscreens, as their absorption region was outside the probe region.²⁸

Damage will occur to CaF_2 crystals over time.^{81,82} To avoid this, the crystal is constantly translated vertically using a motorised delay stage.⁸³ The WLC expands following generation, so is collimated using a concave mirror, and refocused again before passing through the sample. The off-axis parabolic mirrors shown post-sample in Fig. 1.5, were installed to collect probe scatter, to improve the signal-to-noise for measurements involving the synthetic skin mimic in Chapter 3.

1.3.2 Transient absorption spectroscopy

This thesis will predominantly focus upon ultrafast spectroscopy studies of UV filters in solution, as these techniques have been adapted to more closely mimic sunscreen environments that are true-to-life. A popular choice for studies of sunscreen components in solution is pump-probe transient (UV-visible) electronic absorption spectroscopy (TEAS). Since the first foray into the ultrafast photodynamics (encompassing both photochemistry and photophysics) of sunscreens in the solution-phase, a multitude of commercially available UV filters have been investigated using TEAS.^{84–90}

The role of the pump pulse for TEAS experiments is to photoexcite a small proportion of the sample molecules. The dynamics of the molecules in the excited state are then probed using a broadband white light pulse (spectrum provided in Fig. 1.4 and its generation is described in detail in Section 1.3.1.2). The broad range of wavelengths from the probe pulses facilitate the detection of radiative and non-radiative processes that can occur following photoexcitation. Notably, the sample solution is recirculated after the measurement of each pump-probe pair, to ensure that any degradation products formed are not being probed instead of the molecule of interest.²⁷ Examples of TEAS experimental setups used for sunscreen research have been published previously;^{59,91–93} specific details pertaining to the setup used for the experiments in this thesis are provided in Figs. 1.5 and 1.6.

For TEAS experiments, transients (difference spectra that are functions of

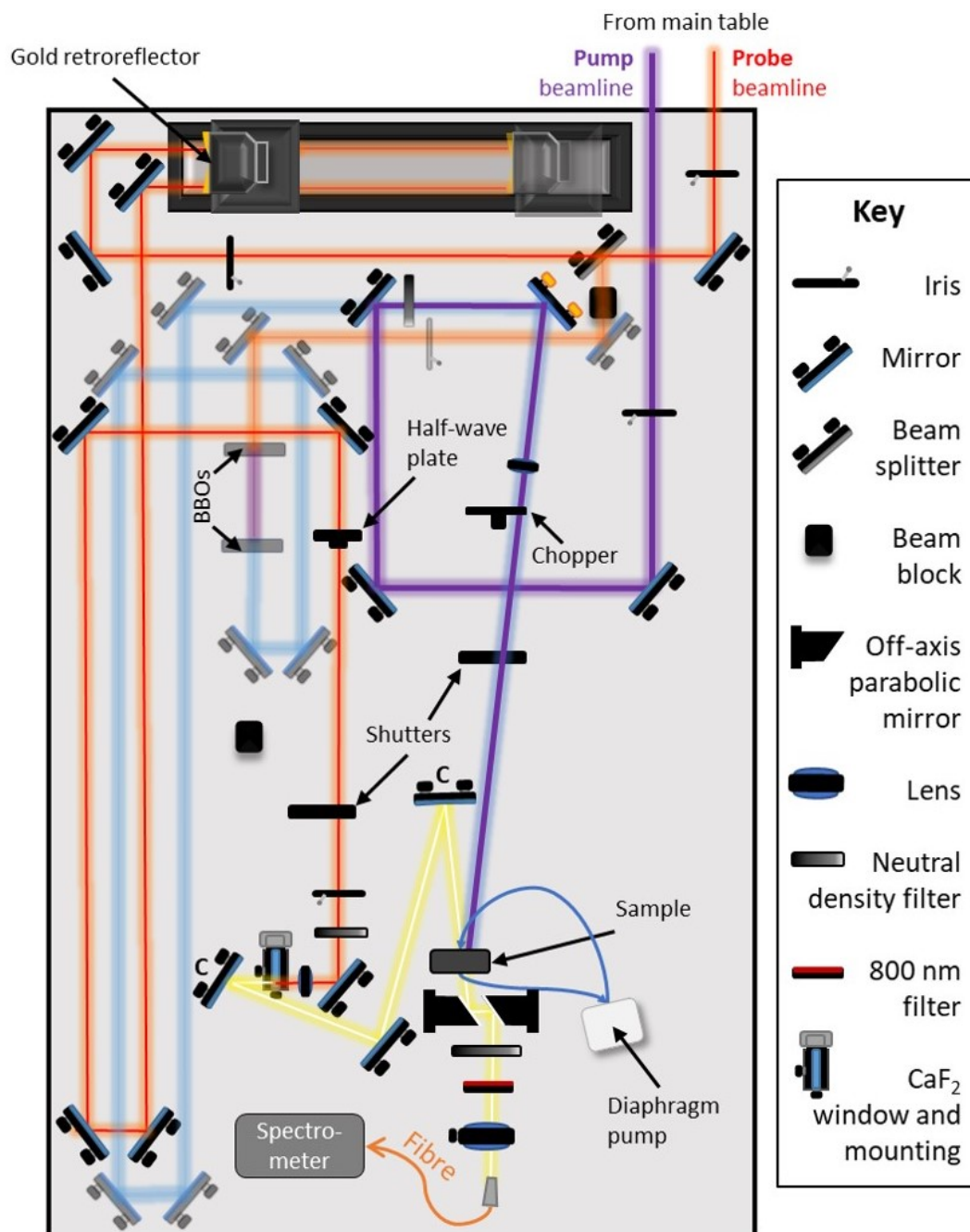


Figure 1.5: Full schematic (not to scale) of the optics used in the TEAS setup in Laboratory E0.19 at the Department of Chemistry at the University of Warwick, which was used for data acquisition in Chapters 2 and 3. The beamlines that are depicted as solid lines were used during experiments, the other beamline that appears faded is the harmonic generation capability, which was not implemented for the results in this thesis.

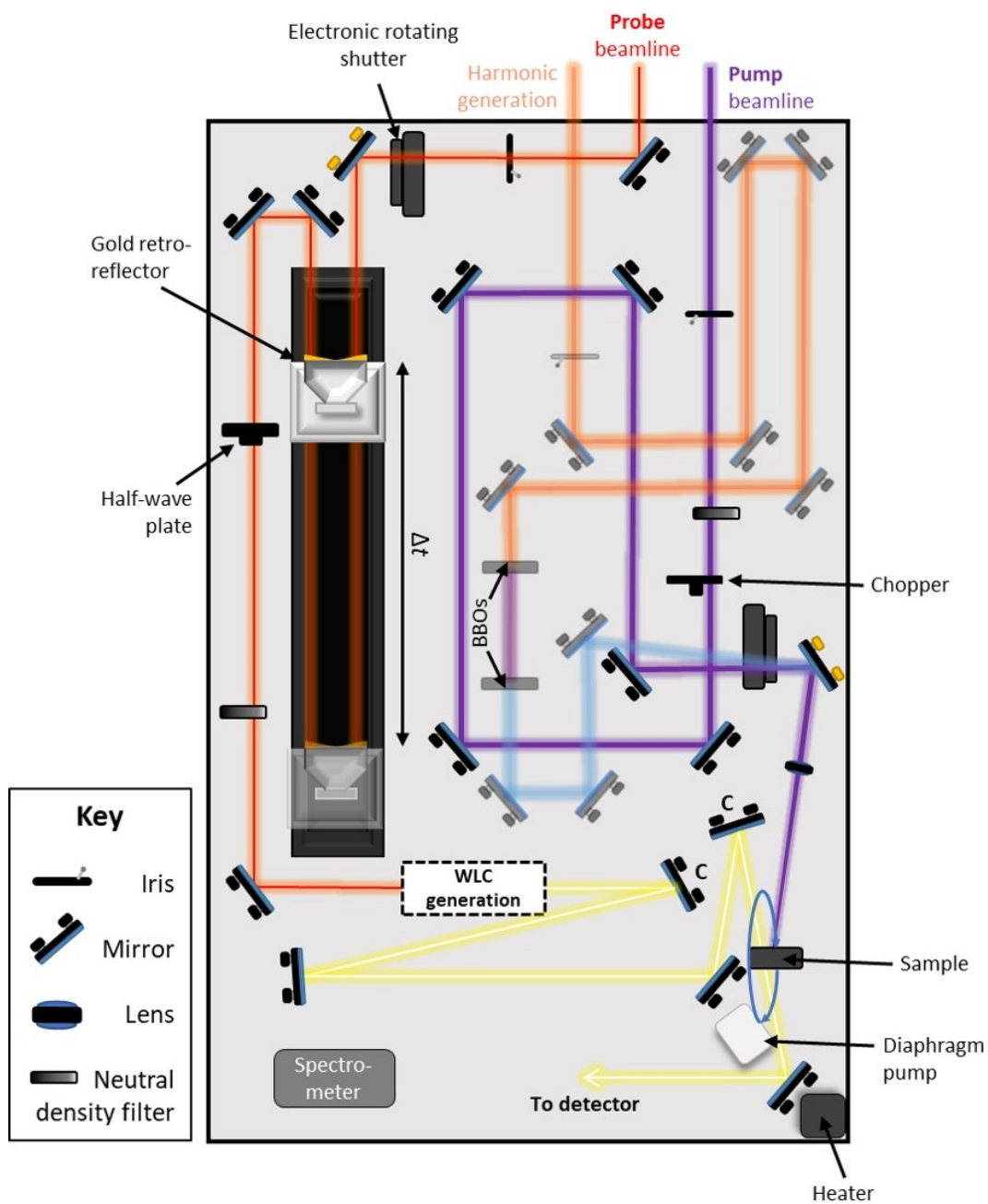


Figure 1.6: Full schematic (not to scale) of the optics used in the TEAS setup in the Warwick Centre for Ultrafast Spectroscopy (WCUS), which was used for data acquisition in 2 and 4. The beamline that appears faded is the harmonic generation capability, which was not implemented for the results in this thesis. The WLC continuum generation for this setup is shown in more detail in Fig. 1.4 and is thus not replicated here.

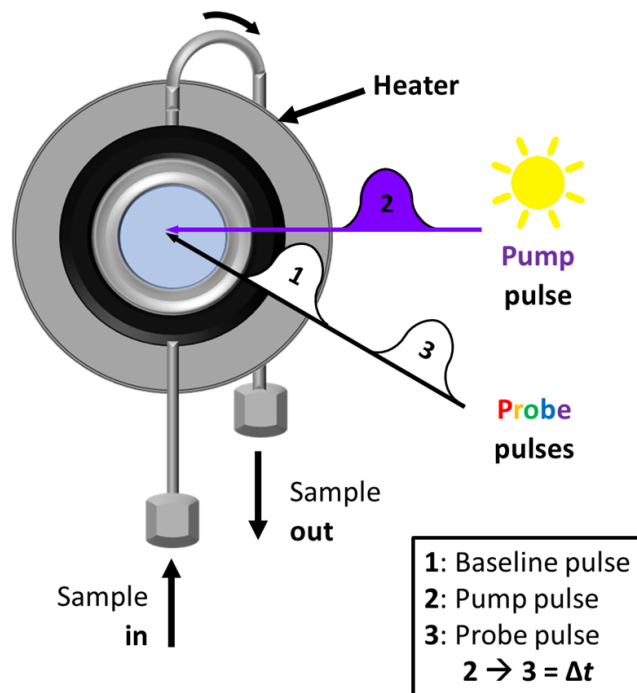


Figure 1.7: Simplified schematic of the flow-through sample cell that is used to heat the sample to skin surface temperature in ultrafast TEAS experiments in Chapter 4. A very similar cell was used in Chapters 2 and 3, except that there is no heating component. Pulse 1 passes through the unpumped sample and the transmitted light intensity (I_0) is recorded. Then, Pulse 2 (a UV pump pulse) photoexcites the sample. Finally, Pulse 3 is the probe pulse for the pumped sample. Pulses 2 and 3 arrive at the sample cell with a predefined time delay between them ($0 \leq \Delta t \leq 2.5$ ns). The sample at this point is replenished between each pump-probe pair of measurements via recirculation.

both wavelength and time delay) are attained via the measurement of the change in optical density (ΔOD) of the sample, before and after photoexcitation.^{27,59} Firstly, a baseline reading is taken of the sample prior to photoexcitation using only the probe pulse. After a time delay (Δt) from when the sample is pumped, the probe pulse will arrive at the sample. The arrival of the pulses at the sample is represented in Fig. 1.7. The Δt is varied by the movement of the gold retroreflectors in the TEAS setups, which alter the path length of the probe beam (prior to supercontinuum white-light generation) according to the delay required. The photoexcited sample will absorb different wavelengths (λ) of the probe, compared to the baseline. It is this difference between the transmitted intensities of the probe, before and after photoexcitation (denoted I_0 and I_p respectively) that can be used to determine the relaxation mechanism of the molecule of interest. Using I_0 and I_p as the parameters,

with the former being a function of wavelength only and the latter being a function of both wavelength and time delay, the definition of ΔOD is shown in Equation 1.14.

$$\Delta\text{OD}(\lambda, \Delta t) = -\log_{10} \left(\frac{I_p(\lambda, \Delta t)}{I_0(\lambda)} \right) \quad (1.14)$$

Equation 1.14 can alternatively be written as:

$$\Delta\text{OD}(\lambda, \Delta t) = \log_{10}(I_0) - \log_{10}(I_p) \quad (1.15)$$

One advantage of using ΔOD as the measure is that it is an instrument-independent quantity,²⁷ so results between different TEAS systems can be directly compared. Equation 1.15, attained using the standard laws of logarithms from Equation 1.14, perhaps makes the difference-spectrum nature of the transients attained more apparent. The optical choppers, noted in the TEAS table diagrams in Figs. 1.5 and 1.6, spin at a rate such that every other excitation pulse is blocked, which for the experiments presented in this thesis is 1 kHz (equating to a pulse being blocked every 500 Hz). This is in order to attain the difference spectra between “pump on” and “pump off”. Further to the optical chopper, there are electronic shutters in the pump beam, which allow for the beam to be blocked during other experimental optimisations to prevent photodegradation of the sample during this time.

The spectra attained in transient absorption experiments are a convolution of the sources of changes in optical density. There are four main sources: two of the processes result in a negative ΔOD signal in accordance with Equation 1.14, and the other two processes result in a positive signal, as shown in Figure 1.8. Similar outlines of photophysical processes can be found elsewhere.^{27,59}

The first of the processes that can occur, resulting in a negative signal, is known as a *ground state bleach*. When a fraction of the molecules in the sample are promoted to the excited electronic state, the number of molecules in the ground electronic state is depleted. Therefore, the absorption from the ground state is now less than in the non-excited sample, creating a so-called ‘transparency effect’. Thus, $I_0 < I_p$, which, following substitution into Equation 1.14 gives a negative ΔOD signal. The ground state bleach region often corresponds to the wavelengths of the ground state absorption of the molecule.

The second cause of a negative signal is *stimulated emission*. This is caused by a photon from the probe pulse inducing the emission of a second photon from the excited molecule, which subsequently relaxes. Therefore, the amount of light received by the detector will increase, thus $I_0 < I_p$ as before and the signal is negative.

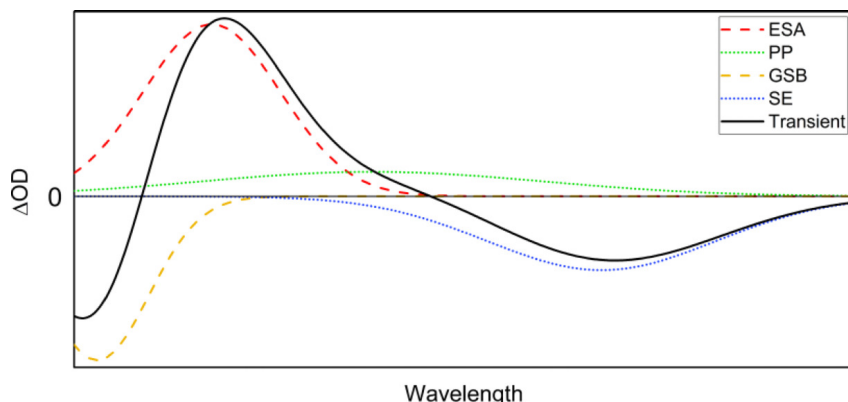


Figure 1.8: Diagram of possible contributions to a transient absorption spectrum for a given time delay.⁵⁹ excited-state absorption (ESA, red dashed line), photoproduct absorption (PP, light green dotted line), ground state bleach (GSB, yellow dashed line), and stimulated emission (SE, blue dotted line). The transient (black solid line) is the sum (convolution) of these contributions.²⁸

Often stimulated emission can be straightforwardly identified as it occurs at similar wavelengths to the fluorescence profile of the molecule, which can be measured using steady-state fluorescence spectroscopy. Stimulated emission is often red-shifted compared to the ground state bleach.

Excited state absorption is the first of the two features that is indicated by a positive ΔOD signal. This feature is due to some wavelengths of the probe being absorbed more in the excited state compared to the ground state. In this case, $I_0 > I_p$ and therefore the signal is positive. The final feature to discuss is the formation of a *photoproduct*. Examples of possible photoproducts are geometric isomers of the original species and photofragments. If these species are formed, they are likely to absorb different regions of the probe pulse compared to the original solvated species. As such, the transmittance of these wavelengths in the pumped sample will decrease, therefore $I_0 > I_p$ as above, and a positive signal is observed. Indications of a photoproduct in ultrafast spectroscopy experiments can often be correlated with the long-term photostability of a molecule, which can be determined using steady-state techniques. For example, UV-visible, Fourier transform infrared (FT-IR) and nuclear magnetic resonance (NMR) spectroscopies can be used to follow the progression of UV irradiation studies,^{94–96} which mimic molecular behaviours after long-term exposure to the sun. Steady-state spectroscopy techniques can therefore be considered a strategy to bridge the gap between ultrafast and ultraslow dynamics.

By deducing the contribution of each positive and negative feature to the overall transient absorption spectrum (TAS; note henceforth TAS represents both

transient absorption spectrum/spectra), then the spectral features can be assigned to specific photophysical processes, both radiative and non-radiative (as shown in Figure 1.2).

A note on resolution There are two aspects to the resolution of TEAS: the first is the instrument response function (IRF), determined by the full width half maximum (FWHM) of the laser pulses. This is determined by taking a Gaussian response from a solvent-only TEAS measurement, and fitting the curve to attain the FWHM value, as demonstrated in the electronic supplementary information (ESI) of all the published papers. An IRF on the attosecond to tens of picoseconds timescales is considered to be “ultrafast”.^{97,98} A second factor is the path length of the beam from laser to sample, as varied by the delay stage. For example, a delay stage whose specification dictates a minimum incremental motion of ~ 50 nm, corresponds to a resolution of ~ 0.2 fs. For the experiments in this thesis, the minimum delay used is 20 fs, and resolution decreases as we progress to longer time delays (more space between data points means lower “resolution”) as this is the best compromise between resolution and scan time. The IRF dictates the fastest process that we can observe, whereas the resolution dictates the amount of detail we have on those processes, with the optimum combination being short pulses and a precise delay stage.

1.3.3 Analysis of transient absorption data

During the acquisition of TAS data, many scans containing a large selection of time delays are taken in order for the data to be averaged. Each time delay transient within each scan is an average of 2500 – 3300 pump-probe pulse pairs (pump on and pump off, dependent on the TEAS setup used), for example to minimise the effect of laser pulse fluctuations. Assuming that the sample is unaffected by photodegradation during data acquisition, increasing the number of scans will reduce noise.

To automate the process of averaging all datasets acquired, then baseline correcting using the average of -1 ps transients, I wrote a MATLAB script (Version R2017b), which is provided and annotated in Appendix A1. This averaged file (generated after Part 1 of the code) was then imported into the fitting software Glotaran (see Section 1.3.3.1 below) to determine the time constants for the excited-state lifetimes of the solution under investigation.

1.3.3.1 Global kinetic fitting model

Although other methods of fitting TAS data exist, the positive and negative aspects of which are detailed in the review by Beckwith *et al.*,⁹⁹ (*e.g.* target analysis, which can be implemented to reproduce the spectra of individual excited-state species), this thesis work implements global kinetic fitting methods to assign the time constants of the relaxation processes occurring following photoexcitation. The global aspect of the fit refers to the fact that all data is analysed simultaneously. Depending on the data being modelled, two types of global model were implemented, these were parallel, where the model assumes that all relaxation processes begin immediately after photoexcitation (at $\Delta t = 0$); and sequential, also termed an unbranched, unidirectional model, where the processes are assumed to begin one after the other, in the form $A \xrightarrow{\tau_1} B \xrightarrow{\tau_2} \dots \xrightarrow{\tau_n} N$.¹⁰⁰

The choice of a parallel or sequential model for each molecule studied was initially based upon a qualitative assessment of the dynamics in the TEAS data obtained. Qualitative analysis, which also relies to an extent upon chemical intuition, can hypothesise the relaxation processes occurring following photoexcitation and their potential timescales. However, global fitting was used to precisely quantify the lifetimes of the excited states involved. Neither the assumptions of a parallel nor sequential model is perfect for the studies in this thesis, as the relaxation pathways found were most commonly branched. In general, if the branching occurred soon after photoexcitation, a parallel model was deemed the most appropriate, as there are concurrent processes occurring for most of the temporal experimental window, which was the case in Chapters 2 and 4. Additionally, in Chapter 2, a parallel model for TEAS was also chosen to align more closely with the fitting methods used in the gas phase. In Chapter 3, a sequential model was deemed more appropriate; this also facilitated more direct comparison between previous studies on sinapate derivatives.^{101–103} A description regarding the choice of model in Chapter 4 can be found in the Results and Discussion section. Ultimately, choosing between the two models was based upon which model assumptions were most appropriate for the system under investigation.

The software used to fit the data was the freely available Glotaran, which is a graphical user interface for the R package TIMP,¹⁰⁴ outlined in detail in the works by Snellenberg, both individually and in collaboration.^{100,105} Data is fitted using this software under the assumption that the system being studied is homogeneous (*i.e.* a discrete set of parameters can be used to describe the data) and separable, whereby each of the modelled spectroscopic properties are convolutions of the individual spectral components, weighted by their respective concentrations (*e.g.* denoted by

the Beer-Lambert law). These assumptions make it possible for a kinetic model to be fitted to the data and subsequently deconvolute the superposition of signals in the time-resolved spectrum (denoted as Φ in this section), using a total of n_{comp} components, where n_{comp} is the number of relaxation processes occurring during the time window of the experiment.¹⁰⁰ This can be denoted mathematically as:

$$\Phi(t, \lambda) = \sum_{j=1}^{n_{\text{comp}}} c_j(t) \epsilon_j(\lambda) \quad (1.16)$$

The variables yet to be defined are c and ϵ , which denote the concentration and spectrum of the j^{th} component respectively. Equation 1.16 can be written equivalently in matrix notation as $\Phi = \mathbf{C}\mathbf{E}^T$, where $\Phi \in \mathbb{R}^{m \times n}$, $\mathbf{C} \in \mathbb{R}^{m \times n_{\text{comp}}}$ and $\mathbf{E} \in \mathbb{R}^{n \times n_{\text{comp}}}$. In this matrix form, it can be more clearly seen that Φ is a spectrum comprised of n time points at m wavelengths.

Typically, the concentrations of the components over time can be modelled using first order kinetics, therefore the solution arises from solving a system of linear first-order ordinary differential equations.¹⁰⁶ The solutions are given by a sum of exponential decays, convoluted with the IRF, of the form shown in Equation 1.17.

$$\Phi(t, \lambda) = \sum_{j=1}^{n_{\text{comp}}} \underbrace{\exp(-k_j t) \circ i(t)}_{c_j(t)} \epsilon_j(\lambda) \quad (1.17)$$

In Equation 1.17, k is the rate of exponential decay of component j , $i(t)$ is the IRF function, with the amplitude of the concentration profile of component j given by ϵ_j . This equation is equivalent to $\Phi = \mathbf{C}(\theta_j) \mathbf{E}^T$ in matrix notation, where θ_j is a vector of non-linear parameters, which are user-defined within the software.¹⁰⁰

Optimisation of the inputted parameters, including the lifetimes of each component, is attained by minimising the residuals using a least squares approach, according to the relation in Equation 1.18.¹⁰⁰ In Chapter 3, the fitted time constants (in seconds) were converted to rate constants by taking the reciprocal.

$$\min \left\| \phi - \sum_{j=1}^{n_{\text{comp}}} c(\theta_j) \epsilon_j \right\|_2^2 \quad (1.18)$$

Within the Glotaran software, there are visual cues to indicate whether the proposed value of n_{comp} is correct, involving a singular value decomposition (SVD) matrix algorithm. This algorithm has the following definition for real matrices:

Definition 1.3.1. $\Phi = \mathbf{U}\Sigma\mathbf{V}^T$ is a SVD if $\mathbf{U} \in \mathbb{R}^{m \times n}$ and $\mathbf{V} \in \mathbb{R}^{n \times n}$ are orthogonal,

and $\Sigma \in \mathbb{R}^{m \times n}$ is diagonal, with diagonal entries $\sigma_1 \geq \sigma_2 \geq \dots \geq \sigma_{n_{\text{comp}}}$, $p = \min(m, n)$.

The SVD of the data matrix can be used to indicate the number of independent spectral and temporal features that are present in the datasets. The columns of \mathbf{U} are the left singular vectors, which in Glotaran indicate the time dependence of components, whereas the columns of \mathbf{V} are the spectral dependence. In addition to plots of the left and right singular vectors and corresponding singular values, decay associated spectra (DAS) and evolution associated difference spectra (EADS, relevant for sequential model only) are also outputted by the software, examples of which are presented in Chapters 3 and 4. The former are interpreted as the loss or gain of an absorption or emission feature within the given lifetime, whereas the EADS provide information pertaining to the spectral evolution *i.e.* the second EAS rises with the first lifetime and decays with the second lifetime.¹⁰⁰ Indeed, Equation 1.16 can be re-written to reflect the contribution of the DAS and EADS, as shown in Equations 1.19 and 1.20 respectively.¹⁰⁵

$$\Phi(t, \lambda) = \sum_{j=1}^{n_{\text{comp}}} c_j^{\text{DAS}}(t, \theta) \text{DAS}_j(\lambda) \quad (1.19)$$

$$\Phi(t, \lambda) = \sum_{j=1}^{n_{\text{comp}}} c_j^{\text{EADS}}(t, \theta) \text{EADS}_j(\lambda) \quad (1.20)$$

Finally, in addition to the number of independent exponential decays included in the model, a so-called “coherence spectrum” would frequently need to be added to the model, to mitigate the artifacts induced by pump-probe overlap around time zero (below the instrument response).¹⁰⁷

1.3.3.2 Chirp correction

Despite the background subtraction and post-processing of TAS data detailed above, there are time-dependent so-called “chirp” artefacts that remain, which require remedial action. Chirp arises from the different wavelengths of the white-light probe pulse travelling at different velocities through optics and other media, which spreads the arrival of the pulse at the sample, an effect known as group velocity dispersion (GVD). As a result of GVD, the probe pulse is stretched in time; in other words, the “time zero”, t_0 is wavelength dependent. Therefore, a correction is applied to ensure that all wavelengths have the same t_0 value.^{26,77,108} To apply the correction, the averaged data outputted from the MATLAB script in Appendix A1 was imported

into the KOALA package.¹⁰⁹ Although chirp correction was not required to fit the data due to the inclusion of the dispersion polynomial coefficients (presented in Equation 1.21 below) in the fitting model, it was used for presentation purposes in the published papers.

Firstly, each wavelength is assigned a value of t_0 according to a minimum user-selected ΔOD value. Then a quadratic polynomial, represented in Fig. 1.9 and shown in Equation 1.21 below, is fitted to the data points.¹⁰⁹

$$t_0(\lambda) = \text{AP} + \text{GVD} \left(\frac{2\pi c}{\lambda} \right) + \frac{1}{2} \text{TOD} \left(\frac{2\pi c}{\lambda} \right)^2 \quad (1.21)$$

In Equation 1.21, further to GVD parameters (measured in fs^2/rad), AP denotes absolute phase (measured in fs) and TOD is third-order dispersion (measured in fs^3/rad^2).^{109,110} This polynomial can equivalently be written as a quadratic function of angular frequency, ω , with AP, GVD and TOD as coefficients, shown in Equation 1.22.

$$t_0(\omega) = \text{AP} + \text{GVD}\omega + \frac{1}{2} \text{TOD}\omega^2 \quad (1.22)$$

Once the ΔOD threshold has been determined for each value of λ or ω , non-linear regression can be applied to fit the polynomial and determine the unknown coefficients in Equations 1.21 and 1.22. Then, for each λ or ω , the attained value of t_0 can be subtracted from each transient to attain the chirp corrected spectra. To ensure that the chirp correction is as accurate as possible, many more time delays are taken around t_0 , similarly to the procedure used by Megerle *et al.*, whereby a constant step size (20 fs for the measurements in this thesis) is chosen as the time delay interval, following a linearly increasing step size thereafter.⁷⁶ This scheme ensures the same number of time delays between -1 and 1 ps, then from 1 to 10 ps, 10 to 100 ps and so on. Furthermore, it gives equal weightings throughout a scan and is a good compromise between accurate chirp correction and data acquisition time.⁷⁶

Fig. 1.9 also highlights another artefact that affects the temporal resolution of the TEAS measurements presented, which is that the red wavelengths within the probe have a much wider FWHM than their blue counterparts. This is due to the energy-time relation shown in Equation 1.7, and also a group velocity mismatch between the pump and spectral components of the probe, which varies as the probe wavelength changes.^{76,111} Other artifacts, such as stimulated Raman amplification and cross-phase modulation (responsible for the “winged” Gaussians in Fig. 1.9) can

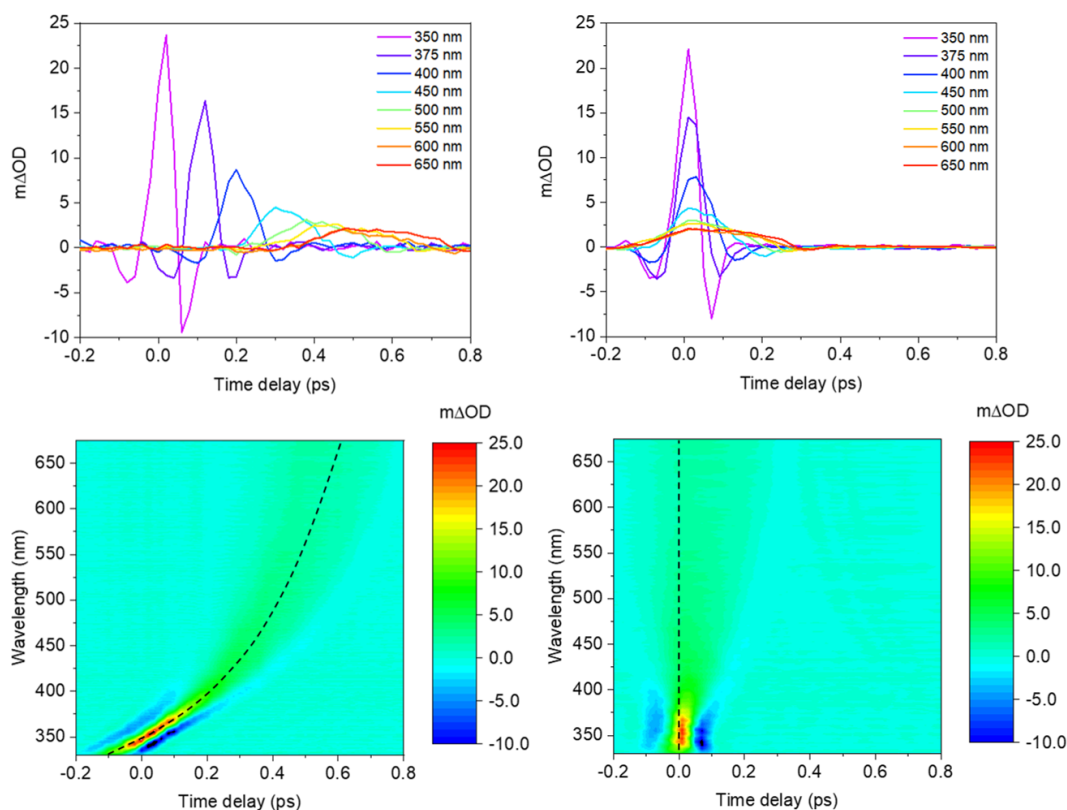


Figure 1.9: Solvent response of methanol, following photoexcitation at 350 nm at high power (1.5 mW). Top row: Selected wavelength transients (IRFs) before chirp correction (left), where the effect of group velocity dispersion (GVD) due to white light probe interaction with the CaF_2 window at the sample can be clearly observed. (Right) The same transients after chirp correction using the KOALA package.¹⁰⁹ All wavelengths are now closely aligned in time. Bottom row: False colour heat maps, showing solvent transients for all wavelengths between -0.2 and 0.8 ps before chirp correction (left) and after chirp correction (right) using the KOALA package¹⁰⁹. In this thesis, heat maps have been chirp corrected for display purposes only, as the effect is accounted for during the fitting process, described in Section 1.3.3.1.

also be introduced.²⁶ The Gaussian peaks are a result of two-photon absorption (one pump and one probe photon) around time zero,¹¹² and the FWHM can be used to determine an approximate temporal resolution and determination of the pump-probe cross correlation function.^{26,112}

1.3.4 Time-resolved ion yield

Ultrafast gas-phase approaches, such as time-resolved ion yield (TR-IY), have been utilised to determine intrinsic behaviours of many small molecules in isolation (in

the absence of solvent). The method of taking knowledge garnered in more basic systems/environments and applying that knowledge to more complex systems is known as a *bottom-up* approach. Such an approach is demonstrated in Chapter 2 during the investigation of homosalate, where an outline of the experimental setup used is detailed in the Methods. In addition, several detailed reviews of this technique have been published previously.^{113–115} In general, during TR-IY experiments, samples are vapourised by heating; this vapour is then seeded into a carrier gas, such as helium or argon. A molecular beam consisting of isolated vibrationally cold molecules, is formed after passing the gaseous mixture into vacuum via a nozzle with a small aperture. Suitable nozzle designs for this supersonic jet expansion can be found in several references.^{116–120} The molecular beam is intercepted by the pump and probe pulses at the centre of time-of-flight optics, usually replicating the arrangement described by Wiley and McLaren.¹²¹ The pump pulse photoexcites the sample, then the probe pulse ionises the resulting species; either the excited molecule or any generated photoproducts following photoexcitation. The probe pulse should have sufficient energy to ionise the molecule from its photoexcited (pumped) state, ideally with only a single photon, known as ‘soft ionisation’. Soft ionisation techniques ensure that the cation formed has minimal amounts of internal energy remaining after ionisation, thus minimising fragmentation. If ionisation (from the excited state) is attained with a single probe photon of equal energy to the pump, this process is known as 1 + 1 resonance-enhanced multiphoton ionisation (1 + 1 REMPI) or resonant two-photon ionisation (R2PI). If the pump and probe photons have different energies, this is denoted 1 + 1' REMPI.^{115,122,123} The parent cation (*i.e.* the cation of the sample molecule), as well as any photofragments generated via the photoexciting pump pulse (which are subsequently ionised by the probe pulse), are detected using a time-of-flight mass spectrometer. Detection with mass spectrometry ensures that the individual monitoring of parent cations or photofragments is possible, owing to their different mass-to-charge (m/z) ratios. As the time delay is varied between the pump and probe pulses, the population of the excited electronic state of the sample molecule, and thus the number of cations produced (the ‘ion yield’) will often change. By measuring the ion yield signal of the parent cation and photofragments by mass selectivity, the lifetime of this excited electronic state can be determined and decay pathways can be postulated.^{115,124}

1.3.5 UV-Visible spectroscopy

For the studies presented in this thesis, UV-Visible (UV-Vis) spectroscopy was an invaluable tool to determine the absorption region of the sunscreen filters under

investigation. The value of the UV-Vis absorption peak was most frequently used as the photoexcitation wavelength for TEAS experiments. Furthermore, full spectra (usually spanning from 200 to 800 nm) were analysed in Chapters 3 and 4 to assess the effect of prolonged UV irradiation on a sample; in conjunction with identifying sunscreen efficacy metrics, such as *in vitro* SPF and critical wavelength (to be introduced later in Section 1.4.4.2). The absorbance signal from the UV-Vis spectrometer is governed by the Beer-Lambert Law, which was discussed earlier in Section 1.2.1. It is noted that, for all measurements, a baseline measurement was taken to ensure that any artifacts were subtracted from the sample spectrum, for example, from the solvent.

All the UV-Vis measurements in this thesis were performed using an Agilent Cary-60 spectrometer, which was used as standard. This is a dual beam instrument, the specification of which is detailed extensively in documentation by the manufacturer.¹²⁵ Briefly, these spectrometers use a Xenon flash light, with a repetition rate of 80 Hz, to facilitate measurements in the range 190 – 1100 nm. The spectral bandwidth is 1.5 nm and is defined by a Czerny-Turner monochromator.¹²⁶ Chapter 2 of the book named *Spectroscopy: Principles and Instrumentation* by Vitha¹²⁷ is highly recommended for a detailed description of the working principles of UV-Vis spectroscopy.

1.3.6 Fluorescence spectroscopy

The identification of fluorescence in UV filters used for sunscreens can be used as an indicator of their efficacy. This is because fluorescence can be indicative of a long-lived excited state, which is unfavourable for a UV filter.²⁷ Fluorescence investigations were carried out in Chapter 2 both in solution and in vacuum. This section outlines the techniques used to identify fluorescence in salicylates, with Figure 1.10 outlining the two types of fluorescence spectra that will be mentioned in the sections to follow.

1.3.6.1 In solution

The purpose of the solution-phase fluorescence spectroscopy carried out in this thesis was two-fold. Firstly, to determine the region of emission compared to absorption. The difference between the band maxima of the absorption and emission peaks is known as Stokes shift. A large Stokes shift can be indicative of a major molecular change following excited-state activation, such as ESIPT, intramolecular charge transfer and molecular geometry changes.¹²⁸ The second purpose was to determine

quantum yield of fluorescence (Φ_F). In all cases, the excitation wavelength was fixed and the emission measured, called an *emission* spectrum. If the Φ_F is defined as the proportion of photons emitted compared to those absorbed, equivalently the proportion of excited-state molecules that decay via fluorescence is $0 \leq \Phi_F \leq 1$. In general, the closer the value of Φ_F to 0, the more favourable the molecule for sunscreens, as the lifetime of the excited-state is likely to be shorter. In this thesis, the method of comparing to a standard was used for quantum yield determination; the equation used in practice to determine Φ_F using this method is defined in Chapter 2.¹²⁹ It is important that the standard matches the absorption and emission of the sample as closely as possible, to obtain the most accurate value.

For the work carried out by myself in this thesis, the workhorse instrument was a Horiba Fluorolog-3; detailed documentation pertaining to the instrumentation and working principles of this instrument are given in documentation by the manufacturer.¹³⁰ Some key details for the Fluorolog-3 instrument are the xenon lamp excitation source, with the luminescence detected by a photomultiplier tube. Once again, the book by Vitha,¹²⁷ specifically Chapter 3, offers a very detailed reference text for the working principles of luminescence measurements. Fluorescence spectroscopy of this kind is extremely sensitive; according to the specification of the Fluorolog-3, concentrations as low as 50 femtomolar of a fluorophore can be measured. A dilute sample ensures that fluorescence is induced evenly from the excitation source throughout the sample, higher concentrations mean that the fluorescence is concentrated at the wall of the cuvette. In general, the absorbance of the sample should be very low (< 0.1) to avoid these inner filter effects. As a result of this instrumental sensitivity, fluorescence measurements are prone to errors and artifacts.¹³¹

1.3.6.2 In vacuum

Laser induced fluorescence (LIF) spectroscopy in vacuum^{132,133} was used in Chapter 2, to give details into the vibronic structure of homosalate (HMS), as well as to confirm whether the molecule fluoresced in vacuum. LIF can access individual vibronic transitions, then identify all those that are resonant by changing the excitation wavelength by very small increments and fixing the emission detection wavelength, known as an *excitation* spectrum. The principles behind an excitation spectrum are shown in Fig. 1.10, alongside those for an emission spectrum, as discussed in Section 1.3.6.1. The signal-to-noise and sensitivity of LIF is aided by the fact that the fluorescence signal is bright, and detected against a dark background.^{115,133} The specific apparatus used for the experiments in this thesis can be found in Chapter 2.

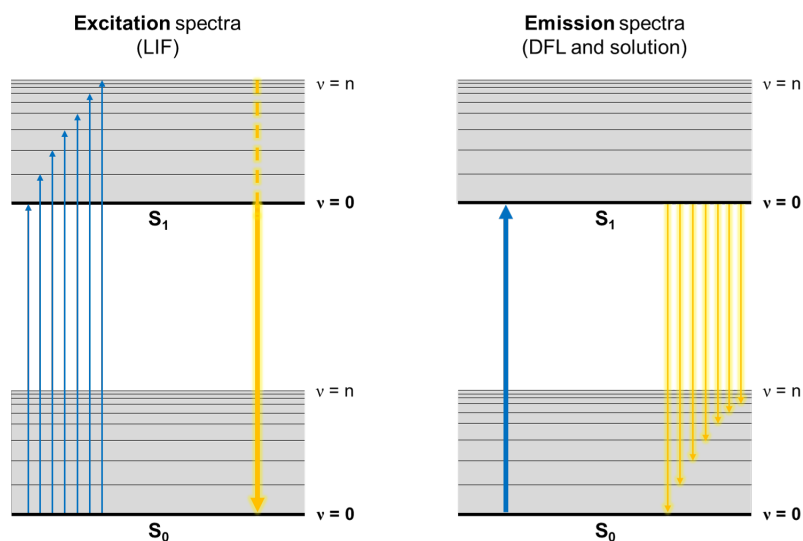


Figure 1.10: Simplified Jablonski diagrams to show the differences between excitation spectra (as carried out in LIF experiments) and emission spectra, as implemented in solution and in DFL experiments. The dotted line in the excitation spectrum diagram represents that fact that emission can occur in states other than $\nu = 0$ in the gas phase.

Similarly to TR-IY described in Section 1.3.4, a molecule is seeded into a molecular beam and photoexcited from the ground vibrational S_0 state. However, in contrast to TR-IY, a probe pulse is not implemented in LIF, as the radiative decay induced by the excitation laser can be detected directly, using a photomultiplier tube or other similar detector.¹¹⁵

LIF offers much greater resolution in the frequency domain compared to the pump-probe techniques used in this thesis, however the temporal resolution is of the order of nanoseconds, compared to the femtosecond resolution of TEAS and TR-IY.¹¹⁵ If needed, LIF can also provide information on the relative intensities and populations of excited states, as fluorescence is proportional to the population of the excited state.^{115,132} Broad features in a LIF spectrum can point to factors such as vibronic congestion, vibrational energy redistribution, or a large change in conformation following electronic excitation of the molecule in question. On the other hand, sharp features indicate an emission lifetime greater than the instrument response from the excited vibronic transition.¹³⁴⁻¹³⁶

Furthermore, the value of the excitation wavelength can be fixed on a vibronic transition of interest in a LIF spectrum, and the resulting emission spectrum measured (Fig. 1.10). This technique is known as dispersed fluorescence (DFL), which is the gas-phase counterpart to the fluorescence spectroscopy in solution, described in

the previous section. DFL can also give an insight into the gas-phase fluorescence lifetimes by monitoring the signal decay over time. Both LIF and DFL are used in Chapter 2 to explore the conformational nature of HMS, and provide additional details on its function as a sunscreen active ingredient. This capability has also been demonstrated in several earlier studies.^{135,137,138}

1.3.7 Computational methods

In Chapters 2 and 4, computational calculations were employed alongside spectroscopic techniques. The following details the techniques that were implemented by myself during the course of this thesis, using the methods detailed in the published articles.

1.3.7.1 Basis sets and functionals

Ideally, it would be possible to employ quantum chemistry to find exact, analytical solutions to the Schrödinger equation (Equation 1.3) for many-body problems. As it stands, this is impossible for systems more complex than atoms or ions with more than one electron, due to the correlated electron-nuclei Coulombic interactions discussed in Section 1.1.1.2. As a result, approximations have to be made to generate numerical solutions to the generalised Schrödinger equation using quantum chemistry.¹³⁹ For example, the Born-Oppenheimer approximation, introduced in Section 1.1.1, significantly reduces the complexity of the quantum system to be modelled.

Approximations also need to be made in order to ensure that the calculations are attainable for current computers to complete in a reasonable amount of time. Molecular orbital wavefunctions, as described earlier in this Introduction (Section 1.1.1.2) are defined as a linear combination (Definition 1.1.1) of atomic orbitals (LCAO). A basis set is a set of mathematical functions that can approximate the molecular orbitals.^{140,141}

There are challenges associated with finding the basis set that best approximates the molecular orbitals. The larger the basis set (with a limit to infinity), the more accurate the approximation will be; however, increasing the size of the basis affects the computational resources needed to carry out the calculation,¹⁴² therefore a compromise is needed. This was particularly pertinent for the studies in this thesis as the number of atoms in the molecules was large: 41 atoms for homosalate in Chapter 2 and 45 atoms for avobenzone in Chapter 4. The basis sets and functionals chosen for the calculations in this thesis were chosen as a good compromise between

computational accuracy and cost. The basis sets used were of two main types: the first is Dunning’s correlation-consistent polarised basis sets^{143,144} in Chapter 2 (cc-pVXZ where X = D, double zeta or T, triple zeta) and Pople basis sets^{145,146} in Chapter 4, specifically 6-31g* and 6-311++g**. In accordance with the requirements of NWChem, the bases utilise atom-centred Gaussian-type orbitals.¹⁴⁷

A functional is, in general terms, a function of a function. It takes a function as its input and outputs a number.¹⁴⁸ For the calculations in this thesis, carried out by myself, the Perdew–Burke–Ernzerhof (PBE)¹⁴⁹ and PBE0¹⁵⁰ functionals were employed, although there are copious others that are used in DFT, one of the most famous being B3LYP.^{151–153}

1.3.7.2 Density functional theory

Density functional theory (DFT) is a type of electronic structure calculation,¹⁴⁸ which relies upon the fact that, if the electronic structure of a molecule is known, then its physical properties can be predicted. The Hohenberg-Kohn theorem¹⁵⁴ gave rise to these foundations of DFT, whereby the ground-state properties of a molecule can be predicted from electron density. The software used to carry out the DFT calculations in this thesis, NWChem, uses the Kohn-Sham approximation,^{147,155} which was a later development based upon the Hohenberg-Kohn theorem, as it introduced basis functions as an approximation for electron orbitals. For the exploration of the excited state of a molecule, time-dependent DFT, herein referred to as TD-DFT, is necessary. TD-DFT is underpinned by the Runge-Gross theorem,¹⁵⁶ which is analogous to the Hohenberg-Kohn theorem for DFT. It is implemented in this thesis for the prediction of excited state vertical excitation energies, alongside their state characters.

An additional technique used, in Chapters 2 and 4, was the Δ -self consistent field (SCF) method. In this instance, it was used to calculate T_1 state energies to compare to the values attained by TD-DFT. Δ SCF can be considered a small extension to ground-state DFT, with both having a similar computational cost.¹⁵⁷ To implement the Δ SCF method in NWChem, the spin multiplicity (S) of the optimised ground-state structure of the molecule (attained using DFT) was set to three,^{158‡} and the difference between the single point energies of the singlet and triplet was calculated.

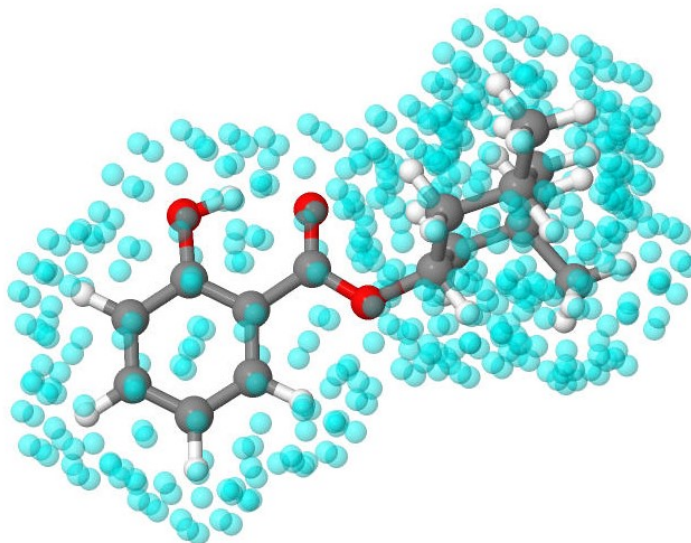


Figure 1.11: Example of the arrangement of the atom-centred spheres (in blue) in the COSMO implicit solvent model, in this instance for homosalate in ethanol.

1.3.7.3 Modelling solvent environments

For the work presented in Chapters 2 and 4, the solvent environment was modelled implicitly¹⁵⁹ using the conductor-like screening model (COSMO)¹⁶⁰ built into the NWChem software.^{147,161} Implicit solvent models, such as COSMO, consider the solvent to be a dielectric polarisable continuum (with a permittivity ϵ), which can model the electrostatic interactions between the solute and the solvent. COSMO specifically employs a scaled-conductor approach, which for solvents with a finite dielectric constant (and by proxy a finite permittivity), can effectively estimate the charge on the surface segments, using Equation 1.23.

$$\mathbf{q} = \left(\frac{\epsilon - 1}{\epsilon + x} \right) \mathbf{q}^* \quad (1.23)$$

In Equation 1.23, \mathbf{q}^* is the charge on the surface assuming that no electric potential at the surface, with \mathbf{q} being the scaled equivalent. The value of x in the scaling factor is kept constant at 0.5 for a neutral molecule.¹⁶²

Solvent molecules are not modelled individually using the COSMO methodology, instead it uses an arrangement of atom-centred spheres, an example of such an

[‡]The multiplicity of an energy level is defined as $2S + 1$, where S is the total spin angular momentum. $S = 1$ in the triplet state as both electrons are in the same spin state - both $m_s = +\frac{1}{2}$.

arrangement is given in Fig. 1.11. The publication by Benazzouz *et al.* also shows an example of a COSMO-modelled charge surface for avobenzene.¹⁶³ This approach is much less computationally expensive than its explicit solvent counterpart,¹⁶⁴ and thus an appropriate level of computational cost could be maintained for the calculations performed in this thesis. Although COSMO can certainly provide a good approximation of the effect of solvation, it has limitations, such as the inability to distinguish between solvents with different properties (*e.g.* hexane and benzene) but very similar dielectric constants.¹⁶²

1.4 Photoprotection

This thesis uses the instrumentation and experimental techniques detailed above (Section 1.3) towards addressing some of the challenges associated with UV photoprotection.^{165,166} The necessity of photoprotection to prevent excess solar UV radiation exposure will be explored in detail in this section.

1.4.1 Solar radiation

Solar radiation consists of a broad spectrum of wavelengths, spanning the infrared (> 700 nm), visible (400 – 700 nm) and UV (100 – 400 nm) regions of the electromagnetic spectrum. The UV region, the most topical within this thesis, is further sub-divided into three groups: the most energetic rays are known as UVC (100 – 290 nm), followed by UVB (290 – 320 nm) and finally UVA (320 – 400 nm).¹⁶⁷ Overall, UV radiation constitutes approximately 10% of the sun’s output prior to its interaction with the Earth’s atmosphere.¹⁶⁸ The atmosphere, including the ozone layer, completely blocks UVC and a large proportion of UVB radiation emitted by the sun from reaching the Earth’s surface, however the incident UVA radiation remains largely unaffected.¹⁶⁹ Therefore, the radiation that affects life on Earth arises from the UVA and UVB regions of the electromagnetic spectrum.¹⁷⁰ The amount of UV light incident at the Earth’s surface can vary, owing to parameters such as vegetation, snow, water, smoke and cloud cover.^{171–175}

Some benefits of moderated exposure to UVA and UVB radiation have been identified, such as the production of Vitamin D, which can prevent bone conditions such as rickets, osteomalacia and osteoporosis.^{176,177} Evidence also exists that exposure to natural sunlight can improve the symptoms of mental health conditions including seasonal affective disorder and schizophrenia, also via the production of vitamin D.^{178,179} Other established benefits of moderate sun exposure and its subsequent Vitamin D production include reduced risks of cardiovascular and autoim-

mune diseases, and improvements in inflammatory skin conditions.¹⁸⁰ These benefits, amongst others, are discussed in separate comprehensive reviews.^{181,182} However, there is a balance to be sought as the long-term adverse effects of overexposure to UV radiation are well-known and characterised, including skin ageing, cataract formation and skin cancer.^{183–189} Malignant melanoma, specifically cutaneous melanoma, is the most aggressive form of skin cancer¹⁹⁰ and has been attributed to 50,000 deaths each year worldwide.¹⁹¹ Despite this, tanning the skin remains a popular cosmetic and sociocultural trend, whereby achieving a tan has been cited as a primary motivation for actively seeking UV exposure.^{180,192} “Tanning” refers to increased levels of melanin pigmentation in the skin, which affords natural photoprotection to humans. These pigments prevent excessive UV radiation from reaching the DNA contained within skin cells.^{193,194} However, the production of melanin is not instantaneous upon an increase in UV exposure.^{93,195,196} Such a delay in the body’s natural production of the pigment means that further measures are necessary to protect ourselves from any possible adverse effects.⁹³

1.4.2 Ultraviolet filters

Sunscreens are a form of artificial photoprotection that have been developed to increase the overall protection from UV radiation on the surface of our skin. They should be used in conjunction with measures such as seeking shade, avoiding UV exposure between the hours of 11:00 and 15:00, and wearing protective clothing.¹⁶⁵ The ingredients that primarily provide UV photoprotection within a sunscreen formulation are aptly named UV (or sunscreen) filters. There are two main types of filter: organic (also referred to as chemical filters) and inorganic (physical filters). The former, which are the sole focus of this thesis, predominantly absorb UV radiation; whereas the latter can also reflect and scatter radiation.^{94,197} A list of some common organic UV filters incorporated into sunscreens are shown in Fig. 1.12. Examples of inorganic filters include zinc oxide (ZnO) and titanium dioxide (TiO₂). These filters should offer high levels of protection from UV for long periods of time (photostability)¹⁹⁸ and dissipate excess energy rapidly (ideally on a picosecond timescale),²⁸ as alluded to in earlier sections of this Introduction. Optimum photostability should not compromise safety, and should therefore be achieved without inducing any adverse effects on human health or the environment, some of which will be outlined in due course.

With regard to photostability, if a UV filter is not suitably photostable, then exposure to UV light can induce degradation into photoproducts, photofragments or radical species.¹⁹⁸ A high-profile example of such a filter is avobenzene (also

Type	Name(s)	Structure	λ_{\max} (nm)	ϵ ($\text{dm}^3 \text{mol}^{-1} \text{cm}^{-1}$)
UVB	Octocrylene		303	12290
	Homosalate Homomenthyl salicylate		308	4300
	Ethylhexyl salicylate Octisalate		305	4130
	Ethylhexyl methoxycinnamate Octinoxate		311	23300
Broad spectrum	Oxybenzone Benzophenone-3		324	9400
UVA	Avobenzene Butyl methoxydibenzoylmethane		357	34140
	Menthyl anthranilate Meradimate		336	5230
	Diethylamino hydroxybenzoyl hexyl benzoate (DHHT)		354	35900

Figure 1.12: List of selected organic UV filters that have been approved by the EU and the FDA in the United States (with the exception of DHHT, which is not FDA approved). The structures of key sunscreen functional groups are highlighted in the structures: salicylates (pink), cinnamate (blue) and benzophenone (green). λ_{\max} is the peak of absorption and ϵ is the absorption coefficient of the filter at λ_{\max} , as reported by Shaath.¹⁹⁹

known in cosmetics nomenclature as butyl methoxydibenzoylmethane), which is the subject of Chapter 4. Use of avobenzene as a UVA filter is widespread globally; in a sunscreen survey conducted by Wang *et al.*,²⁰⁰ 54% of the products from the year 2009 included in their study contained avobenzene, up from 16% in 1997. Exposure to UV light can enable avobenzene to undergo *enol-keto* tautomerisation, which is unfavourable given that any depletion in the *enol* species will cause a decrease in the levels of UVA protection afforded by the molecule, as the *keto* form absorbs in

the UVC region.²⁰¹ This *keto* form of avobenzone is an example of a photoproduct, a light-induced molecular species that differs from the original.

Aside from the problems involved with the use of avobenzone, other UV filters, such as those in the benzophenone and cinnamate families, have been shown to penetrate the skin's surface and induce endocrine disruption,²⁰² which will be revisited later in Section 1.4.2.2. Also, as alluded to above, some UV filters commonly found in sunscreens induce detrimental environmental impacts. These impacts include adverse effects to aquatic life, such as: acute and chronic toxicity, effects on reproduction, mutagenicity, bioaccumulation and coral bleaching.²⁰³⁻²¹⁰ Reducing the concentrations of these active ingredients is seen as a priority and there are efforts to phase out the most harmful of the existing UV filters. It also remains necessary to increase the repertoire of UV filters that formulators can choose from, particularly for UVA protection where current options are lacking.²¹¹

1.4.2.1 Nature-inspired UV filters

Concerns surrounding existing organic UV filters, such as the induction of coral bleaching noted above,²⁰⁶⁻²⁰⁸ are encouraging formulators to turn to nature-inspired photoprotection for the next generation of sunscreens, to improve compatibility both in terms of our skin and the natural environment.^{212,213} This is a significant motivator for the study presented in Chapter 3.

Plants have developed protective barriers within the epidermis layer of their leaves, to prevent UV photodamage during sun exposure.²¹⁴⁻²¹⁷ This photoprotective layer, composed of the common metabolite sinapoyl malate, is analogous to melanin pigments in human skin.²¹⁷ Sinapoyl malate is a sinapate (sinapic acid based) ester that has been identified in the *Arabidopsis* and *Brassica* plant families, amongst other natural sources.²¹⁶⁻²²⁰ Laser spectroscopy studies on these so-called 'plant sunscreens' were pioneered by Dean *et al.* in the frequency domain.¹³⁵ Following this initial study of sinapic acid, sinapoyl malate and other derivatives,¹³⁵ TEAS has been used to investigate the photodynamics of sinapoyl malate to determine its potential as a future sunscreen filter,^{101,221} as well as several other sinapic acid and ester derivatives.^{102,103,222-226} In general, all these studies agree that, in solution, the relaxation mechanism following UV photoexcitation is internal conversion from a $\pi\pi^*$ state, mediated by a *trans-cis* isomerisation reaction coordinate.²²⁷ An illustrative example can be found in Fig. 1 in Chapter 3, using the case study of ethyl sinapate.¹⁰²

Four sinapate derivatives that were analysed by Dean *et al.*:¹³⁵ methyl sinapate (MS), isopropyl sinapate (IS), sinapoyl methyl lactate (SML) and sinapoyl dimethyl malate (SDM), shown in Figure 1.13, have been studied using a combination of

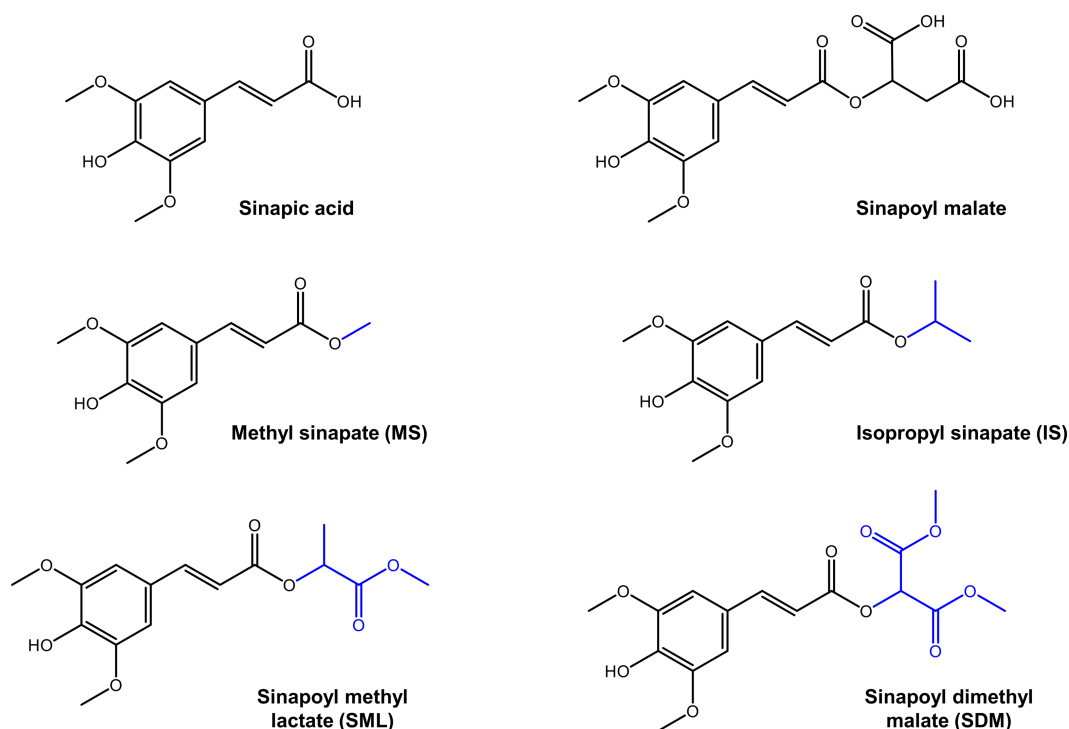


Figure 1.13: Structures of sinapic acid, sinapoyl malate (the ester found in plant leaves), and the four structures investigated by both Liu *et al.* and Dean *et al.*:^{135,222} methyl sinapate (MS), isopropyl sinapate (IS), sinapoyl methyl lactate (SML) and sinapoyl dimethyl malate (SDM), with the groups added to the sinapate ester moiety shown in blue for reference.²⁸

TEAS and TD-DFT techniques.^{222,228} Liu *et al.*²²² determined that isomerisation time had a non-linear dependence on size of the sinapate ester derivative in aqueous buffer solution (0.1 M NaH₂PO₄, 0.1 M Na₂HPO₄, pH = 6.8). However, all four compounds returned to the ground state faster than had been seen in previous studies of sinapoyl malate.^{101,224} Therefore, Liu *et al.*²²² proposed that, at least in buffer solution, all four compounds displayed more favourable energy dissipation characteristics than sinapoyl malate. This could, in turn, be applicable for sunscreen use, as this provides evidence that molecular functionality can be tuned to improve characteristics for sunscreen inclusion. This was an additional motivation for the study presented in Chapter 3.

An interesting discussion pertaining to the detection (or lack thereof) of the *cis*-isomer in TEAS studies of MS^{101,103,222} can be found in a review published by Holt and Stavros.²⁸ A potential explanation for the discrepancy was given as differences in probe windows between the TEAS instruments used. The shortest wavelength that Liu *et al.*²²² could resolve in their probe window was 380 nm,

compared to 330 nm in other studies.^{101,103} The *cis*-isomer of MS can be detected at 360 nm using steady-state spectroscopy, which is outside of the TEAS probe window of Liu *et al.*²²² Therefore, this species could not be detected in their ultrafast TEAS measurements, evidenced by the lack of a time constant outside of the maximum time delay. However, it could be observed following continuous irradiation with UV light, by observing changes in the UV-visible absorption spectra after pre-defined timescales, on the order of several minutes. An initial decrease in absorbance due to the formation of the *cis* isomer was observed, which eventually became constant, suggesting an equilibrium between the two isomers. A similar method was used by Horbury *et al.* in the study of the *E* and *Z* form of ethyl sinapate,¹⁰² which was also employed in Chapter 3.

Notably, Liu *et al.*²²² took an additional step towards simulating the effect of applying a sunscreen to the surface of the skin, by including the sinapate esters within a poly(vinyl alcohol) (PVA) hydrogel film. PVA hydrogels have previously been shown to be a mimic for the skin's surface and other biological tissues such as heart valves, cartilage tissue and corneal implants.²²⁹ They are also used for medical applications such as wound dressings.²³⁰ Liu *et al.*²²² observed a spectral red-shift of approximately 10 nm when each of the sinapate derivatives were dissolved into the film, with the peak of absorption now situated at 330 nm, an advantage when developing candidate UVA filters. In addition, the elongation of the time constants observed in the film environment is evidence for restriction of motion. This is similar to the observations made by Horbury *et al.* with sinapoyl malate in very viscous solvents (ethylene glycol and glycerol).²²¹ In Chapter 3, a different synthetic skin mimic is used, namely VITRO-CORNEUM[®]. This skin mimic was preferred as it is transmissible enough to attain valid TEAS measurements and its sister product, VITRO-SKIN[®] has been used extensively for SPF testing and other *in vitro* sunscreen tests.^{231–236}

1.4.2.2 Antioxidant potential and endocrine disruption

Although ideal ultrafast and steady-state characteristics are encouraging, they do not guarantee that a UV filter is suited to a cosmetic product, as biological sunscreen safety concerns^{237,238} cannot be identified with these techniques alone. As a result biologically relevant quantities (antioxidant potentials and endocrine disruption assays) were also measured in Chapter 3 and a brief introduction is therefore given in this section.

Antioxidant potential Antioxidant compounds are beneficial for inclusion in sunscreens,²³⁸ due to their ability to scavenge reactive oxygen species (ROS, including free radicals) that can be formed on the skin due to UV exposure.²³⁹ ROS, in turn, can indirectly incite DNA and protein damage in the skin.^{240,241} Previous studies have sought to identify multi-functional sunscreen compounds that demonstrate effectiveness for both UV photoprotection and antioxidant potential.^{242–245}

In Chapter 3, the antioxidant potential of the nature-inspired UV filter diethyl sinapate (DES) was determined *in vitro* using a 2,2-diphenyl-1-picrylhydrazyl (DPPH) assay;^{246–248} such assays were first developed by Blois in 1958.²⁴⁹ DPPH is a stable free radical, and it is the scavenging of this radical that is the basis for the assessment of a molecule's antioxidant capability.²⁵⁰ The methodology is explored in more detail in Chapter 3.

Endocrine disruption Endocrine disrupting chemicals (EDCs) are defined in detail in the review by Schug *et al.*:²⁵¹ in summary, an EDC is a chemical, or combination of chemicals, that interfere with hormone action. Disruption can occur via several mechanisms; for example, EDCs can bind to hormone receptors to enhance, or conversely reduce, the effect of the hormone in the body. EDCs can also affect the amount of different hormones in the body, by affecting their synthesis, metabolism, storage and transport, or a combination of these.²⁵¹

Some UV filter compounds found in sunscreens have been shown to penetrate the skin's surface and induce endocrine disruption,²⁰² with comprehensive reviews on this subject listing adverse effects including reproductive/developmental toxicity.^{252,253} As an example, molecules in the cinnamate family have been a popular choice for UVB protection in commercial sunscreens. However, cinnamates (including EHMC) undergo *trans-cis* isomerisation following exposure to UV radiation,^{86,254–261} with endocrine disruption concerns existing particularly for the *cis* form.^{262–264} This isomerisation also results in a reduction in the UVB protection afforded by EHMC, due to the *cis* form of EHMC having a lower extinction coefficient.^{265,266}

The effect of symmetric functionalisation on the photostability of the cinnamate family of sunscreen molecules has been investigated as a way of alleviating toxicological concerns resulting from *trans-cis* isomerisation, specifically by adding an additional methyl acrylate moiety on to methyl cinnamate.²⁶⁷ This functional group addition also red-shifted the absorption to the UVA region, where additional options are needed,²⁶⁸ perhaps by extension of the conjugation of the chromophore.²⁶⁹ Symmetrical functionalisation was also a key motivation for the study presented in Chapter 3, to ensure that the effects of isomerisation upon UVA excitation were

minimised.

The endocrine disruption assays carried out in Chapter 3 were for the alpha oestrogen receptor (ER α)^{270,271} and the xenobiotic receptor pregnane X (PXR).²⁷² Both the agonist and antagonist properties were measured; agonists bind to receptors and activate their biological response, whereas antagonists reduce or completely inhibit the biological activity of the receptor.²⁷³ It is important to verify that the candidate sunscreen does not have agonist or antagonist properties: for example, disruption to the activity of the ER α receptor can induce oestrogenic effects, which can be very serious (an increased incidence of testicular and breast cancers, for example).^{274,275} PXR is an important defence mechanism for the removal of toxic substances from the human body, such as chemicals not naturally produced or expected (xenobiotics).²⁷⁶

1.4.3 Sunscreen formulations

The history of sunscreen development has been detailed comprehensively in a fascinating article by Urbach.²⁷⁷ One of the earliest examples of a sunscreen formulation was benzyl salicylate contained in an oil phase, in 1935.^{277,278} Salicylates are still in use today and two such molecules in the salicylate family are the subject of Chapter 2.

Nowadays, although there are a vast number of sunscreen products available worldwide, continued research and innovation is still needed in order to overcome the challenges that remain and create the ideal formulation. In the publication by Osterwalder and Herzog,²⁷⁹ four key areas where improvements could be made are identified and summarised, these are: technology, compliance from consumers, measurement/assessment and norms/standards. These sentiments are shared by Burnett *et al.*²⁸⁰ and both agree that the provision of optimum photoprotection relies upon the convergence of these four criteria.

The overall aim of the technology category is to ensure that there is a versatile repertoire of ingredients for inclusion in sunscreen blends. These blends should reduce the amount of UV radiation reaching the skin over a broad spectral range, with UV filters being central to these efforts.²⁷⁹ The technology category also incorporates the sunscreen formulation, which if not correct will result in the active ingredients not being applied uniformly, nor performing to the best of their ability.^{279,281}

A sunscreen formulation should also have preferential sensory properties to encourage consumers to apply enough of the product regularly.²⁸² Ingredients such as silicones and silicas are added to avoid any unpleasant greasy and sticky textures.^{280,283} Moreover, the product should be easy to apply uniformly to ensure

homogeneity of the ingredients on the skin. Compliance can only be improved if technologies exist to create aesthetically pleasing formulations that are perceived to offer high levels of sun protection, without any adverse dermatological effects.²⁸² Examples of such effects include contact dermatitis or allergies following application of the product to the surface of the skin, or photocontact dermatitis, caused by exposure of the product to UV light.^{237,284–288} This ultimate combination remains challenging for sunscreen developers to attain.

1.4.4 How effective is your sunscreen?

1.4.4.1 Metrics

As alluded to by Osterwalder and Herzog,^{279,281} the assessment of the effectiveness of a sunscreen, *i.e.* how much protection is provided over the entire UVA and UVB range, is crucial. In addition, the standard procedures for measuring efficacy and communicating this to consumers via product labelling could also be improved, a measure that could also improve consumer compliance.²⁸¹

One of the best-known indicators of sunscreen efficacy is its sun protection factor (SPF), which is a ubiquitous measure of the levels of protection that a sunscreen will provide against sunburn.²⁸¹ It is defined by the relation shown in Equation 1.24, whose parameters have historically been ascertained *in vivo*, *i.e.* with groups of human volunteers. The abbreviation MED in Equation 1.24 stands for minimal erythemal dose: the UV dose (measured in terms of time, or fluence, units J/m²) needed to induce a minimally detectable redness in the skin, typically 24 hours after irradiation.^{289,290} Erythema is induced mainly by UVB radiation, with UVA wavelengths contributing to a much lower extent.²⁹¹ A higher value for the SPF indicates better protection from the wavelengths that induce erythema.

$$\text{SPF} = \frac{\text{MED (with sunscreen)}}{\text{MED (without sunscreen)}} \quad (1.24)$$

Nowadays, defining SPF via measurement of MED *in vivo* is not the only method used, owing to its subjective nature in end-point interpretation and incurring variability between individuals and laboratories.^{281,292,293} Furthermore, SPF measurements are expensive, time-consuming, with reproducibility issues and small sample sizes. There are also ethical concerns involved with irradiating volunteers with a known carcinogen.^{294,295}

These issues have motivated the development of a reliable *in vitro* SPF test; a faster, cheaper and more ethical alternative to *in vivo* testing, as these

tests do not involve human subjects.²⁹⁶ In this context, *in vitro* testing refers to applying a thin layer (up to 2.5 mg cm⁻²) of a sunscreen to a synthetic skin substrate and determining the SPF via spectrophotometric absorbance and/or transmittance measurements.^{294,297} One form of the equation for *in vitro* SPF determination is shown in Equation 1.25.^{298,299} The term $A(\lambda)$ refers to the value of the erythral action spectrum at a given wavelength (*i.e.* how much redness is induced by a particular wavelength),^{298,300} $E(\lambda)$ is the solar spectrum irradiance^{298,299,301} and $T(\lambda)$ is the transmittance of the sample, for the set of wavelengths tested. $A(\lambda)$ and $E(\lambda)$ are constants for any given wavelength.

$$\text{SPF} = \frac{\int_{290}^{400} A(\lambda)E(\lambda) d\lambda}{\int_{290}^{400} A(\lambda)E(\lambda)T(\lambda) d\lambda} \quad (1.25)$$

Even though the need for *in vitro* SPF testing is apparent, a consensus is yet to be reached on a standardised methodology that suitably correlates with *in vivo* results.^{290,294} Many of the challenges that remain in creating a standardised *in vitro* methodology are issues of reproducibility. Differences between laboratories should be accounted for, both in terms of access to instrumentation and ambient laboratory conditions (*e.g.* temperature, humidity).²⁹⁶ In addition, a method is required that will be accurate for all sunscreen samples, which are heterogeneous by nature, with different viscosities and active ingredients. The transmittance properties between any two sunscreen thin layers are a source of variation, even from the same sample. The synthetic skin substrates used for *in vitro* SPF testing are not necessarily identical between tests either, therefore unifying the physical and chemical properties of synthetic skin substrates, as well as the method of applying the test sample to the substrate, remains a key priority.^{28,296} An example method of sample application to a test substrate is described as part of the methodology in Chapter 4.

1.4.4.2 Ideal sunscreen formulation

Contrary to popular belief, SPF alone is not a sufficient measure of sunscreen efficacy. According to the European Commission, sunscreen formulations should satisfy additional performance criteria in addition to a high SPF.^{283,302} A sunscreen should demonstrate: (i) a ratio of UVA protection factor (UVA-PF) to SPF of at least one third³⁰³ and (ii) a critical wavelength of more than 370 nm in order to be marketed as ‘broad-spectrum’.^{268,279,304} The additional criteria, denoted (i) and (ii), ensure close to uniform protection from all UVA and UVB wavelengths, akin to

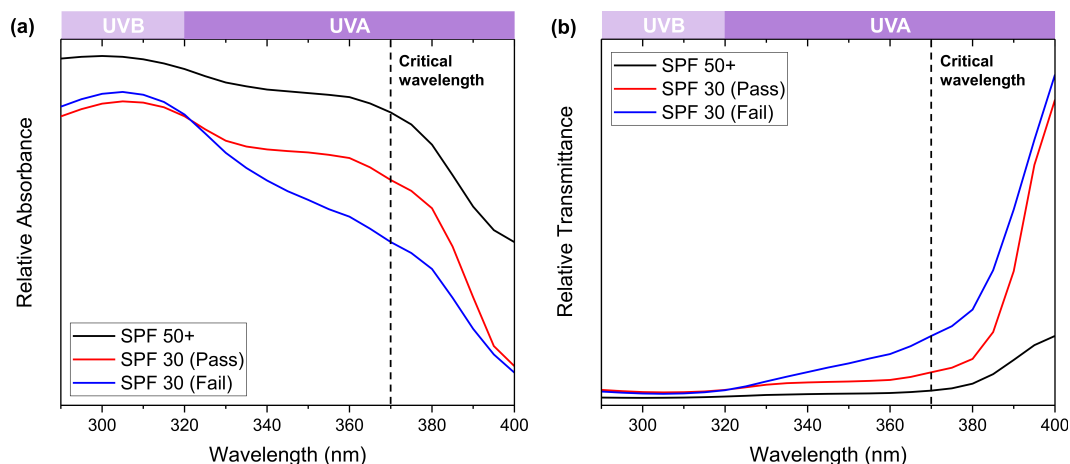


Figure 1.14: (a) Expected absorbance profiles of sunscreens with SPF 50+ (black line), SPF 30 satisfying UVA protection requirements (red line) and SPF 30 that does not satisfy UVA protection criteria (blue line), as calculated *in silico* using a sunscreen simulator.³⁰⁸ (b) Corresponding transmission profiles for sunscreens with SPF 50+ (black line), SPF 30 satisfying UVA protection requirements (red line), and SPF 30 sunscreen that does not satisfy these requirements (blue line), calculated *in silico* using a sunscreen simulator.³⁰⁸ The critical wavelength (370 nm), the wavelength at which more than 10% of the protection should be offered by the formulation, is indicated by the dashed line in both figures. In addition, the regions referred to as UVA (320 – 400 nm) and UVB (290 – 320 nm) are indicated.²⁸

having the skin covered by clothing or avoiding the sun altogether.^{283,305} Standardised approaches exist to attain the UVA-PF both *in vitro* and *in vivo* to calculate the ratio specified in (i). New sunscreen formulations are thoroughly characterised through the combined use of *in vitro* and *in vivo* approaches.^{211,306,307} A critical wavelength of 370 nm, specified in (ii), means that over 10% of the protection afforded by the sunscreen covers the range 370 – 400 nm. Indeed, products with a high SPF (≥ 30) do not necessarily satisfy criteria (i) and (ii). For demonstration purposes in this thesis (and previously a review published by Holt and Stavros)²⁸, the SPF and UVA protection afforded by three different combinations of UV filters have been calculated *in silico* using a sunscreen simulator,³⁰⁸ as demonstrated in Figure 1.14. Specific details pertaining to the equations needed for these simulations can be found in the publication by Herzog and Osterwalder.³⁰⁹ Figure 1.14 demonstrates the absorbance and transmittance profiles for simulated formulations with different SPFs (50+ and 30, denoted by the black and red lines respectively) that would satisfy the minimum requirements (i) and (ii) outlined above. As a separate comparison, the red and blue lines denote two formulations that would both offer an SPF of 30 and a critical wavelength beyond 370 nm. However, the blue formulation fails to provide

the necessary ratio of UVA to UVB protection, despite having marginally higher levels of UVB protection. Figure 1.14(b) indicates that protection from wavelengths beyond 380 nm requires improvement, as the transmittance of these formulations in this region is high and could invoke skin damage.

1.5 Summary

This Introduction explores the underlying principles that govern the concept of a molecule being able to offer photoprotection (Sections 1.1 and 1.2), and the analytical techniques used to study these properties in real time (Section 1.3). Finally, an overview on the factors that constitute effective photoprotection, and the associated quantitative metrics, concludes this first Chapter (Section 1.4). In general, all three upcoming results chapters have the same underlying principle: to investigate the photoprotection properties of current and candidate UV filters for sunscreen use. This was achieved with a focus on TEAS, although complementary experimental and computational methods (*e.g.* those described in this Introduction) have also been used to support the conclusions made and enhance the overall scope of each Chapter.

Chapter 2 on HMS and EHS used a wide variety of techniques, including TEAS, TR-IY, solution- and gas-phase fluorescence and computational methods to make in-depth conclusions on their mechanisms of action. The first combined frequency and time-resolved studies by Tan *et al.*³¹⁰ on EHMC demonstrated that frequency- and time-resolved techniques are a powerful combination for developing knowledge of intrinsic molecular properties, which in turn could be applied within the cosmetics and healthcare industries.³¹¹ This sentiment is reiterated in Chapter 2.

Then, Chapter 3 builds upon previous work on nature-inspired sunscreens, as discussed in Section 1.4.2.1, through the study of diethyl sinapate (DES), a candidate UVA absorber that was symmetrically-functionalised. In this Chapter, a combination of TEAS, long-term UV irradiation and biological tests combine to demonstrate DES as a promising future additive for sunscreens. The additional emphasis on molecular design in this Chapter could also inspire the adaptation of existing sunscreen filters, in order to enhance their photoprotection properties.

Whilst new-and-improved UVA filters are found, investigating the causes of instability of those that are currently available remains of importance. With this in mind, Chapter 4 extends prior work⁸⁴ on the worldwide-approved benchmark UVA filter avobenzene. Application of TEAS, UV-Vis spectroscopy, DFT and TD-DFT methodologies, combined with industry-standard *in vitro* SPF and UVA-PF metrics

were used to assign its relaxation mechanism in both volatile solvents and commercial emollients at skin surface temperature. This could have a significant impact on experiments of this kind in the future, as the gap between “model” and “real-life” conditions is reduced and results are thus more applicable to real-world applications. Overall, this thesis demonstrates that these techniques can combine to offer a detailed insight into the photoprotection offered by new and potential sunscreen filters in a host of different environments; from the simplicity of in vacuum to the complexities of formulations.

References

- [1] D. W. Ball, *The Basics of Spectroscopy*, Spie Press, 2001, vol. 49.
- [2] C. Truesdell, *Naturwissenschaften*, 1976, **63**, 53–62.
- [3] G. Jaeger, *Am. J. Phys.*, 2014, **82**, 896–905.
- [4] K. Dorai, S. Chaturvedi and N. Mukunda, *Resonance*, 2018, **23**, 1077–1100.
- [5] S. M. Stewart and R. B. Johnson, *Blackbody radiation: A history of thermal radiation computational aids and numerical methods*, CRC Press, 2016.
- [6] J. Liang, *Chemical Modeling for Air Resources*, Academic Press, Boston, 2013, pp. 43–63.
- [7] M. Planck, *Verh. Deutsch. Phys. Gesell.*, 1900, **2**, 237–245.
- [8] H. Kragh, *Phys. World*, 2000, **13**, 31–36.
- [9] S. Klassen, *Sci. Educ.*, 2011, **20**, 719–731.
- [10] A. Einstein, *Ann. Phys.*, 1905, **17**, 1–16.
- [11] L. De Broglie, *Ann. Phys.*, 1925, **3**, 10–22.
- [12] C. J. Davisson and L. H. Germer, *Proc. Natl. Acad. Sci. U.S.A.*, 1928, **14**, 317.
- [13] T. L. Dimitrova and A. Weis, *Am. J. Phys.*, 2008, **76**, 137–142.
- [14] D. C. Galehouse, *Int. J. Theor. Phys.*, 1981, **20**, 787–807.
- [15] E. Schrödinger, *Ann. Phys.*, 1926, **385**, 437–490.
- [16] M. Born and R. Oppenheimer, *Ann. Phys.*, 1927, **389**, 457–484.
- [17] W. Heisenberg, *Z. Phys.*, 1927, **43**, 172–198.
- [18] E. H. Kennard, *Z. Phys.*, 1927, **44**, 326–352.

- [19] V. Jijnasu, *Stud. Hist. Philos. Sci. B*, 2016, **55**, 62–71.
- [20] D. Sen, *Curr. Sci.*, 2014, 203–218.
- [21] J. Franck and E. G. Dymond, *Trans. Faraday Soc.*, 1926, **21**, 536–542.
- [22] E. Condon, *Phys. Rev.*, 1926, **28**, 1182–1201.
- [23] N. S. Bayliss and E. G. McRae, *J. Phys. Chem.*, 1954, **58**, 1002–1006.
- [24] T. J. Martinez, *Nature*, 2010, **467**, 412–413.
- [25] M. A. Collins, *Theor. Chem. Acc.*, 2002, **108**, 313–324.
- [26] M. Lorenc, M. Ziolek, R. Naskrecki, J. Karolczak, J. Kubicki and A. Maciejewski, *Appl. Phys. B*, 2002, **74**, 19.
- [27] L. A. Baker and V. G. Stavros, *Sci. Prog.*, 2016, **99**, 282.
- [28] E. L. Holt and V. G. Stavros, *Int. Rev. Phys. Chem.*, 2019, **38**, 243–285.
- [29] D. F. Swinehart, *J. Chem. Educ.*, 1962, **39**, 333.
- [30] M. A. El-Sayed, *J. Chem. Phys.*, 1963, **38**, 2834–2838.
- [31] D. J. Nesbitt and R. W. Field, *J. Phys. Chem.*, 1996, **100**, 12735–12756.
- [32] D. R. Yarkony, *Rev. Mod. Phys.*, 1996, **68**, 985.
- [33] D. R. Yarkony, *Acc. Chem. Res.*, 1998, **31**, 511.
- [34] F. Bernardi, M. Olivucci and M. A. Robb, *Chem. Soc. Rev.*, 1996, **25**, 321.
- [35] S. Matsika and P. Krause, *Annu. Rev. Phys. Chem.*, 2011, **62**, 621.
- [36] W. Fuß, S. Lochbrunner, A. Müller, T. Schikarski, W. Schmid and S. Trushin, *Chem. Phys.*, 1998, **232**, 161.
- [37] G. A. Worth and L. S. Cederbaum, *Annu. Rev. Phys. Chem.*, 2004, **55**, 127.
- [38] J. P. Malhado, M. J. Bearpark and J. T. Hynes, *Front. Chem.*, 2014, **2**, 97.
- [39] B. Dick, Y. Haas and S. Zilberg, *Chem. Phys.*, 2008, **347**, 65–77.
- [40] Y. Haas and S. Zilberg, *J. Photoch. Photobio. A*, 2001, **144**, 221–228.

- [41] D. Polli, P. Altoe, O. Weingart, K. M. Spillane, C. Manzoni, D. Brida, G. Tomasello, G. Orlandi, P. Kukura, R. A. Mathies *et al.*, *Nature*, 2010, **467**, 440–443.
- [42] M. N. Ashfold, A. L. Devine, R. N. Dixon, G. A. King, M. G. Nix and T. A. Oliver, *Proc. Natl. Acad. Sci.*, 2008, **105**, 12701–12706.
- [43] R. González-Luque, T. Climent, I. González-Ramírez, M. Merchán and L. Serrano-Andrés, *J. Chem. Theory Comput.*, 2010, **6**, 2103–2114.
- [44] B. M. Uzhinov and M. N. Khimich, *Russ. Chem. Rev.*, 2011, **80**, 553.
- [45] H. C. Joshi and L. Antonov, *Molecules*, 2021, **26**, 1475.
- [46] J. Jankowska and A. L. Sobolewski, *Molecules*, 2021, **26**, 5140.
- [47] J. Zhao, S. Ji, Y. Chen, H. Guo and P. Yang, *Phys. Chem. Chem. Phys.*, 2012, **14**, 8803–8817.
- [48] S. Lower and M. El-Sayed, *Chem. Rev.*, 1966, **66**, 199–241.
- [49] G. Baryshnikov, B. Minaev and H. Ågren, *Chem. Rev.*, 2017, **117**, 6500–6537.
- [50] M. Kasha, *Discuss. Faraday Soc.*, 1950, **9**, 14–19.
- [51] R. C. Evans, P. Douglas and H. D. Burrow, *Applied photochemistry*, Springer, 2013.
- [52] A. Kikuchi, Y. Nakabai, N. Oguchi-Fujiyama, K. Miyazawa and M. Yagi, *J. Lumin.*, 2015, **166**, 203.
- [53] R. M. Sayre, J. C. Dowdy, A. J. Gerwig, W. J. Shlelds and R. V. Lloyd, *Photochem. Photobiol.*, 2005, **81**, 452.
- [54] D. Dondi, A. Albini and N. Serpone, *Photochem. Photobiol. Sci.*, 2006, **5**, 835–843.
- [55] V. Lhiaubet-Vallet, M. Marin, O. Jimenez, O. Gorchs, C. Trullas and M. A. Miranda, *Photochem. Photobiol. Sci.*, 2010, **9**, 552.
- [56] B. Herzog, J. Giesinger and V. Settels, *Photochem. Photobiol. Sci.*, 2020, **19**, 1636–1649.
- [57] M. Bertolotti, *The history of the laser*, CRC press, 2004.

- [58] J. Hecht, *Appl. Opt.*, 2010, **49**, F99–F122.
- [59] R. Berera, R. van Grondelle and J. T. M. Kennis, *Photosynth. Res.*, 2009, **101**, 105.
- [60] C. Chen and H. Chen, *Optik*, 2013, **124**, 5199–5201.
- [61] D. J. L. Coxon, M. Staniforth, B. G. Breeze, S. E. Greenough, J. P. Goss, M. Monti, J. Lloyd-Hughes, V. G. Stavros and M. E. Newton, *J. Phys. Chem. Lett.*, 2020, **11**, 6677–6683.
- [62] M. Monti, S. Tao, M. Staniforth, A. Crocker, E. Griffin, A. Wijesekara, R. Hatton and J. Lloyd-Hughes, *J. Phys. Chem. C*, 2018, **122**, 20669–20675.
- [63] D. Zhao and E. E. Chia, *Adv. Opt. Mater.*, 2020, **8**, 1900783.
- [64] M. G. Burdanova, A. P. Tsapenko, M. V. Kharlamova, E. I. Kauppinen, B. P. Gorshunov, J. Kono and J. Lloyd-Hughes, *Adv. Opt. Mater.*, 2021, **9**, 2101042.
- [65] J. Hebling, M. C. Hoffmann, H. Y. Hwang, K.-L. Yeh and K. A. Nelson, *Phys. Rev. B*, 2010, **81**, 035201.
- [66] M. C. Hoffmann, J. Hebling, H. Y. Hwang, K.-L. Yeh and K. A. Nelson, *Phys. Rev. B*, 2009, **79**, 161201.
- [67] *Mai Tai SP manual*, 2002, https://www.spectra-physics.com/mam/celum/celum_assets/sp/resources/284A_Rev_G_Mai_Tai_Users_Manual.pdf?1, Accessed 4th November 2021.
- [68] H. A. Haus, *IEEE J. Sel. Top. Quantum Electron.*, 2000, **6**, 1173–1185.
- [69] D. Strickland and G. Mourou, *Opt. Commun.*, 1985, **55**, 447.
- [70] J. Squier, F. Salin, G. Mourou and D. Harter, *Opt. Lett.*, 1991, **16**, 324.
- [71] G. Cerullo and S. De Silvestri, *Rev. Sci. Instrum.*, 2003, **74**, 1–18.
- [72] G. C. Bhar, P. Kumbhakar, U. Chatterjee, A. M. Rudra, Y. Kuwano and H. Kouta, *Appl. Opt.*, 1998, **37**, 7827–7831.
- [73] P. Malý, J. Ravensbergen, J. T. Kennis, R. Van Grondelle, R. Croce, T. Mančal and B. Van Oort, *Sci. Rep.*, 2017, **7**, 1–7.
- [74] A. K. Dharmadhikari, F. A. Rajgara, N. C. S. Reddy, A. S. Sandhu and D. Mathur, *Opt. Express*, 2004, **12**, 695–700.

- [75] D. Majus, V. Jukna, E. Pileckis, G. Valiulis and A. Dubietis, *Opt. Express*, 2011, **19**, 16317–16323.
- [76] U. Megerle, I. Pugliesi, C. Schriever, C. F. Sailer and E. Riedle, *Appl. Phys. B*, 2009, **96**, 215–231.
- [77] S. A. Kovalenko, A. L. Dobryakov, J. Ruthmann and N. P. Ernsting, *Phys. Rev. A*, 1999, **59**, 2369.
- [78] A. Brodeur and S. Chin, *J. Opt. Soc. Am. B*, 1999, **16**, 637–650.
- [79] W. Ryba-Romanowski, B. Macalik, A. Strzyp, R. Lisiecki, P. Solarz and R. M. Kowalski, *Opt. Mater.*, 2014, **36**, 1745–1748.
- [80] M. Ziolk, R. Naskrecki and J. Karolczak, *Opt. Commun.*, 2004, **241**, 221–229.
- [81] C. B. Schaffer, A. Brodeur and E. Mazur, *Meas. Sci. Technol.*, 2001, **12**, 1784–1794.
- [82] T. Jia, X. X. Li, D. H. Feng, C. F. Cheng, R. X. Li, H. Chen and Z. Z. Xu, *Appl. Phys. A*, 2005, **81**, 645–649.
- [83] R. Huber, H. Satzger, W. Zinth and J. Wachtveitl, *Opt. Commun.*, 2001, **194**, 443–448.
- [84] A. D. Dunkelberger, R. D. Kieda, B. M. Marsh and F. Fleming Crim, *J. Phys. Chem. A*, 2015, **119**, 6155.
- [85] L. A. Baker, S. L. Clark, S. Habershon and V. G. Stavros, *J. Phys. Chem. Lett.*, 2017, **8**, 2113.
- [86] Y. Peperstraete, M. Staniforth, L. A. Baker, N. d. N. Rodrigues, N. C. Cole-Filipiak, W.-D. Quan and V. G. Stavros, *Phys. Chem. Chem. Phys.*, 2016, **18**, 28140.
- [87] L. A. Baker, M. D. Horbury and V. G. Stavros, *Opt. Express*, 2016, **24**, 10700.
- [88] C. Ma, C. T.-L. Chan, R. C.-T. Chan, A. K.-W. Wong, B. P.-Y. Chung and W.-M. Kwok, *Phys. Chem. Chem. Phys.*, 2018, **20**, 24796.
- [89] L. A. Baker, L. C. Grosvenor, M. N. R. Ashfold and V. G. Stavros, *Chem. Phys. Lett.*, 2016, **664**, 39.
- [90] M.-H. Kao, R. K. Venkatraman, M. Sneha, M. Wilton and A. J. Orr-Ewing, *J. Phys. Chem. A*, 2021, **125**, 636–645.

- [91] A. Maciejewski, R. Naskrecki, M. Lorenc, M. Ziolek, J. Karolczak, J. Kubicki, M. Matysiak and M. Szymanski, *J. Mol. Struct.*, 2000, **555**, 1.
- [92] C. Ruckebusch, M. Sliwa, P. Pernot, A. de Juan and R. Tauler, *J. Photoch. Photobio. C*, 2012, **13**, 1.
- [93] L. A. Baker, B. Marchetti, T. N. V. Karsili, V. G. Stavros and M. N. R. Ashfold, *Chem. Soc. Rev.*, 2017, **46**, 3770.
- [94] N. Serpone, D. Dondi and A. Albini, *Inorg. Chim. Acta*, 2007, **360**, 794.
- [95] A. C. Cozzi, P. Perugini and S. Gourion-Arsiquaud, *Eur. J. Pharm. Sci.*, 2018, **121**, 309.
- [96] M. Han, D. Ishikawa, E. Muto and M. Hara, *J. Lumin.*, 2009, **129**, 1163.
- [97] G. Fleming, *Chemical applications of ultrafast spectroscopy*, Oxford University Press, New York, NY, 1986.
- [98] M. Maiuri, M. Garavelli and G. Cerullo, *J. Am. Chem. Soc.*, 2019, **142**, 3–15.
- [99] J. S. Beckwith, C. A. Rumble and E. Vauthey, *Int. Rev. Phys. Chem.*, 2020, **39**, 135–216.
- [100] J. J. Snellenberg, *MSc thesis*, Vrije Universiteit Amsterdam, 2010.
- [101] L. A. Baker, M. D. Horbury, S. E. Greenough, F. Allais, P. S. Walsh, S. Habershon and V. G. Stavros, *J. Phys. Chem. Lett.*, 2016, **7**, 56.
- [102] M. D. Horbury, A. L. Flourat, S. E. Greenough, F. Allais and V. G. Stavros, *Chem. Commun.*, 2018, **54**, 936.
- [103] L. A. Baker, M. Staniforth, A. L. Flourat, F. Allais and V. G. Stavros, *ChemPhotoChem*, 2018, **2**, 743.
- [104] K. M. Mullen and I. H. M. Van Stokkum, *J. Stat. Soft.*, 2007, **18**, 1.
- [105] J. Snellenburg, S. Laptanok, R. Seger, K. Mullen and I. Van Stokkum, *J. Stat. Soft.*, 2012, **49**, 1.
- [106] I. H. van Stokkum, D. S. Larsen and R. van Grondelle, *Biochim. Biophys. Acta*, 2004, **1657**, 82.
- [107] B. Dietzek, T. Pascher, V. Sundström and A. Yartsev, *Laser Phys. Lett.*, 2007, **4**, 38.

- [108] M. Ziolk, M. Lorenc and R. Naskrecki, *Appl. Phys. B*, 2001, **72**, 843–847.
- [109] M. P. Grubb, A. J. Orr-Ewing and M. N. Ashfold, *Rev. Sci. Instrum.*, 2014, **85**, 064104.
- [110] I. Walmsley, L. Waxer and C. Dorrer, *Rev. Sci. Instrum.*, 2001, **72**, 1–29.
- [111] I. Z. Kozma, P. Krok and E. Riedle, *J. Opt. Soc. Am. B*, 2005, **22**, 1479–1485.
- [112] M. Rasmusson, A. N. Tarnovsky, E. Åkesson and V. Sundström, *Chem. Phys. Lett.*, 2001, **335**, 201–208.
- [113] I. V. Hertel and W. Radloff, *Rep. Prog. Phys.*, 2006, **69**, 1897.
- [114] V. G. Stavros and J. R. R. Verlet, *Annu. Rev. Phys. Chem.*, 2016, **67**, 211.
- [115] N. d. N. Rodrigues, M. Staniforth and V. G. Stavros, *Proc. R. Soc. A*, 2016, **472**, 20160677.
- [116] M. V. Johnston, *Trend. Anal. Chem.*, 1984, **3**, 58.
- [117] U. Even, J. Jortner, D. Noy, N. Lavie and C. Cossart-Magos, *J. Chem. Phys.*, 2000, **112**, 8068.
- [118] D. Irimia, R. Kortekaas and M. H. M. Janssen, *Phys. Chem. Chem. Phys.*, 2009, **11**, 3958.
- [119] D. Irimia, D. Dobrikov, R. Kortekaas, H. Voet, D. A. van den Ende, W. A. Groen and M. H. M. Janssen, *Rev. Sci. Instrum.*, 2009, **80**, 113303.
- [120] C. Meng and M. H. M. Janssen, *Rev. Sci. Instrum.*, 2015, **86**, 023110.
- [121] W. C. Wiley and I. H. McLaren, *Rev. Sci. Instrum.*, 1955, **26**, 1150.
- [122] T. Streibel and R. Zimmermann, *Annu. Rev. Anal. Chem.*, 2014, **7**, 361.
- [123] F. Gunzer, S. Krüger and J. Grotemeyer, *Mass Spectrom. Rev.*, 2019, **38**, 202.
- [124] M. Staniforth and V. G. Stavros, *Proc. R. Soc. A*, 2013, **469**, 20130458.
- [125] *Cary 60 manual*, 2019, <https://www.agilent.com/cs/library/usermanuals/Public/G6860-90001.pdf>, Accessed July 22nd, 2021.
- [126] M. Czerny and A. Turner, *Zeitschrift für Physik*, 1930, **61**, 792–797.
- [127] M. F. Vitha, *Spectroscopy: Principles and Instrumentation*, John Wiley & Sons, 2018.

- [128] N. N. Mohd Yusof Chan, A. Idris, Z. H. Zainal Abidin, H. A. Tajuddin and Z. Abdullah, *RSC Adv.*, 2021, **11**, 13409–13445.
- [129] C. Würth, M. Grabolle, J. Pauli, M. Spieles and U. Resch-Genger, *Nat. Protoc.*, 2013, **8**, 1535–1550.
- [130] *Fluorolog-3 manual*, 2002, https://www.horiba.com/fileadmin/uploads/Scientific/Downloads/UserArea/Fluorescence/Legacy/Complete_FluoroLog3_Manual.pdf, Accessed July 15th, 2021.
- [131] R. J. Clarke and A. Oprysa, *J. Chem. Educ.*, 2004, **81**, 705.
- [132] J. L. Kinsey, *Annu. Rev. Phys. Chem.*, 1977, **28**, 349–372.
- [133] R. N. Zare, *Annu. Rev. Anal. Chem.*, 2012, **5**, 1–14.
- [134] A. Lindinger, J. P. Toennies and A. F. Vilesov, *Chem. Phys. Lett.*, 2006, **429**, 1–7.
- [135] J. C. Dean, R. Kusaka, P. S. Walsh, F. Allais and T. S. Zwier, *J. Am. Chem. Soc.*, 2014, **136**, 14780.
- [136] W. Chin, M. Mons, I. Dimicoli, F. Piuzzi, B. Tardivel and M. Elhanine, *Eur. Phys. J. D*, 2002, **20**, 347–355.
- [137] N. d. N. Rodrigues, N. C. Cole-Filipiak, K. N. Blodgett, C. Abeysekera, T. S. Zwier and V. G. Stavros, *Nat. Commun.*, 2018, **9**, 5188.
- [138] N. d. N. Rodrigues, M. Staniforth, J. D. Young, Y. Peperstraete, N. C. Cole-Filipiak, J. R. Gord, P. S. Walsh, D. M. Hewett, T. S. Zwier and V. G. Stavros, *Faraday Discuss.*, 2016, **194**, 709.
- [139] C. Ochsenfeld, J. Kussmann and D. S. Lambrecht, *Rev. Comput. Chem.*, 2007, **23**, 1.
- [140] K. I. Ramachandran, D. Gopakumar and K. Namboori, in *Basis Sets. In: Computational Chemistry and Molecular Modeling: Principles and Applications*, Springer Berlin Heidelberg, Berlin, Heidelberg, 2008, pp. 115–138.
- [141] K. L. Schuchardt, B. T. Didier, T. Elsethagen, L. Sun, V. Gurumoorthi, J. Chase, J. Li and T. L. Windus, *J. Chem. Inf. Model.*, 2007, **47**, 1045–1052.
- [142] F. Jensen, *Wiley Interdiscip. Rev. Comput. Mol. Sci.*, 2013, **3**, 273–295.

- [143] T. H. Dunning Jr, *J. Chem. Phys.*, 1989, **90**, 1007–1023.
- [144] R. A. Kendall, T. H. Dunning Jr and R. J. Harrison, *J. Chem. Phys.*, 1992, **96**, 6796–6806.
- [145] W. J. Hehre, R. Ditchfield and J. A. Pople, *J. Chem. Phys.*, 1972, **56**, 2257–2261.
- [146] R. Krishnan, J. S. Binkley, R. Seeger and J. A. Pople, *J. Chem. Phys.*, 1980, **72**, 650–654.
- [147] M. Valiev, E. J. Bylaska, N. Govind, K. Kowalski, T. P. Straatsma, H. J. Van Dam, D. Wang, J. Nieplocha, E. Apra, T. L. Windus *et al.*, *Comp. Phys. Commun.*, 2010, **181**, 1477–1489.
- [148] K. A. Baseden and J. W. Tye, *J. Chem. Educ.*, 2014, **91**, 2116–2123.
- [149] J. P. Perdew, K. Burke and M. Ernzerhof, *Phys. Rev. Lett.*, 1996, **77**, 3865.
- [150] C. Adamo and V. Barone, *J. Chem. Phys.*, 1999, **110**, 6158–6170.
- [151] A. D. Becke, *J. Chem. Phys.*, 1992, **96**, 2155–2160.
- [152] C. Lee, W. Yang and R. G. Parr, *Phys. Rev. B*, 1988, **37**, 785.
- [153] S. F. Sousa, P. A. Fernandes and M. J. Ramos, *J. Phys. Chem. A*, 2007, **111**, 10439–10452.
- [154] P. Hohenberg and W. Kohn, *Phys. Rev.*, 1964, **136**, B864.
- [155] W. Kohn and L. J. Sham, *Phys. Rev.*, 1965, **140**, A1133–A1138.
- [156] E. Runge and E. K. Gross, *Phys. Rev. Lett.*, 1984, **52**, 997.
- [157] J. Gavnholt, T. Olsen, M. Engelund and J. Schiøtz, *Phys. Rev. B*, 2008, **78**, 075441.
- [158] T. Kowalczyk, S. R. Yost and T. V. Voorhis, *J. Chem. Phys.*, 2011, **134**, 054128.
- [159] M. Kolar, J. Fanfrlik, M. Lepšik, F. Forti, F. J. Luque and P. Hobza, *J. Phys. Chem. B*, 2013, **117**, 5950–5962.
- [160] A. V. Marenich, C. J. Cramer and D. G. Truhlar, *J. Phys. Chem. B*, 2009, **113**, 6378–6396.

- [161] E. Apra, E. J. Bylaska, W. A. De Jong, N. Govind, K. Kowalski, T. P. Straatsma, M. Valiev, H. J. van Dam, Y. Alexeev, J. Anchell *et al.*, *J. Chem. Phys.*, 2020, **152**, 184102.
- [162] A. Klamt, *Wiley Interdiscip. Rev. Comput. Mol. Sci.*, 2018, **8**, e1338.
- [163] A. Benazzouz, L. Moity, C. Pierlot, V. Molinier and J.-M. Aubry, *Colloids Surf. A*, 2014, **458**, 101–109.
- [164] J. Chen, C. L. Brooks III and J. Khandogin, *Curr. Opin. Struct. Biol.*, 2008, **18**, 140–148.
- [165] S. Lautenschlager, H. C. Wulf and M. R. Pittelkow, *The Lancet*, 2007, **370**, 528–537.
- [166] J. Krutmann, T. Passeron, Y. Gilaberte, C. Granger, G. Leone, M. Narda, S. Schalka, C. Trullas, P. Masson and H. W. Lim, *J. Eur. Acad. Dermatol.*, 2020, **34**, 447–454.
- [167] J. Nash, P. R. Tanner and P. J. Matts, *Dermatol. Clin.*, 2006, **24**, 63.
- [168] J. E. Frederick, H. E. Snell and E. K. Haywood, *Photochem. Photobiol.*, 1989, **50**, 443.
- [169] Y. Matsumi and M. Kawasaki, *Chem. Rev.*, 2003, **103**, 4767.
- [170] J. F. Bornman, P. W. Barnes, S. A. Robinson, C. L. Ballaré, S. D. Flint and M. M. Caldwell, *Photochem. Photobiol. Sci.*, 2015, **14**, 88.
- [171] J. R. Herman and E. A. Celarier, *J. Geophys. Res.-Atmos.*, 1997, **102**, 28003.
- [172] R. L. McKenzie, P. J. Aucamp, A. F. Bais, L. O. Björn and M. Ilyas, *Photochem. Photobiol. Sci.*, 2007, **6**, 218.
- [173] A. F. Bais, G. Bernhard, R. L. McKenzie, P. J. Aucamp, P. J. Young, M. Ilyas, P. Jöckel and M. Deushi, *Photochem. Photobiol. Sci.*, 2019, **18**, 602.
- [174] N. D. Paul and D. Gwynn-Jones, *Trends Ecol. Evol.*, 2003, **18**, 48.
- [175] J. B. Kerr and V. E. Fioletov, *Atmos. Ocean*, 2008, **46**, 159.
- [176] A. Mithal, D. A. Wahl, J.-P. Bonjour, P. Burckhardt, B. Dawson-Hughes, J. A. Eisman, G. El-Hajj Fuleihan, R. G. Josse, P. Lips and J. Morales-Torres, *Osteoporos. Int.*, 2009, **20**, 1807.

- [177] P. Lips and N. M. van Schoor, *Best Pract. Res. Clin. Endocrinol. Metab.*, 2011, **25**, 585.
- [178] A. Wirz-Justice, P. Graw, K. Kräuchi, A. Sarrafzadeh, J. English, J. Arendt and L. Sand, *J. Affect. Disord.*, 1996, **37**, 109.
- [179] M. B. Humble, *J. Photoch. Photobio. B*, 2010, **101**, 142.
- [180] R. M. Lucas, S. Yazar, A. R. Young, M. Norval, F. R. de Gruijl, Y. Takizawa, L. E. Rhodes, C. A. Sinclair and R. E. Neale, *Photochem. Photobiol. Sci.*, 2019, **18**, 641.
- [181] M. F. Holick, *Anticancer Res.*, 2016, **36**, 1345.
- [182] P. H. Hart, M. Norval, S. N. Byrne and L. E. Rhodes, *Annu. Rev. Pathol.*, 2019, **14**, 55.
- [183] G. J. Fisher, Z. Wang, S. C. Datta, J. Varani, S. Kang and J. J. Voorhees, *New Engl. J. Med.*, 1997, **337**, 1419.
- [184] R. P. Gallagher and T. K. Lee, *Prog. Biophys. Mol. Bio.*, 2006, **92**, 119.
- [185] M. Wlaschek, I. Tantcheva-Poór, L. Naderi, W. Ma, L. A. Schneider, Z. Razi-Wolf, J. Schüller and K. Scharffetter-Kochanek, *J. Photoch. Photobio. B*, 2001, **63**, 41.
- [186] H. R. Taylor, S. K. West, F. S. Rosenthal, B. Muñoz, H. S. Newland, H. Abbey and E. A. Emmett, *New Engl. J. Med.*, 1988, **319**, 1429.
- [187] F. R. De Gruijl, *Eur. J. Cancer*, 1999, **35**, 2003.
- [188] D. L. Narayanan, R. N. Saladi and J. L. Fox, *Int. J. Dermatol.*, 2010, **49**, 978.
- [189] P. A. Morganroth, H. W. Lim and C. T. Burnett, *Am. J. Lifestyle Med.*, 2013, **7**, 168.
- [190] A. R. Rhodes, *Cancer*, 1995, **75**, 613.
- [191] A. C. Geller, R. W. Clapp, A. J. Sober, L. Gonsalves, L. Mueller, C. L. Christiansen, W. Shaikh and D. R. Miller, *J. Clin. Oncol.*, 2013, **31**, 4172.
- [192] N. A. Kasparian, J. K. McLoone and B. Meiser, *J. Behav. Med.*, 2009, **32**, 406.
- [193] M. Brenner and V. J. Hearing, *Photochem. Photobiol.*, 2008, **84**, 539.

- [194] J.-P. Ortonne, *Brit. J. Dermatol.*, 2002, **146**, 7.
- [195] B. A. Gilchrest and M. S. Eller, *Journal of Investigative Dermatology Symposium Proceedings*, 1999, pp. 35–40.
- [196] F. Solano, *Molecules*, 2020, **25**, 1537.
- [197] C. Antoniou, M. G. Kosmadaki, A. J. Stratigos and A. D. Katsambas, *J. Eur. Acad. Dermatol. Venereol.*, 2008, **22**, 1110.
- [198] J. F. Nash and P. R. Tanner, *Photodermatol. Photoimmunol. Photomed.*, 2014, **30**, 88.
- [199] N. A. Shaath, *Photochem. Photobiol. Sci.*, 2010, **9**, 464.
- [200] S. Q. Wang, P. R. Tanner, H. W. Lim and J. F. Nash, *Photochem. Photobiol. Sci.*, 2013, **12**, 197.
- [201] S. Afonso, K. Horita, J. P. S. e Silva, I. F. Almeida, M. H. Amaral, P. A. Lobão, P. C. Costa, M. S. Miranda, J. C. G. E. da Silva and J. M. S. Lobo, *Photoch. Photobio. B*, 2014, **140**, 36.
- [202] J. A. Ruskiewicz, A. Pinkas, B. Ferrer, T. V. Peres, A. Tsatsakis and M. Aschner, *Toxicol. Rep.*, 2017, **4**, 245.
- [203] M. S. Díaz-Cruz, M. Llorca and D. Barceló, *Trend. Anal. Chem.*, 2008, **27**, 873.
- [204] J. M. Brausch and G. M. Rand, *Chemosphere*, 2011, **82**, 1518.
- [205] C.-B. Park, J. Jang, S. Kim and Y. J. Kim, *Ecotox. Environ. Safe.*, 2017, **137**, 57.
- [206] R. Danovaro, L. Bongiorno, C. Corinaldesi, D. Giovannelli, E. Damiani, P. Astolfi, L. Greci and A. Pusceddu, *Environ. Health Persp.*, 2008, **116**, 441.
- [207] R. B. Raffa, J. V. Pergolizzi Jr., R. Taylor Jr. and J. M. Kitzen, *J. Clin. Pharm. Ther.*, 2019, **44**, 134.
- [208] C. A. Downs, E. Kramarsky-Winter, R. Segal, J. Fauth, S. Knutson, O. Bronstein, F. R. Ciner, R. Jeger, Y. Lichtenfeld, C. M. Woodley, P. Pennington, K. Cadenas, A. Kushmaro and Y. Loya, *Arch. Environ. Con, Tox.*, 2016, **70**, 265.

- [209] M. Schlumpf, S. Durrer, O. Faass, C. Ehnes, M. Fuetsch, C. Gaille, M. Henseler, L. Hofkamp, K. Maerkel, S. Reolon, B. Timms, J. A. F. Tresguerres and W. Lichtensteiger, *Int. J. Androl.*, 2008, **31**, 144.
- [210] Y. Huang, J. C.-F. Law, T.-K. Lam and K. S.-Y. Leung, *Sci. Total Environ.*, 2020, 142486.
- [211] A. Fourtanier, D. Moyal and S. Seite, *Photochem. Photobiol. Sci.*, 2012, **11**, 81.
- [212] K. Morabito, N. C. Shapley, K. G. Steeley and A. Tripathi, *Int. J. Cosmet. Sci.*, 2011, **33**, 385.
- [213] N. Saewan and A. Jimtaisong, *J. Cosmet. Dermatol.*, 2015, **14**, 47.
- [214] B. W. Shirley, *Trends Plant Sci.*, 1996, **1**, 377.
- [215] M. Ruegger and C. Chapple, *Genetics*, 2001, **159**, 1741–1749.
- [216] C. Milkowski, A. Baumert, D. Schmidt, L. Nehlin and D. Strack, *Plant J.*, 2004, **38**, 80–92.
- [217] A. K. Bharti and J. P. Khurana, *Photochem. Photobiol.*, 1997, **65**, 765–776.
- [218] O. Hendrawati, Q. Yao, H. K. Kim, H. J. Linthorst, C. Erkelens, A. W. Lefeber, Y. H. Choi and R. Verpoorte, *Plant Sci.*, 2006, **170**, 1118.
- [219] N. Nićiforović and H. Abramovič, *Compr. Rev. Food Sci. Food Saf.*, 2014, **13**, 34–51.
- [220] V. Nguyen, J. D. Stewart, I. Ioannou and F. Allais, *Front. Chem.*, 2021, **9**, 350.
- [221] M. D. Horbury, W.-D. Quan, A. L. Flourat, F. Allais and V. G. Stavros, *Phys. Chem. Chem. Phys.*, 2017, **19**, 21127.
- [222] Y. Liu, X. Zhao, J. Luo and S. Yang, *J. Lumin.*, 2019, **206**, 469.
- [223] L. A. Baker, M. Staniforth, A. L. Flourat, F. Allais and V. G. Stavros, *ChemPhysChem*, 2020, **21**, 2006.
- [224] J. Luo, Y. Liu, S. Yang, A. L. Flourat, F. Allais and K. Han, *J. Phys. Chem. Lett.*, 2017, **8**, 1025.

- [225] X. Zhao, F. Ji, Y. Liang, P. Li, Y. Jia, X. Feng, Y. Sun, Y. Shi, L. Zhu and G. Zhao, *J. Lumin.*, 2020, **223**, 117228.
- [226] M. D. Horbury, M. A. Turner, J. S. Peters, M. Mention, A. L. Flourat, N. D. Hine, F. Allais and V. G. Stavros, *Front. Chem.*, 2020, **8**, 633.
- [227] T. T. Abiola, A. L. Whittock and V. G. Stavros, *Molecules*, 2020, **25**, 3945.
- [228] X. Zhao, J. Luo, S. Yang and K. Han, *J. Phys. Chem. Lett.*, 2019, **10**, 4197.
- [229] S. Jiang, S. Liu and W. Feng, *J. Mech. Behav. Biomed.*, 2011, **4**, 1228.
- [230] E. A. Kamoun, E.-R. S. Kenawy and X. Chen, *J. Adv. Res.*, 2017, **8**, 217.
- [231] A. Springsteen, R. Yurek, M. Frazier and K. F. Carr, *Anal. Chim. Acta*, 1999, **380**, 155–164.
- [232] A. M. Bode and E. Roh, *Cells*, 2020, **9(7)**, 1674.
- [233] D. Garoli, M. G. Pelizzo, P. Nicolosi, A. Peserico, E. Tonin and M. Alaibac, *J. Dermatol. Sci.*, 2009, **56**, 89–98.
- [234] M. Douguet, C. Picard, G. Savary, F. Merlaud, N. Loubat-Bouleuc and M. Grisel, *Colloids Surf. B*, 2017, **154**, 307–314.
- [235] D. G. Beasley and T. A. Meyer, *Am. J. Clin. Dermatol.*, 2010, **11**, 413–421.
- [236] O. V. Dueva-Koganov, C. Rocafort, S. Orofino, U. Osterwalder and J. Brito, *Int. J. Cosmet. Sci.*, 2010, **32**, 313–313.
- [237] M. Lodén, H. Beitner, H. Gonzalez, D. Edström, U. Åkerström, J. Austad, I. Buraczewska-Norin, M. Matsson and H. Wulf, *Br. J. Dermatol.*, 2011, **165**, 255.
- [238] J. P. Paiva, R. R. Diniz, A. C. Leitão, L. M. Cabral, R. S. Fortunato, B. A. Santos and M. de Pádula, *Crit. Rev. Toxicol.*, 2020, **50**, 707–723.
- [239] S. Pillai, C. Oresajo and J. Hayward, *Int. J. Cosmet. Sci.*, 2005, **27**, 17–34.
- [240] R. Haywood, P. Wardman, R. Sanders and C. Linge, *J. Invest. Dermatol.*, 2003, **121**, 862.
- [241] S. I. Liochev, *Free Radic. Biol. Med.*, 2013, **60**, 1–4.

- [242] A. L. Morocho-Jácome, T. B. Freire, A. C. de Oliveira, T. S. de Almeida, C. Rosado, M. V. R. Velasco and A. R. Baby, *J. Cosmet. Dermatol.*, 2021, **20**, 729–737.
- [243] E. Gregoris, S. Fabris, M. Bertelle, L. Grassato and R. Stevanato, *Int. J. Pharm.*, 2011, **405**, 97.
- [244] L. C. Tomazelli, M. M. de Assis Ramos, R. Sauce, T. M. Cândido, F. D. Sarruf, C. A. S. de Oliveira Pinto, C. A. de Oliveira, C. Rosado, M. V. R. Velasco and A. R. Baby, *Int. J. Pharm.*, 2018, **552**, 401–406.
- [245] E. Damiani, P. Astolfi, L. Cionna, F. Ippoliti and L. Greci, *Free Radic. Res.*, 2006, **40**, 485–494.
- [246] S. B. Kedare and R. Singh, *J. Food Sci. Technol.*, 2011, **48**, 412–422.
- [247] L. M. Magalhães, M. A. Segundo, S. Reis and J. L. Lima, *Anal. Chim. Acta*, 2008, **613**, 1–19.
- [248] K. Mishra, H. Ojha and N. K. Chaudhury, *Food Chem.*, 2012, **130**, 1036–1043.
- [249] M. S. Blois, *Nature*, 1958, **181**, 1199–1200.
- [250] O. P. Sharma and T. K. Bhat, *Food Chem.*, 2009, **113**, 1202–1205.
- [251] T. T. Schug, R. Abagyan, B. Blumberg, T. J. Collins, D. Crews, P. L. DeFur, S. M. Dickerson, T. M. Edwards, A. C. Gore, L. J. Guillette *et al.*, *Green Chem.*, 2013, **15**, 181–198.
- [252] J. Wang, L. Pan, S. Wu, L. Lu, Y. Xu, Y. Zhu, M. Guo and S. Zhuang, *Int. J. Environ. Res. Public Health*, 2016, **13**, 782.
- [253] M. Krause, A. Klit, M. Blomberg Jensen, T. Søbørg, H. Frederiksen, M. Schlumpf, W. Lichtensteiger, N. E. Skakkebaek and K. T. Drzewiecki, *Int. J. Androl.*, 2012, **35**, 424.
- [254] S. P. Huong, V. Andrieu, J.-P. Reynier, E. Rocher and J.-D. Fourneron, *J. Photoch. Photobio. A*, 2007, **186**, 65.
- [255] Y. Miyazaki, Y. Inokuchi, N. Akai and T. Ebata, *J. Phys. Chem. Lett.*, 2015, **6**, 1134.
- [256] K. Yamazaki, Y. Miyazaki, Y. Harabuchi, T. Taketsugu, S. Maeda, Y. Inokuchi, S.-n. Kinoshita, M. Sumida, Y. Onitsuka, H. Kohguchi, M. Ehara and T. Ebata, *J. Phys. Chem. Lett.*, 2016, **7**, 4001.

- [257] S.-n. Kinoshita, Y. Miyazaki, M. Sumida, Y. Onitsuka, H. Kohguchi, Y. Inokuchi, N. Akai, T. Shiraogawa, M. Ehara, K. Yamazaki, Y. Harabuchi, S. Maeda, T. Taketsugu and T. Ebata, *Phys. Chem. Chem. Phys.*, 2018, **20**, 17583.
- [258] S.-n. Kinoshita, Y. Inokuchi, Y. Onitsuka, H. Kohguchi, N. Akai, T. Shiraogawa, M. Ehara, K. Yamazaki, Y. Harabuchi, S. Maeda *et al.*, *Phys. Chem. Chem. Phys.*, 2019, **21**, 19755–19763.
- [259] P. Morlière, O. Avice, T. S. E. Melo, L. Dubertret, M. Giraud and R. Santus, *Photochem. Photobiol.*, 1982, **36**, 395.
- [260] K. M. Krokidi, M. A. P. Turner, P. A. J. Percy and V. G. Stavros, *Mol. Phys.*, 2020, e1811910.
- [261] S.-n. Kinoshita, Y. Harabuchi, Y. Inokuchi, S. Maeda, M. Ehara, K. Yamazaki and T. Ebata, *Phys. Chem. Chem. Phys.*, 2021, **23**, 834–845.
- [262] A. Sharma, K. Bányiová, P. Babica, N. E. Yamani, A. R. Collins and P. Čupr, *Sci. Total Environ.*, 2017, **593-594**, 18.
- [263] A. Sharma, K. Řiháčková and P. Čupr, *Sci. Total Environ.*, 2019, **657**, 902.
- [264] M. Schlumpf, B. Cotton, M. Conscience, V. Haller, B. Steinmann and W. Lichtensteiger, *Environ. Health Persp.*, 2001, **109**, 239.
- [265] S. Pattanaargson, T. Munhapol, P. Hirunsupachot and P. Luangthongaram, *J. Photoch. Photobio. A*, 2004, **161**, 269–274.
- [266] T. M. Karpkird, S. Wanichwecharungruang and B. Albinsson, *Photochem. Photobiol. Sci.*, 2009, **8**, 1455.
- [267] J. M. Woolley, J. S. Peters, M. A. P. Turner, G. J. Clarkson, M. D. Horbury and V. G. Stavros, *Phys. Chem. Chem. Phys.*, 2019, **21**, 14350.
- [268] S. Q. Wang, H. Xu, J. W. Stanfield, U. Osterwalder and B. Herzog, *J. Am. Acad. Dermatol.*, 2017, **77**, 42.
- [269] X. He, A. F. Bell and P. J. Tonge, *Org. Lett.*, 2002, **4**, 1523.
- [270] M. Jia, K. Dahlman-Wright and J. Å Gustafsson, *Best Pract. Res. Clin. Endocrinol. Metab.*, 2015, **29**, 557–568.
- [271] E. K. Shanle and W. Xu, *Chem. Res. Toxicol.*, 2011, **24**, 6–19.

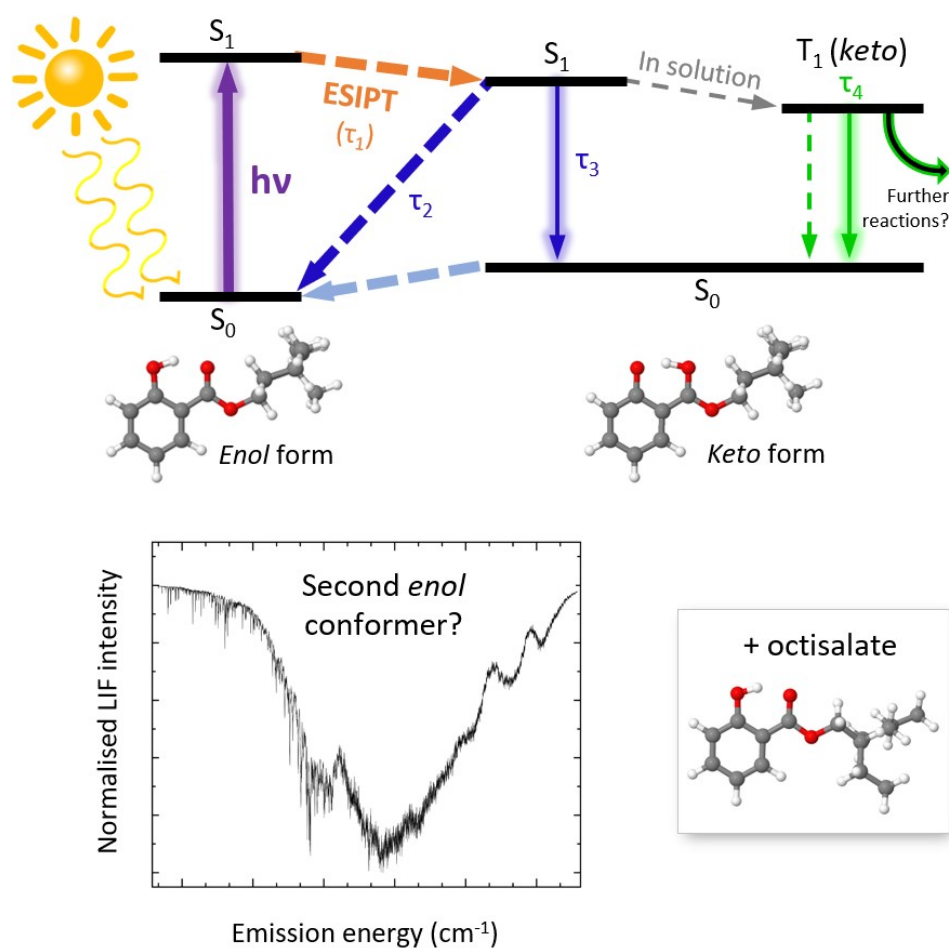
- [272] J. Orans, D. G. Teotico and M. R. Redinbo, *Mol. Endocrinol.*, 2005, **19**, 2891–2900.
- [273] J. Lintelmann, A. Katayama, N. Kurihara, L. Shore and A. Wenzel, *Pure Appl. Chem.*, 2003, **75**, 631–681.
- [274] P. Balaguer, F. François, F. Comunale, H. Fenet, A.-M. Boussioux, M. Pons, J.-C. Nicolas and C. Casellas, *Sci. Total Environ.*, 1999, **233**, 47–56.
- [275] P. Fechner, F. Pröll, M. Carlquist and G. Proll, *Anal. Bioanal. Chem.*, 2009, **393**, 1579–1585.
- [276] S. A. Kliewer, B. Goodwin and T. M. Willson, *Endocr. Rev.*, 2002, **23**, 687–702.
- [277] F. Urbach, *J. Photoch. Photobio. B*, 2001, **64**, 99–104.
- [278] Y. Ma and J. Yoo, *J. Cosmet. Dermatol.*, 2021, **20**, 1044–1049.
- [279] U. Osterwalder and B. Herzog, *Photochem. Photobiol. Sci.*, 2010, **9**, 470.
- [280] M. E. Burnett, J. Y. Hu and S. Q. Wang, *Dermatol. Ther.*, 2012, **25**, 244.
- [281] U. Osterwalder and B. Herzog, *Br. J. Dermatol.*, 2009, **161**, 13.
- [282] R. Jansen, U. Osterwalder, S. Q. Wang, M. Burnett and H. W. Lim, *J. Am. Acad. Dermatol.*, 2013, **69**, 867.e1.
- [283] U. Osterwalder, M. Sohn and B. Herzog, *Photodermatol. Photoimmunol. Photomed.*, 2014, **30**, 62.
- [284] M. E. Burnett and S. Q. Wang, *Photodermatol. Photoimmunol. Photomed.*, 2011, **27**, 58.
- [285] J. B. Mancuso, R. Maruthi, S. Q. Wang and H. W. Lim, *Am. J. Clin. Dermatol.*, 2017, **18**, 643.
- [286] S. Schauder and H. Ippen, *Contact Dermatitis*, 1997, **37**, 221.
- [287] T. Wong and D. Orton, *Clin. Dermatol.*, 2011, **29**, 306.
- [288] A. C. de Groot and D. W. Roberts, *Contact Dermatitis*, 2014, **70**, 193.
- [289] H. Hönigsmann, *Photodermatol. Photoimmunol. Photomed.*, 2002, **18**, 75.
- [290] A. R. Young, J. Claveau and A. B. Rossi, *J. Am. Acad. Dermatol.*, 2017, **76**, S100.

- [291] J. A. Parrish, K. F. Jaenicke and R. R. Anderson, *Photochem. Photobiol.*, 1982, **36**, 187.
- [292] B. L. Diffey, C. T. Jansén, F. Urbach and H. C. Wulf, *Photodermatol. Photoimmunol. Photomed.*, 1997, **13**, 64.
- [293] K. Waterston, L. Naysmith and J. L. Rees, *J. Invest. Dermatol.*, 2004, **123**, 958.
- [294] L. Ferrero, M. Pissavini and O. Doucet, *Photochem. Photobiol. Sci.*, 2010, **9**, 540.
- [295] M. Pissavini, C. Tricaud, G. Wiener, A. Lauer, M. Contier, L. Kolbe, C. Trullás Cabanas, F. Boyer, V. Nollent, E. Meredith, E. Dietrich and P. J. Matts, *Int. J. Cosmet. Sci.*, 2018, **40**, 263.
- [296] M. Rohr, E. Klette, S. Ruppert, R. Bimzcok, B. Klebon, U. Heinrich, H. Tronnier, W. Johncock, S. Peters, F. Pflücker, T. Rudolph, H. Flösser-Müller, K. Jenni, D. Kockott, J. Lademann, B. Herzog, S. Bielfeldt, C. Mendrok-Edinger, C. Hanay and L. Zastrow, *Skin Pharmacol. Physiol.*, 2010, **23**, 201.
- [297] A. Dimitrovska Cvetkovska, S. Manfredini, P. Ziosi, S. Molesini, V. Dissette, I. Magri, C. Scapoli, A. Carrieri, E. Durini and S. Vertuani, *Int. J. Cosmet. Sci.*, 2017, **39**, 310.
- [298] B. P. Binks, P. D. Fletcher, A. J. Johnson, I. Marinopoulos, J. Crowther and M. A. Thompson, *J. Photoch. Photobio. A*, 2017, **333**, 186.
- [299] A. Springsteen, R. Yurek, M. Frazier and K. F. Carr, *Anal. Chim. Acta*, 1999, **380**, 155.
- [300] A. W. Schmalwieser, S. Wallisch and B. Diffey, *Photochem. Photobiol. Sci.*, 2012, **11**, 251.
- [301] N. d. N. Rodrigues and V. G. Stavros, *Sci. Prog.*, 2018, **101**, 8.
- [302] S. Q. Wang, J. W. Stanfield and U. Osterwalder, *J. Am. Acad. Dermatol.*, 2008, **59**, 934.
- [303] B. Diffey, *Int. J. Cosmet. Sci.*, 2009, **31**, 63.
- [304] B. L. Diffey, P. R. Tanner, P. J. Matts and J. F. Nash, *J. Am. Acad. Dermatol.*, 2000, **43**, 1024.

- [305] E. Q. Coyne, M. K. Lichtman, J. Simons, A. K. Sarkar and T. M. Runger, *J. Am. Acad. Dermatol.*, 2018, **79**, 373.
- [306] P. J. Matts, V. Alard, M. W. Brown, L. Ferrero, H. Gers-Barlag, N. Issachar, D. Moyal and R. Wolber, *Int. J. Cosmet. Sci.*, 2010, **32**, 35.
- [307] D. Moyal, *Expert Rev. Dermatol.*, 2008, **3**, 307.
- [308] *BASF Sunscreen Simulator*, https://sunscreensimulator.basf.com/Sunscreen_Simulator/login, Accessed May 4th, 2021.
- [309] B. Herzog and U. Osterwalder, *Pure Appl. Chem.*, 2015, **87**, 937.
- [310] E. M. M. Tan, M. Hilbers and W. J. Buma, *J. Phys. Chem. Lett.*, 2014, **5**, 2464.
- [311] V. G. Stavros, *Nat. Chem.*, 2014, **6**, 955.

Chapter 2

Insights into the photoprotection mechanism of the UV filter homosalate





Cite this: DOI: 10.1039/d0cp02610g

Insights into the photoprotection mechanism of the UV filter homosalate†

Emily L. Holt,[‡] Konstantina M. Krokidi,^{‡,a} Matthew A. P. Turner,^{‡,ab} Piyush Mishra,^{‡,c} Timothy S. Zwier,^{‡,c} Natércia d. N. Rodrigues^{‡,*,a} and Vasilios G. Stavros^{‡,*,a}

Homosalate (HMS) is a salicylate molecule that is commonly included within commercial sunscreen formulations to provide protection from the adverse effects of ultraviolet (UV) radiation exposure. In the present work, the mechanisms by which HMS provides UV photoprotection are unravelled, using a multi-pronged approach involving a combination of time-resolved ultrafast laser spectroscopy in the gas-phase and in solution, laser-induced fluorescence, steady-state absorption spectroscopy, and computational methods. The unique combination of these techniques allow us to show that the *enol* tautomer of HMS undergoes ultrafast excited state intramolecular proton transfer (ESIPT) upon photoexcitation in the UVB (290–320 nm) region; once in the *keto* tautomer, the excess energy is predominantly dissipated non-radiatively. Sharp transitions are observed in the LIF spectrum at close-to-origin excitation energies, which points towards the potential presence of a second conformer that does not undergo ESIPT. These studies demonstrate that, overall, HMS exhibits mostly favourable photophysical characteristics of a UV filter for inclusion in sunscreen formulations.

Received 13th May 2020,
Accepted 8th June 2020

DOI: 10.1039/d0cp02610g

rsc.li/pccp

Introduction

Salicylates are defined as salts or esters derived from salicylic acid, several of which have uses within the personal care and pharmaceutical industries.¹ In addition to being included in cosmetics for fragrance and antioxidant properties,^{1,2} salicylates are used as chemical (organic) filters in sunscreen blends, for solar protection *via* absorption of ultraviolet (UV) radiation, specifically UVB radiation (290–320 nm).^{3,4} Even though regulated exposure to UV radiation has positive effects on human health, such as facilitating the synthesis of vitamin D, the use of UV filters in sunscreen formulations is necessary to prevent the adverse effects of overexposure, such as an increased risk of skin cancers.^{5–12}

Despite having a low extinction coefficient compared to other available UV filters,¹³ salicylates are an appealing choice for sunscreen formulators for several reasons. Firstly, the minimal solvatochromic shift that is observed in salicylates

upon significant changes in solvent polarity has been demonstrated in at least 13 different solvents.^{14,15} This negligible shift in peak absorption implies that a range of excipients may be used in a formulation without changing the protection range of wavelengths afforded by these molecules. Furthermore, salicylates contained within sunscreen formulations can serve as solubilizers for other UV filters such as avobenzone, which to date remains the most widely implemented UVA (320–400 nm) filter in the world.^{16–18} In addition, salicylates have a favourable safety record, with few reports of allergenic effects of these compounds.^{19,20} However, a consensus is yet to be reached on whether salicylates used in sunscreens are photostable, that is, if they do not degrade upon prolonged UV exposure. Many publications report that they are indeed photostable,^{18,21–23} while other reports also exist to the contrary.^{24,25}

The molecule chosen as the focus of this study is homomenthyl salicylate (herein referred to as homosalate, HMS); its molecular structure and the range of UV protection it provides is shown in Fig. 1. This molecule is approved for use in sunscreen formulations worldwide and can be employed in substantial quantities (*e.g.* up to 15% w/w in the United States).²⁶ Recent studies in rat models have shown that HMS has low dermal permeability and does not cause any endocrine disruption, both of which are major concerns for many existing UV filters used in sunscreen formulations.^{27,28} In addition, HMS has been deemed to have a favourable toxicological profile.²⁹ However, in the MCF-7 cell line, HMS was shown to

^a Department of Chemistry, University of Warwick, Gibbet Hill Road, Coventry, CV4 7AL, UK. E-mail: v.stavros@warwick.ac.uk, n.das-neves-rodrigues@warwick.ac.uk

^b Molecular Analytical Science Centre for Doctoral Training, Senate House, University of Warwick, Coventry, CV4 7AL, UK

^c Department of Chemistry, Purdue University, West Lafayette, Indiana 47907-2084, USA

† Electronic supplementary information (ESI) available: See DOI: 10.1039/d0cp02610g. The underlying data of this publication can be accessed *via* the Zenodo Archive at DOI: 10.5281/zenodo.3698070.

‡ These authors contributed equally to this work.

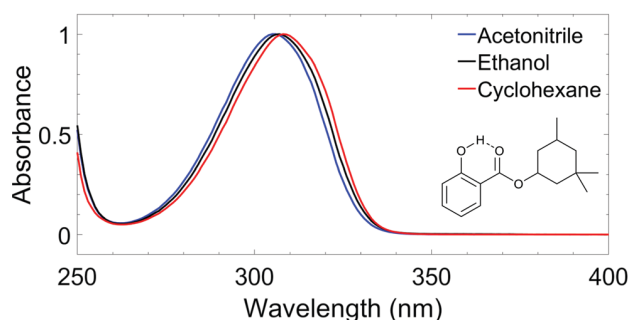


Fig. 1 (a) Normalised UV-visible spectra of homosalate (HMS) in acetonitrile (blue line), ethanol (black line) and cyclohexane (red line), with molecular structure of HMS (*enol* form) inset. The dashed line indicates the presence of an intramolecular hydrogen bond.

have cytotoxic and genotoxic characteristics, and extensive studies on the toxicological effects of HMS are recommended.³⁰

In this study, femtosecond (fs, 10^{-15} s) pump-probe spectroscopy techniques in both the gas-phase and in solution have been used to elucidate the excited state photodynamics of HMS upon absorption of UVB radiation. By using ultrafast spectroscopy, a deeper insight into the specific relaxation mechanism(s) of salicylates upon exposure to solar radiation can be gained, which in turn can be beneficial to determine whether molecules of this type dissipate their incident UV radiation safely, *i.e.* quickly and without generating any harmful and/or reactive photoproducts.^{31,32} Other UV filters with an intramolecular hydrogen bond have previously been investigated with these techniques.^{33–35} For example, upon excitation at its UVA absorption maximum, oxybenzone was shown to exhibit excited state intramolecular proton transfer (ESIPT), followed by a molecular rotation which facilitated a fast decay to the ground electronic state on a picosecond timescale, an ideal behaviour for a UV filter.³³ Conversely, menthyl anthranilate (MenA) was shown to undergo hydrogen atom dislocation, rather than transfer, and a significant energetic barrier towards a nearby conical intersection (CI) was found to prevent fast and efficient excited state relaxation.³⁵ Due to its long-lived nature (\gg nanoseconds), MenA is not an ideal candidate for inclusion in sunscreen formulations as it is vulnerable to detrimental relaxation pathways.³⁵ Therefore, the effect of the intramolecular hydrogen bond in these salicylates is worthy of further investigation. A review of sunscreen molecules that undergo *keto-enol* tautomerisation and ESIPT, studied by ultrafast spectroscopy techniques, has been published previously.³⁶

In the present work, a *bottom-up* approach is employed to investigate the ultrafast molecular dynamics of HMS upon photoexcitation with UVB radiation. The starting point is taken to be HMS in the gas-phase, whereby the influence of external stimuli is eliminated, focusing on establishing the intramolecular photodynamic processes in operation. Complexity is then increased through the addition of a solvent; the added intermolecular interactions act as a stepping stone towards simulating the photoprotection mechanisms of single UV filters within a complex sunscreen formulation. It is crucial that

photodynamics of UV filters such as salicylates in these simpler mixtures are well understood before progressing to studies of more realistic blends.³² The ultrafast pump-probe spectroscopy measurements conducted in this work are supported by laser-induced fluorescence measurements and computational calculations, which can assist with the assignment of spectral features to molecular photodynamics. The results of these complementary techniques combine, not only to enrich our understanding of the photoprotection mechanisms within HMS, thus informing on its inclusion in sunscreens and other cosmetic formulations, but also to compile further information for future UV filter design and sunscreen formulation development.

Methods

Ultrafast laser spectroscopy setup

A fundamental laser beam centred at 800 nm with ~ 40 fs pulse width, ~ 3 mJ per pulse and 1 kHz repetition rate was produced by a commercial femtosecond laser system comprised of a Ti:sapphire oscillator (Spectra-Physics Tsunami) and a regenerative amplifier (Spectra-Physics Spitfire XP). This fundamental beam was subsequently split into three beams of ~ 1 mJ per pulse each, two of which were used to pump two separate optical parametric amplifiers (Light Conversion, TOPAS-C), producing the pump beams for the experiments both in the gas-phase and in solution. Experiments in the gas-phase employed a single-wavelength probe, while in solution the probe beam consisted of a white light continuum, as detailed below.

Experiments in vacuum

a. Time-resolved ion yield (TR-IY). The time-resolved ion yield (TR-IY) apparatus used for the present experiments has been previously described in detail;³⁷ specific details relevant to the present work are provided herein.

Homosalate (HMS, provided by Lipotec SAU) was studied as provided and without any further purification. HMS was vaporised *via* heating to approximately 130 °C and subsequently seeded into helium buffer gas (~ 3 bar). The gaseous mixture was then expanded into vacuum ($\sim 10^{-7}$ mbar) *via* an Even-Lavie pulsed solenoid valve³⁸ to create the sample molecular beam. The pump and probe beams intersected the molecular beam, while the pump-probe time delay (at predefined time intervals Δt) was controlled by a gold retroreflector mounted on a motorised delay stage along the 800 nm fundamental beam path (used to generate the 200 nm probe, see below). The maximum temporal window provided by the delay stage was 1.3 nanoseconds (ns). At the laser-molecular beam intersection point, the pump photoexcited the sample and the probe ionised the excited species.

The pump wavelengths for TR-IY measurements ($\lambda_{\text{pump}} = 305\text{--}335$ nm) were chosen in order to sample the different absorption regions probed in our laser induced fluorescence measurements (see Results and discussion section below), starting from the $S_1(v=0)$ origin of HMS ($29\,833.4\text{ cm}^{-1}$, ~ 335 nm) and evaluating the effect of photoexcitation with higher energies.

The 200 nm probe beam used to photoionize any excited species was generated by successive frequency conversion of the remaining ~ 1 mJ part of the fundamental 800 nm beam using barium borate (BBO) crystals in the following sequence: type I, type II, type I.

The pump–probe ion signal was monitored with a time-of-flight (TOF) mass spectrometer apparatus, equipped with a detector consisting of two microchannel plates (MCPs) coupled to a metal anode. The output from the MCP was measured by a digital oscilloscope (LeCroy LT372 Waverunner) and gated in ion flight time over the mass channel of the parent (HMS^+) ion. The parent TOF signal was then monitored as a function of pump–probe time delay (Δt), resulting in the TR-IY transients. For all TR-IY measurements, the polarizations of the pump and probe beams were kept at magic angle (54.7°) with respect to each other in order to minimize any rotational effects.³⁹ Additionally, power dependence studies were conducted to ensure single-photon initiated dynamics under the current experimental conditions, as shown in Section S1.1.1 (S1.1.1), Fig. S1 of the ESI.[†]⁴⁰

The quoted time constants were extracted from the TR-IY transients by a non-linear curve fitting algorithm (further discussed in the ESI,[†] S1.1.2), comprising a sum of exponential decays convoluted with a Gaussian instrument response function (IRF, typically ~ 170 fs at relevant powers for this experiment, see S1.1.3, Fig. S2, ESI[†]). The kinetic model employed in these fits assumes parallel dynamics, *i.e.* it assumes that all processes start at $\Delta t = 0$. The standard errors provided by the kinetic fit have been herein reported as estimated errors associated with quoted time constants.

b. Laser induced fluorescence (LIF) and dispersed fluorescence (DFL). To complement our gas-phase ultrafast laser spectroscopy studies, high frequency resolution laser induced fluorescence (LIF) measurements were carried out using a separate laser system to the one described above; a detailed description of this apparatus has been provided in previous publications^{41–43} and therefore only specific details pertaining to the present studies are given here.

Helium was used as the seed gas at a pressure of 3–4 bar, flowing over a sample of HMS maintained at 110°C to produce sufficient vapour pressure. A pulsed valve (Parker General Valve Series 9) with an orifice of $500\ \mu\text{m}$ operating at 20 Hz was used to supersonically cool the sample as it expanded into vacuum. The sample was interrogated with the doubled output of a Nd:YAG (Quantel Q-smart 450) pumped tunable dye laser (Radiant Dyes Narrowscan). LIF excitation scans were recorded by collecting the emission from the jet-cooled molecules with a set of collection/steering optics, and imaging the emission onto a UV-enhanced photomultiplier tube (PMT). The PMT was protected by long-pass filters to reduce the scattered light from the laser. A sampling gate was placed around the fluorescence decay profile, digitized by an oscilloscope (Tektronix, model 3052B), and integrated. The tunable dye laser (Exciton laser dye: DCM) was scanned in the $29\,800\text{--}32\,800\ \text{cm}^{-1}$ ($335.5\text{--}305.0\ \text{nm}$) range.

This setup was also employed to obtain gas-phase dispersed fluorescence (DFL) spectra of HMS. These spectra were obtained by fixing the laser wavelength resonant with selected

transitions in the excitation spectrum, and imaging the fluorescence onto the entrance slit of a $\frac{3}{4}$ m monochromator. Since the fluorescence was spread over a large range, red-shifted from the excitation frequency, distinct peaks were not observed in the DFL spectrum. In order to obtain the shape of the broad DFL spectra, the slit width was set at 1 mm and an intensified CCD camera (Andor SOLIS iStar) collected the total dispersed emission signal impinging on the CCD at a fixed grating position. The grating position was tuned point-by-point and the entire spectrum for a given central grating position was integrated. Fluorescence lifetime traces were also recorded by exciting select transitions, and directly recording the time profile of the fluorescence signal from the PMT on the digital oscilloscope. The gas-phase fluorescence lifetimes of HMS were extracted from the resulting transients following the same method as for the TR-IY transients (see above and further details in the ESI,[†] S1.1.4 and Fig. S3), using, in this case, an instrument response full width at half maximum of 8 ns.

Experiments in solution

a. Transient electronic absorption spectroscopy (TEAS). The ultrafast transient electronic (UV-visible) absorption spectroscopy (TEAS) setup used in the present studies, which uses the aforementioned ultrafast laser spectroscopy setup, has been described previously;⁴⁴ specific details regarding these experiments are provided below.

Three separate solutions of HMS dissolved in cyclohexane (CHX, Fisher Scientific, $>99.9\%$), ethanol (EtOH, VWR Chemicals, $>99.9\%$) and acetonitrile (ACN, Fisher Scientific, $>99.9\%$) were prepared to a concentration of ~ 10 mM. To prevent photodegradation of the sample over time, a diaphragm pump (Simdos K2) was used to recirculate the solutions *via* a flow-through sample cell (Harrick Scientific) between two CaF_2 windows (thickness 1–2 mm, 25 mm diameter). PTFE spacers maintained a sample path length of $100\ \mu\text{m}$. This path length ensured a sample absorbance of less than 0.5.

The wavelength of the pump pulses (λ_{pump}) was chosen to be the peak absorption of HMS in each solvent, shown in Fig. 1: $\lambda_{\text{pump}} = 309\ \text{nm}$ in CHX, $307\ \text{nm}$ in EtOH and $306\ \text{nm}$ in ACN. The fluence of the pump pulses at all wavelengths was $\sim 0.5\ \mu\text{J}\ \text{cm}^{-2}$. The probe consisted of broadband white light pulses ($320\text{--}720\ \text{nm}$), generated by focusing a 5 mW portion of the fundamental 800 nm beam onto a CaF_2 crystal (2 mm thick). The pump–probe time delays in our TEAS setup were controlled by a gold retroreflector mounted on a motorised delay stage, similar to that described for the TR-IY setup. In this instance, the delay stage was situated along the portion of the 800 nm fundamental that generates the white light continuum, and facilitated a maximum Δt of 2 ns. The fluence of the probe pulse was changed post-sample by a neutral density filter as required to avoid saturating the detector.

The transient absorption data collected with this setup was quantitatively analysed *via* global analysis fitting using Glotaran, a graphical user interface for the R package TIMP.^{45–47} The fitting was carried out assuming both parallel and sequential kinetic models; more details regarding the fitting procedures

and the IRF of our TEAS experiments are given in the ESI,[†] in Sections S1.2.1 and S1.2.2 (Fig. S4) respectively. Moreover, similar to our experiments in the gas-phase, TEAS power dependence studies were carried out to ensure single-photon initiated dynamics for our experiments in solution (S1.2.3, Fig. S5 and S6, ESI[†]).

Steady-state spectroscopy

UV-visible spectroscopy measurements were conducted for solutions ($\sim 100 \mu\text{M}$) of HMS in each solvent (CHX, EtOH and ACN) using a quartz cuvette of 10 mm path length in a Agilent Cary-60 spectrophotometer. All fluorescence measurements of HMS (emission spectra and lifetimes, see S1.2.4, ESI,[†] for further details) were acquired using a Horiba Fluorolog-3. Each solution of HMS was prepared in this instance to a concentration of around $\sim 10 \mu\text{M}$ to ensure that the absorbance of the solution was under 0.1. More detailed information pertaining to these fluorescence measurements, alongside the UV-visible spectra of all fluorescence samples, can be found in Fig. S7 (ESI[†]). The quantum yield of HMS was also determined; full experimental details can be found in the ESI,[†] (S1.2.5).

Computational methods

All calculations were conducted in the NWChem software package.⁴⁸ Density functional theory (DFT) geometry optimisation was performed on two conformers of HMS, each of which was suspected to be close to a local geometric energy minimum. This relaxation was conducted with the PBE functional and cc-pVTZ basis set.⁴⁹ The single-point energies of each of these structures were calculated with the functionals PBE and PBE0, both with the cc-pVTZ basis set. These were also calculated with the post Hartree-Fock method MP2 using the cc-pVDZ basis set, in order to compare relative energies in the gas-phase. These results can be found in Table S1 in the ESI.[†] Of the two previously mentioned structures of HMS, the one of lowest energy—herein referred to as the *enol* form (conformer 1), see Fig. 2a—was selected as the likely global minimum and carried forward for further testing. These calculations were conducted in vacuum as well as in implicitly modelled EtOH, CHX and ACN using the COSMO solvent model inbuilt in NWChem to generate four structures.^{50–52} The higher energy conformer, also an *enol* with an intramolecular hydrogen bond (H-bond) between the *enol* OH and ester oxygen, was also retained for further testing (herein referred to as conformer 2). The structures of both conformers are presented in the ESI,[†] Fig. S8.

The global minimum *enol* structure (conformer 1) was then relaxed in the first excited singlet state (S_1 , $\pi\pi^*$) in order to predict the structure of the system after photoexcitation in vacuum. This was achieved by first relaxing at the PBE/cc-pVTZ and then the PBE0/cc-pVTZ level of theory. Following this, the species was further relaxed in each of the implicit solvents. These relaxations resulted in the *keto* form of HMS shown in Fig. 2a, which was again taken forward for further analysis employing the PBE0/cc-pVTZ level of theory as is now described. Using each of the eight structures, *enol* and *keto* structures in all three implicit solvents and vacuum, time-dependent DFT was carried out in order to find singlet (S_n) and triplet (T_n) vertical

excitations. The energy of the T_1 state was more accurately calculated using a ΔSCF methodology.⁵³ This was achieved by conducting single point energy calculations with state multiplicity set to 3 (triplet state) on each of the previously obtained *enol* and *keto* structures; the results were then compared to the S_0 energies for each form, once again in all three solvents as well as in vacuum. Conformer 2 also underwent excited state relaxation along the first excited singlet state (S_1 , $\pi\pi^*$), conducted at the PBE0/cc-pVTZ level of theory. In this case, tautomerisation did not occur. In order to calculate comparable energies with the excited-state relaxed geometries, single point energy calculations were conducted on both conformers 1 and 2 (previously optimized with PBE/cc-pVTZ) in vacuum at the PBE0/cc-pVTZ level of theory.

In order to estimate the excited state barrier between the *enol* and *keto* forms (conformer 1), a set of linear interpolations of internal coordinates (LIIC) were acquired. Vertical excitations, again at the PBE0/cc-pVTZ level of theory, were calculated in vacuum for each step, and the resulting ground state (S_0), S_1 and S_2 energies were plotted. The results of these calculations along a LIIC are shown in Fig. 2b (for S_0 and S_1 ; results for S_2 are shown in the ESI,[†] Fig. S9).

Finally, two further reaction pathways were probed, both of which involving the rotation around the aliphatic bond between the aromatic ring and the large ester unit of HMS. In both cases this bond was fixed in 10 degree increments between 0 and 180 degrees. The first path involved then relaxing all remaining degrees of freedom in the ground state at the PBE/cc-pVTZ level of theory. This allowed for the estimation of the barrier height between the two conformers discussed previously. The second path involved relaxing all other degrees of freedom in the S_1 at the PBE0/cc-pVTZ level of theory. This allowed for the investigation of a potential CI between the ground and excited states.

Results and discussion

Gas-phase experiments

TR-IY HMS parent ion (HMS^+) transients are presented in Fig. 3 along with the extracted time constants at $\lambda_{\text{pump}} = 305 \text{ nm}$, 320 nm and 335 nm (the latter of which corresponds to photoexcitation centred at the S_1 origin of HMS, see below), with $\lambda_{\text{probe}} = 200 \text{ nm}$. In all cases, the gas-phase photodynamics of HMS following UV photoexcitation are described by two time constants. In what follows, we will firstly focus on discussing the assignment of τ_1 and addressing apparent discrepancies between our time- and frequency-resolved studies, after which the discussion regarding the assignment of τ_2 will become straight-forward.

The first time constant, τ_1 , is defined within our IRF (typically $\sim 170 \text{ fs}$, see Fig. S2, ESI[†]). We assign τ_1 to ESIPT, involving migration of the proton on the $-\text{OH}$ group along the $\text{O}-\text{H}\cdots\text{O}$ coordinate towards the neighbouring carbonyl group (thus forming the *keto* tautomer). We draw confidence that the tautomerisation occurs within 170 fs from previous literature on similar systems

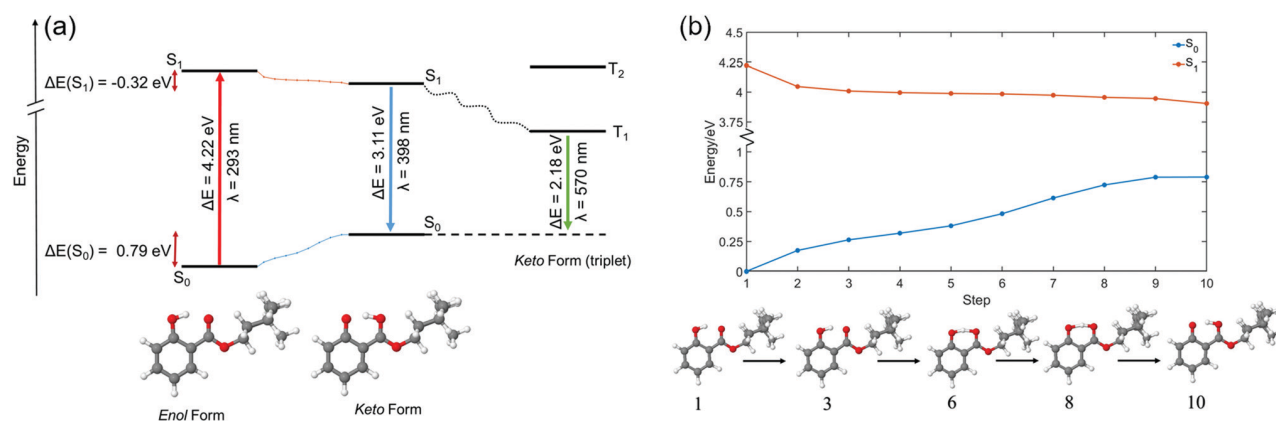


Fig. 2 (a) A representation of the different energy levels of HMS (conformer 1) in vacuum in the *enol* (left) and *keto* (right) form, as predicted using the PBE0/cc-pVTZ level of theory. In (a), the red arrow represents the absorption of a photon, the blue arrow represents fluorescence, and the green arrow represents phosphorescence. The dotted lines in blue and orange between the S_0 and S_1 states are indicative of the linear interpolation of internal coordinates calculated for HMS in vacuum at the PBE0/cc-pVTZ level of theory, shown in further detail in (b) alongside the predicted structures of HMS at selected steps. These calculations suggest that, when in the ground state, conformer 1 of HMS exists in the *enol* form, whereas in the first excited singlet state (S_1) HMS converts to the *keto* state in an energetically barrierless process.

such as methyl salicylate where ESIPT occurs within 100 fs;^{54–57} we add here that power studies in the gas-phase were carried out to verify single-photon-induced dynamics (presented in S1.1.1 and Fig. S1, ESI[†]). In fact, our computational studies, the results of which are presented in Fig. 2, predict a barrierless S_1 -*enol* to S_1 -*keto* tautomerisation for conformer 1 of HMS, with the *keto* tautomer lying 0.32 eV lower in energy than the *enol* tautomer (see Fig. 2). In addition, the large Stokes shift observed in the DFL spectrum of HMS upon photoexcitation at its $S_1(\nu = 0)$ origin, as shown in Fig. S3 in the ESI[†], suggests a significant geometry change upon excitation to the S_1 state. The experimentally observed Stokes shift in the gas-phase is approximately 0.72 eV, which compares with the theoretically calculated 1.1 eV difference between the S_1 - S_0 transitions for the *enol* and *keto* tautomers (in vacuum, see Fig. 2a and Tables S2 and S3 in the ESI[†]). While there is a discrepancy of approximately 0.4 eV between the experimental and theoretical value for this Stokes shift, DFT methods have generally been found to overestimate transition energies.^{58,59} Nevertheless, the experimental observation of a large Stokes shift upon photoexcitation to the S_1 state of HMS, in accordance with and in addition to the large computationally predicted Stokes shift, supports the hypothesis that ESIPT would take place in HMS within τ_1 .

We note, however, that sharp features in the LIF spectrum of HMS, shown in Fig. 4, are retained even at energies $> 1000 \text{ cm}^{-1}$ above the $S_1(\nu = 0)$ origin. Excitation energies above $31\,000 \text{ cm}^{-1}$ result in a loss of the fine structure, which could point towards vibronic congestion.⁶⁰ The rotational band contours of the LIF origin peak (see ESI[†], S2.1.1 and Fig. S10) suggest a significantly longer S_1 origin lifetime than the IRF-limited τ_1 extracted from our TR-IY measurements. We reconcile these contradictory observations by considering previously published work in which the existence of different conformers is suggested for closely related salicylates. For example, Bisht *et al.* proposed two potential conformers in salicylic acid undergoing different excited state dynamics,⁶¹ while Zhou *et al.* hypothesised that

the slowest dynamics observed in their studies on methyl salicylate could be due to a conformer in which the ESIPT process is hindered.⁶² Moreover, both Zhou *et al.* and Massaro *et al.*⁶³ report an energy difference between the two lowest energy conformers of methyl salicylate in the ground state (~ 0.1 – 0.2 eV) that is comparable to the energy difference predicted by our computational studies for conformers 1 and 2 of HMS (0.17 eV, see Fig. S8 in the ESI[†]). In addition, Zhou *et al.* have shown that interconversion of the two lowest energy conformers in the ground state has a significant barrier ($+0.63 \text{ eV}$ with respect to the lowest energy conformer), preventing this interconversion.⁶² The energy of this barrier for HMS was calculated by fixing the dihedral angle that dictates the path of conformer 1 to conformer 2 in 10 degree increments. Following this, all other degrees of freedom were relaxed at the PBE/cc-pVTZ level of theory and the energy of each intermediate state was plotted (Fig. S11, ESI[†]). This gave rise to the same barrier energy observed by Zhou *et al.* of $+0.63 \text{ eV}$ with respect to conformer 1.⁶² Taken together, and given that our calculations show that there is a stable excited state structure of the *enol* tautomer of conformer 2, we propose that conformer 2 is photoexcited and trapped in its *enol* structure (*i.e.* not undergoing ESIPT), which fluoresces, thus accounting for the sharp features observed in our LIF measurements. However, the (apparent) low abundance of this conformer makes it difficult to identify from our TR-IY measurements. We add that further experiments (such as spectral hole-burning) are warranted to confirm the existence (and spectral location) of conformer 1 and 2.

The second time constant, τ_2 , clearly decreases with increasing photoexcitation energy, *i.e.* energy dissipation becomes faster with increasing energy. This behaviour is typical of systems for which there is an energetic barrier to be surmounted in order for a key relaxation pathway to be accessed.^{64,65} Presumably, when exciting HMS at the $S_1(\nu = 0)$ origin (within the 500 cm^{-1} bandwidth of the pump pulse used in our time-resolved measurements, see Fig. 4) excited state population is unable

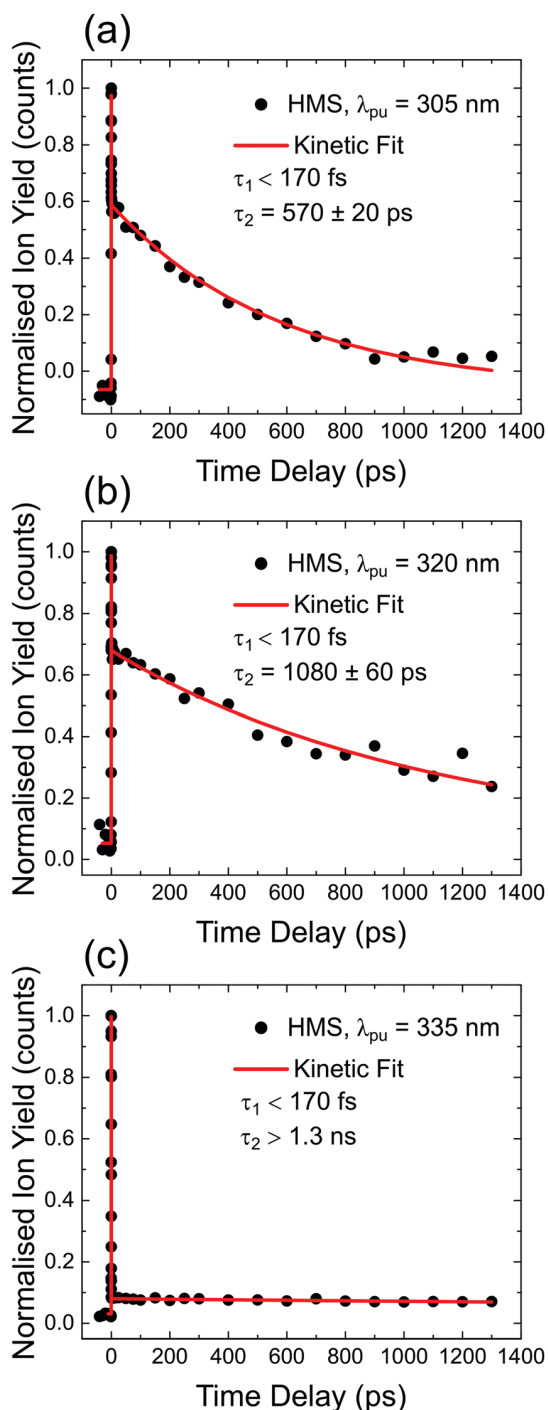


Fig. 3 TR-IY magic angle transients for HMS photoexcited at (a) 305 nm, (b) 320 nm and (c) 335 nm, the $S_1(v=0)$ origin of HMS, with a 200 nm probe. Black circles are experimental points, while the red curves correspond to kinetic fits (discussed in S1.2 in the ESI†), from which the time constants shown inset are extracted. The baseline for all plots is zero within the signal-to-noise ratio of our measurements.

to access any nearby CIs and therefore fluorescence takes place to the ground state as excited state population samples the shallow S_1 energy potential. Indeed, the LIF measurements presented in Fig. 4 show that there is significant fluorescence

from the vibrational levels accessed by $\lambda_{\text{pump}} = 335$ nm used in our TR-IY measurements, further supporting our assignment of $\tau_2 > 1.3$ ns (at this pump wavelength) to a long-lived, fluorescent S_1 state. As the pump energy is increased, τ_2 decreases considerably, now being defined within the temporal window of our measurements (1.3 ns). It is plausible that, at these higher pump energies, excited state population would be increasingly more likely to access a nearby CI within the S_1 state through which it would undergo internal conversion (IC) to the S_0 state. Nevertheless, while fluorescence may not be the predominant relaxation pathway at above-origin pump energies (for which IC becomes increasingly competitive), the strong LIF signal at these energies is evidence that it is still an active relaxation pathway for conformer 1.

We add that attempts were made to theoretically examine the CI between the S_0 and S_1 states. Owing to the size of HMS, and therefore the relatively high computational expenditure, it was not possible to perform a CI search using multistate CASPT2 as has been conducted in other studies.⁵⁵ Based on previous studies, the CI could be presupposed to be located along the rotation of the aliphatic bond between the aromatic ring and the large ester unit of HMS.^{55,66} As such, this coordinate was evaluated for HMS by fixing the dihedral angle in 10 degree increments between 0 and 180 degrees, relaxing all other degrees of freedom in the first excited state in TDDFT, and observing the relative energies of this and the ground state. We observed that between 40 and 130 degrees, where the internal H-bond is broken, the calculation relaxed to a structure with a negative excitation energy. This is a common error when using TDDFT to study a CI, owing to the inexactness of the ground state and excited state energies.⁶⁷ Whilst this is indicative that a CI likely occurs on this coordinate, exact energies, structures, and energetic barriers are unreliable as TDDFT is significantly less accurate in cases such as this with extensive state mixing.⁶⁸

Gas-phase fluorescence lifetime measurements taken upon photoexcitation at 305–335 nm, an example of which is presented in the ESI,† (S1.1.4), yielded fluorescence lifetimes of 12–20 ns. Attempts to detect gas-phase phosphorescence from HMS were unsuccessful, suggesting that triplet states are unlikely to be involved in the gas-phase photodynamics of HMS on the time-scales of the present measurements. Nevertheless, one could envisage that excited state population would migrate to nearby triplet states (the existence of which is confirmed by our computational work) and then undergo reverse intersystem crossing (ISC) back into a singlet state (namely S_0), thus justifying the absence of observable phosphorescence. Moreover, it is also possible that photoreactions would take place from the excited triplet state manifold. The absence of observable phosphorescence does not, therefore, conclusively rule out ISC as a potential relaxation pathway for HMS in the gas-phase.

In summary, our gas-phase and computational results suggest that conformer 1 of HMS (the lowest energy conformer) undergoes ultrafast *enol-keto* tautomerisation, followed by either fluorescence from the S_1 surface or, in the case of higher photoexcitation energies which allow for a higher lying CI to be accessed, fast repopulation of the S_0 state *via* IC.

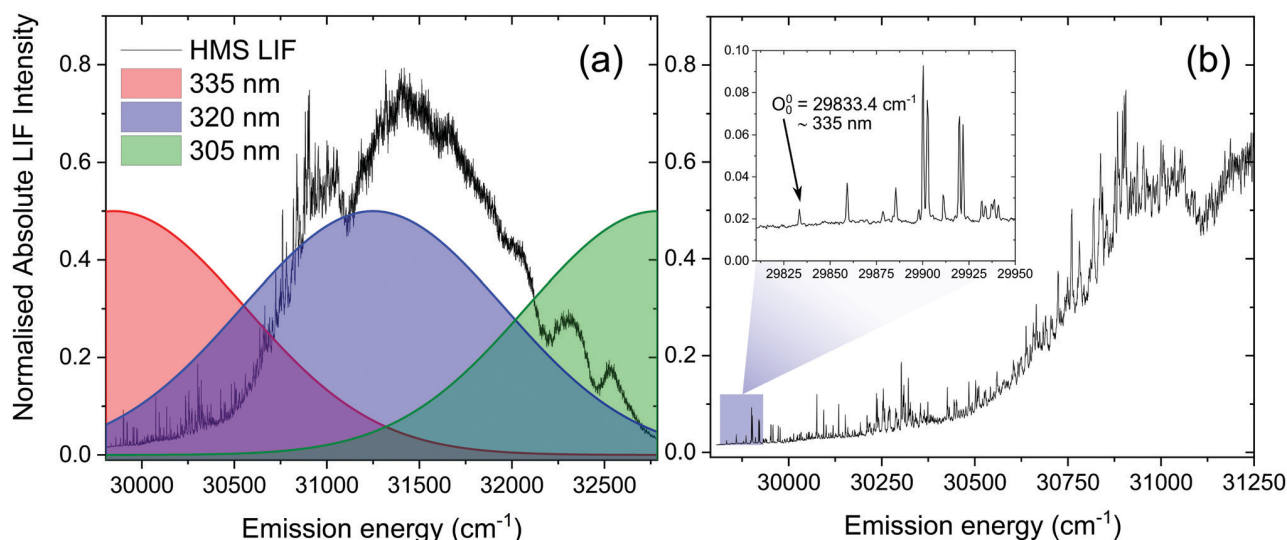


Fig. 4 (a) LIF spectrum of vaporised HMS upon photoexcitation in the 29 806–32 787 cm^{-1} energy region, with Gaussian curves (FWHM = 500 cm^{-1}) demonstrating the regions photoexcited in the TR-IY measurements with $\lambda_{\text{pump}} = 335 \text{ nm}$ (red), 320 nm (blue) and 305 nm (green). (b) The same LIF spectrum in more detail, with the inset showing the peak and energy corresponding to the $S_1(\nu = 0)$ origin of HMS.

Furthermore, we suggest that the sharp peaks in the LIF spectrum of HMS around $S_1(\nu = 0)$ origin energies – which do not agree with a fast ESIPT process taking place – are due to the presence of a second conformer in the molecular beam. We found no evidence of phosphorescence within the timescales of our experiments and, therefore, propose that any contribution from triplet states to the gas-phase photodynamics of HMS, while possible, would be small.

Transient electronic absorption spectroscopy (TEAS)

To gain further insights into the behaviour of HMS in environments with different polarities and protic natures, ultrafast spectroscopy studies were conducted in solution, in line with a *bottom-up* approach.

Given the similarities of the UV-visible spectra of HMS in different solvents (as shown in Fig. 1), it could be expected that the excited state dynamics of HMS would not differ dramatically in the different solvent environments. Indeed, all transient absorption spectra (TAS) of HMS, displayed as both false colour heat maps and line-outs at selected pump–probe time delays in Fig. 5, resemble one another and reveal similar dynamics; as such, it seems appropriate that the results should be discussed together.

Each solute/solvent combination displays a strong excited state absorption (ESA) in the range 330–360 nm, with evidence of a positive feature, tailing off at $\sim 400 \text{ nm}$. A separate ESA feature appears between 500–590 nm. There is also a stimulated emission (SE) feature, the negative ΔOD feature between probe wavelengths of 430–500 nm. A quantitative insight into the assignment of these spectral features has been attained by following the global fitting procedure described in the ESI† (Section S1.2.1). As is the case for the time-resolved gas-phase data, this procedure implements a parallel model, which assumes all processes begin immediately after excitation. The results of this fitting are shown in Table 1, and the quality of

this fit at selected wavelengths is evident in Fig. 5, with full residual information given in Fig. S12 (ESI†). A parallel model has been chosen to model our data in solution, in line with fitting to our gas-phase data. Nevertheless, for comparison, the data in solution has also been fitted using a sequential model, yielding similar time constants as presented in the ESI† (Section S2.2.1 and Table S4). The quality of these fits at selected wavelengths is demonstrated in Fig. S13 (ESI†).

For all sets of TEAS data (in all solvents and at all pump wavelengths), τ_1 is defined within instrument response (Fig. S4, ESI†). Following consideration of our previous observations and discussion regarding our gas-phase results, and given that ESIPT has been observed experimentally on comparable timescales in similar systems in solution (*e.g.* methyl salicylate), we assign τ_1 in our studies in solution to *enol-keto* tautomerisation.^{69–72} Further evidence for ESIPT in HMS is two-fold. Akin to the dispersed fluorescence observations in gas-phase, there is a large Stokes shift ($\sim 120 \text{ nm}$, see Fig. S14 in the ESI†) upon photoexcitation of HMS at its respective absorption peak in each solvent, which is indicative of a significant structural change upon photoexcitation to the S_1 state. This observation is similar to that previously reported for methyl salicylate and ethylhexyl salicylate.^{72,73} Moreover, our computational studies reveal that the S_1 -*keto* tautomer is lower in energy than its S_1 -*enol* counterpart and it is therefore anticipated that ESIPT would remain barrierless for HMS in solution.

The elucidation of the remaining time constants extracted from our TEAS data for HMS is assisted herein by comparison with the previously studied HMS analogue, ethylhexyl salicylate (EHS, also known as octisalate), for which the ester unit connects to an alkane chain rather than the cycloalkane unit of HMS (structure inset in Fig. S15a, ESI†).^{73,74} Equivalent TEAS studies on EHS following the same experimental methodology as for HMS have been performed and the results are presented in

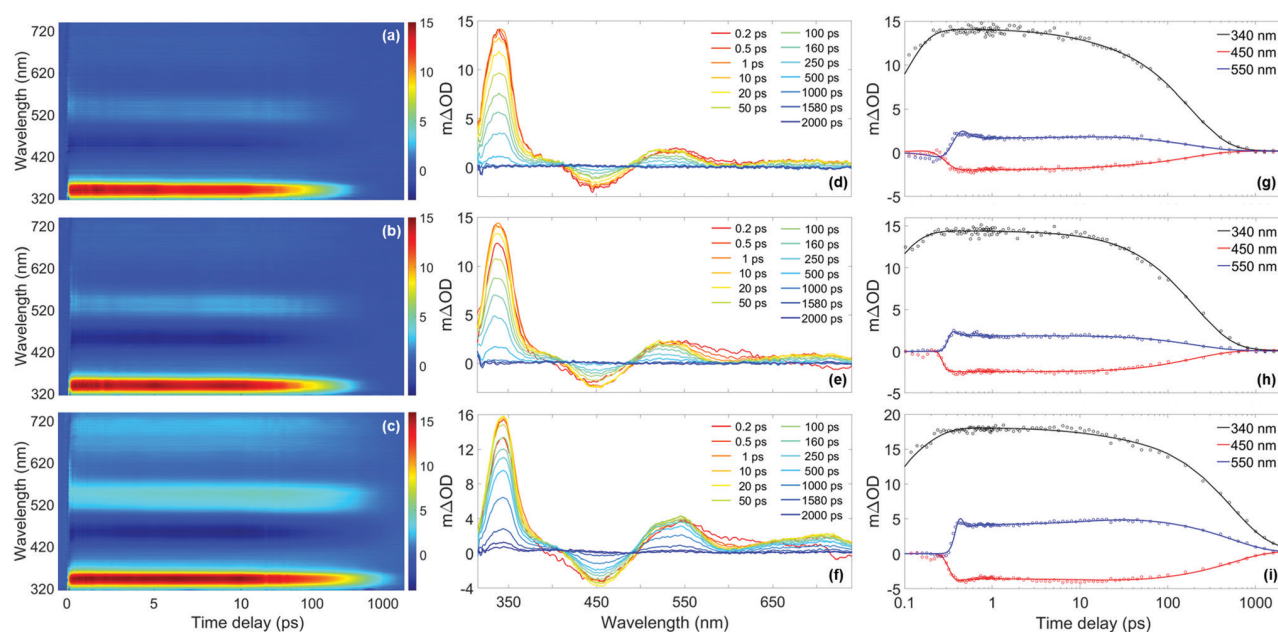


Fig. 5 (a)–(c) False colour heat maps showing all transient absorption spectra (TAS) of homosalate (HMS) in acetonitrile (ACN) ($\lambda_{\text{pump}} = 306$ nm), ethanol (EtOH) ($\lambda_{\text{pump}} = 307$ nm) and cyclohexane (CHX) ($\lambda_{\text{pump}} = 309$ nm) respectively. In these plots, the time delay axis is shown as a linear scale until 10 ps and as a logarithmic scale thereafter. (d)–(f) TAS at selected pump–probe time delays for HMS in ACN, EtOH and CHX respectively. These plots are attained by taking vertical slices through the false colour heat maps at the given time delay and are presented on the same $m\Delta\text{OD}$ scale as the corresponding false colour heat map. (g)–(i) Kinetic fits of the transient data at 340 nm (black), 450 nm (red) and 550 nm (blue) for HMS in ACN, EtOH and CHX respectively. The circles denote the raw data at each wavelength and the solid line is the fit attained using the parallel model described in the main text. In each case, the time delay axis is presented on a logarithmic scale. False colour heat maps containing residuals for every datapoint can be found in the ESI† (Fig. S12).

full in the ESI† (Section S2.2.2: TAS data Fig. S15–S17, time constants Tables S5 and S6, residuals Fig. S12, ESI†). Overall, the photodynamical behaviour of EHS is virtually unaltered from that observed for HMS. As such, we assume that comparisons between the photodynamic behaviours of HMS and EHS are valid. Moreover, EHS also produces an emission peak at 450 nm (as reported by Krishnan and Nordlund)⁷³ that is very similar to the emission of HMS shown in Fig. S14 (ESI†), in terms of both central wavelength and bandwidth, further validating the comparison between these two molecules.

In light of the aforementioned assumption (and returning to discuss τ_2 below), τ_3 and τ_4 for HMS have been assigned. The faster of these time constants, τ_3 , is likely due to the decay of the S_1 -*keto* tautomer *via* fluorescence. The presence of

fluorescence is confirmed in the TAS of HMS in all solvents by the appearance of the SE feature centred at 450 nm, which directly corresponds to the peaks observed in the emission spectra (Fig. S14, ESI†). For additional confirmation of the assignment of τ_3 , the fluorescence lifetimes of HMS in all three solvents have been determined; these were found to be within our instrument response (< 1.2 ns, see S1.2.4, ESI† for further details). More exact fluorescence lifetimes for EHS have been quoted by Krishnan and Nordlund, and range from 150 ps in methanol to 460 ps in toluene.⁷³ Krishnan and Nordlund's results are in good agreement with the values of τ_3 that have been extracted for both HMS and EHS in our studies, as shown in Table 1 and Table S5 (ESI†), respectively. These time constants, alongside the fluorescence lifetimes obtained in the present and previous studies, thus support our assignment of τ_3 in both EHS and HMS to fluorescence, dependent on rate-determining internal conversion (IC) and intersystem crossing (ISC, see below).⁷³

Our assignment of $\tau_4 > 2$ ns to the lifetime of the triplet state following ISC is in the first instance supported by additional TAS of HMS and EHS, with $\Delta t = 3$ ns, which are presented in the ESI,† (Fig. S18). The spectral features in these TAS (see ESI,† S2.2.3 for further details) resemble those reported by Sugiyama *et al.*⁷⁴ as the absorption spectra of the T_1 state, lending credibility to our assignment. The hypothesis that τ_4 is associated with the lifetime of a triplet state is also corroborated by our computational results, which reveal the existence of nearby triplet states in HMS that are accessible in all three solvents (Table S3, ESI†). While a number of decay pathways

Table 1 Extracted transient electronic absorption spectroscopy (TEAS) time constants for three homosalate solutions, following photoexcitation at their respective absorption maxima, obtained *via* global fitting techniques using a parallel model.⁴⁵ Whilst the error for τ_1 is given by half the instrument response in each solvent (Fig. S4, ESI), the errors presented for τ_2 to τ_4 are those provided by the fitting software package; the quality of the fits can be gauged from the corresponding kinetic fits (Fig. 5) and residuals (Fig. S12, ESI)

Time constant	Ethanol	Cyclohexane	Acetonitrile
τ_1 (fs)	55 ± 35	105 ± 30	80 ± 40
τ_2 (ps)	10.4 ± 0.4	14.2 ± 0.5	9.4 ± 0.4
τ_3 (ps)	199 ± 2	532 ± 6	180 ± 2
τ_4 (ns)	$> 2^a$	$> 2^a$	$> 2^a$

^a Outside the temporal window of the instrument (2 ns).

could be accessible to the triplet states of HMS and EHS, such as phosphorescence or reverse ISC,⁷⁵ we are unable to pinpoint which, if any, dominates in the present measurements. Phosphorescence quantum yields (Φ_P) have been reported to be 4.9% in HMS and 5.4% in EHS in ethanol at 77 K.⁷⁴ However, cryogenic cooling, solvent deoxygenation, heavy atom perturbation or a combination of these approaches have been required to observe phosphorescence in salicylates.^{74,76} As such, it is likely that under our experimental conditions, phosphorescence is quenched.

Although both fluorescence and ISC do occur in HMS and EHS as discussed, these are unlikely to be the dominant relaxation pathways for these molecules, given the expected low quantum yields of radiative decay. In EHS, the fluorescence quantum yield (Φ_F), has been reported to be 0.6–1.9% (depending on solvent),⁷³ while for HMS we have determined Φ_F values of 3.5% in ACN, 4.6% in EtOH and 11.6% in CHX (upper limits, see S1.2.5 (ESI[†]) for further details). As such, the remaining time constant extracted from our TEAS measurements, τ_2 , is assigned to vibrational cooling and IC to the S_0 -*keto* species. It is then energetically favourable for the S_0 -*enol* species to be reformed, according to the S_0 energy differences between the *keto* and *enol* forms calculated using DFT (between 0.76 and 0.80 eV). Further to this, a full list of excited-state energies can be found in Tables S2 and S3 of the ESI.[†] Fast, non-radiative relaxation for ground-state recovery is favourable for sunscreen applications,⁷⁷ therefore HMS and EHS mostly satisfy this criterion.

In summary, our studies in solution on HMS (and EHS) reveal an initial ultrafast process which, similarly to the system in the gas-phase, we assign to ESIPT (*enol*–*keto* tautomerisation). The S_1 state of the *keto* tautomer then undergoes radiative and non-radiative decay, with IC (and some component of vibrational cooling) predominantly taking place alongside low yield components of fluorescence and ISC. While it appears from our results that solvent environments have only minor effects on the observed photodynamics of HMS, it is clear that solvation seems to facilitate ISC and thus introduce an additional competing (yet non-dominant) decay pathway for HMS. This is an important consideration for sunscreen design, since the presence of triplet states is undesirable in sunscreen formulations due to the increased probability of harmful side-reactions.

To conclude our discussion, we propose that our work provides further valuable guidance for sunscreen design with regards to the choice between salicylates, such as HMS, and anthranilates, such as MenA. As reported in previous work,³⁵ the potential energy cut along the ESIPT coordinate for methyl anthranilate (MA, a precursor to MenA) is nearly flat, resulting in there being no energetic drive for ESIPT to take place. In HMS, on the other hand, computational work reveals a significant energetic drive for ESIPT (Fig. 2b), with the (apparent) absence of a barrier for this process being allied to a relatively more stable *keto* tautomer.

The marked differences in the excited state surfaces of HMS when compared to MA are likely associated with the differences in electron affinity of the nitrogen and oxygen atoms, ultimately resulting in different strengths for the intramolecular H-bond,

a crucial factor for the ESIPT process. It has been reported that not only systems with strong intramolecular H-bonds readily undergo ESIPT, but also that a weaker intramolecular H-bond may slow down or even preclude the ESIPT process.⁷⁸ In addition, recent work on a range of amino- and hydroxy-type H-bonding molecules^{57,79} has shown that molecules containing an OH group tend to undergo ultrafast ESIPT (within 80 fs), whereas molecules containing NH groups undergo ESIPT within a wide range of (typically longer) timescales. As such, in the first instance formulation scientists could be encouraged to look for compounds with strong intramolecular H-bonds, by preferring O–H···O compounds over N–H···O species, for example; intramolecular H-bond strength seems to influence the molecule's potential energy landscape such as to allow fast internal conversion to take place (*via* a CI along a rotation reaction coordinate), a closer-to-ideal photophysical behaviour for a sunscreen.

Conclusions

In the present work we have explored the excited state dynamics of the UV filter homosalate (HMS) after photoexcitation in the 305–335 nm wavelength range, both in vacuum and in solution. We found that these dynamics are almost unaltered in solution when compared to the gas-phase and can be broadly described by an initial ultrafast decay, which is in all cases assigned to ESIPT; followed by fast internal conversion to the ground state and lower quantum yields of fluorescence and intersystem crossing. In line with previous observations on analogous molecules (*e.g.* methyl salicylate), we also report on experimental observations in the gas-phase that point towards the presence of a second, long-lived conformer of HMS which does not undergo ESIPT.

Interestingly, the studies presented here on HMS (and also for EHS in solution) are in stark contrast with the behaviour observed for the comparable UVA filter menthyl anthranilate (MenA).³⁵ In the gas- and solution-phase studies of MenA, it was found that the ESIPT process is incomplete, *i.e.* H-atom dislocation occurs.³⁵ Furthermore, while there is a nearby S_1/S_0 conical intersection (CI), a large energetic barrier needs to be surmounted in order for it to be accessed. This barrier hinders fast and efficient excited state relaxation in MenA, effectively rendering its photophysical behaviour unfavourable for sunscreen use.

From our observations in the present study, it appears that by substituting the amino group of MenA with the hydroxy group in HMS, a CI becomes accessible and the excited state energy can be dissipated effectively. It is therefore evident that the ESIPT process plays a key role in the photodynamics of both HMS and MenA, ultimately defining their suitability for use as UV filters in sunscreen formulations. As such, a more detailed understanding of the ESIPT process (*e.g.* substituent position and functional group effects) in this type of molecule is warranted and could be crucial for sunscreen design. For example, investigating the effect of substituent position on the photodynamics of HMS, *i.e.* placing the hydroxy group in the *meta* and *para* positions on the chromophore where ESIPT is no longer possible,

constitutes an interesting avenue for future work, both in the gas-phase and in solution.

Overall, and within the limits of our studies, HMS appears to have mostly favourable excited-state relaxation characteristics and, on this basis alone, its inclusion in sunscreen formulations is justified. Nevertheless, favourable photodynamics do not guarantee that the molecule is completely safe when applied to the skin. The proposed triplet states in solution, despite their low quantum yield, could be of concern to formulation scientists, owing to their ability to produce singlet oxygen, a cytotoxin that can also incite allergenic responses.⁸⁰ The effects of potential triplet-triplet state energy transfer of HMS to other UV filters also warrants further investigation.

Conflicts of interest

There are no conflicts of interest to declare.

Acknowledgements

The authors would like to thank Juan Cebrián and Laurent Blasco, from Lipotec SAU, for fruitful collaboration and for providing the HMS samples for these experiments. The authors also thank the Warwick Centre for Ultrafast Spectroscopy (WCUS) for the use of the Cary 60 and Fluorolog-3. E. L. H. and M. A. P. T. thank the Engineering and Physical Sciences Research Council (EPSRC) for a PhD studentship through the EPSRC Centre for Doctoral Training in Molecular Analytical Science, grant number EP/L015307/1. Computing facilities were provided by the Scientific Computing Research Technology Platform of the University of Warwick. We acknowledge the use of Athena at HPC Midlands+, which was funded by the EPSRC by Grant EP/P020232/1, in this research, as part of the HPC Midlands+ consortium. K. M. K. also thanks the EPSRC for doctoral funding. P. M. and T. S. Z. gratefully acknowledge support from the Department of Energy Basic Energy Sciences Gas-Phase Chemical Physics program under Grant No. DE-FG02-96ER14656. N. d. N. R. thanks the University of Warwick's Institute of Advanced Study and Institute for Advanced Teaching and Learning for a joint Early Career Fellowship. Finally, V. G. S. thanks the EPSRC for an equipment grant (EP/J007153), the Leverhulme Trust for a research grant (RPG-2016-055) and the Royal Society and Leverhulme Trust for a Royal Society Leverhulme Trust Senior Research Fellowship. This project has also received funding from the European Union's Horizon 2020 Research and Innovation programme, under the grant agreement no. 828753.

References

- 1 D. Ekinici, M. Sentürk and Ö. İ. Küfrevioğlu, *Expert Opin. Ther. Pat.*, 2011, **21**, 1831–1841.
- 2 M. T. Baltazar, R. J. Dinis-Oliveira, J. A. Duarte, M. L. Bastos and F. Carvalho, *Curr. Med. Chem.*, 2011, **18**, 3252–3264.
- 3 N. Serpone, D. Dondi and A. Albini, *Inorg. Chim. Acta*, 2007, **360**, 794–802.
- 4 N. A. Shaath, *Photochem. Photobiol. Sci.*, 2010, **9**, 464–469.
- 5 M. F. Holick, *Anticancer Res.*, 2016, **36**, 1345–1356.
- 6 P. H. Hart, M. Norval, S. N. Byrne and L. E. Rhodes, *Annu. Rev. Pathol.: Mech. Dis.*, 2019, **14**, 55–81.
- 7 Y. Matsumura and H. N. Ananthaswamy, *Toxicol. Appl. Pharmacol.*, 2004, **195**, 298–308.
- 8 F. R. de Gruijl, *Eur. J. Cancer*, 1999, **35**, 2003–2009.
- 9 L. A. Baker, B. Marchetti, T. N. V. Karsili, V. G. Stavros and M. N. R. Ashfold, *Chem. Soc. Rev.*, 2017, **46**, 3770–3791.
- 10 M. Wlaschek, I. Tantcheva-Poór, L. Naderi, W. Ma, L. A. Schneider, Z. Razi-Wolf, J. Schüller and K. Scharffetter-Kochanek, *J. Photochem. Photobiol., B*, 2001, **63**, 41–51.
- 11 G. J. Fisher, Z. Wang, S. C. Datta, J. Varani, S. Kang and J. J. Voorhees, *N. Engl. J. Med.*, 1997, **337**, 1419–1429.
- 12 J. D'Orazio, S. Jarrett, A. Amaro-Ortiz and T. Scott, *Int. J. Mol. Sci.*, 2013, **14**, 12222–12248.
- 13 C. Couteau, M. Pommier, E. Papisaris and L. J. M. Coiffard, *Pharmazie*, 2007, **62**, 449–452.
- 14 L. E. Agrapidis-Paloympis, R. A. Nash and N. A. Shaath, *J. Soc. Cosmet. Chem.*, 1987, **38**, 209–221.
- 15 L. Beyere, S. Yarasi and G. R. Loppnow, *J. Raman Spectrosc.*, 2003, **34**, 743–750.
- 16 G. J. Mturi and B. S. Martincigh, *J. Photochem. Photobiol., A*, 2008, **200**, 410–420.
- 17 A. Benazzouz, L. Moity, C. Pierlot, V. Molinier and J.-M. Aubry, *Colloids Surf., A*, 2014, **458**, 101–109.
- 18 M. D. Palm and M. N. O'Donoghue, *Dermatol. Ther.*, 2007, **20**, 360–376.
- 19 C. G. Mortz, H. Thormann, A. Goossens and K. E. Andersen, *Dermatitis*, 2010, **21**, 7–10.
- 20 A. R. Heurung, S. I. Raju and E. M. Warshaw, *Dermatitis*, 2014, **25**, 289–326.
- 21 C. L. Hexsel and H. W. Lim, in *Preventive Dermatology*, ed. R. Norman, Springer London, London, 2010, pp. 81–91.
- 22 N. Lowe, *Dermatol. Clin.*, 2006, **24**, 9–17.
- 23 D. R. Sambandan and D. Ratner, *J. Am. Acad. Dermatol.*, 2011, **64**, 748–758.
- 24 C. Couteau, A. Faure, J. Fortin, E. Papisaris and L. J. M. Coiffard, *J. Pharm. Biomed. Anal.*, 2007, **44**, 270–273.
- 25 C. A. Bonda and D. Lott, in *Principles and Practice of Photoprotection*, ed. S. Q. Wang and H. W. Lim, Springer International Publishing, Cham, 2016, pp. 247–273.
- 26 S. Q. Wang and H. W. Lim, *J. Am. Acad. Dermatol.*, 2011, **65**, 863–869.
- 27 T. H. Kim, B. S. Shin, K.-B. Kim, S. W. Shin, S. H. Seok, M. K. Kim, E. J. Kim, D. Kim, M. G. Kim, E.-S. Park, J.-Y. Kim and S. D. Yoo, *J. Toxicol. Environ. Health, Part A*, 2014, **77**, 202–213.
- 28 M. Erol, I. Çok, Ö. B. Gayret, P. Günes, Ö. Yigit, E. Sayman, A. Günes, D. S. Çelik, S. Hamilçikan, S. Altınay and O. Ercan, *Toxicol. Ind. Health*, 2017, **33**, 775–791.
- 29 J. F. Nash, *Dermatol. Clin.*, 2006, **24**, 35–51.
- 30 S. Yazar and S. K. Ertekin, *J. Cosmet., Dermatol. Sci. Appl.*, 2020, **19**, 246–252.

- 31 L. A. Baker, S. E. Greenough and V. G. Stavros, *J. Phys. Chem. Lett.*, 2016, **7**, 4655–4665.
- 32 E. L. Holt and V. G. Stavros, *Int. Rev. Phys. Chem.*, 2019, **38**, 243–285.
- 33 L. A. Baker, M. D. Horbury, S. E. Greenough, P. M. Coulter, T. N. V. Karsili, G. M. Roberts, A. J. Orr-Ewing, M. N. R. Ashfold and V. G. Stavros, *J. Phys. Chem. Lett.*, 2015, **6**, 1363–1368.
- 34 M. T. Ignasiak, C. Houée-Levin, G. Kciuk, B. Marciniak and T. Pedzinski, *ChemPhysChem*, 2015, **16**, 628–633.
- 35 N. D. N. Rodrigues, N. C. Cole-Filipiak, M. D. Horbury, M. Staniforth, T. N. V. Karsili, Y. Peperstraete and V. G. Stavros, *J. Photochem. Photobiol., A*, 2018, **353**, 376–384.
- 36 N. D. N. Rodrigues and V. G. Stavros, *Sci. Prog.*, 2018, **101**, 8–31.
- 37 A. Iqbal, L.-J. Pegg and V. G. Stavros, *J. Phys. Chem. A*, 2008, **112**, 9531–9534.
- 38 U. Even, J. Jortner, D. Noy, N. Lavie and C. Cossart-Magos, *J. Chem. Phys.*, 2000, **112**, 8068–8071.
- 39 F. P. M. Baskin, J. Spencer and A. H. Zewail, *J. Chem. Phys.*, 1987, **86**, 2483–2499.
- 40 S. R. Gandhi and R. B. Bernstein, *Chem. Phys.*, 1986, **105**, 423–434.
- 41 N. R. Pillsbury, J. A. Stearns, C. W. Müller, D. F. Plusquellic and T. S. Zwier, *J. Chem. Phys.*, 2008, **129**, 114301.
- 42 C. A. Arrington, C. Ramos, A. D. Robinson and T. S. Zwier, *J. Phys. Chem. A*, 1998, **102**, 3315–3322.
- 43 F. A. Ensminger, J. Plassard and T. S. Zwier, *J. Chem. Phys.*, 1995, **102**, 5246.
- 44 S. E. Greenough, G. M. Roberts, N. A. Smith, M. D. Horbury, R. G. McKinlay, J. M. Żurek, M. J. Paterson, P. J. Sadler and V. G. Stavros, *Phys. Chem. Chem. Phys.*, 2014, **16**, 19141–19155.
- 45 J. Snellenburg, S. Laptенок, R. Seger, K. Mullen and I. H. M. van Stokkum, *J. Stat. Soft.*, 2012, **49**, 1–22.
- 46 K. M. Mullen and I. H. M. van Stokkum, *J. Stat. Soft.*, 2007, **18**, 1–46.
- 47 I. H. M. van Stokkum, D. S. Larsen and R. van Grondelle, *Biochim. Biophys. Acta*, 2004, **1657**, 82–104.
- 48 M. Valiev, E. J. Bylaska, N. Govind, K. Kowalski, T. P. Straatsma, H. J. J. Van Dam, D. Wang, J. Nieplocha, E. Apra, T. L. Windus and W. A. de Jong, *Comput. Phys. Commun.*, 2010, **181**, 1477–1489.
- 49 J. P. Perdew, K. Burke and M. Ernzerhof, *Phys. Rev. Lett.*, 1996, **77**, 3865.
- 50 A. Klamt and G. Schüürmann, *J. Chem. Soc., Perkin Trans. 2*, 1993, 799–805.
- 51 D. M. York and M. Karplus, *J. Phys. Chem. A*, 1999, **103**, 11060–11079.
- 52 P. Winget, D. M. Dolney, D. J. Giesen, C. J. Cramer and D. G. Truhlar, Department of Medicinal Chemistry and Supercomputer Institute, University of Minnesota, Minneapolis, MN, 1999, p. 55455.
- 53 R. J. Charlton, R. M. Fogarty, S. Bogatko, T. J. Zuehlsdorff, N. D. M. Hine, M. Heeney, A. P. Horsfield and P. D. Haynes, *J. Chem. Phys.*, 2018, **148**, 104108.
- 54 J. L. Herek, S. Pedersen, L. Bañares and A. H. Zewail, *J. Chem. Phys.*, 1992, **97**, 9046–9061.
- 55 J. D. Coe, B. G. Levine and T. J. Martínez, *J. Phys. Chem. A*, 2007, **111**, 11302–11310.
- 56 F. Ling, D. Liu, S. Li, W. Li, B. Zhang and P. Wang, *J. Chem. Phys.*, 2019, **151**, 094302.
- 57 A. Watwiangkham, T. Roongcharoen and N. Kungwan, *J. Photochem. Photobiol., A*, 2020, **389**, 112267.
- 58 S. Grimme and F. Neese, *J. Chem. Phys.*, 2007, **127**, 154116.
- 59 D. Jacquemin, Y. Zhao, R. Valero, C. Adamo, I. Ciofini and D. G. Truhlar, *J. Chem. Theory Comput.*, 2012, **8**, 1255–1259.
- 60 J. C. Dean, R. Kusaka, P. S. Walsh, F. Allais and T. S. Zwier, *J. Am. Chem. Soc.*, 2014, **136**, 14780–14795.
- 61 P. B. Bisht, H. Petek and K. Yoshihara, *J. Chem. Phys.*, 1995, **103**, 5290–5307.
- 62 P. Zhou, M. R. Hoffmann, K. Han and G. He, *J. Phys. Chem. B*, 2014, **119**, 2125–2131.
- 63 R. D. Massaro, Y. Dai and E. Blaisten-Barojas, *J. Phys. Chem. A*, 2009, **113**, 10385–10390.
- 64 A. L. Sobolewski and W. Domcke, *Phys. Chem. Chem. Phys.*, 1999, **1**, 3065–3072.
- 65 A. L. Sobolewski and W. Domcke, *Chem. Phys. Lett.*, 1999, **300**, 533–539.
- 66 N. D. N. Rodrigues, M. Staniforth and V. G. Stavros, *Proc. R. Soc. A*, 2016, **472**, 1–29.
- 67 A. Toniolo, M. Ben-Nun and T. Martinez, *J. Phys. Chem. A*, 2002, **106**, 4679–4689.
- 68 R. O. Jones, *Rev. Mod. Phys.*, 2015, **87**, 897.
- 69 P. Zhou and K. Han, *Acc. Chem. Res.*, 2018, **51**, 1681–1690.
- 70 M. Rini, A. Kummrow, J. Dreyer, E. T. J. Nibbering and T. Elsaesser, *Faraday Discuss.*, 2003, **122**, 27–40.
- 71 S. J. Formosinho and L. G. Arnaut, *J. Photochem. Photobiol., A*, 1993, **75**, 21–48.
- 72 K.-Y. Law and J. Shoham, *J. Phys. Chem.*, 1994, **98**, 3114–3120.
- 73 R. Krishnan and T. M. Nordlund, *J. Fluoresc.*, 2008, **18**, 203–217.
- 74 K. Sugiyama, T. Tsuchiya, A. Kikuchi and M. Yagi, *Photochem. Photobiol. Sci.*, 2015, **14**, 1651–1659.
- 75 M. Kasha, J. Heldt and D. Gormin, *J. Phys. Chem.*, 1995, **99**, 7281–7284.
- 76 J. Catalán and C. Díaz, *J. Phys. Chem. A*, 1998, **102**, 323–328.
- 77 L. A. Baker and V. G. Stavros, *Sci. Prog.*, 2016, **99**, 282–311.
- 78 B. M. Uzhinov and M. N. Khimich, *Russ. Chem. Rev.*, 2011, **80**, 553–577.
- 79 N. Kanlayakan, K. Kerdpol, C. Prommin, R. Salaeh, W. Chansen, C. Sattayanon and N. Kungwan, *New J. Chem.*, 2017, **41**, 8761–8771.
- 80 J. M. Allen, C. J. Gossett and S. K. Allen, *Chem. Res. Toxicol.*, 1996, **9**, 605–609.

Electronic Supplementary Information:

Insights into the photoprotection mechanism of the UV filter homosalate

S1 Supplementary methods

S1.1 Gas-phase experiments

S1.1.1 Power dependence measurements

The TR-IY signal dependence on both the pump and probe laser powers was evaluated to ensure single-photon-induced photodynamics take place under the current experimental conditions. Firstly, TR-IY transients were collected at three different values of laser power; the logarithm of transient subtracted signal (raw signal minus background signal, *i.e.* pump-only, probe-only and background noise) with respect to the logarithmic value of power for each time delay ($\log(\text{signal})$ *vs.* $\log(\text{power})$) is then plotted and finally fit using a linear function using least squares regression. The gradient of this fit provides us with the physical information regarding the signal power dependence — a gradient of 1 (within error) is taken to be indicative of single-photon-induced dynamics. In Fig. S1, an exemplar power study plot is shown for photoexcitation at $\lambda_{\text{pump}} = 305$ nm ($\lambda_{\text{probe}} = 200$ nm) and at $\Delta t = 0$. The error of the gradient is the standard error for the parameter, given by the following equation:

$$\frac{b}{\sqrt{n-2}} \sqrt{\frac{1}{r^2} - 1} \quad (\text{S1})$$

where b is the fitted gradient from the least squares regression analysis undertaken, n is the number of datapoints on the line, and r is the value of the Pearson correlation coefficient¹ for the fitted data.

Similar power dependence studies were carried out for other pump wavelengths, with similar results (not shown). The error bars shown in Fig. S1 represent two standard deviations from the average data point, which was collected from four consecutive scans. The large error associated with each data point on these plots is a reflection of the low signal-to-noise ratio of these experiments, a consequence of the small pump-probe signal (in comparison to the pump alone and probe alone signals). Albeit inconclusive, the linear fit to these data, as presented in Fig. S1, seems to suggest that the feature associated with τ_1 may be linearly dependent on pump power, which would be indicative of single-photon pump-initiated photodynamics via S_1 . We also note here that the large

amplitude of the feature from which these data were extracted (particularly noticeable in Fig. 3(c) in the main manuscript) is likely to have a considerable contribution from probe-initiated reverse dynamics, considering the high absorption cross section of our 200 nm probe.

S1.1.2 Kinetic fit

We fit our TR-IY data for the homosalate (HMS) parent ion (HMS⁺) transients using a multi-parameter function that can be analytically described as follows:

$$S(t) = g(t) * \sum_{i=0}^n A_i e^{-\frac{t}{\tau_i}} H(t) + \text{offset} \quad (\text{S2})$$

Equation S2 describes the convolution of a Gaussian function $g(t)$ (corresponding to the instrument response function, see below) with a sum of exponential decay functions starting at time zero ($\Delta t = 0$). A_i is then the amplitude of the i -th decay, τ_i the time constant corresponding to the i -th decay and $H(t)$ is a step function defined in Equation S3.

$$H(t) = \begin{cases} 0 & \text{if } t < 0 \\ 1 & \text{if } t \geq 0 \end{cases} \quad (\text{S3})$$

This kinetic fit assumes parallel excited state decay pathways, *i.e.* it assumes that all dynamics begin at $\Delta t = 0$.

S1.1.3 Instrument response function and time zero $\Delta t = 0$

As mentioned in the main manuscript, the instrument response function (IRF) defines the time resolution of our time-resolved measurements. In order to estimate the IRF, TR-IY measurements of Xenon (Xe) were performed, following $2 + 1$ non-resonant ionization (see Fig. S2 for one such measurement, for $\lambda_{\text{pump}} = 330$ nm). The resulting transient, which consists of the cross-correlation between the pump and probe laser pulses, was fit with a Gaussian function; the full width at half maximum (FWHM) of this Gaussian fit, which was determined to be ~ 170 fs, was taken to be our IRF.

S1.1.4 Dispersed fluorescence and fluorescence lifetime

Fig. S3a shows the dispersed fluorescence spectrum of HMS which was obtained following the methodology described in the main paper. Briefly, the laser wavelength was fixed to be resonant with selected transitions in the excitation spectrum and the resulting fluorescence was then dispersed with a grating and collected by an intensified CCD. Upon photoexcitation to the $S_1(v = 0)$ origin of HMS, the resulting dispersed fluorescence spectrum reveals a large Stokes shift of ~ 5800 cm⁻¹ or 0.72 eV (see Fig. S3a).

Fluorescence lifetime traces were also recorded by exciting select transitions and directly recording the time profile of the fluorescence signal from the photomultiplier tube on the digital oscilloscope. The gas-phase fluorescence lifetimes of HMS were extracted from the resulting transients following the same method described in section 1.2, using in this case an instrument response of 8 ns. Fig. S3b shows one example of such fluorescence lifetimes measurements, for which excitation was to the $S_1(v = 0)$ of HMS; a fluorescence lifetime of 12.7 ± 0.2 ns was extracted from this fit.

S1.2 Experiments in solution

S1.2.1 Fitting procedure

The spectra collected with our transient electronic absorption spectroscopy (TEAS) setup, further described in the main paper, are chirped, *i.e.* $\Delta t = 0$ is different for each probe wavelength, due to group velocity dispersion (GVD) artefacts.² To account for this chirp effect, a third order polynomial is included within the fitting algorithm within the Glotaran software package.³ This package also convolutes the Gaussian IRF (see Section S1.2.2) with exponential functions to extract the fitted lifetimes (τ_n) for the parallel kinetic model used for this data. In the false colour heat maps and corresponding heat maps presented in the main manuscript and this ESI, the chirp is corrected using the KOALA package.⁴

S1.2.2 Instrument response functions

The IRF for our TEAS setup is determined by evaluating solvent-only responses at given probe wavelengths. The resulting transients were fitted with a Gaussian function, given by Eq. S4. In this equation, A denotes the peak amplitude of the fitted curve, t_0 is the fitted time zero, indicating the centre of the curve, and σ is the standard deviation of the curve. The fits attained using Eq. S4 are shown in Fig. S4.

$$f(t) = A \exp\left(-\frac{(t - t_0)^2}{2\sigma^2}\right) + \text{offset} \quad (\text{S4})$$

To convert from the fitted standard deviation to the full width half maximum (FWHM), which is the quoted IRF, a scaling factor of $2\sqrt{2\ln 2}$ was applied to the standard deviation σ . After application of this scaling factor, the extracted IRF lifetimes are ~ 80 fs in acetonitrile, ~ 65 fs in ethanol and ~ 55 fs in cyclohexane.

S1.2.3 Power dependence measurements

Power dependence measurements were taken for each solution of HMS and ethylhexyl salicylate (EHS) in all three solvents: ethanol, acetonitrile and cyclohexane, to ensure a linear dependence on power across all spectral features of the TAS and exclude the possibility of multiphoton transitions, following the relation ($\log(\text{Signal})$ *vs.* $\log(\text{Power})$). A gradient of 1 (within error) is suggestive of

single photon mediated photodynamics. The power of the pump wavelength was varied for each set of measurements by reducing the output of the TOPAS-C. At each power, 20 datasets were taken and subsequently averaged.

Slices of the transients were taken in the wavelength domain where significant spectral features occur, then the slices were smoothed by using an integration window of ± 5 nm. The outcome of this power dependence study is shown in Fig. S5 for HMS in ethanol and Fig. S6 for EHS in ethanol. In each case, the error of the gradient is the standard error for the parameter, given by Eq. S1. The values of r that have been substituted into Eq. S1 to attain the gradient standard error presented in Figs. S5 and S6 are as follows:

Fig. S5: (a) 0.962, (b) 0.989, (c) 0.961

Fig. S6: (a) 0.991, (b) 0.993, (c) 0.996

To calculate the error bars in each case, all 20 scans taken at each power were averaged together, and alongside the mean value for each datapoint (\bar{x}), the standard deviation (σ) was also recorded. The standard deviation at each single wavelength was then summed across the integrated wavelength region to account for error propagation. The error bars presented in Figs. S5 and S6 are thus equivalent to $\log(\bar{x} \pm 2\sigma)$.

S1.2.4 Fluorescence of homosalate

Emission spectra were measured for HMS in each of three solvents: acetonitrile, ethanol and cyclohexane. Solutions were prepared to a concentration of ~ 10 μM and the path length for spectrum acquisition was 10 mm. The emission spectra were collected using a Horiba Fluorolog-3 instrument; the excitation wavelength was chosen to be the λ_{max} of each solution, 306 nm in acetonitrile, 307 nm in ethanol and 309 nm in cyclohexane, which were produced by a Xenon arc lamp with a slit width of 5 nm.

Fluorescence lifetimes for the three solutions of HMS were also determined. The same samples as the fluorescence measurements above were used to assess the lifetimes, and a 1 cm path length quartz fluorescence cuvette was used. Instead of a Xe arc lamp, the excitation source was a NanoLED with a central wavelength of 318 nm. An exponential decay function was fitted to the fluorescence signal *vs.* time transients to extract the respective fluorescence lifetimes, which were found to be within the instrument response of 1.2 ns in all instances.

S1.2.5 Fluorescence quantum yield of homosalate

The fluorescence quantum yield of HMS, $\Phi_{\text{F}}(\text{HMS})$, was determined in all three solvents following the methodology described by Würth *et al.*,⁵ by comparing the fluorescence emission to that of a known standard, 1,4-diphenyl-1,3-butadiene (DPB) in cyclohexane. All three solutions were prepared such that they had an absorbance value of 0.1 or below, which corresponds to a concentration of approximately 10 μM for HMS solutions and approximately 0.5 μM for the solution of DPB in

cyclohexane. The UV-visible spectra of the sample and standard solutions are shown in Fig. S7a.

Five repeats of the emission spectra were taken for each of the fluorescence samples. These five emission spectra were averaged, and this average was used for the final calculation of $\Phi_{\text{F}}(\text{HMS})$ using Eq. S5.⁵ The averaged spectra are shown in Fig. S7b.

$$\Phi_{\text{F}}^x = \frac{F_x A_s n_x^2}{F_s A_x n_s^2} \Phi_{\text{F}}^s \quad (\text{S5})$$

The parameters in Eq. S5 are defined as follows: Φ_{F}^x is the fluorescence quantum yield of the sample solution, Φ_{F}^s the fluorescence quantum yield of the standard, F_x is the integrated area of the fluorescence curves of the sample (320 – 600 nm), with F_s being the equivalent integral for the reference standard (320 – 600 nm); secondly A_s and A_x are the absorbance of the standard and sample respectively; finally n_s^2 is the refractive index of the solvent of the standard solution (cyclohexane) and n_x^2 is the refractive index of the sample solution. The value of Φ_{F}^s for these quantum yield calculations was 0.44.⁶ However, as this value is for 330 nm excitation and fluorescence quantum yield is a wavelength dependent quantity, some caution should be exercised with the attained homosalate quantum yields.

S2 Supplementary results and discussion

S2.1 Gas-phase experiments discussion

S2.1.1 LIF linewidths

The first four peaks of the LIF spectrum of HMS were fitted with Lorentzian functions as shown in Fig. S10. As the LIF peaks are rotational band contours (the linewidths are those typical of a molecule the size of homosalate with rotational temperature of approximately 2 K), the Γ parameter in the Lorentzian fit gives an approximate lower bound to the lifetime of the vibrational level in S_1 by $\tau = \hbar/\Gamma$.⁷ Following this analysis, the linewidth of the origin peak of HMS is $\sim 0.84 \text{ cm}^{-1}$, which corresponds to a lifetime of the S_1 -*enol* species of $\sim 6 \text{ ps}$. We stress, however, that this is a lower limit value, which is reflected in the measured fluorescence lifetimes.

S2.2 Transient electronic absorption spectroscopy (TEAS) discussion

S2.2.1 Sequential fitting of homosalate

In the main manuscript, we have presented the results from fitting the TEAS data for HMS employing a parallel kinetic model, to allow for better comparison with the gas-phase data. To assess the effect of different model assumptions, we have also used a sequential model (that assumes $A \xrightarrow{\tau_1} B \xrightarrow{\tau_2} C \cdots \xrightarrow{\tau_4} E$) to fit the same data. The results of the sequential fitting are shown in Table S4. Selected wavelength transients to demonstrate the quality of the fit are shown in Fig. S13. These results demonstrate that the time constants extracted from fitting our TEAS data with a sequential model are similar to those yielded by a parallel kinetic model.

S2.2.2 TEAS measurements of ethylhexyl salicylate

TAS of ethylhexyl salicylate (EHS, also known as octisalate) were taken to compare the effects of the alkyl moiety on the action of the salicylate chromophore. The results are shown in Fig. S15, with TAS at selected pump-probe time delays in Fig. S16 and the quality of the fit shown for selected wavelengths in Fig. S17. The elucidated time constants, which were determined using the same methods as HMS, are listed in Table S5 for a parallel model and Table S6 for a sequential model.

As perhaps indicated by the similarities between the HMS and EHS in their UV-visible spectra (Fig. S15, see Fig. 1 in the main paper for equivalent spectra for HMS), there are comparable spectral features in the TAS for both of these molecules. The TAS for HMS can be found in Fig. 5 of the manuscript. Both sets of TAS share a prominent excited state absorption feature between *ca.* 320 – 400 nm, and a stimulated emission feature centred at 450 nm. Akin to HMS, four time constants were required to adequately fit the TAS obtained for EHS; the residuals for this fit are

shown in Fig. S12 (d), (e) and (f). The four time constants for EHS are comparable to those extracted for HMS, *i.e.* all four time constants are of the same orders of magnitude.

Given the similarities between HMS and EHS (and by comparison with previously published work), the extracted time constants can be confidently assigned to the same processes as were elucidated for HMS in the main paper. However, according to the results presented here, relaxation of EHS has been found to be relatively faster, perhaps indicating that the suggested internal conversion relaxation pathway from the S_1 state (plus any vibrational cooling that may take place alongside it, described by τ_2) may be facilitated by a molecular motion that is hindered by the larger or more rigid structure of the ester substituent in HMS when compared to EHS. Fluorescence, described by τ_3 , was also found to have a slightly shorter decay lifetime for EHS when compared to HMS. As τ_1 is defined within the constraints of the IRF, any differences in the rate of intramolecular excited-state proton transfer for EHS *vs.* HMS are inconclusive. Similarly, it cannot be determined from our TEAS measurements whether the rate of intersystem crossing is affected, as for both HMS and EHS τ_4 is beyond the temporal window of the instrument.

In summary, whilst the photophysical processes occurring within HMS and EHS following photoexcitation in the UVB region may be the same in both molecules, suggesting that these processes are predominantly dictated by the salicylate chromophore, the alkyl chains of EHS as opposed to the cycloalkane structure of HMS may facilitate slightly faster rates of decay. From these results, it follows that EHS may be a preferential sunscreen candidate to HMS, given the reduction in the value of the fitted time constants.

S2.2.3 Longer-time scans

To further investigate any long-lived features in the TAS of both HMS and EHS, a second ultrafast transient absorption setup at the Warwick Centre for Ultrafast Spectroscopy was used; this setup was used as it has a longer delay stage and time delays of up to 3 ns could be accessed, as opposed to 2 ns. A full characterisation of this TEAS setup can be found in the publication by Woolley *et al.*,⁸ although it is very similar to the setup used for all other TEAS studies in this work. For each time delay, 100 scans were taken and subsequently averaged. The pump wavelength was chosen to be the peak absorption (shown in Fig. 1) and the fluence of the pump and probe pulses was kept consistent between both setups for fair comparison. The results are shown in Fig. S18. These TAS demonstrate that there is a consistent positive long-lived feature in the TAS at probe wavelengths between *ca.* 360 – 480 nm, which is assigned to the T_1 state of HMS and EHS respectively. As mentioned in the main manuscript, the spectral features observed in these TAS resemble the triplet absorption spectra collected by Sugiyama *et al.*⁹ for both HMS and EHS at room temperature (25 °C), 2–17 μ s after photoexcitation, lending credibility to our hypothesis (see manuscript for further discussion).

S3 Supplementary figures

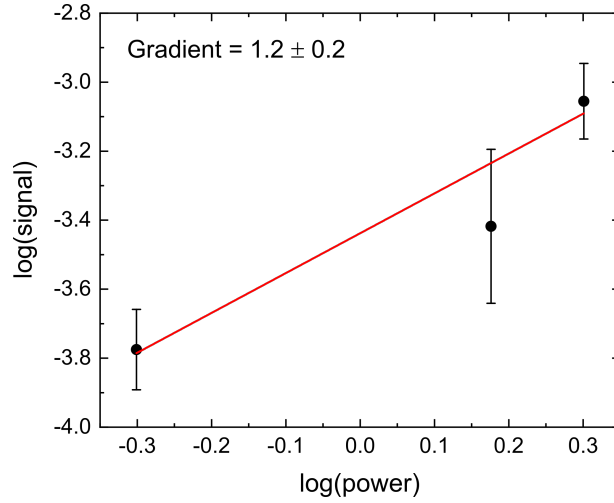


Fig. S1 Power dependence study for HMS in vacuum photoexcited at $\lambda_{\text{pump}} = 305$ nm at $\Delta t = 0$ ps. Black circles correspond to data points which are an average of four consecutive scans; the error bars on each data point correspond to two standard deviations from this average. The red line denotes the line of best fit attained by linear least squares regression.

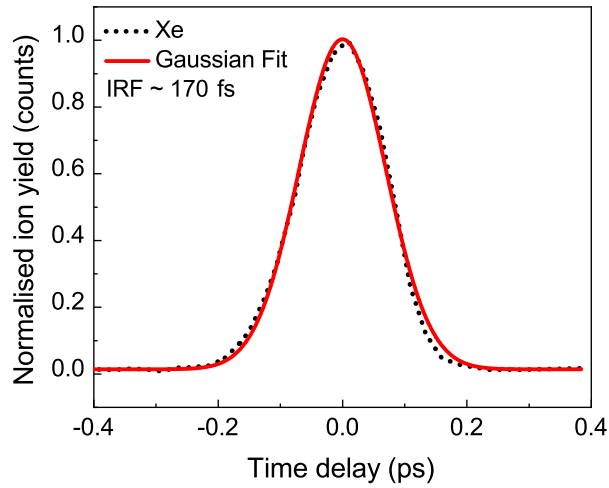


Fig. S2 Gaussian fit (red line) to the Xe TR-IY transients at $\lambda_{\text{pump}} = 330$ nm (black dotted line). The FWHM of the fitting curve presented provides us with the pump-probe beam cross-correlation width of ~ 170 fs, which we quote as our IRF.

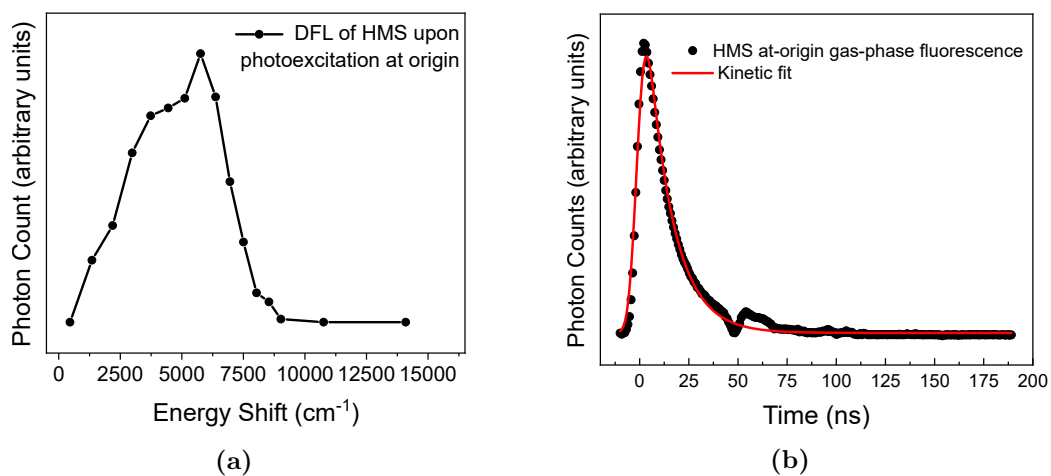


Fig. S3 (a) Dispersed fluorescence spectrum of HMS. (b) Fitted transient (black dotted line, with line of best fit shown in red) to extract the fluorescence lifetime of HMS at origin.

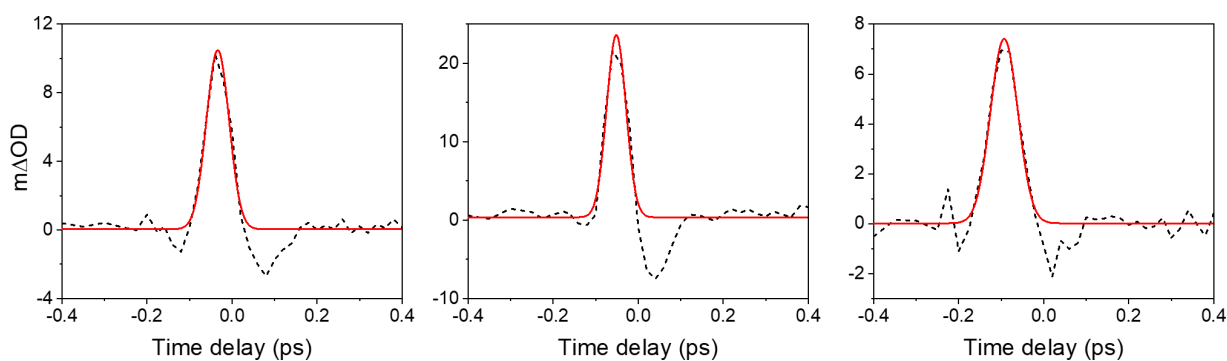


Fig. S4 Selected transients for solvent-only time-zero IRFs at given probe wavelengths, plotted using black dashed lines (pump wavelengths were kept the same as for TEAS measurements for each solution): (a) ethanol at 330 nm, IRF \sim 65 fs (b) cyclohexane at 320 nm, IRF \sim 55 fs and (c) acetonitrile at 330 nm, IRF \sim 80 fs. These IRFs have been extracted from a Gaussian fit function, with the line of best fit shown in red.

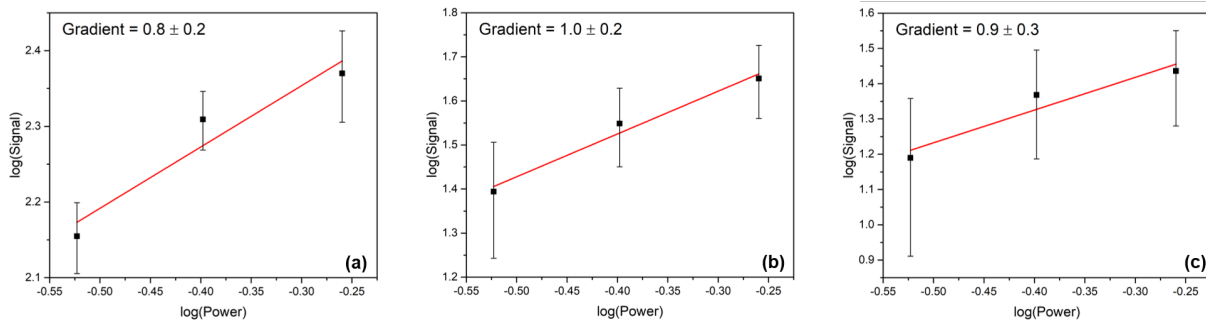


Fig. S5 Power dependency study for HMS in ethanol for key features at $\Delta t = 1$ ps at the following probe wavelengths: (a) 340 nm (b) 450 nm and (c) 530 nm. Explanation of the derivation of the error bars is given in the text in Section S1.2.3.

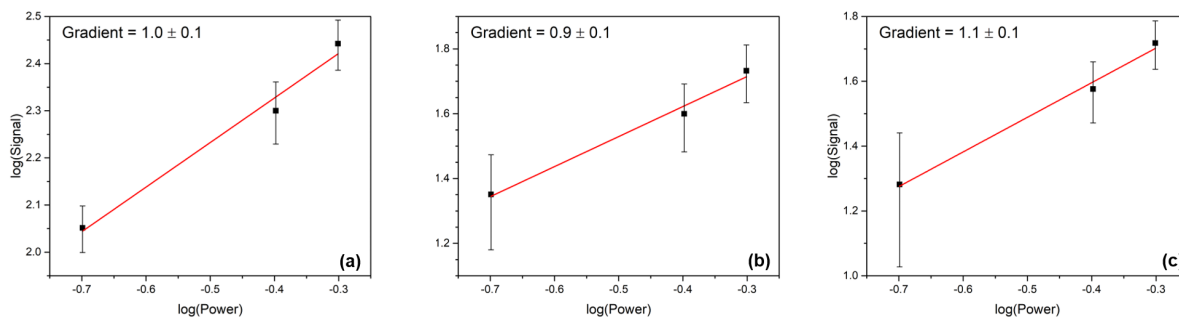


Fig. S6 Power dependency study for ethylhexyl salicylate (octisalate) in ethanol for key features at $\Delta t = 1$ ps at the following probe wavelengths: (a) 340 nm (b) 450 nm and (c) 530 nm. Explanation of the derivation of the error bars is given in the text in Section S1.2.3.

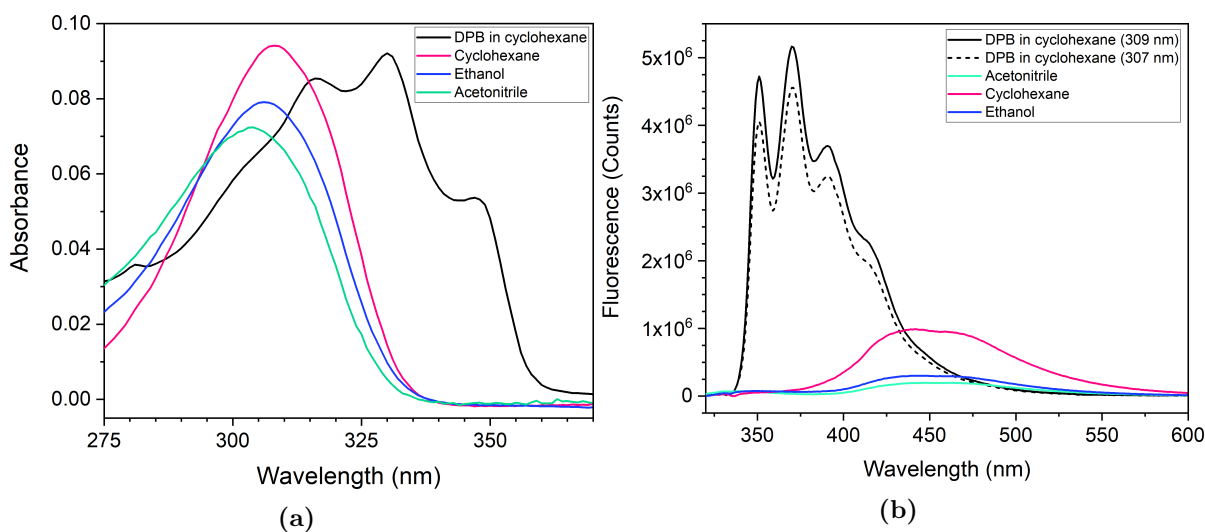


Fig. S7 (a) UV-visible spectra taken of three $\sim 20 \mu\text{M}$ solutions of HMS in cyclohexane (pink line), ethanol (blue line) and acetonitrile (green line), with the standard solution, $\sim 0.5 \mu\text{M}$ 1,4-diphenyl-1,3-butadiene (DPB) in cyclohexane, shown in black. (b) Averaged fluorescence spectra, attained from averaging five separate scans, which were integrated and the values substituted into Eq. S5.

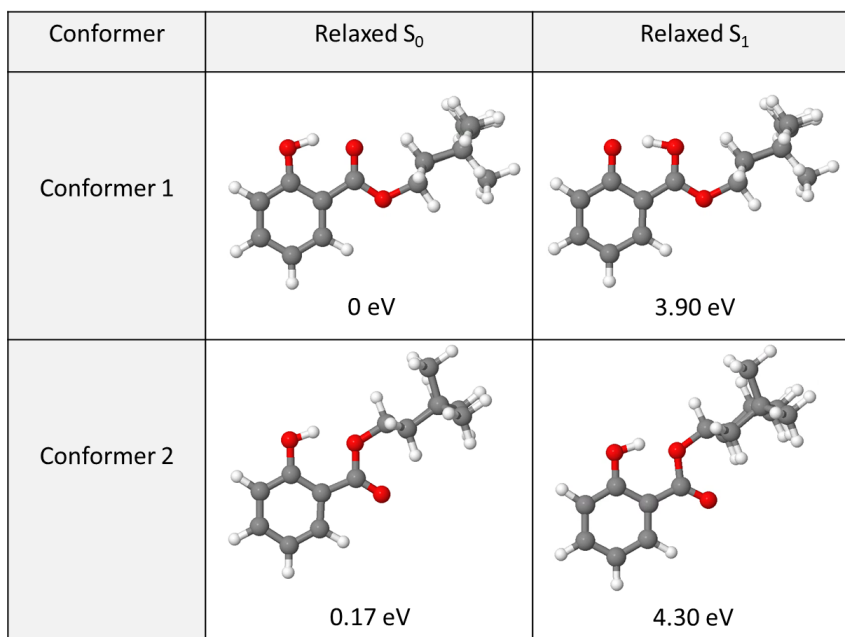


Fig. S8 Structure and relative energies (relative to conformer 1 in the S_0 state, the lowest energy structure/state) of the two lowest energy conformers of HMS in both the S_0 and S_1 states. The ground state energies were calculated by relaxing the geometry of both conformers at the PBE/cc-pVTZ level of theory and then conducting a single point energy calculation on each at the PBE0/cc-pVTZ level of theory. The excited state energies were calculated by relaxing each conformer with respect to the S_1 state at the PBE0/cc-pVTZ level of theory.

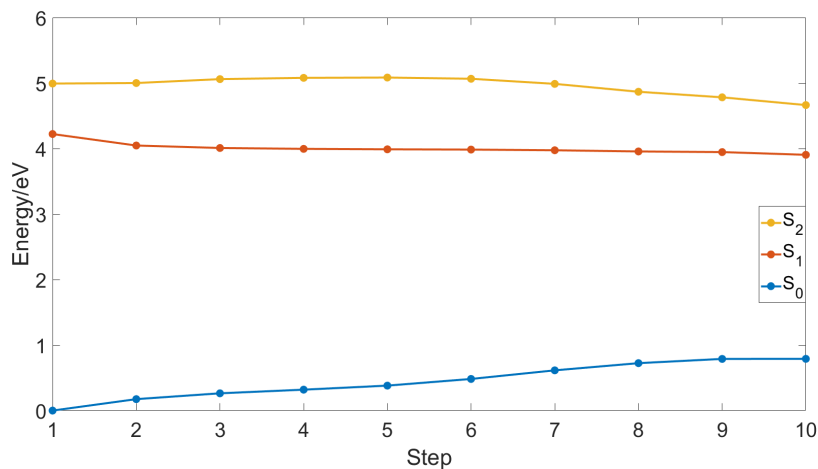


Fig. S9 S_0 , S_1 , and S_2 energies of HMS in specific steps between the *enol* and *keto* forms. These steps were generated through a linear interpolation of internal coordinates (LIIC). This figure is an expansion upon Fig. 2b in the main text to demonstrate the lack of intersection between the S_1 and S_2 states over the examined reaction coordinate. As the second conformer does not yield a stable *keto* structure in the S_1 state, it is not possible to study a LIIC along its respective proton transfer coordinate.

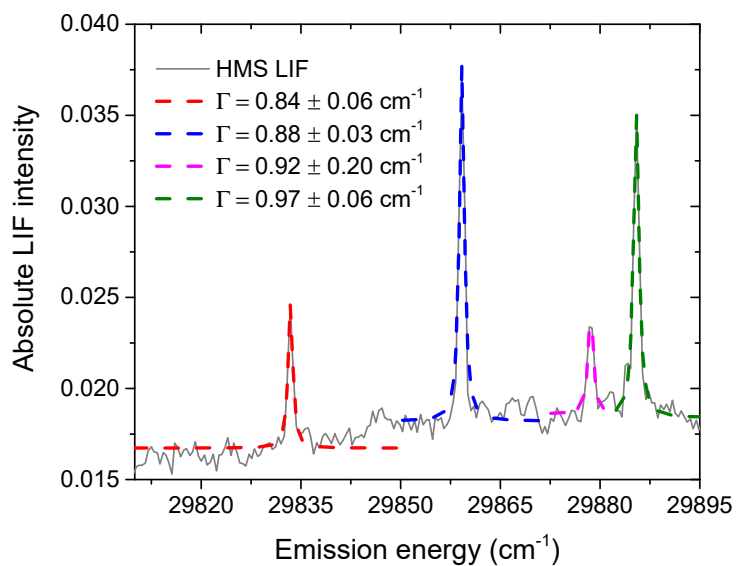


Fig. S10 Lorentzian fits (dashed lines) to the first four peaks of the LIF spectrum of HMS (raw data presented as a grey solid line). These Lorentzian fits return Γ values of 0.84 cm^{-1} for the peak centred at 29833.4 cm^{-1} ($S_1(v=0)$ origin of HMS, red dashed line), 0.88 cm^{-1} for the peak at 29859.2 cm^{-1} (blue dashed line), 0.92 cm^{-1} for the peak at 29878.6 cm^{-1} (pink dashed line) and 0.97 cm^{-1} for the peak at 29885.5 cm^{-1} (green dashed line).

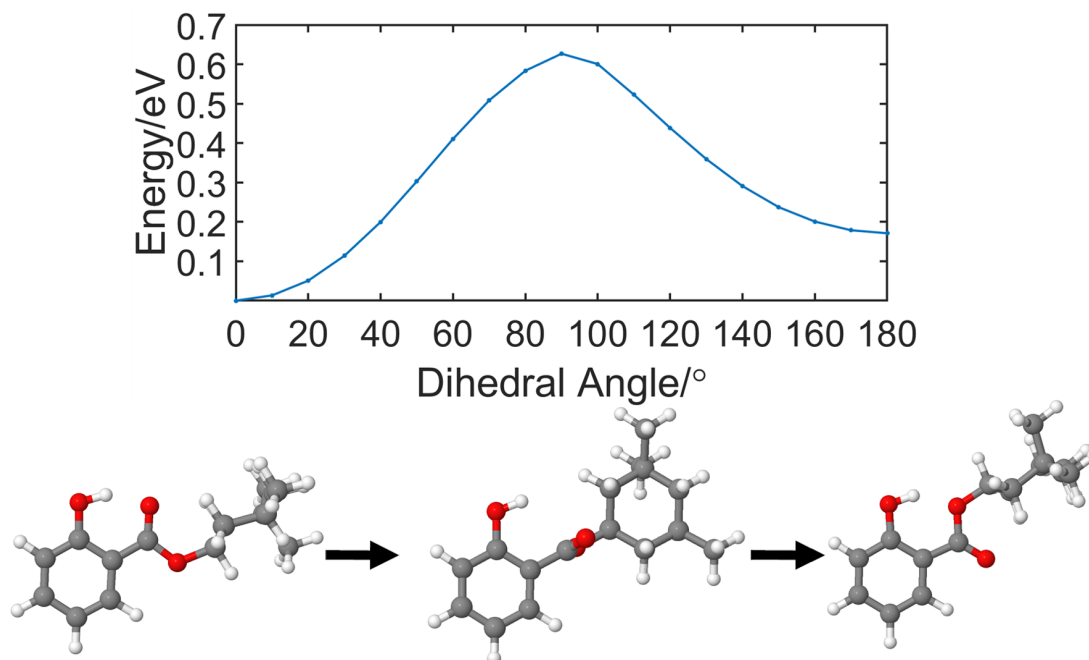


Fig. S11 S_0 energy of *enol* form along the rotation coordinate between conformer 1 and conformer 2. This was generated by fixing the dihedral angle shown at 10 degree increments between 0 and 180 degrees and relaxing all other internal coordinates in the ground state at the PBE/cc-pVTZ level of theory. This is an upper bound to the energy barrier between the two conformers.

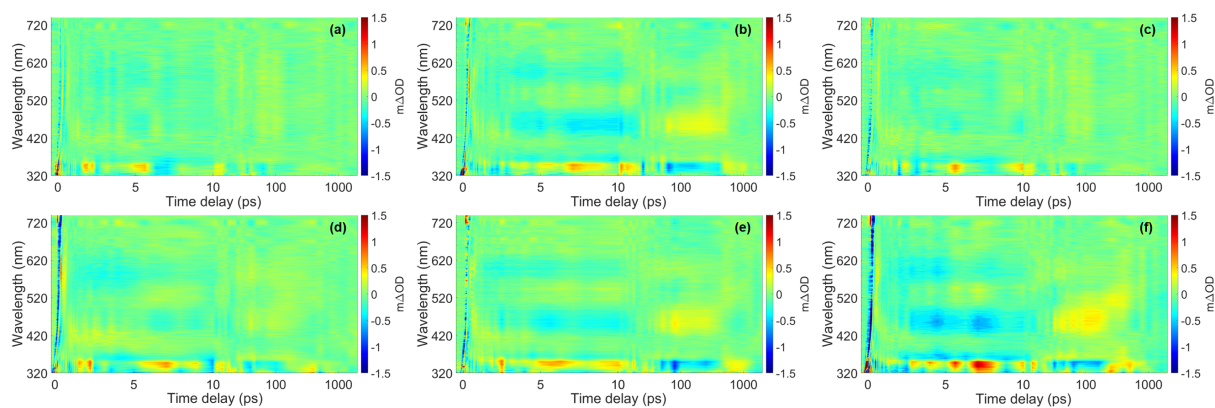


Fig. S12 False colour heat maps showing the residuals attained from the parallel fitting procedure (compared to raw data) for HMS in (a) acetonitrile, (b) cyclohexane and (c) ethanol, and for EHS in (d) acetonitrile, (e) cyclohexane and (f) ethanol

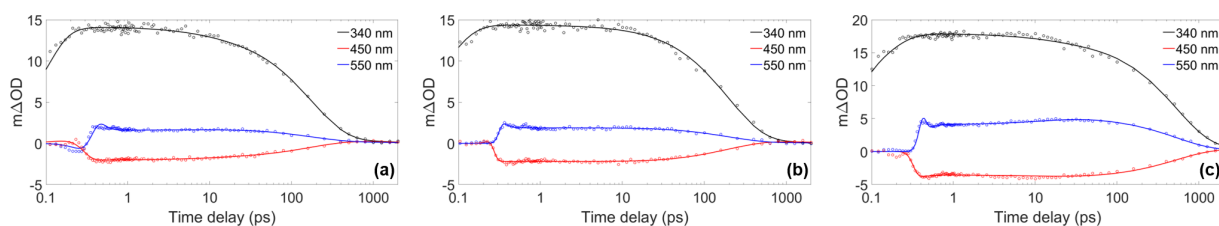


Fig. S13 Kinetic fits of the transient data at 340 nm (black), 450 nm (red) and 550 nm (blue) for HMS in (a) acetonitrile, (b) ethanol and (c) cyclohexane. The circles represent the raw data and the solid line is the fit attained using the sequential model described in Section S2.2.1.

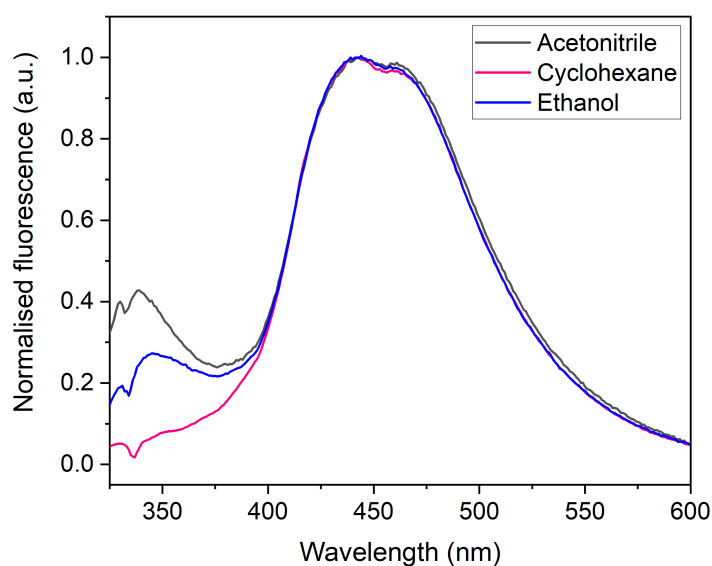


Fig. S14 Normalised emission spectra with solvent baseline subtraction of HMS in cyclohexane, ethanol and acetonitrile. Excitation was carried out at the respective peak maxima of each solution: $305 \leq \lambda_{\text{pump}} \leq 310$ nm. The slit width was 2.5 nm. The slight discrepancy in the spectra at ~ 330 nm is due to Stokes Raman scattering effects that could not be fully subtracted from the fluorescence spectra.¹⁰ All three solutions display an emission peak at 450 nm. We note, however, the presence of a smaller peak at 350 nm in polar solvents, a phenomenon that has also been observed in the molecular analogue methyl salicylate, although the cause of this dual fluorescence remains uncertain.¹¹

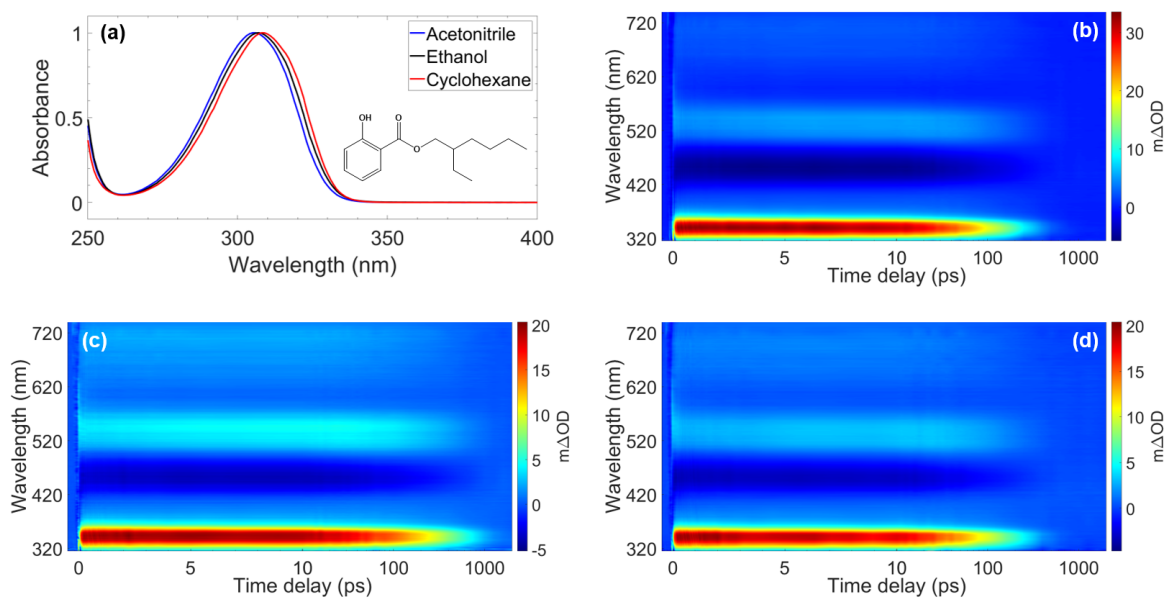


Fig. S15 (a) UV-visible absorption spectra of EHS in three different solvents, with the molecular structure of EHS inset. TAS of ~ 10 mM solutions of EHS in (b) ethanol ($\lambda_{\text{max}} = 307$ nm), (c) cyclohexane ($\lambda_{\text{max}} = 309$ nm) and (d) acetonitrile ($\lambda_{\text{max}} = 305$ nm).

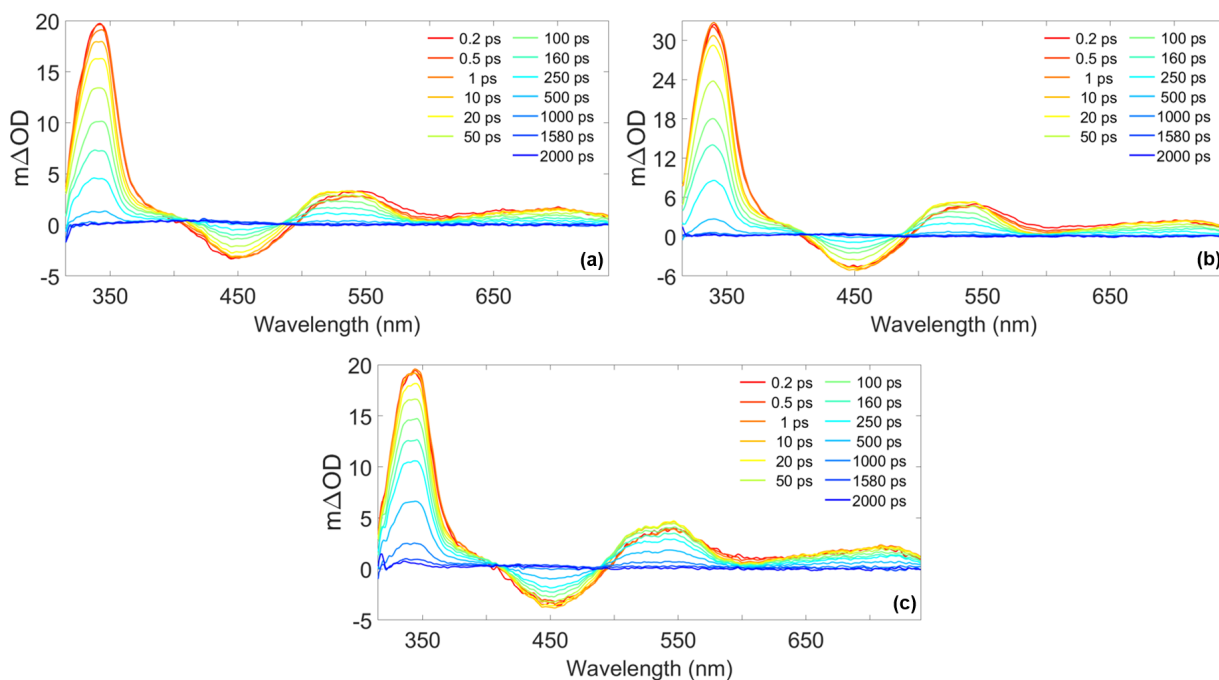


Fig. S16 TAS at selected pump-probe time delays for EHS in (a) acetonitrile, (b) ethanol and (c) cyclohexane. These plots are attained by taking vertical slices through the false colour heat maps at the given time delay.

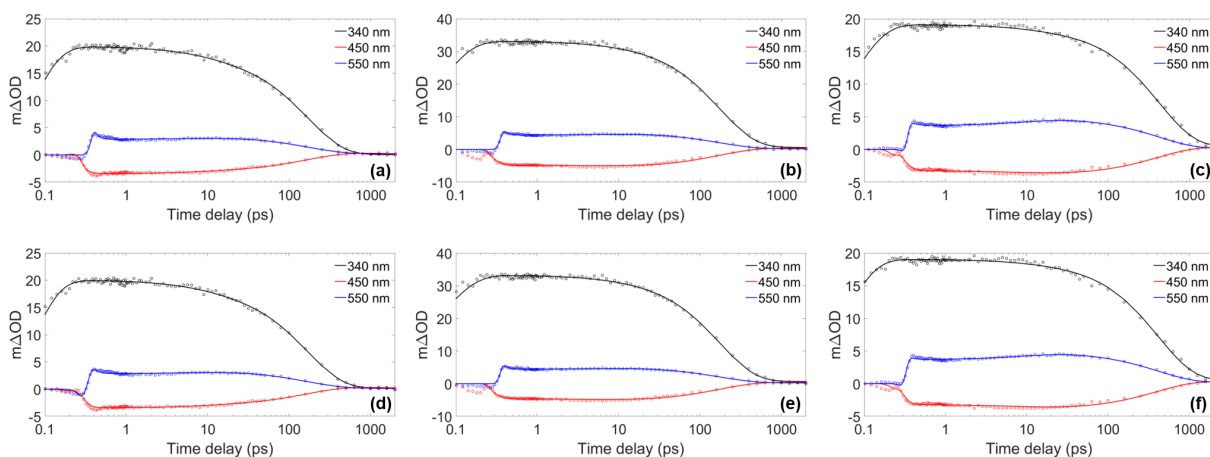


Fig. S17 Kinetic fits of the transient data at 340 nm (black), 450 nm (red) and 550 nm (blue) for EHS in acetonitrile, ethanol and cyclohexane respectively, fitted using: (a)–(c) a parallel model, the same as that used for HMS (described in the manuscript) and (d)–(f) a sequential model, as described in section S2.2.1. The circles denote the raw data at each wavelength and the solid line is the fit attained. In each case, the time delay axis is presented on a logarithmic scale.

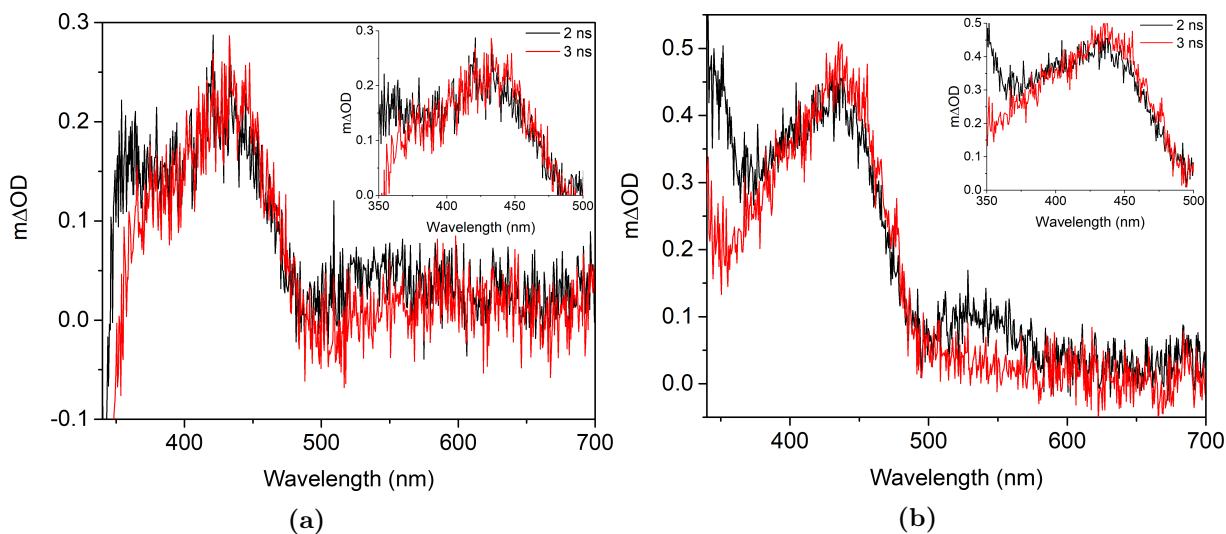


Fig. S18 (a) TAS of HMS in cyclohexane ($\lambda_{\text{pump}} = 309$ nm) taken at $\Delta t = 2$ ns (black) and $\Delta t = 3$ ns (red), attained using the TEAS setup characterised by Woolley *et al.*⁸ Inset is a zoom-in of the data between 350 and 500 nm to more clearly display the long-lived positive signal. (b) TAS of EHS in cyclohexane ($\lambda_{\text{pump}} = 309$ nm) taken at $\Delta t = 2$ ns (black) and $\Delta t = 3$ ns (red). Inset is a zoom-in of the data between 350 and 500 nm to more clearly display the long-lived positive signal.

S4 Supplementary tables

Table S1 This table shows the difference in energies of conformer 1 and conformer 2 ($E_2 - E_1$) in the gas-phase. Both conformers were relaxed at the PBE/cc-pVTZ level of theory. Following this, the single point energies of these structures were calculated using PBE/cc-pVTZ and PBE0/cc-pVTZ, as well as the post Hartree-Fock method MP2/cc-pVDZ.

Level of Theory	$E_2 - E_1$
PBE/cc-pVTZ	0.17 eV
PBE0/cc-pVTZ	0.17 eV
MP2/cc-pVDZ	0.10 eV

Table S2 Calculated singlet and triplet excited state vertical energies from the optimised ground state geometry of the *enol* form of HMS in cyclohexane using TD-DFT at the PBE0/cc-pvtz level of theory

Environment	Singlets			Triplets		
	State	Energy (eV)	Character	State	Energy (eV)	Character
Vacuum				ΔT_1	3.3282	
	S ₁	4.2220	$\pi\pi^*$	T ₁	3.2149	$\pi\pi^*$
	S ₂	4.9928	$n\pi^*$	T ₂	3.4260	$\pi\pi^*$
	S ₃	5.3280	$\pi\pi^*$	T ₃	3.2714	$\pi\pi^*$
	S ₄	6.0780	$\pi\pi^*$	T ₄	4.6214	$n\pi^*$
	S ₅	6.9246	$n\pi^*$	T ₅	5.1866	$n\pi^*$
Acetonitrile				ΔT_1	3.3490	
	S ₁	4.2917	$\pi\pi^*$	T ₁	3.2749	$\pi\pi^*$
	S ₂	4.9808	$n\pi^*$	T ₂	3.4721	$\pi\pi^*$
	S ₃	5.3383	$\pi\pi^*$	T ₃	4.2983	$\pi\pi^*$
	S ₄	5.9317	$n\pi^*$	T ₄	4.6229	$n\pi^*$
	S ₅	6.0869	$n\pi^*$	T ₅	5.1041	$n\pi^*$
Cyclohexane				ΔT_1	3.3364	
	S ₁	4.2518	$\pi\pi^*$	T ₁	3.2423	$\pi\pi^*$
	S ₂	4.9826	$n\pi^*$	T ₂	3.4447	$\pi\pi^*$
	S ₃	5.3341	$\pi\pi^*$	T ₃	4.2825	$\pi\pi^*$
	S ₄	6.0381	$n\pi^*$	T ₄	4.6167	$n\pi^*$
	S ₅	6.2335	$n\pi^*$	T ₅	5.1490	$n\pi^*$
Ethanol				ΔT_1	3.3334	
	S ₁	4.2914	$\pi\pi^*$	T ₁	3.2724	$\pi\pi^*$
	S ₂	5.0225	$n\pi^*$	T ₂	3.4700	$\pi\pi^*$
	S ₃	5.3222	$\pi\pi^*$	T ₃	4.2990	$\pi\pi^*$
	S ₄	5.9212	$n\pi^*$	T ₄	4.6685	$n\pi^*$
	S ₅	6.0698	$n\pi^*$	T ₅	5.1444	$n\pi^*$

Table S3 Calculated singlet and triplet excited state vertical energies from the optimised ground state geometry of the *keto* form of HMS in cyclohexane using TD-DFT at the PBE0/cc-pvtz level of theory.

Environment	Singlets			Triplets		
	State	Energy (eV)	Character	State	Energy (eV)	Character
Vacuum				ΔT_1	2.1752	
	S ₁	3.1149	$\pi\pi^*$	T ₁	1.9677	$\pi\pi^*$
	S ₂	3.8748	$n\pi^*$	T ₂	3.2909	$\pi\pi^*$
	S ₃	4.9279	$\pi\pi^*$	T ₃	3.6810	$n\pi^*$
	S ₄	5.5817	$\pi\pi^*$	T ₄	3.9888	$\pi\pi^*$
	S ₅	5.9169	$\sigma\pi^*$	T ₅	4.9728	$\pi\pi^*$
Acetonitrile				ΔT_1	2.1748	
	S ₁	3.1638	$\pi\pi^*$	T ₁	2.0821	$\pi\pi^*$
	S ₂	3.8806	$n\pi^*$	T ₂	3.2680	$\pi\pi^*$
	S ₃	4.9272	$\pi\pi^*$	T ₃	3.7012	$n\pi^*$
	S ₄	5.4921	$n\pi^*$	T ₄	3.9675	$\pi\pi^*$
	S ₅	5.5897	$\pi\pi^*$	T ₅	5.0146	$\pi\pi^*$
Cyclohexane				ΔT_1	2.1592	
	S ₁	3.1254	$\pi\pi^*$	T ₁	1.9980	$\pi\pi^*$
	S ₂	3.8506	$n\pi^*$	T ₂	3.2811	$\pi\pi^*$
	S ₃	4.9257	$\pi\pi^*$	T ₃	3.6629	$n\pi^*$
	S ₄	5.5521	$\pi\pi^*$	T ₄	3.9756	$\pi\pi^*$
	S ₅	5.8401	$n\pi^*$	T ₅	4.9805	$\pi\pi^*$
Ethanol				ΔT_1	2.2286	
	S ₁	3.2289	$\pi\pi^*$	T ₁	2.1780	$\pi\pi^*$
	S ₂	4.0426	$n\pi^*$	T ₂	3.2718	$\pi\pi^*$
	S ₃	4.9389	$\pi\pi^*$	T ₃	3.8665	$n\pi^*$
	S ₄	5.5077	$n\pi^*$	T ₄	3.9875	$\pi\pi^*$
	S ₅	5.6220	$\pi\pi^*$	T ₅	5.0896	$\pi\pi^*$

Table S4 Extracted transient electronic absorption spectroscopy time constants for HMS solutions upon photoexcitation at λ_{\max} , obtained via global fitting techniques using a sequential model.³ Whilst the error for τ_1 is given by half the instrument response in each solvent (Fig. S4), the errors presented for τ_2 to τ_4 are those provided by the fitting software package; the quality of the fits can be gauged from the corresponding residuals (Fig. S12) and kinetic fits (Fig. S13).

Time constant	Ethanol	Cyclohexane	Acetonitrile
τ_1 (fs)	55 ± 35	105 ± 30	80 ± 40
τ_2 (ps)	10.4 ± 0.4	14.2 ± 0.5	9.1 ± 0.4
τ_3 (ps)	199 ± 2	533 ± 6	176 ± 2
τ_4 (ns)	$> 2^*$	$> 2^*$	$> 2^*$

* Outside the temporal window of the instrument (2 ns).

Table S5 Extracted transient electronic absorption spectroscopy time constants for EHS solutions upon photoexcitation at λ_{\max} , obtained via global fitting techniques using a parallel model.³ Whilst the error for τ_1 is given by half the instrument response in each solvent (Fig. S4), the errors presented for τ_2 to τ_4 are those provided by the fitting software package; the quality of the fits can be gauged from the corresponding residuals (Fig. S12) and kinetic fits (Fig. S17).

Time constant	Ethanol	Cyclohexane	Acetonitrile
τ_1 (fs)	65 ± 35	50 ± 30	50 ± 40
τ_2 (ps)	8.8 ± 0.4	10.8 ± 0.3	9.3 ± 0.3
τ_3 (ps)	176 ± 2	412 ± 4	169 ± 2
τ_4 (ns)	$> 2^*$	$> 2^*$	$> 2^*$

* Outside the temporal window of the instrument (2 ns).

Table S6 Extracted transient electronic absorption spectroscopy time constants for EHS solutions upon photoexcitation at λ_{\max} , obtained via global fitting techniques using a sequential model.³ Whilst the error for τ_1 is given by half the instrument response in each solvent (Fig. S4), the errors presented for τ_2 to τ_4 are those provided by the fitting software package; the quality of the fits can be gauged from the corresponding kinetic fits (Fig. S17).

Time constant	Ethanol	Cyclohexane	Acetonitrile
τ_1 (fs)	60 ± 35	65 ± 30	50 ± 40
τ_2 (ps)	9.0 ± 0.3	10.9 ± 0.3	9.6 ± 0.4
τ_3 (ps)	176 ± 2	422 ± 4	170 ± 2
τ_4 (ns)	$> 2^*$	$> 2^*$	$> 2^*$

* Outside the temporal window of the instrument (2 ns).

References

- [1] J. L. Rodgers and W. A. Nicewander, *The American Statistician*, 1988, **42**, 59–66.
- [2] I. Walmsley, L. Waxer and C. Dorrer, *Review of Scientific Instruments*, 2001, **72**, 1–29.
- [3] J. Snellenburg, S. Laptinok, R. Seger, K. Mullen and I. Van Stokkum, *Journal of Statistical Software*, 2012, **49**, 1–22.
- [4] M. P. Grubb, A. J. Orr-Ewing and M. N. R. Ashfold, *Review of Scientific Instruments*, 2014, **85**, 064104.
- [5] C. Würth, M. Grabolle, J. Pauli, M. Spieles and U. Resch-Genger, *Nature Protocols*, 2013, **8**, 1535–1550.
- [6] B. Hudson and B. Kohler, *Annual Review of Physical Chemistry*, 1974, **25**, 437–460.
- [7] Y. Chiang, P. V. Demekhin, A. I. Kuleff, S. Scheit and L. S. Cederbaum, *Physical Review A*, 2010, **81**, 032511.
- [8] J. M. Woolley, M. Staniforth, M. D. Horbury, G. W. Richings, M. Wills and V. G. Stavros, *The Journal of Physical Chemistry Letters*, 2018, **9**, 3043–3048.
- [9] K. Sugiyama, T. Tsuchiya, A. Kikuchi and M. Yagi, *Photochemical & Photobiological Sciences*, 2015, **14**, 1651–1659.
- [10] R. J. Clarke and A. Oprysa, *Journal of Chemical Education*, 2004, **81**, 705.
- [11] F. Ling, D. Liu, S. Li, W. Li, B. Zhang and P. Wang, *The Journal of Chemical Physics*, 2019, **151**, 094302.

Chapter 3

Towards symmetry driven and nature inspired UV filter design

The image shows a screenshot of a Nature Communications article titled "Towards symmetry driven and nature inspired UV filter design" by Michael D. Horbury, Emily L. Holt, Louis M.M. Mouterde, Patrick Balaguer, Juan Cebrián, Laurent Blasco, Florent Allais, and Vasilios G. Stavros. A blue arrow points from the article to a photograph of a flamenco dancer in a red dress. Another blue arrow points from the photograph to a news article on the Warwick website. The Warwick news article is titled "'Flamenco dancing' molecule could lead to better protecting sunscreen" and lists several media outlets that have covered the story: the Daily Mirror, Daily Express, The Telegraph, and The Independent. Below these are three more news items with flags: a German article "Flamenco-tanzende Moleküle als Sonnenschutz für Ihre Haut", a Vietnamese article "Flamenco Dancing, phân tử xoắn xoắn 100 tỷ một giây – có thể dẫn đến kem chống nắng tốt hơn", and a Russian article "Молекула «танцующего фламенко» защитит от солнечных лучей".

nature COMMUNICATIONS

ARTICLE
<https://doi.org/10.1038/s41467-019-12719-2> OPEN

Towards symmetry driven and nature inspired UV filter design

Michael D. Horbury^{1,6*}, Emily L. Holt^{1,2}, Louis M.M. Mouterde³, Patrick Balaguer⁴, Juan Cebrián⁵, Laurent Blasco⁵, Florent Allais³ & Vasilios G. Stavros^{1*}

WARWICK
News & Events

Brexit | Press Releases | Expert Comment | Media Centre Services | Knowledge Centre | Team | Events | Social Media

'Flamenco dancing' molecule could lead to better protecting...

'Flamenco dancing' molecule could lead to better protecting sunscreen

DAILY Mirror **DAILY EXPRESS**

The Telegraph **INDEPENDENT**

'Flamenco dancing' molecule steps up sunscreen protection
By Sarah Knapton

Flamenco-tanzende Moleküle als Sonnenschutz für Ihre Haut

Flamenco Dancing, phân tử xoắn xoắn 100 tỷ một giây – có thể dẫn đến kem chống nắng tốt hơn

Молекула «танцующего фламенко» защитит от солнечных лучей

ARTICLE

<https://doi.org/10.1038/s41467-019-12719-z>

OPEN

Towards symmetry driven and nature inspired UV filter design

Michael D. Horbury^{1,6*}, Emily L. Holt^{1,2}, Louis M.M. Mouterde³, Patrick Balaguer⁴, Juan Cebrián⁵, Laurent Blasco⁵, Florent Allais³ & Vasilios G. Stavros^{1*}

In plants, sinapate esters offer crucial protection from the deleterious effects of ultraviolet radiation exposure. These esters are a promising foundation for designing UV filters, particularly for the UVA region (400 - 315 nm), where adequate photoprotection is currently lacking. Whilst sinapate esters are highly photostable due to a *cis-trans* (and *vice versa*) photoisomerization, the *cis*-isomer can display increased genotoxicity; an alarming concern for current cinnamate ester-based human sunscreens. To eliminate this potentiality, here we synthesize a sinapate ester with equivalent *cis*- and *trans*-isomers. We investigate its photostability through innovative ultrafast spectroscopy on a skin mimic, thus modelling the as close to true environment of sunscreen formulas. These studies are complemented by assessing endocrine disruption activity and antioxidant potential. We contest, from our results, that symmetrically functionalized sinapate esters may show exceptional promise as nature-inspired UV filters in next generation sunscreen formulations.

¹Department of Chemistry, University of Warwick, Gibbet Hill, Coventry CV4 7AL, UK. ²Molecular Analytical Science Centre for Doctoral Training, Senate House, University of Warwick, Coventry CV4 7AL, UK. ³URD Agro-Biotechnologies Industrielles (ABI), CEBB, AgroParisTech, 51110 Pomacle, France. ⁴IRCM, Inserm, Univ Montpellier, ICM, Montpellier, France. ⁵Lubrizol Advanced Materials, C/Isaac Peral 17-Pol. Industrial Cami Ral, 08850 Gava, Spain. ⁶Present address: School of Electronic and Electrical Engineering, University of Leeds, Leeds, LS2 9JT, UK. *email: m.d.horbury@leeds.ac.uk; v.stavros@warwick.ac.uk

Naturally occurring sinapate esters¹ have shown promise as starting points for a generation of ultraviolet (UV) filters that offer exemplary photoprotection. They exhibit high levels of photostability under UV exposure, due to an efficient *trans-cis* and *cis-trans* photoisomerization resulting in a photo-equilibrium between these isomers. More specifically, the photoisomerization is proposed to consist of three dynamical processes in the excited electronic state. After the initial absorption of UV radiation, the sinapate esters undergo a geometry relaxation. The geometry relaxation is then followed by evolution on the excited state potential energy surface followed by photoisomerization, which forms either the *cis*- or *trans*-isomer, mediated by a conical intersection between the excited and ground electronic states^{2–5}. During this relaxation, the excess electronic energy is converted into vibrational energy, leading to the isomers being formed vibrationally hot. This vibrational energy is eventually lost to the surrounding solvent bath^{6,7}. These processes are illustrated in Fig. 1 (along with their associated rate constants); starting from the *trans*-isomer of the ester ethyl sinapate (ES) as an example.

Not only do these sinapate esters display high UV photostability, they also demonstrate potent antioxidant capabilities⁸. However, they are not without their issues, which must be taken into consideration if to be included in any future sunscreen formulation: firstly, their absorption does not completely span the UVA region (400–315 nm), thus lacking optimum UVA photoprotection; secondly, their UVA λ_{\max} is close to the UVB (315–280 nm), of which there are already a plethora of effective UVB filters; thirdly, the two isomers have differing absorption profiles, with the *cis*-isomer having (in general) the weaker absorption^{4,5,9}; finally, the genotoxicity of the *cis*-isomer has been shown to be significantly higher in a related cinnamate¹⁰. One must also keep in mind that given the growing concern over several other EU and FDA approved UV filters flagged as human-toxic^{10,11} and eco-toxic^{12–14}, this inevitably adds further considerations before any sunscreens agent can be included in a sunscreen formulation.

A highly intuitive solution to the issues introduced by the *cis*- and *trans*-isomer conundrum is to add identical ester moieties across the acrylic double bond, leading to indistinguishable *trans*- and *cis*-isomers. Concurrently, this serves to increase π -system conjugation and thus red-shift the UVA λ_{\max} when compared to the exemplar sinapate ester ES. Indeed, ES has been previously

studied using femtosecond (fs) transient electronic (UV/visible) absorption spectroscopy (TEAS) by our group⁴. TEAS has proven to be a powerful tool for observing the photoisomerization of sinapate esters, particularly in identifying the formation of any photoproducts^{2–3,7,15}. However, while the addition of identical ester moieties across the double bond spectrally shifts (to lower energy) in the absorbance (a positive attribute towards UVA filter design), this alone does not indicate whether such an approach maintains the desired properties (*vide supra*) that may facilitate symmetry driven sinapate esters being promising UV filters.

To address this, we have synthesized diethyl 2-(4-hydroxy-3,5-dimethoxybenzylidene)malonate (diethyl sinapate), abbreviated DES hereon. Structures of both DES and its precursor ES are shown in Fig. 1. In this instance, we utilize a combination of TEAS and steady-state spectroscopy to investigate the photostability of DES. The combination of time-resolved and steady-state spectroscopies, enables one to link the ultrafast with the ultraslow dynamics, providing detailed insight into how photo-physical processes involved at the very early stages of the photon-molecule interaction, influence the longer-term photostability. TEAS measurements were taken of DES blended with a commercial sunscreen emollient, C12–15 alkyl-benzoate (AB) deposited on a synthetic skin mimic, VITRO-CORNEUM® (VC). The dynamical measurements taken using this innovative approach, makes the data accrued directly valid to real-world applications of sunscreen formulas, with potentially transformative repercussions to the cosmeceutical industry. We also make crucial advances in other aspects of the work through: (a) developing two greener synthetic procedures to produce DES; (b) performing endocrine disruption measurements of DES for the alpha oestrogen receptor (ER α) and the xenobiotic receptor (PXR); and (c) determining the antioxidant potential of DES using a 2,2-diphenyl-1-picrylhydrazyl (DPPH) assay. The spectroscopic advances along with (a)-(c) enable us to propose whether DES shows promise as a potential nature-inspired sunscreens agent.

Results

Synthesis of DES. DES can be readily obtained through the Knoevenagel-Doebner condensation of syringaldehyde and ethyl malonate. All the synthetic procedures that have been reported in the literature for such a condensation are not only quite

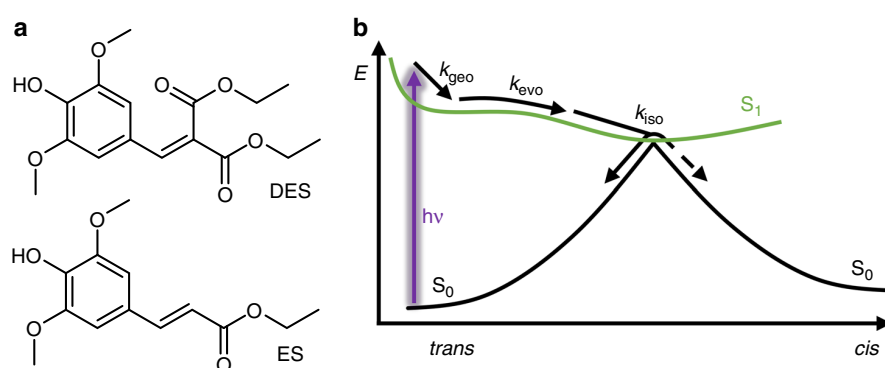


Fig. 1 Sinapate structures and photoisomerization scheme. **a** The geometric structures of diethyl sinapate (DES) and ethyl sinapate (ES), demonstrating the symmetrical functionalization of DES compared to its precursor ES. **b** Schematic illustrating the dynamical processes involved in the photoisomerization of ES. Following photoexcitation with a UV photon (represented by the purple arrow), to the first electronically excited (S_1) state, *trans*-ES undergoes three processes during its subsequent relaxation to the electronic ground (S_0) state (black curve). Each process is indicated by a labelled arrow: k_{geo} represents the rate of the geometry rearrangement; k_{evo} is the rate of evolution in the electronic excited state, such as vibrational cooling, along with solvent rearrangement; and k_{iso} is the rate for the photoisomerization. At the S_1/S_0 conical intersection, where the green and black curves meet, there are two possible pathways: relaxation to the S_0 state of the *trans*- or *cis*-ES species, represented by the solid black and dashed black arrows respectively

hazardous, as they use toxic reagents/solvents such as piperidine and benzene, but they also require energy consuming conventional heating. Here we use microwave-heating to reduce energy consumption and eliminate benzene, while reducing the reaction time from 7.5 h to 30 min. Although this procedure brought significant improvements, it still required piperidine; moreover, one could also question the relevancy of microwaves at the industrial scale. A proline-mediated Knoevenagel-Doebner condensation in ethanol¹⁶ under conventional heating, recently developed in our group, was successfully implemented to the synthesis of DES at the multigram scale allowing for full replacement of piperidine. Finally, whatever the synthetic procedure used (i.e. microwave-assisted or proline-mediated condensation), we also succeeded in replacing column chromatography purification by a simple precipitation. Ultimately, this leads to a more sustainable and environmentally friendly synthetic route of DES.

Transient absorption spectroscopy. The transient absorption spectra (TAS) of DES in AB (10 mM) after being applied to the surface of VC (termed DES VC/AB hereon) and allowed to absorb into the substrate, are shown as a false colour map in Fig. 2a. TAS of DES in AB (1 mM) are also shown in Supplementary Fig. 1 for comparison. We note the difference in initial DES concentration. This is due to the dilution of the sample as it absorbs into VC, meaning we are unable to accurately determine the concentration of DES on VC. That being said, due to the signal strength in the TAS (in comparison to the TAS for DES in AB), we modestly estimate ~ 1.5 mM. Additional TAS were collected of DES in ethanol and cyclohexane (see Supplementary Figs. 2 and 3) to provide a range of solvent environments as comparisons. A saturated solution (<1 mM) of DES in cyclohexane was used, while in ethanol a concentration of 1 mM was used. All samples were photoexcited at their UVA λ_{max} : VC/AB = 335 nm; AB = 335 nm; ethanol = 336 nm; and cyclohexane = 325 nm (see Supplementary Fig. 4 for UV/visible spectra).

After initial excitation, likely due to an optically bright $^1\pi\pi^*$ state, akin to what has been seen in ES⁴, the TAS of DES VC/AB consists of a single excited state absorption which rapidly decays within a pump-probe time-delay (Δt) of <100 fs (not apparent in Fig. 2, see Supplementary Fig. 5) as the excited population on the

$^1\pi\pi^*$ state evolves from the Franck-Condon region. This has been previously assigned to geometry relaxation (intramolecular vibrational redistribution)^{17,18}, labelled k_{geo} in Fig. 1, and we conjecture a similar mechanism is in operation here. The geometry relaxation reveals three distinct spectral features that consist of: (i) a ground state bleach (~ 350 nm) corresponding to where the DES electronic ground state absorbs; (ii) a strong excited state absorption (~ 380 nm); and (iii) a second weaker excited state absorption (~ 540 nm). (i)–(iii) are in accordance with what has been observed from $^1\pi\pi^*$ state-driven dynamics for ES⁴, indicating that the additional CO₂Et has little influence in the spectroscopic signatures of DES relative to ES; we return to discuss this further in the post narrative.

As the TAS evolve in time, the excited state absorption at ~ 540 nm has decayed to zero ΔOD , (where ΔOD denotes change in optical density) by $\Delta t = \sim 4$ ps. The decay of the excited state absorption (both features) is attributed to, in part, repopulation of the electronic ground state from the $^1\pi\pi^*$ state. This is likely mediated by a photoisomerization pathway, labelled k_{iso} in Fig. 1⁴. However, a remnant of the excited state absorption at ~ 380 nm and the ground state bleach feature remain. In previous spectroscopy-driven studies on sinapates, this has been attributed to the formation of the isomer photoproduct, or due to a phenoxy radical species due to an instantaneous two-photon ionization^{2,4,6,7,19,20}. However, in DES the *cis*- and *trans*-isomer are identical (ruling out the isomer photoproduct) and both the absorption at 380 nm and the ground state bleach decay over time. The decay of these features rules out the formation of the radical as it would be expected to persist beyond the maximum Δt ^{2,4,6,7,19,20}. This alludes to additional transient species being involved in the relaxation of DES, not seen in ES or any related sinapate or cinnamate in the condensed phase^{2,4,5,7,15,19}. Whilst, it appears that these features decay completely back to the baseline, closer examination of the TAS at $\Delta t = 2$ ns, shown in Fig. 2c, shows that a very small amount of the ground state bleach is still present, which is not attributed to the solvent; see Supplementary Fig. 7 for solvent-only TAS. We add that we do not see evidence of vibrational cooling of the electronic ground state, as previously seen for ES⁴. This is due to the presence of the absorption feature at 380 nm masking the spectral signature

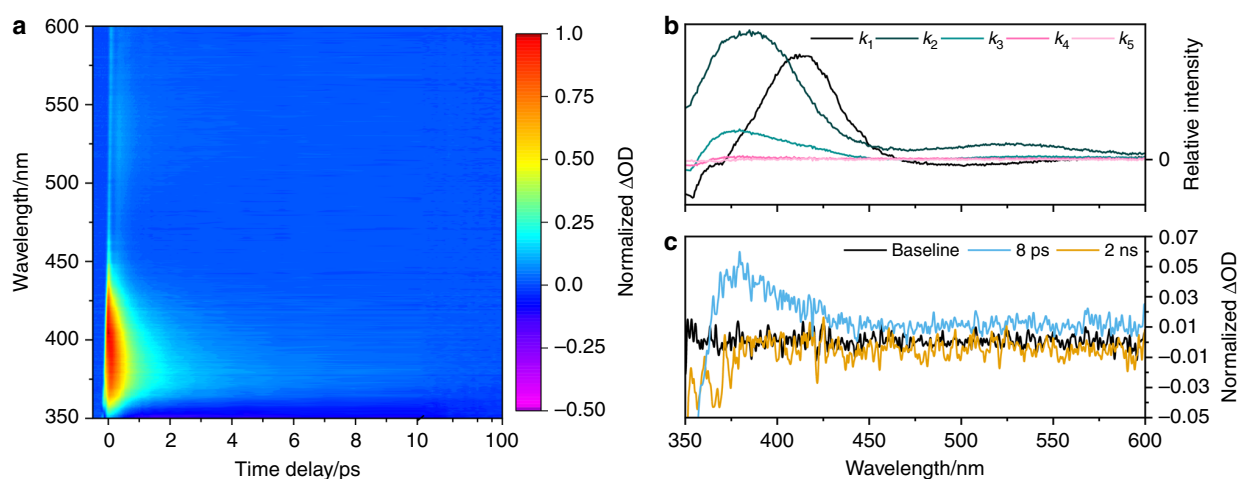


Fig. 2 Ultrafast spectroscopy results for DES. **a** Transient absorption spectrum (TAS) of DES in C12–15 alkyl benzoate deposited on a synthetic skin mimic, VITRO-CORNEUM® (VC/AB) photoexcited at 335 nm, shown as a false colour map, with the intensity scale representing a change in normalized optical density (ΔOD). The time-delay is plotted linearly from -0.5 to 10 ps then as a log scale from 10 to 100 ps. **b** Evolution associated difference spectra (EADS) from the sequential global fit of the TAS of DES in VC/AB photoexcited at 335 nm. Zoomed-in plots showing only k_4 and k_5 for this system can be found in Supplementary Fig. 6a). **c** Selected TAS at specific Δt highlighting the absorption at 380 nm (8 ps, green) and incomplete ground state bleach recovery (2 ns, orange)

associated with vibrational cooling. The absence of vibrational cooling has been seen in several other sinapates and cinnamates^{2,3,21}.

To recover the kinetic parameters from the TAS presented (see Fig. 2a and Supplementary Figs. 1–3), we carried out a sequential ($A \xrightarrow{k_1} B \dots \xrightarrow{k_n} n$) global fit, across the entire spectral region of our probe, using the software package Glotaran^{22,23}. The rate-constants (k_i) for DES in VC/AB returned from the sequential global fit are shown in Table 1 (the corresponding rate-constants for DES in other solvents are shown in Supplementary Table 1), while the evolution associated difference spectra (EADS) are shown in Fig. 2b and Supplementary Figs. 1–3. Additional zoomed-in plots of EADS associated with k_4 and k_5 are also shown in Supplementary Fig. 6. We also add that solvent only time-zero responses (representing our instrument response) are shown in Supplementary Fig. 8 and the residuals to all fits are shown in Supplementary Fig. 9. Furthermore, the EADS of k_4 and k_5 are overlaid with the corresponding TAS at a comparable time delay; these are shown in Supplementary Fig. 10. Finally, we note that a more concentrated solution of DES in ethanol (10 mM, the highest possible within our experimental constraints) was tested for evidence of aggregation. There was no evidence (by comparison with the 1 mM counterpart) to suggest that DES aggregates were formed. Further studies would be warranted at higher concentrations, but this is beyond the scope of current experimental capabilities.

Steady-state spectroscopy. To complement the time-resolved measurements, steady-state irradiation measurements were carried out, to determine the long-term photostability of DES.

Table 1 Summary of rate constants

	k_1/s^{-1} ($\times 10^{12}$)	k_2/s^{-1} ($\times 10^{12}$)	k_3/s^{-1} ($\times 10^{11}$)	k_4/s^{-1} ($\times 10^{10}$)	k_5/s^{-1} ($\times 10^8$)
VC/AB	7 ± 2	3.0 ± 0.3	4.24 ± 0.07	1.02 ± 0.06	$\ll 5$

Rate-constants (k_i) resulting from the sequential global fit of the TAS of DES in VC/AB shown in Fig. 2a. The errors are quoted to 2σ . Rate-constants for DES in AB, ethanol and cyclohexane can be found in Supplementary Table 1

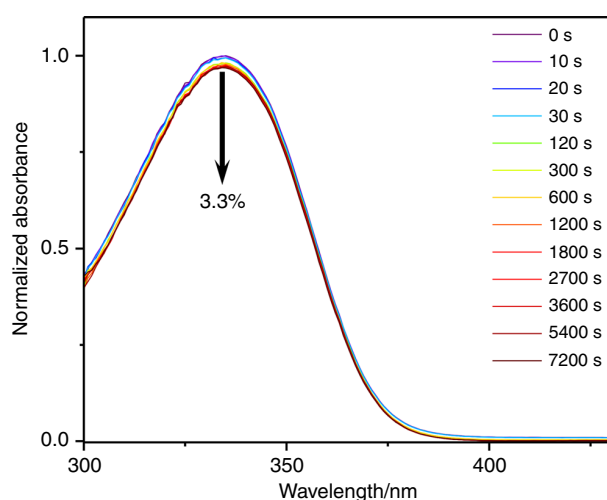


Fig. 3 Long-term photostability of DES. UV/visible spectra of DES in C12-15 alkyl benzoate (AB), at varying durations of irradiation at 335 nm and replicating solar intensity. The downwards arrow (in black) denotes the observed 3.3% decrease in absorbance after 7200 s of irradiation

UV/visible spectra were taken at various time-intervals during the irradiation of the sample at its UVA λ_{\max} at solar intensity (0.2 mW cm^{-2}). The resulting UV/visible spectra of DES in AB are shown in Fig. 3. It is clear from these spectra that over a period of two hours, DES only experiences a minor reduction in its absorbance, 3.3%, while for the UVA λ_{\max} of ethanol and cyclohexane a drop of 3.1% and 1.6%, respectively, was observed (see Supplementary Fig. 11 for additional spectra). Hampered by scattering issues within the spectrometer, we were unable to perform these measurements for DES in VC/AB. For comparison, *trans*-ES in cyclohexane experiences a 16% loss in absorbance over a period of 45 min, a consequence of establishing a photo-equilibrium between the two (*trans* and *cis*) structural isomers⁴.

In addition to the photostability measurements of DES, we have also calculated the critical wavelength of DES from its UV/visible spectrum in ethanol, see Supplementary Methods for additional methodological information. Critical wavelength is the industrial standard for determining if there is sufficient UVA

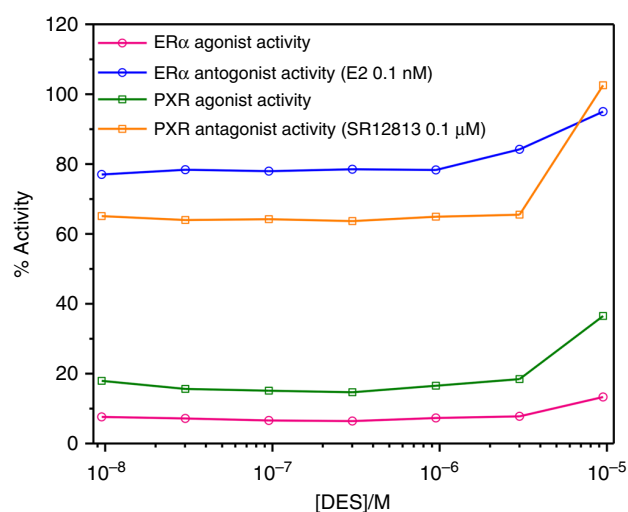


Fig. 4 Endocrine disruption assay results. Endocrine disruption activity of DES, as determined by assays on several cell lines, for the alpha oestrogen receptor ER α (circle) as either an agonist (magenta) or antagonist (blue), and for the xenobiotic receptor PXR (square) as either an agonist (green) or antagonist (orange). The activity of ER α is regulated by the steroid and oestrogen sex hormone 17 β -estradiol (E2). A known agonist for PXR is SR 12813

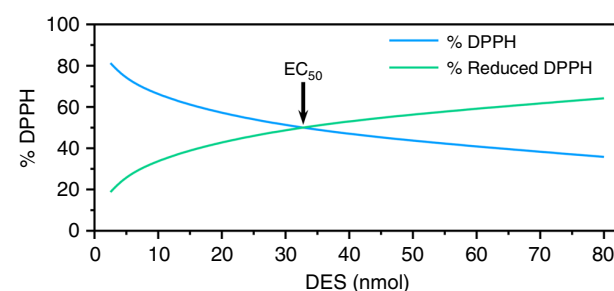


Fig. 5 Determination of the antiradical activity of DES. The determination of the antiradical activity of DES has been determined via 2,2-diphenyl-1-picrylhydrazyl (DPPH) assay. These tests involve adding DES solution in ethanol at different concentration to homogeneous DPPH solution. The EC₅₀, i.e. the amount of DES needed to reduce the initial number of DPPH free radicals by half, is provided by the crossing point of % DPPH (blue) and % reduced DPPH (green), which occurs at 32.7 nmol

Table 2 Antioxidant potentials

	Irganox 1010	Trolox	BHT	BHA	ES	DES
EC ₅₀ (nmol)	6.9	4.0	7.1	3.7	13.7	32.7
[antioxidant]/[DPPH]	0.18	0.11	0.19	0.10	0.36	0.86

EC₅₀ (nmol) and [antioxidant]/[DPPH] values for DES, ES and several commercially available antioxidants

protection. The value we retrieved was 364 nm (see Supplementary Fig. 12).

Endocrine disruption potential of DES. Endocrine disruption activity of DES was assayed on two types of receptors, see Supplementary Methods for details. The first receptor selected was the ER α receptor, which is a member of the nuclear hormone receptors family, whose activity is regulated by the steroid and oestrogen sex hormone 17 β -estradiol (E2). The second receptor is the PXR receptor, a member of the steroid and xenobiotic sensing nuclear receptors family, with a known agonist being SR 12813. Endocrine disruption assays, shown in Fig. 4, demonstrate that DES is neither an agonist nor antagonist ligand for either ER α or PXR.

Antioxidant potential of DES. While the photostability of sinapates is a major interest for use as UV filters, their potent antioxidant capabilities are an added benefit. Therefore, to determine if DES also exhibits antioxidant potential, a DPPH assay was carried out. This method determines the H-donor capacity of the antioxidant to quench the stable DPPH free radical, as previously reported⁸. In this study, the EC₅₀ value corresponds to the amount of antioxidant needed to reduce half of the initial population of DPPH radicals. The lower the EC₅₀ value, the higher the antioxidant potential. DES's EC₅₀ value was determined as being 32.7 nmol, as highlighted in Fig. 5. For ease of comparison with other studies, we have converted this value to a ratio, quoted as [antioxidant]/[DPPH]; this gives a value of 0.86 for DES. In addition, we have included DPPH assays on several commercially available antioxidants, presented in Table 2.

Discussion

The spectroscopic measurements, both time-resolved and steady-state, have demonstrated that the addition of the second ester moiety has not impeded the high UV photostability that the sinapate backbone possesses⁴. Indeed this has had the opposite effect, highlighted by the minimal drop ($\leq 3.3\%$) in the absorbance of DES after 2 h of UV irradiation at solar intensities, see Fig. 3. Alongside this increase in photostability, the critical wavelength of DES has significantly red-shifted compared to ES, cf. 364 nm for DES compared to 352 nm for ES. While this falls slightly short of current UVA filters, i.e. avobenzene is 378 nm, it is clearly a step in the right direction (see Supplementary Fig. 12 for details). We shall now focus on the photochemistry responsible for the apparent DES photostability.

To recover the photodynamics observed in the TAS, we performed a sequential global fit across the entire spectral window of our probe. This resulted in four dynamical processes, described by rate constants $k_{1,2,3,4}$, being recovered; we note that k_5 is used to describe the long-lived ground state bleach, which does not recover within the time-window of our experiment (except for the cyclohexane data, in which all spectral features return to baseline). We recognized that there are multiple sources we can attribute this incomplete ground state bleach recovery including a potential molecular photoproduct, or a trapped excited state population such as a triplet state (note an absorption feature and

no ground state bleach is observed for DES in ethanol, see Supplementary Fig. 2). Triplet states have been seen previously for sinapate and cinnamate esters in the gas-phase, with their population being mediated by an $n\pi^*$ state^{7,24,25}. These could be a potential source of the small depletion in our steady-state irradiation studies (see Fig. 3 and Supplementary Fig. 11), qualitatively in line with the (very) minor contribution of EADS for k_5 (see Fig. 2b and Supplementary Fig. 6). From inspection of the EADS linked to $k_{1,2,3}$ (except for DES in cyclohexane where k_2 is absent) these appear to have similar features to EADS seen in related sinapate esters in polar solvents^{3,4}. Therefore, we believe that the EADS for DES describe similar dynamical processes, whereby: k_1 represents a prompt geometry relaxation out of the Franck-Condon region; k_2 describes further evolution along the excited state, including vibrational cooling and solvent rearrangement; and k_3 is the rate-constant for photoisomerization, repopulating the electronic ground state. Under this description $k_1 = k_{\text{geo}}$, $k_2 = k_{\text{evo}}$ and $k_3 = k_{\text{iso}}$ (see Fig. 1). Importantly, we note that due to the symmetrical nature of DES, it is not possible to determine if the photoisomerization occurs completely or is an aborted photoisomerization²⁶.

Interestingly however, additional spectral and dynamical (through the returned k_4) features are observed in the TEAS measurements of DES when compared to related sinapate esters (e.g. ES) and cinnamates^{2,4,5,7,15,19}. These features pertain to the ground state bleach and an excited state absorption at 380 nm. We believe that these features are likely due to an electronic excited state, the front-runner being most likely a $^1n\pi^*$ state, previously implicated to play a role in the photodynamics of cinnamates^{24,25,27,28}. The decay of the absorption at 380 nm corresponds to an almost complete recovery of the ground state bleach. Importantly, whether this additional decay pathway happens following bifurcation of the excited state population or subsequent to photoisomerization is unknown.

While the overall picture of DES photochemistry, mainly the photoisomerization (or aborted photoisomerization) is similar in all solvents and constitutes the main finding (from a dynamics viewpoint) of the present work, differences in these dynamics, reflected in the associated rate-constants (see Table 1 and Supplementary Table 1), do exist and warrant discussion. We also choose to focus our discussion on the differences between DES in VC/AB compared to DES in various solvent environments and, where appropriate, the insights we draw into the intrinsic properties of photoexcited DES when mounted on a skin mimic.

First, comparing DES in VC/AB and DES in AB, the major difference is the almost three-fold increase in k_4 for DES in AB compared to DES in VC/AB. The reason for this could rest in population trapped in this excited state, experiencing a greater barrier towards ground state recovery for DES in VC/AB. Second, comparing DES in VC/AB with DES in cyclohexane, the six-fold increase in k_4 for DES in cyclohexane may also be reconciled by relative barrier heights. Interestingly for DES in cyclohexane, there is complete ground state bleach recovery. Understandably, a decreased residence time in this state for DES in cyclohexane could also explain the apparent ground state bleach recovery, given there is less opportunity for competing pathways. The (positive) knock-on effects of this could (tentatively)

explain our steady-state irradiation data of DES in cyclohexane, which show the smallest amount of depletion following prolonged irradiation.

Like DES in cyclohexane, the TAS at 2 ns for DES in ethanol has no apparent ground state bleach, however the presence of a new absorption feature at ~350 nm is likely the cause for the absence of the ground state bleach. This peak appears to grow in as the absorption at 380 nm and the ground state bleach recover. We believe that this feature is due to the presence of the phenoxyl radical generated via an instantaneous two-photon ionization, as seen in numerous previous studies in related cinnamates and sinapates^{2,20,21}. However, this absorption feature in the TAS is very small, and hence we are unable to confirm its two-photon (pump) dependency through TAS. We add here that the presence of the phenoxyl radical in the present measurements is an artefact of the ultrafast spectroscopic measurements; its two-photon dependence makes it highly unlikely to occur in nature. Unfortunately, the presence of this peak has also hindered our ability to accurately fit the TAS using the sequential global fitting model, thus we were only able to accurately extract k_1 , k_2 and k_3 , as the fit significantly overestimates k_4 for the decay of the absorption at 380 nm and ground state bleach recovery.

Ultimately, while this additional decay pathway is present, it does not appear to impact the long-term photostability of DES. Characterisation of this additional state and how it is populated will inevitably benefit from high level theoretical and (complementary) experimental work, the latter utilizing different probe techniques, to elucidate how the excited state population evolves in DES. This, however, is beyond the scope of the current work.

Aside from the photostability of DES, another consideration in its candidacy as a next generation sunscreen is whether or not it acts an endocrine disruptor, a topic which continues to draw controversies for current UV sunscreens^{11–13}. Due to these controversies and the general concern over endocrine disrupting chemicals²⁹, it is becoming a significant factor in the design of sunscreen agents. The endocrine disruption measurements of DES showed no adverse effects to the ER α or PXR receptors.

Likewise, potent antioxidant potential is an additional benefit in sunscreen design. Whilst the DPPH assays demonstrate that DES can act as an antioxidant, its activity (0.86) is lower than both ES (0.36)⁸, as well as antioxidants already used in commercial sunscreen formulas BHT (0.19), BHA (0.10) and α -tocopherol (0.21)³⁰. These antioxidants are only included in sunscreening formulas in small quantities compared to UV filters. Therefore, while the antioxidant potential of DES is lower, its concentration will be significantly greater, thus alleviating its low antioxidant activity. We have also included Irganox 1010 (0.18) and Trolox (0.11), which are used in the polymer and pharmaceutical industry respectively.

Amidst growing concerns of increasing exposure of society to solar radiation, the results presented herein demonstrate the promising potential of a symmetry driven and nature-inspired sunscreen for commercial use in sunscreen formulations; particularly given the improved environmentally friendly synthetic route. The symmetric functionalisation across the acrylic double bond ensures that the *cis*- and *trans*-isomers are equivalent, negating concerns over genotoxicity of isomeric photoproducts. Concurrently, the absorption has been spectrally shifted into the UVA region, where there is a growing need for UV filters. Moreover, the overall photodynamics measured for DES in an emollient used in commercial sunscreen formulas are consistent when deposited on a synthetic skin mimic. It thus demonstrates that whilst the dynamics are mildly dependent on DES environment, it highlights the need of 'as close to a true environment' real-world setting for these measurements.

Our studies may thus provide a blueprint for tuning molecular functionality, ultimately aiding additional beneficial properties such as enhanced antioxidant potential by modifying the ester group, which has little impact on the photodynamics (cf. ES versus DES)^{2–4,7}. It is worth noting that the ester groups may not necessarily need to be symmetrical per se. Asymmetrical substitution, provided the intrinsic properties of the *cis*- and *trans*-isomers are commensurate, i.e. photophysical and photochemical properties, antioxidant capacity and endocrine disruption activity, could be promising sources of additional UV filters. However, such an asymmetric substitution may require more sophisticated (i.e. expensive) synthetic procedures, as well as additional considerations when testing for suitability. Our demonstration of customized photoprotection has also much broader ramifications; not only can it be applied to materials for human photoprotection, but also towards developing materials for plastics and resins, given their exposure to UV radiation. Finally, DES displays no endocrine disruption activity, which is a significant requirement in next generation UV filters given ever-growing concerns over current filters on both human health and aquatic life^{11–14}.

Methods

Spectroscopy. The TEAS setup used to observe the photochemistry of DES has been previously characterized by Greenough et al.^{31,32}, and is reproduced in detail here. Fundamental femtosecond laser pulses (3 W, 1 kHz repetition rate) with a central wavelength of 800 nm were derived from a Ti:Sapphire regenerative amplifier (Spitfire XP, Spectra-Physics), seeded by a Ti:Sapphire oscillator (Tsunami, Spectra-Physics). This fundamental pulse train was split into three 1 W beams, two of which were utilized for our TEAS experiments. The first 1 W beam was used to generate pump pulses with a fluence of 200–800 $\mu\text{J cm}^{-2}$ using an optical parametric amplifier (TOPAS-C, Spectra-Physics). The second 1 W beam was split further into two portions: (i) 950 mW and (ii) 50 mW. Beam (i) can be used for harmonic generation, however this capability was not implemented here. The probe pulses were a broadband white light supercontinuum generated by focussing (ii) in a vertically translated CaF₂ window, providing a probe spectral window of 345–735 nm. The pump-probe time delay (Δt) was varied by adjusting the optical delay of the probe pulse, the maximum obtainable Δt was 2 ns. The probe beam is collected after passing through the sample, by a pair of 2" diameter, UV-enhanced aluminium, off-axis-parabolic mirrors with a focal length of 100 mm; these mirrors were incorporated into the setup to compensate for the additional scatter induced by VC. The beam then passes through a CaF₂ lens to collimate the probe, before being focussed into a fibre coupled spectrometer (Avantes, AvaSpec-ULS1650F) by a second CaF₂ lens. Changes in the optical density (ΔOD) of the samples were calculated from transmitted probe intensities. Samples of DES were made to a concentration of 1 mM in C12–15 alkyl benzoate (Lubrizol), ethanol (absolute, VWR) and cyclohexane (99.99%, VWR). It should be noted that we attained a saturated cyclohexane solution. For DES on VITRO-CORNEUM® (IMS Inc., VC) a DES sample at a concentration of 10 mM in C12–15 alkyl benzoate was applied to VITRO-CORNEUM®. A higher concentration (10 mM) of DES in ethanol was used to test for evidence of aggregation. The sample delivery system was a flow-through cell (Demountable Liquid Cell by Harrick Scientific Products Inc.) consisting of two CaF₂ windows; the windows were spaced 100 μm apart. The sample was circulated using a diaphragm pump (SIMDOS, KNF) and replenished from a 25 mL reservoir to provide each pulse-pair with fresh sample. For VC/AB the sample thickness was measured to be 120 μm and was mounted on the front of a CaF₂ window.

Steady-state UV/visible absorption spectra of DES in AB, ethanol and cyclohexane, were using a UV/visible spectrometer (Cary 60, Agilent Technologies). The samples, of concentration ~25 μM , were irradiated with an arc lamp (Fluorolog 3, Horiba) for 2 h, with the UV/visible spectra taken at various time points, at the corresponding TEAS excitation wavelength, using an 8 nm bandwidth of the irradiation source. The fluence was set to 100–200 $\mu\text{J cm}^{-2}$ to mimic solar incidence conditions.

Synthesis of DES. DES was synthesized in one step using either a microwave-assisted or a proline-mediated Knoevenagel condensation between lignin-derived syringaldehyde and diethyl malonate (Fig. 6)³³.

In the first synthetic procedure, syringaldehyde (4 mmol, 728 mg) and diethyl malonate (13 mmol, 2 mL) were mixed together. Piperidine (2 mmol, 200 μL) was then added to the reaction mixture, the tube sealed and placed into a Monowave 400 microwave system. Constant power (50 W) was applied until reaching a temperature of 100 °C which was then maintained for 30 additional minutes.

The reaction mixture was purified by either, Purification 1: flash chromatography (cyclohexane/ethyl acetate 8/2). Fraction containing the wanted product was evaporated under vacuum to give pure DES (1.1 g, 85%); or

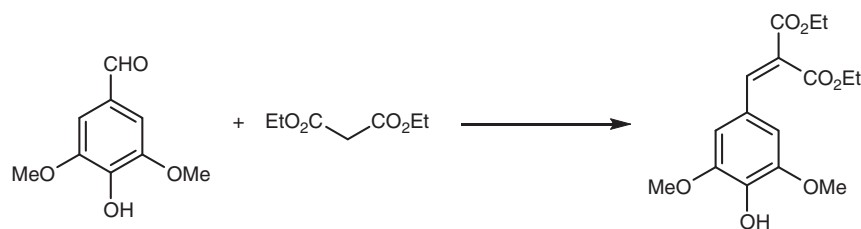


Fig. 6 Preparation of DES. DES synthesized through Knoevenagel condensation of syringaldehyde and diethyl malonate

Purification 2: The reaction mixture was cooled down to room temperature and added dropwise to a 1 N HCl aqueous solution (50 mL) at 0 °C. The resulting precipitate was recovered by filtration and washed with cold water resulting in pure DES (1.05 g, 80%).

In the second synthetic procedure, syringaldehyde (4 mmol, 728 mg) and diethyl malonate (13 mmol, 2 mL) were mixed together in ethanol (0.5 M, 8 mL). Proline (2 mmol, 235 mg) was then added and the reaction mixture was refluxed overnight. The reaction mixture was cooled down to room temperature and added dropwise to a 1 N HCl aqueous solution (50 mL) at 0 °C. The resulting precipitate was recovered by filtration and washed with cold water to afford pure DES (1.04 g, 80%).

Antioxidant measurements. 190 μ L of homogeneous DPPH solution (200 μ M) in ethanol was added to a well containing 10 μ L of the potential antiradical molecule solution in ethanol at different concentrations (from 400 μ M to 12.5 μ M). The reaction was monitored by a microplate Multiskan FC, performing 1 scan every 5 min for 7.5 h at 515 nm. The use of different amounts of DES give the EC₅₀ value, which is described as the efficient concentration needed to reduce the initial population of DPPH by half.

This procedure has been applied to commercially available antioxidants to provide benchmark values: Irganox1010 antioxidant used in polymers, Trolox antioxidant used in the pharmaceutical industry, BHT and BHA antioxidants are used in the cosmetic and food/feed industries.

Data availability

The TEAS (Fig. 2, Supplementary Figs. 1–3) and corresponding fitting residuals (Supplementary Fig. 9), UV/visible absorption spectroscopy (Fig. 3, Supplementary Figs. 4, 11, 12), DPPH assay (Fig. 4) and endocrine disruption data (Fig. 5), is freely available in the Zenodo data repository with the identifier <https://doi.org/10.5281/zenodo.327515>.

Received: 2 April 2019; Accepted: 26 September 2019;

Published online: 18 October 2019

References

- Dixon, R. A. et al. The phenylpropanoid pathway and plant defence—a genomics perspective. *Mol. Plant Pathol.* **3**, 371–390 (2002).
- Baker, L. A. et al. Ultrafast photoprotecting sunscreens in natural plants. *J. Phys. Chem. Lett.* **7**, 56–61 (2016).
- Horbury, M., Quan, W.-D., Flourat, A., Allais, F. & Stavros, V. Elucidating nuclear motions in a plant sunscreen during photoisomerization through solvent viscosity effects. *Phys. Chem. Chem. Phys.* **19**, 21127–21131 (2017).
- Horbury, M., Flourat, A. L., Greenough, S. E., Allais, F. & Stavros, V. Investigating isomer specific photoprotection in a model plant sunscreen. *Chem. Commun.* **54**, 936–939 (2018).
- Luo, J. et al. Ultrafast barrierless photoisomerization and strong ultraviolet absorption of photoproducts in plant sunscreens. *J. Phys. Chem. Lett.* **8**, 1025–1030 (2017).
- Horbury, M. D., Baker, L. A., Rodrigues, N. D., Quan, W.-D. & Stavros, V. G. Photoisomerization of ethyl ferulate: a solution phase transient absorption study. *Chem. Phys. Lett.* **673**, 62–67 (2017).
- Baker, L. A., Staniforth, M., Flourat, A., Allais, F. & Stavros, V. G. Gas-solution phase transient absorption study of the plant sunscreen derivative methyl sinapate. *ChemPhotoChem* **2**, 743–748 (2018).
- Reano, A. F. et al. Structure–activity relationships and structural design optimization of a series of p-hydroxycinnamic acids-based bis- and trisphenols as novel sustainable antiradical/antioxidant additives. *ACS Sustain. Chem. Eng.* **3**, 3486–3496 (2015).
- Challice, J. S. & Williams, A. H. Paper chromatographic separation and behavior of the cis- and trans-isomers of cinnamic acid derivatives. *J. Chromatogr. A* **21**, 357–362 (1966).
- Sharma, A. et al. Different DNA damage response of cis and trans isomers of commonly used UV filter after the exposure on adult human liver stem cells and human lymphoblastoid cells. *Sci. Total Environ.* **593**, 18–26 (2017).
- Krause, M. et al. Sunscreens: are they beneficial for health? An overview of endocrine disrupting properties of UV-filters. *Int. J. Androl.* **35**, 424–436 (2012).
- Burnett, M. E. & Wang, S. Q. Current sunscreen controversies: a critical review. *Photodermatol. Photoimmunol. Photomed.* **27**, 58–67 (2011).
- Loden, M. et al. Sunscreen use: controversies, challenges and regulatory aspects. *Br. J. Dermatol.* **165**, 255–262 (2011).
- Skotarczak, K. et al. Photoprotection: facts and controversies. *Eur. Rev. Med. Pharmacol. Sci.* **19**, 98–112 (2015).
- Vengris, M. et al. Ultrafast dynamics of isolated model photoactive yellow protein chromophores: “Chemical Perturbation Theory” in the laboratory. *J. Phys. Chem. B* **109**, 4197–4208 (2005).
- Peyrot, C., Peru, A. A. M., Mouterde, L. M. M. & Allais, F. Proline-mediated Knoevenagel–Doebner condensation in ethanol: a sustainable access to p-hydroxycinnamic acids. *ACS Sustainable Chem. Eng.* **7**, 9422–9427 (2019).
- Espagne, A., Paik, D. H., Changenet-Barret, P., Martin, M. M. & Zewail, A. H. Ultrafast photoisomerization of photoactive yellow protein chromophore analogues in solution: influence of the protonation state. *ChemPhysChem* **7**, 1717–1726 (2006).
- Kuramochi, H., Takeuchi, S. & Tahara, T. Ultrafast structural evolution of photoactive yellow protein chromophore revealed by ultraviolet resonance femtosecond stimulated Raman spectroscopy. *J. Phys. Chem. Lett.* **3**, 2025–2029 (2012).
- Peperstraete, Y. et al. Bottom-up excited state dynamics of two cinnamate-based sunscreen filter molecules. *Phys. Chem. Chem. Phys.* **18**, 28140–28149 (2016).
- Larsen, D. S. et al. Incoherent manipulation of the photoactive yellow protein photocycle with dispersed pump-dump-probe spectroscopy. *Biophys. J.* **87**, 1858–1872 (2004).
- Horbury, M. D., Baker, L., Quan, W., Greenough, S. E. & Stavros, V. Photodynamics of potent antioxidants: ferulic and caffeic acids. *Phys. Chem. Chem. Phys.* **18**, 17691–17697 (2016).
- Snellenburg, J. J., Laptinok, S. P., Seger, R., Mullen, K. M. & Van Stokkum, I. H. M. Glotaran: A Java-based graphical user interface for the R package TIMP. *J. Stat. Softw.* **49**, 1–22 (2012).
- Mullen, K. M. & Van Stokkum, I. H. M. TIMP: an R package for modeling multi-way spectroscopic measurements. *J. Stat. Softw.* **18**, 1–46 (2007).
- Rodrigues, N. D. N. et al. Towards elucidating the photochemistry of the sunscreen filter ethyl ferulate using time-resolved gas-phase spectroscopy. *Farad. Discuss.* **194**, 709–729 (2016).
- Kinoshita, S.-n. et al. Direct observation of the doorway ¹nπ* state of methylcinnamate and hydrogen-bonding effects on the photochemistry of cinnamate-based sunscreens. *Phys. Chem. Chem. Phys.* **21**, 19755–19763 (2019).
- Sampedro Ruiz, D., Cembran, A., Garavelli, M., Olivucci, M. & Fuß, W. Structure of the conical intersections driving the cis–trans photoisomerization of conjugated molecules. *Photochem. Photobiol.* **76**, 622–633 (2002).
- Karsili, T. N. V., Marchetti, B., Ashfold, M. N. R. & Domcke, W. *Ab Initio* study of potential ultrafast internal conversion routes in oxybenzone, caffeic acid and ferulic acid: implications for sunscreens. *J. Phys. Chem. A* **118**, 11999–12010 (2014).
- Molina, V. & Merchán, M. On the absorbance changes in the photocycle of the photoactive yellow protein: a quantum-chemical analysis. *Proc. Natl Acad. Sci.* **98**, 4299–4304 (2001).
- Colborn, T., Vom Saal, F. S. & Soto, A. M. Developmental effects of endocrine-disrupting chemicals in wildlife and humans. *Environ. Health Perspect.* **101**, 378–384 (1993).
- Mishra, K., Ojha, H. & Chaudhury, N. K. Estimation of antiradical properties of antioxidants using DPPH assay: a critical review and results. *Food Chem.* **130**, 1036–1043 (2012).

31. Greenough, S. E. et al. Solvent induced conformer specific photochemistry of guaiacol. *Phys. Chem. Chem. Phys.* **16**, 16187–16195 (2014).
32. Greenough, S. E. et al. Ultrafast photo-induced ligand solvolysis of cis-[Ru(bipyridine)₂(nicotinamide)₂]²⁺: experimental and theoretical insight into its photoactivation mechanism. *Phys. Chem. Chem. Phys.* **16**, 19141–19155 (2014).
33. Mouterde, L. M. M. & Allais, F. Microwave-assisted Knoevenagel-Doebner reaction: an efficient method for naturally occurring phenolic acids synthesis. *Front. Chem.* **6**, 426 (2018).

Acknowledgements

The authors would like to thank the Warwick Centre for Ultrafast Spectroscopy (WCUS) for the use of the Cary 60 and Fluorolog 3. M.D.H. thanks the Leverhulme Trust for postdoctoral funding. E.L.H. thanks the EPSRC for a PhD studentship through the EPSRC Centre for Doctoral Training in Molecular Analytical Science, grant number EP/L015307/1. L.M.M.M. and F.A. thank the ANR for the SINAPUV grant (ANR-17-CE07-0046), and the Grand Reims, the Conseil Départemental de la Marne and the Region Grand Est for financial support. Finally, V.G.S. thanks the EPSRC for an equipment grant (EP/J007153), the Leverhulme Trust for a research grant (RPG-2016-055) and the Royal Society and Leverhulme Trust for a Royal Society Leverhulme Trust Senior Research Fellowship.

Author contributions

M.D.H. and E.L.H. acquired and analysed the time-resolved and steady-state spectroscopic data (equal contributions) and prepared the manuscript. L.M.M.M., P.B. and F.A. conceived and performed the synthesis, conducted DPPH assay and endocrine disruption measurements as well as contributing to the preparation of the manuscript. J.C. and L.B. provided invaluable direction for modelling a closer-to-realistic sunscreen environment (synthetic skin mimic) as well as critiquing the manuscript. V.G.S. conceived the experiments and provided guidance in data analysis and interpretation, and the writing of the manuscript.

Competing interests

The authors declare no competing interests.

Additional information

Supplementary information is available for this paper at <https://doi.org/10.1038/s41467-019-12719-z>.

Correspondence and requests for materials should be addressed to M.D.H. or V.G.S.

Peer review information *Nature Communications* thanks the anonymous reviewers for their contribution to the peer review of this work. Peer reviewer reports are available.

Reprints and permission information is available at <http://www.nature.com/reprints>

Publisher's note Springer Nature remains neutral with regard to jurisdictional claims in published maps and institutional affiliations.



Open Access This article is licensed under a Creative Commons Attribution 4.0 International License, which permits use, sharing, adaptation, distribution and reproduction in any medium or format, as long as you give appropriate credit to the original author(s) and the source, provide a link to the Creative Commons license, and indicate if changes were made. The images or other third party material in this article are included in the article's Creative Commons license, unless indicated otherwise in a credit line to the material. If material is not included in the article's Creative Commons license and your intended use is not permitted by statutory regulation or exceeds the permitted use, you will need to obtain permission directly from the copyright holder. To view a copy of this license, visit <http://creativecommons.org/licenses/by/4.0/>.

© The Author(s) 2019

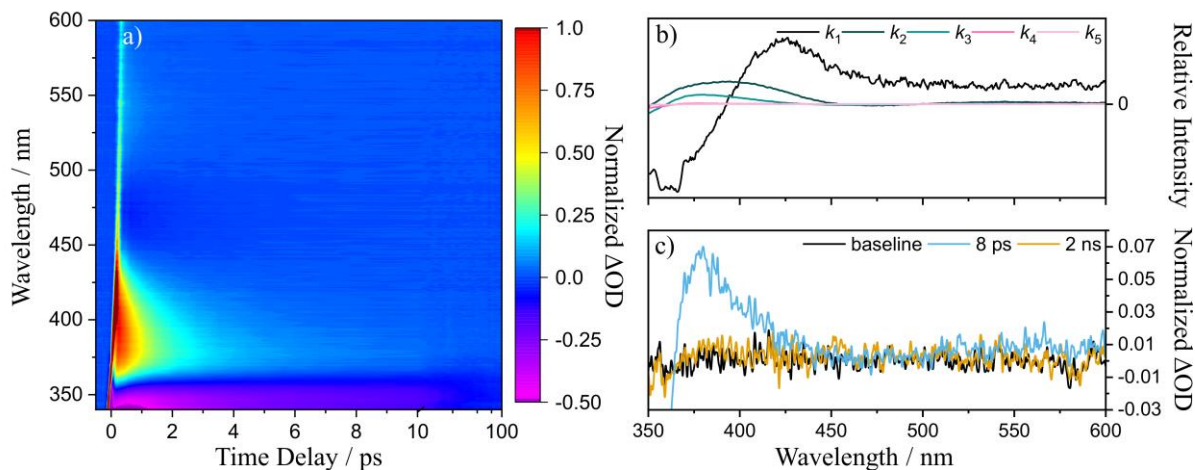
Supplementary Information

Towards Symmetry Driven and Nature Inspired UV Filter Design

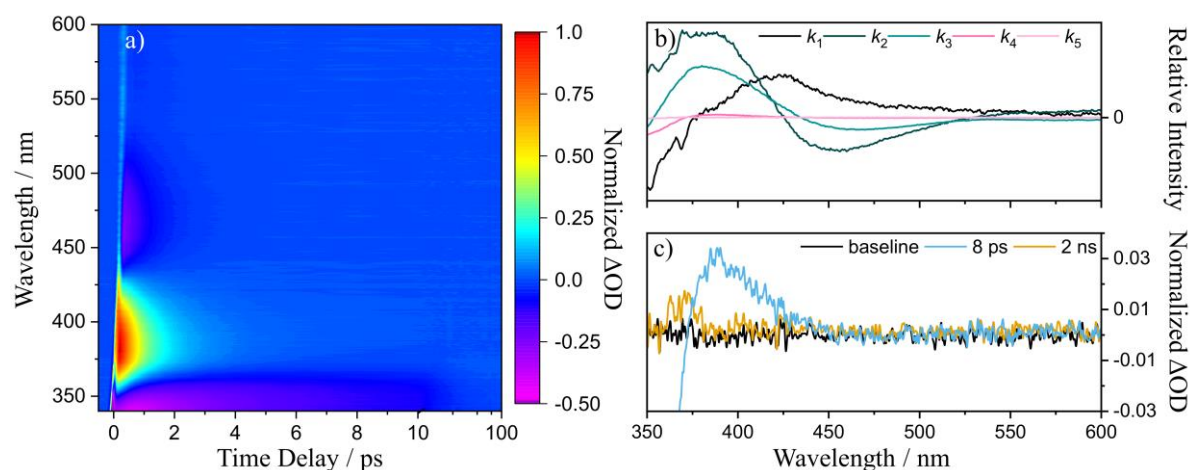
Horbury *et al.*

Supplementary Figures

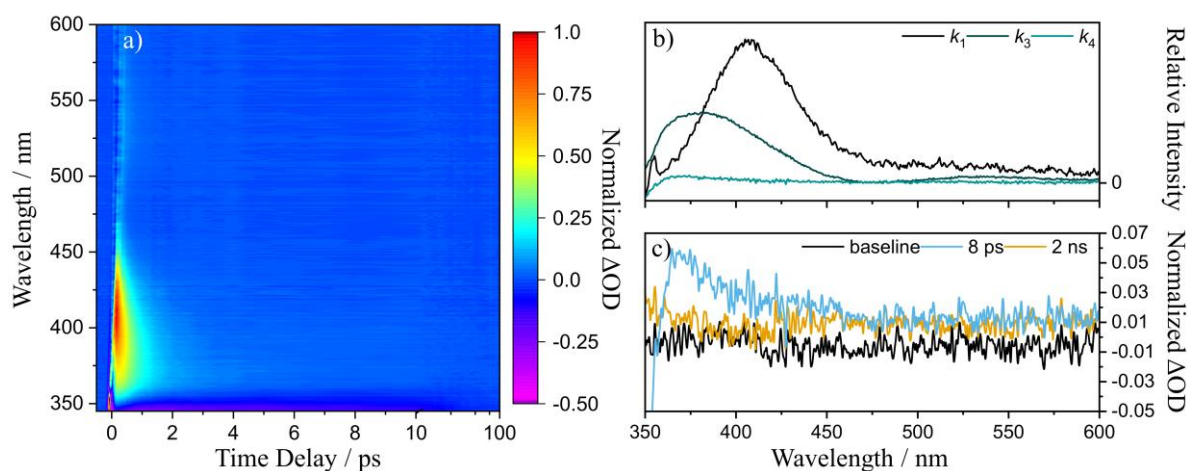
The transient absorption spectrum/spectra (TAS) for DES in alkyl benzoate (AB, C12–15), ethanol (EtOH) and cyclohexane excited at their UVA λ_{max} 335, 336 and 325 nm respectively, are shown in Supplementary Figures 1-3. The resulting rate constants are shown in Supplementary Table 1.



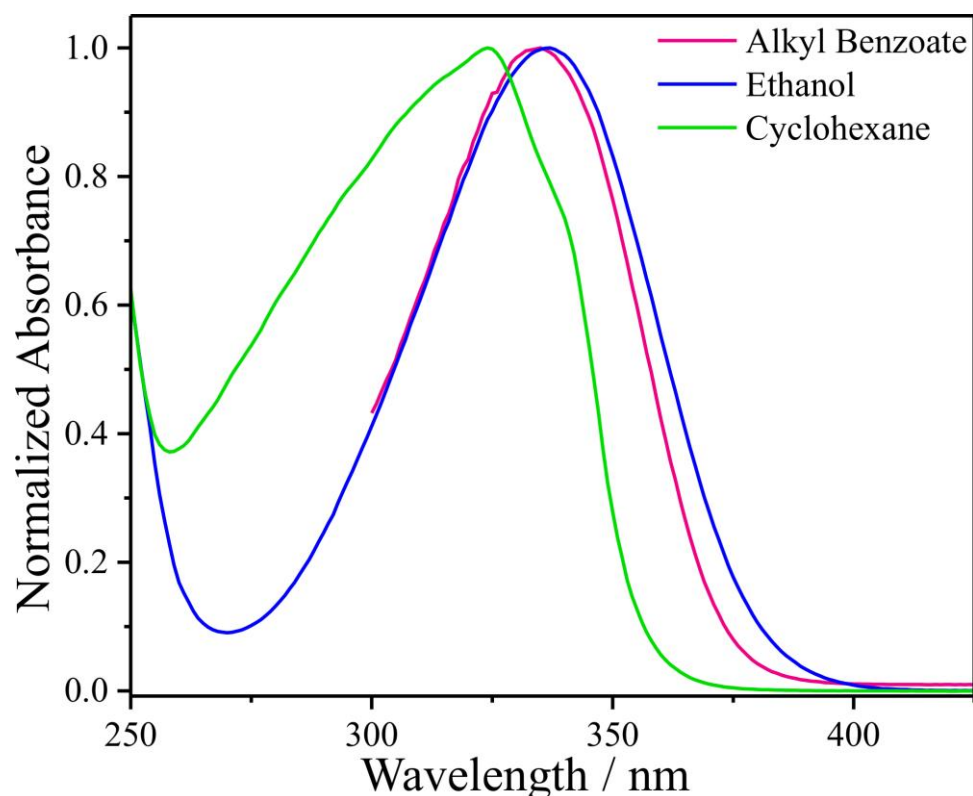
Supplementary Figure 1. Ultrafast spectroscopy results for DES in AB. a) Transient absorption spectrum (TAS) of DES in AB photoexcited at 335 nm, shown as a false colourmap, with the intensity scale representing change in normalized optical density (ΔOD). The time-delay is plotted linearly from -0.5 to 10 ps then as a log scale from 10 to 100 ps. b) Evolution associated difference spectra from the sequential global fit of the TAS of DES in AB photoexcited at 335 nm. c) Selected TAS at specific Δt highlighting the absorption at 380 nm (8 ps, blue) and incomplete ground state bleach recovery (2 ns, orange).



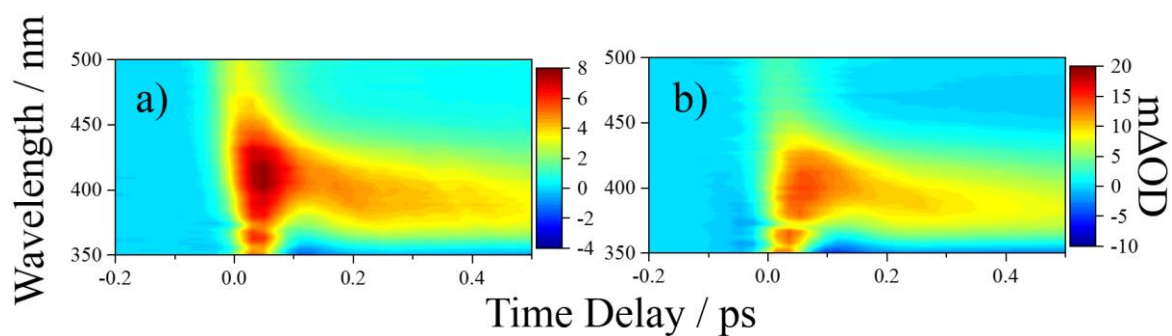
Supplementary Figure 2. Ultrafast spectroscopy results for DES in ethanol (EtOH). a) TAS of DES in EtOH photoexcited at 336 nm, shown as a false colourmap, with the intensity scale representing change in normalized optical density (ΔOD). The time-delay is plotted linearly from -0.5 to 10 ps then as a log scale from 10 to 100 ps. b) Evolution associated difference spectra from the sequential global fit of the TAS of DES in EtOH photoexcited at 336 nm. c) Selected TAS at specific Δt highlighting the absorption at 380 nm (8 ps, blue) and evidence of a long-lived photoproduct (2 ns, orange).



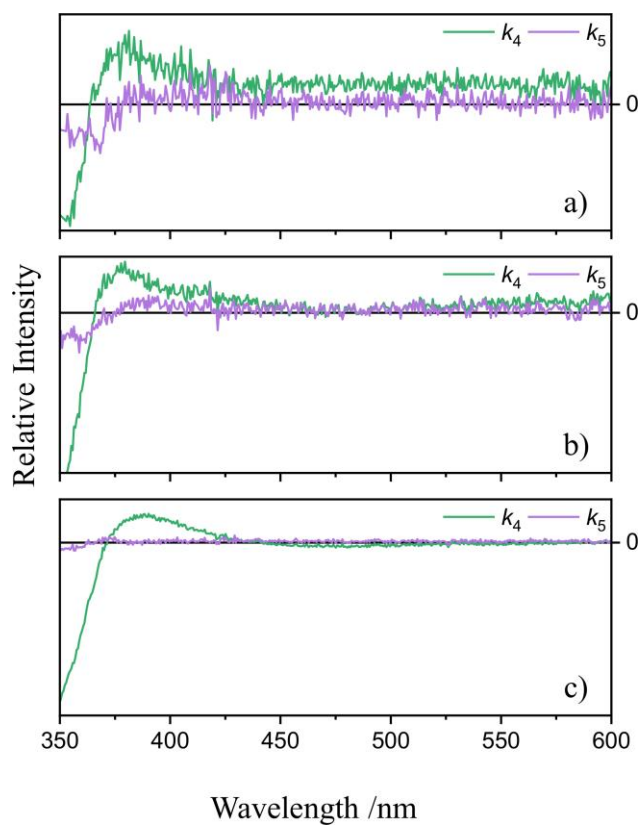
Supplementary Figure 3: Ultrafast spectroscopy results for DES in cyclohexane. a) TAS of DES in cyclohexane photoexcited at 325 nm, shown as a false colourmap, with the intensity scale representing change in normalized optical density (ΔOD). The time-delay is plotted linearly from -0.5 to 10 ps then as a log scale from 10 to 100 ps. b) Evolution associated difference spectra from the sequential global fit of the TAS of DES in cyclohexane photoexcited at 325 nm. c) Selected TAS at specific Δt highlighting the absorption at 380 nm (8 ps, blue) and lack of a photoproduct (2 ns, orange).



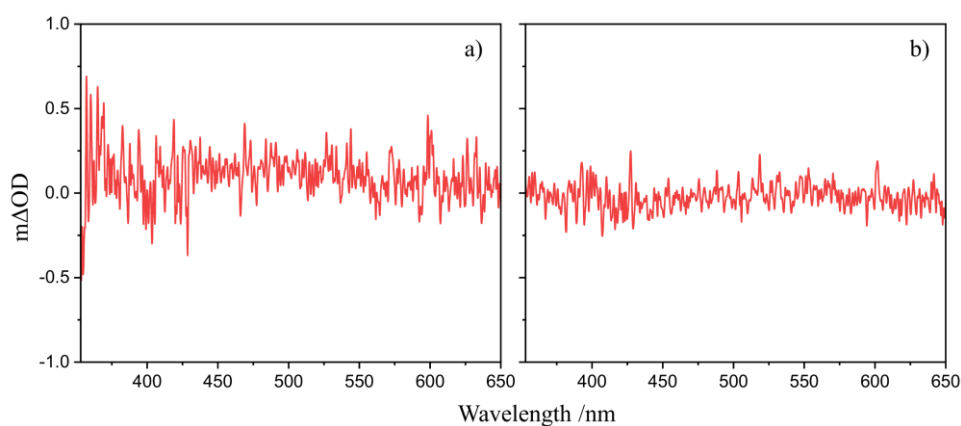
Supplementary Figure 4: Absorbance region of DES in various solvents. Ultraviolet/visible spectra of diethyl 2-(4-hydroxy-3,5-dimethoxybenzylidene)malonate (DES, $\sim 1 \mu\text{M}$) in, C12–15 alkyl benzoate (magenta), ethanol (blue) and cyclohexane (green). We note the cut off in absorption of DES in alkyl benzoate below 300 nm, as the absorption of alkyl benzoate saturates the spectrometer.



Supplementary Figure 5: Zoomed-in excited state absorption plots. False colour map of the transient absorption spectra of DES in a) AB on the surface of VITRO-CORNEUM® (VC) and b) AB, showing the initial blue shifting of the excited state absorption.

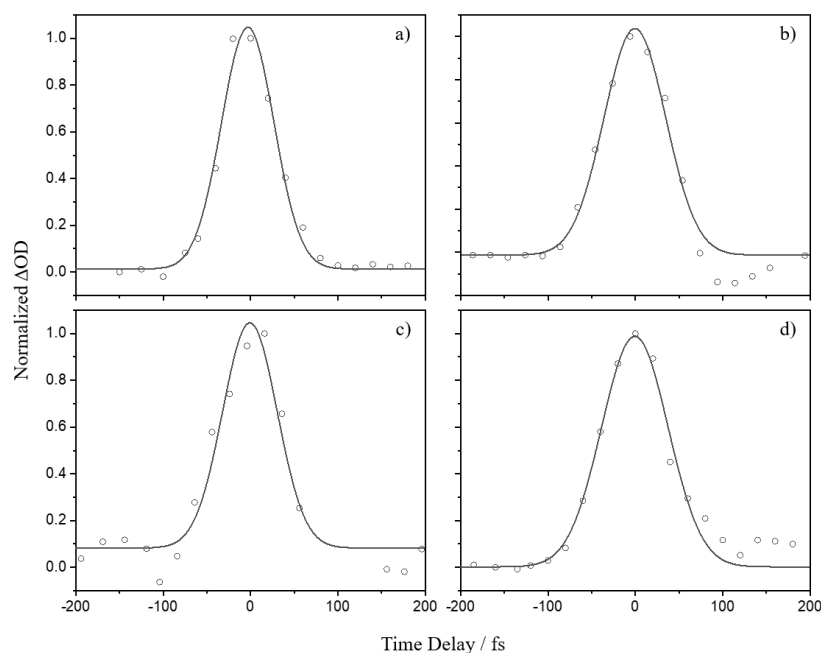


Supplementary Figure 6: Evolution associated difference spectra (EADS) of k_4 and k_5 only. Zoomed-in plots of EADS k_4 and k_5 for DES in a) VC/AB, b) AB and c) ethanol.

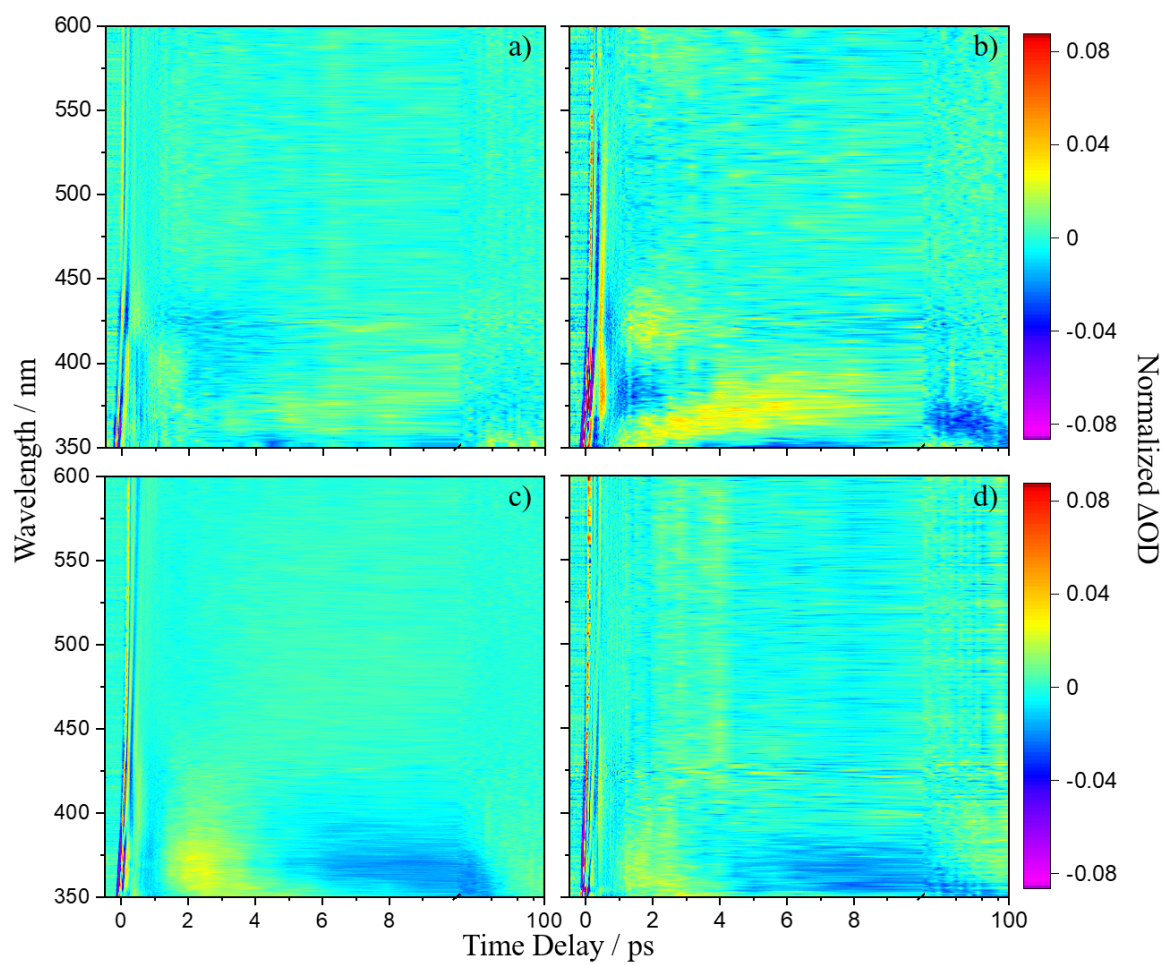


Supplementary Figure 7: Solvent-only responses. TAS of a) VC/AB and b) AB at 1 ps.

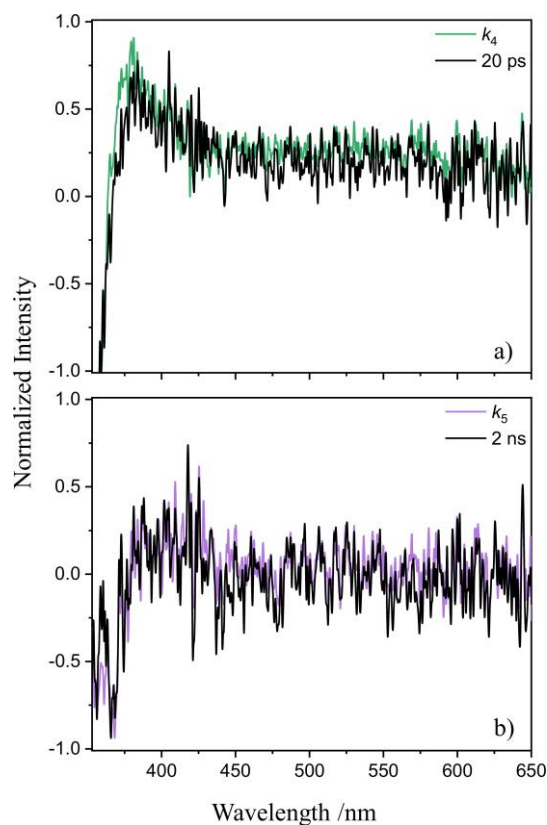
To account for the chirp of our probe pulse, a third order polynomial is included within the fitting algorithm. Additionally, the fit is convoluted with an instrument response function (IRF) to account for the temporal resolution of our pulses, whose value is taken from Gaussian fits of the solvent-only time zero response (see Supplementary Figure 8).



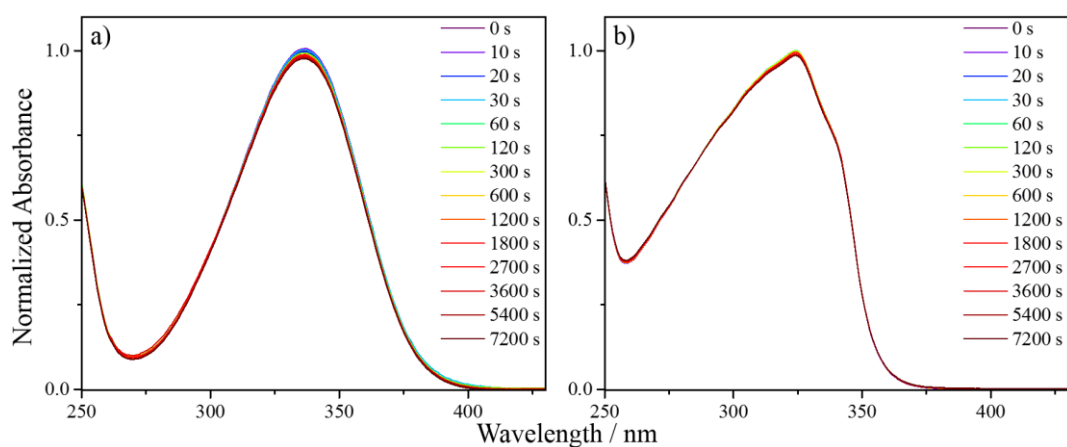
Supplementary Figure 8: Instrument responses in all solvents. Selected transients for solvent-only time-zero responses of a) VC/AB (380 nm), b) AB (380 nm), c) ethanol (310 nm) and d) cyclohexane (360 nm). The probe wavelength was chosen which showed the most Gaussian-like response. The solid line represents the fitted to the experimental data with a Gaussian function. The extracted full width half maxima are: a) 80 fs, b) 80 fs, c) 80 fs and d) 90 fs. These values are used as our IRFs in the corresponding global fits.



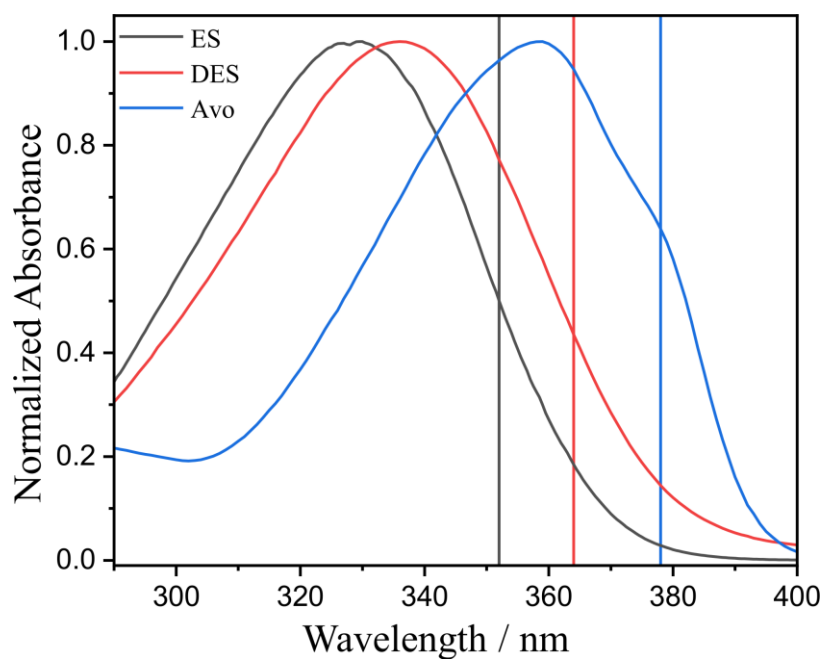
Supplementary Figure 9: False colour maps of fitting residuals. Residuals from the global fit of DES in a) VC/AB, b) AB, c) ethanol and d) cyclohexane.



Supplementary Figure 10: TAS of DES in VC/AB overlaid on EADS. a) TAS at 20 ps overlaid on the EADS associated with k_4 , and b) TAS at 2 ns overlaid with the EADS associated with k_5 . Note normalisation is based on the largest amplitude feature.



Supplementary Figure 11: Additional solar irradiance studies. UV/visible spectra of DES in a) ethanol and b) cyclohexane at varying durations of irradiation at 336 and 325 nm respectively at solar intensity. The percentage reduction in the UVA λ_{\max} was 3.1% and 1.6% respectively.



Supplementary Figure 12: Critical wavelengths. UV/visible spectra of DES (red), ES (black) and avobenzene (blue, Avo) in ethanol. The calculated critical wavelengths are DES = 364 nm, ES = 352 nm and Avo = 378 nm, marked by the vertical line in the corresponding colour.

Supplementary Table

Supplementary Table 1: Summary of rate constants. Rate-constants (k_n) resulting from the sequential global fit of the TAS of DES in VC/AB, AB, ethanol and cyclohexane shown in Supplementary Figures 2,3 and 4 respectively. The errors are quoted to 2σ .

	$k_1 / \text{s}^{-1} (\times 10^{13})$	$k_2 / \text{s}^{-1} (\times 10^{12})$	$k_3 / \text{s}^{-1} (\times 10^{11})$	$k_4 / \text{s}^{-1} (\times 10^{10})$	$k_5 / \text{s}^{-1} (\times 10^8)$
VC/AB	0.7 ± 0.2	3.0 ± 0.3	4.24 ± 0.07	1.02 ± 0.06	$\ll 5$
AB	2.5 ± 2.5	2.1 ± 0.2	5.3 ± 0.1	2.6 ± 0.1	$\ll 5$
Ethanol	1.1 ± 0.5	11 ± 5	12.6 ± 0.6	15.5 ± 0.1	$\ll 5$
Cyclohexane	0.7 ± 0.2	n/a	16 ± 1	6.3 ± 0.2	n/a

Supplementary Methods

The critical wavelength for a sunscreen is defined as the wavelength at which the integrated area underneath the spectral absorbance curve reaches 90% of the total area between 290 and 400 nm¹. To attain the critical wavelengths of DES, ES and avobenzone (Avo), UV/visible spectra of each compound were taken in ethanol using a UV/visible spectrometer (Cary 60, Agilent Technologies). These spectra are shown in Supplementary Fig. 12. The area under each absorption curve between 290 and 400 nm was determined using the cumulative trapezoidal method function in MATLAB (R2017b), which is defined mathematically as follows:

$$\int_{290}^{400} f(\lambda) d\lambda \approx \sum_{k=1}^N \frac{f(\lambda_{k-1}) + f(\lambda_k)}{2} \Delta x_k \quad (1)$$

where $\lambda_0 = 290 \text{ nm} < \lambda_1 < \dots < \lambda_{N-1} < \lambda_N = 400 \text{ nm}$, and Δx_k is the interval between each wavelength datapoint. The critical wavelength was then assigned to be the value where 90% of the total area resides under the curve. The critical wavelength is marked by a vertical line in Supplementary Fig. 12.

The successful synthesis of DES was confirmed by ¹H NMR; the assignments of the peaks are given as follows:

¹H NMR (300 MHz, CDCl₃): $\delta = 7.62$ (s, 1H, H-1), 6.75 (s, 2H, H-3 and H-7), 4.30 (q, J = 7.23 Hz, 4H, H-16 and H-13), 3.86 (s, 6H, H-9 and H-10), 1.31 (t, J = 7.14 Hz, 6H, H-14 and H-17). ¹³C NMR (75 MHz, CDCl₃): $\delta = 167.2$ (s, C-15), 164.3 (s, C-12), 146.9 (d, C-1), 142.2 (d, C-4 and C-6), 137.3 (s, C-5), 124.0 (s, C-2), 123.8 (s, C-11), 106.64 (d, C-3 and C-7), 61.6 (t, C-16), 61.4 (t, C-13), 56.1 (q, C-9 and C-10), 14.1 (q, C-17), 13.9 (q, C-14).

For the endocrine disruption measurements, cell culture material was from Life Technologies (Cergy-Pontoise, France) except the 96-well Cell star plates, which were from Greiner Labortechnik (Poitiers, France). Luciferin (sodium salt) and geneticin were purchased from Promega (Charbonnières, France). R1881 was from NEN Life Science Products (Paris, France). Estradiol, SR12813, hygromycin and puromycin were purchased from Sigma Aldrich (Saint-Quentin Fallavier, France). Stock solutions were made in dimethyl sulfoxide (DMSO) at 10 mM and dilutions from this stock solution were prepared in a culture medium.

HELN and HELN hER α cells were already described.² Briefly, Hela cells were stably transfected with the ERE- β Globin-Luciferase-SVNeomycin plasmid, with or without the pSG5-hER α -puromycin plasmid leading to the HELN and HELN hER α -cell lines. HG5LN and HG5LN PXR cells were already described.³ The Hela cells were stably transfected with the GAL4RE₅- β Globin-Luciferase-SVNeomycin plasmid, with or without the pSG5-GAL4(DBD)-hPXR(LBD)-puromycin plasmid leading to the HG5LN and HG5LN-hPXR cell lines.

Cells were cultured at 37°C under humidified 5% CO₂ atmosphere. HG5LN, HG5LN PXR and HELN cells were cultured in red phenol (DMEM)-F12 medium (Thermofisher, Villebon sur Yvette, France) supplemented with 1% penicillin/streptomycin and 5% fetal calf serum (FCS). HELN hER α cells were cultured in DMEM-F12 without red phenol supplemented with penicillin/streptomycin (1%) and dextran-coated charcoal-treated fetal calf serum (DCC-FCS) (5%) (Test medium)

Cells were seeded in 96-well white opaque flat bottom plates at 25,000 cells per well in 150 μ L of test medium. DES (four replicates per plate) was added 24h later using automated workstation (Biomek 3000, Beckman Coulter, Villepinte, Paris) and cells were incubated at 37°C for 16h. Then, the medium was removed and 50 μ L of test medium containing luciferin at 0.3 mM was added per well. After 5 min, the production of light was measured in living cells using microplate luminometer (MicroBeta, PerkinElmer SAS, Courtaboeuf, France).

Agonistic activities of HELN hER α and HG5LN hPXR cells were tested in the presence of increasing concentrations (10nM-10 μ M) of DES. Results were expressed as a percentage of maximal luciferase activity. Maximal luciferase activity (100%) was obtained in the presence of 10 nM E2 for ER α , and 3 μ M SR12813 for PXR. Antagonistic assays were performed using a concentration of agonist yielding approximately 60-85% of maximal luciferase activity. The antagonistic activity of DES tested at (10 nM – 10 μ M) was determined by co-incubation with the agonist E2 at 0.1nM for ER α , and the agonist SR12813 at 100 nM for PXR.

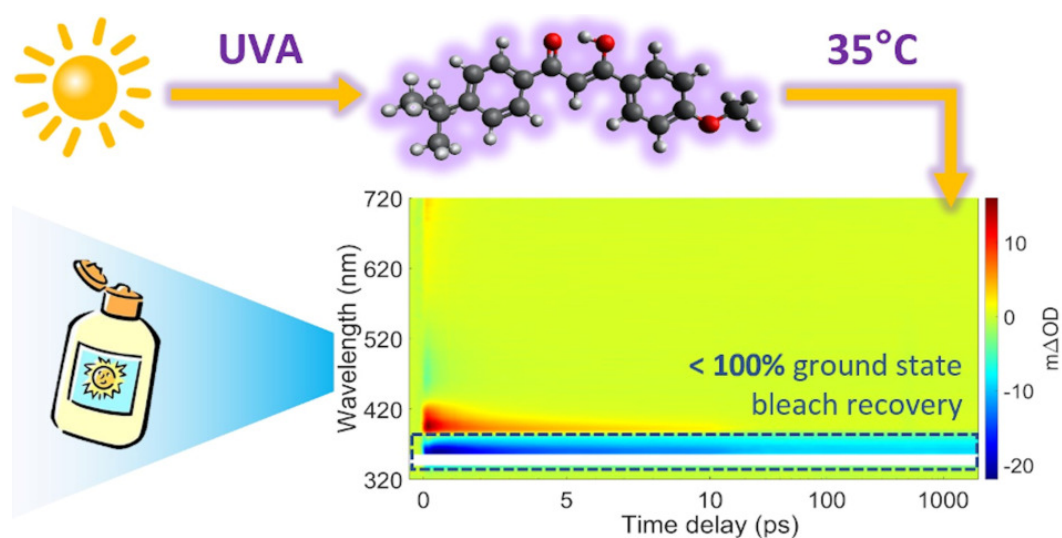
DES was also tested for non-specific modulation of luciferase expression on the HELN and HG5LN cell line, which are devoid of hER α and hPXR. DES showed non-specific induction of luciferase expression at 10 μ M.

Supplementary References

1. Diffey BL, Tanner PR, Matts PJ, Nash JF, In vitro assessment of the broad-spectrum ultraviolet protection of sunscreen products. *J. Am. Acad. Dermatol.* **6**, 1024-1035 (2000)
2. Delfosse V, *et al.* Structural and mechanistic insights into bisphenols action provide guidelines for risk assessment and discovery of bisphenol A substitutes. *Proc. Natl. Acad. Sci. USA* **109**, 14930-14935 (2012).
3. Delfosse V, *et al.* Synergistic activation of human pregnane X receptor by binary cocktails of pharmaceutical and environmental compounds. *Nat. Commun.* **6**, 8089 (2015).

Chapter 4

Determining the photostability of avobenzone in sunscreen formulation models using ultrafast spectroscopy





Cite this: DOI: 10.1039/d1cp03610f

Determining the photostability of avobenzone in sunscreen formulation models using ultrafast spectroscopy†

Emily L. Holt,^{ab} Natércia d. N. Rodrigues,^{ac} Juan Cebrían^c and Vasilios G. Stavros^{id,*a}

Avobenzone is an ultraviolet (UV) filter that is often included in sunscreen formulations despite its lack of photostability. Its inclusion is necessary due to few existing alternatives for photoprotection in the UVA region (320–400 nm). To better understand and predict the photostability of avobenzone, ultrafast transient electronic absorption spectroscopy (TEAS) has been used to study the effects of solvent (including emollients), concentration and skin surface temperature on its excited-state relaxation mechanism, following photoexcitation with UVA radiation (~350 nm). Subtle differences between the excited-state lifetimes were found between the systems, but the TEAS spectral features were qualitatively the same for all solution and temperature combinations. Alongside TEAS measurements, UV filter/emollient blends containing avobenzone were irradiated using simulated solar light and their degradation tracked using steady-state UV-visible spectroscopy. Sun protection factor (SPF) and UVA protection factor (UVA-PF) assessments were also carried out on representative oil phases (higher concentration blends), which could be used to formulate oil-in-water sunscreens. It was found that there was an apparent concentration dependence on the long-term photoprotective efficacy of these mixtures, which could be linked to the ultrafast photodynamics by the presence of a ground-state bleach offset. This combination of techniques shows potential for correlating long-term behaviours (minutes to hours) of avobenzone with its ultrafast photophysics (femtoseconds to nanoseconds), bridging the gap between fundamental photophysics/photochemistry and commercial sunscreen design.

Received 5th August 2021,
Accepted 18th October 2021

DOI: 10.1039/d1cp03610f

rsc.li/pccp

Introduction

Avobenzone (also known as butyl methoxydibenzoylmethane) is a UVA (320–400 nm) filter that is commonly included in sunscreen formulations to protect the skin from the detrimental effects of solar UV radiation.¹ Despite its complex photochemistry and reported lack of photostability upon UV light exposure,^{2,3} its inclusion in formulations is often a necessity due to a lack of approved UVA filters, particularly in the United States.⁴

Avobenzone exists predominantly in a chelated enol form in its ground electronic state, however, photoproducts can form via enol–keto tautomerization, following photoexcitation

induced by incident solar rays. The diketo tautomer photoproduct can then undergo further photochemistry that introduces reactive triplet states; these, in turn, can cause indirect degradation of formulations and induce damage on the skin via oxidative stress.^{3,5,6} Furthermore, the diketo form absorbs UVA radiation much less efficiently than the enol form, thus the level of protection offered by avobenzone-containing formulations after irradiation is decreased.⁷ The structures of the enol and diketo tautomers, along with their absorption profiles in ethanol before and after irradiation, are shown in Fig. 1. The tautomerisation and subsequent decrease in efficacy of irradiated avobenzone has also been demonstrated using several different comparable methods in earlier publications.^{7–14}

Previous studies have sought to identify ingredients that stabilise the more effective chelated enol form of avobenzone, such as compatible UV filters or antioxidants.^{15–17} Micellar and lipid microparticle encapsulation of avobenzone have also been shown to have a role in enhancing its photostability.^{9,18} Deuteration of the diketo methylene/enol moiety affects the tautomerisation equilibrium, by shifting it towards the ketone form.¹⁹ Many photofragments of avobenzone have also

^a Department of Chemistry, University of Warwick, Gibbet Hill Road, Coventry, CV4 7AL, UK. E-mail: v.stavros@warwick.ac.uk

^b Molecular Analytical Science Centre for Doctoral Training, Senate House, University of Warwick, Coventry, CV4 7AL, UK

^c Lubrizol Life Science Beauty, Calle Isaac Peral, 17 Pol. Ind. Camí Ral, 08850 Barcelona, Spain

† Electronic supplementary information (ESI) available: See DOI: 10.1039/d1cp03610f. The underlying data of this publication can be accessed via the Zenodo archive at DOI: 10.5281/zenodo.5531347

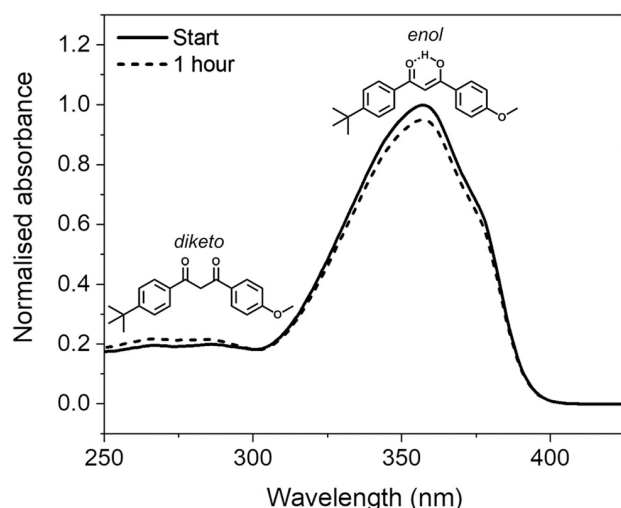


Fig. 1 Normalised UV-visible spectra of $5 \mu\text{g mL}^{-1}$ ($\sim 16 \mu\text{M}$) solution of avobenzone in ethanol taken before and after one hour of irradiation (solid and dotted lines, respectively), using a xenon lamp at solar irradiance ($\sim 1000 \text{ W m}^{-2}$). Inset are the molecular structures of the chelated enol and diketo tautomers of avobenzone that give rise to the spectral peaks at $\sim 350 \text{ nm}$ and $\sim 270 \text{ nm}$, respectively.

been identified, which in turn may induce cytotoxic and skin sensitization effects.^{20–22}

Transient electronic absorption spectroscopy (herein abbreviated as TEAS), is an ultrafast pump-probe technique that has been utilised previously to explore the photoprotection mechanisms of many individual UV filters in solution, including avobenzone; additional examples include benzophenone-3, ethylhexyl methoxycinnamate, homosalate, ethylhexyl salicylate, octocrylene and diethylamino hydroxybenzoyl hexyl benzoate.^{23–28} An ideal sunscreen filter should be able to dissipate excited state energy safely (ideally non-radiatively) and rapidly (within femtoseconds, $1 \text{ fs} = 10^{-15} \text{ s}$, to picoseconds, $1 \text{ ps} = 10^{-12} \text{ s}$). This reduces the likelihood of harmful side reactions such as forming triplet states, or fragmentation of the molecule.^{29,30} Furthermore, a rapid return to the ground state after photoexcitation implies that the molecule quickly becomes available to absorb UV radiation again. To investigate properties such as these, the femtosecond resolution of TEAS can be used to full advantage to determine the excited-state relaxation mechanisms of UV filters in real-time.³¹

A previous TEAS study of avobenzone in cyclohexane, methanol and acetonitrile by Dunkelberger *et al.* identified changes to its electronic excited-state lifetime that were dependent on solvent polarity.²³ Solvent-dependent effects have also been observed by chromatography, NMR and UV-visible spectroscopy;^{7–10,32,33} these techniques (amongst others) are often used in conjunction with TEAS to correlate the long-term behaviours (minutes to hours) of molecules such as avobenzone, with their ultrafast photophysical processes. Computational methods such as density functional theory (DFT), including time-dependent DFT (TD-DFT), can also be used to guide the assessment of a molecule's suitability for sunscreen use.^{28,34,35} As an example, Wang *et al.* include both experimental (including ultrafast) data and computational

methods in their study of UV-induced photochemical reactions in diketo avobenzone derivatives.³⁶

However, TEAS studies have not been widely used in conjunction with industry-standard efficacy tests that sunscreen formulations are subject to, such as sun protection factor (SPF) and UVA protection factor (UVA-PF) determination. These tests are ultimately conducted *in vivo* on human volunteers, but due to practical and ethical considerations are initially performed using analogous *in vitro* techniques.^{37,38} *In vitro* testing involves applying a thin layer (up to 2.5 mg cm^{-2}) of a sunscreen to a synthetic skin substrate and determining the SPF/UVA-PF via spectrophotometric absorbance and/or transmittance measurements.^{31,39} *In vitro* SPF values are both measured and predicted upon solar irradiation by Binks *et al.*, in their study of mixtures (solutions and emulsions) of UV filters including avobenzone, using squalane and propane-1,2-diol as solvent.¹³

A fundamental understanding of the underlying photochemical processes that UV filters (such as avobenzone) undergo is crucial for improving overall sunscreen performance. However, if these studies could mimic the final sunscreen and conditions of use more closely, they may better inform formulation design. Therefore, the present study aims to enhance the understanding of what causes instability of avobenzone on a molecular level and how this may affect long-term sunscreen performance. Importantly, the TEAS methods used in this study have been extended to more closely mimic real-life conditions. We demonstrate, to the best of our knowledge, the first examples of TEAS measurements targeting the effects of skin surface temperature on avobenzone photostability in industry-relevant emollients, compared to ethanol and cyclohexane. Temperature effects in avobenzone and related enol benzoylacetones observed previously include differing decay rates of avobenzone photoproducts and changes to the intramolecular H-bond strength, respectively.^{3,40} In addition to TEAS, steady-state UV-visible spectroscopy and SPF/UVA-PF tests were used to correlate how the ultrafast dynamics could be influencing the long-term absorption profile of avobenzone upon prolonged irradiation, in combination with additional UV filters.

Alongside recent spectroscopic advances examining the photodynamics of UV sunscreen filter candidates on skin mimics at room temperature,^{41–43} our temperature-dependent TEAS setup could be incorporated into studies of this type in the future. These latest developments further increase the applicability of laser spectroscopy methods to commercial sunscreen design.

Experimental

Sample preparation

The avobenzone (Eusolex[®] 9020 by Merck) studied in solution and emollient mixtures was used as purchased without further purification. Solutions of avobenzone for ultrafast TEAS measurements were prepared to a concentration of $\sim 10 \text{ mM}$ (equivalent to $\sim 3 \text{ mg mL}^{-1}$) and $\sim 1 \text{ mM}$ (equivalent to $\sim 0.3 \text{ mg mL}^{-1}$) in ethanol (absolute, Fisher Scientific) and cyclohexane ($> 99.9\%$, VWR Chemicals), respectively, and $\sim 10 \text{ mM}$ in the cosmetic grade

emollients diisopropyl adipate (Schercemol™ DIA ester, referred to as DIA) and lauryl lactate (Schercemol™ LL ester, herein LL), both provided by Lubrizol. All solvents and emollients were used as acquired.

For the data presented in Fig. 1, a solution of avobenzone in ethanol was prepared to an exact concentration of $5 \mu\text{g mL}^{-1}$ ($\sim 16 \mu\text{M}$). For the steady-state UV-visible spectroscopy measurements shown in Fig. 3, mixtures of avobenzone and additional UV filters in DIA and LL, were prepared by combining $\sim 4 \mu\text{g mL}^{-1}$ of avobenzone, $\sim 10 \mu\text{g mL}^{-1}$ ethylhexyl methoxycinnamate (EHMC, Eusolex® 2292, Merck) and $\sim 13 \mu\text{g mL}^{-1}$ octocrylene (Eusolex® OCR, Merck) in each emollient and stirred until the filters were dissolved. These masses correspond to a ratio of 3:7.5:10 (avobenzone:EHMC:octocrylene), mimicking the ratios of the maximum permitted w/w% in a completed sunscreen blend in the United States.

For sun protection factor (SPF) and UVA-PF testing (more details on the exact methodologies for these tests are given below), five oil phase samples containing varying amounts of avobenzone, EHMC and octocrylene in emollient were made. These mixtures were prepared in batches of 25 g; Table S1 (ESI†) shows the mass of each ingredient included in each batch. The oil phases were made by combining the ingredients in a beaker and mixing using an overhead mechanical stirrer until a homogeneous mixture was achieved. The mixture was gently heated on a hot plate ($\sim 30 \text{ }^\circ\text{C}$) as it was mixed to allow for the solvation of avobenzone. Once the oil phase mixture was clear, stirring and heating were stopped, and the mixture was left to cool to room temperature. Samples 1 and 2 contain a mixture of the three UV filters (avobenzone, EHMC and octocrylene) in the same proportion as the samples for steady-state measurements, *i.e.*, 3:7.5:10, respectively, differing only in the emollient used: DIA was used for Sample 1 and LL for Sample 2. Samples 3 and 4 constitute a 5-fold and 10-fold decrease in the w/w% of UV filters respectively, compared to Sample 1. Finally, Sample 5 reverses the w/w% of EHMC and octocrylene included in the blend, compared to Sample 1. For comparison to the concentrations used for TEAS measurements, the 10 mM solution in ethanol is approximately equal to a concentration of 0.4% w/w.

Instrumentation

Ultrafast spectroscopy. TEAS measurements were conducted at the Warwick Centre for Ultrafast Spectroscopy; this setup has been described in detail previously.⁴⁴ Briefly, femtosecond laser pulses (800 nm, 13 W, 1 kHz repetition rate) were generated using a commercially available Ti:sapphire regenerative amplifier (Duel Ascend Pumped Spitfire Ace, Spectra-Physics), seeded by a Ti:sapphire oscillator (Mai Tai, Spectra-Physics). The beam is then split into four fractions of approximately equal power (3.5 W); one of which is further split in a 2.5:1 ratio to create the pump and probe beams needed for TEAS experiments. The 2.5 W portion of the fundamental 800 nm beam is converted into the 350 nm required for photoexcitation using an optical parametric amplifier (TOPAS Prime with UV extension, Light Conversion). The power of the pump beam was recorded to be

approximately 0.5 mW at the sample, which corresponds to a fluence of 0.65 mJ cm^{-2} . This was kept consistent except for the $\sim 1 \text{ mM}$ solutions in ethanol and cyclohexane, where the fluence was increased, up to $\sim 1.1 \text{ mJ cm}^{-2}$, to increase signal. Only $\sim 5\%$ power of the remaining 1 W fundamental beam is required to generate the supercontinuum white-light (320–720 nm) probe pulses; this is achieved by focusing the fundamental 800 nm beam ($< 50 \text{ mW}$) onto a vertically translated CaF_2 crystal (2.5 cm diameter, 2 mm thick). The relative polarization between the pump and probe is maintained at magic angle (54.7°). The different time delays are created by a gold retroreflector, mounted on to an automatic motorised delay stage in the probe beam line, which lengthens or shortens this beam path according to the requirements of the experiment. An optical chopper blocks every other excitation pulse to attain the reported difference spectra between “pump on” and “pump off”. All reported TEAS datasets were the average of at least 5 scans, with a scan comprising a data matrix of all wavelengths and time delays. Each time delay in turn averages a total of 2500 “shots”, *i.e.* pump-on, pump off pairs. Each set of ≥ 5 scans were repeated twice, using freshly made samples on separate days, with similar results both times.

All transients were analysed with the software package Glotaran⁴⁵ using global kinetic analysis with a parallel model. A parallel model sums exponential functions that decay independently of one another.⁴⁶ The implementation of this method and its assumptions have been excellently summarised in the review by Beckwith *et al.*,⁴⁷ briefly, a parallel model assumes that all dynamic processes occur instantaneously and concurrently following excitation. For presentation purposes, all transient absorption spectra were chirp-corrected using the KOALA package detailed in the publication by Grubb *et al.*⁴⁸ Characterisation of the instrument response is given in the ESI† (Supplementary Methods and Fig. S1).

Increasing the sample temperature to $\sim 35 \text{ }^\circ\text{C}$ in the interaction region, to mimic the surface temperature of the skin, was attained by using a temperature-controllable flow-through cell (Harrick Scientific), which was connected via a K-type thermocouple to a home-built controller enclosing Panasonic KT4 electronics. The path length of the sample was $25 \mu\text{m}$ as set by PTFE spacers placed between two CaF_2 windows. The CaF_2 windows were 2.5 cm in diameter and 2 mm thick. The sample was photoexcited at $\sim 350 \text{ nm}$ and replenished between each pair of pulses using a diaphragm pump (Simdos 02). For measurements at room temperature (recorded as being between $\sim 21\text{--}23 \text{ }^\circ\text{C}$), all apparatus and procedures remained the same, except that the heater was switched off for the duration of these measurements.

Sample irradiation and steady-state spectroscopy. For the irradiations in Fig. 1 and 3, a Newport 91191-1000 solar simulator was used as the light source, with a 0.8 optical density (OD) filter in place to attenuate the output to “one sun” ($\sim 1000 \text{ W m}^{-2}$).⁴⁹ The sample was contained in the same 10 mm path length quartz cuvette for both irradiation and spectral measurements. During irradiation, the cuvette was kept in a constant position. In all cases, UV-visible spectra were obtained using an Agilent Cary-60 spectrophotometer, with absorbance measurements taken at 1 nm increments.

SPF and UVA-PF testing. The oil phases were applied to separate poly(methyl methacrylate) (PMMA) plates, following the procedure detailed in the Supplementary Methods (SM) in the ESI†. The amount of each oil phase sample applied to the plates, along with the calculated final coverages achieved for each plate, are given in Table S2 (ESI†). The SPF and UVA-PF measurements were carried out *in vitro* using a LabSphere UV-2000 transmittance analyser (LabSphere, Inc.), and the samples were irradiated using a SUNTEST CPS+ (III) solar simulator (Atlas Material Testing Solutions). Full details for the SPF and UVA-PF protocols can be found in the ESI† (SM).

Results and discussion

The photostability and photoprotection afforded by avobenzone were assessed using TEAS at skin surface temperature to reflect real-world conditions of use, by heating the sample at the interaction region. A review of the literature, which is included in the Supplementary Discussion in the ESI†, concludes that any

temperature within the range 32–38 °C is justifiable as a skin surface temperature for investigations relating to sunscreens; therefore, the experiments reported here were performed at 35 °C as the midpoint of this range. The results for the ~10 mM ethanol and cyclohexane solutions at skin surface temperature are shown in the top two rows of Fig. 2, with equivalent measurements for solutions at room temperature and with a 10-fold reduction in concentration to ~1 mM, shown in Fig. S2 and S3 (ESI†), respectively. The TEAS results for the ~10 mM avobenzone/emollient solutions, diisopropyl adipate (DIA) and lauryl lactate (LL), also shown in Fig. 2 will be returned to below, once the dynamics in the volatile solvents have been discussed.

From the results in Fig. 2, the spectral features (which appear instantaneously following photoexcitation) are comparable between the ethanol and cyclohexane datasets, as such the following description applies to both solute/solvent combinations. The overlap of probe wavelengths with the ground-state absorption region of avobenzone gives rise to the intense ground-state bleach (GSB) feature between 330–380 nm; a more detailed exploration into the implications of the incomplete GSB recovery observed will

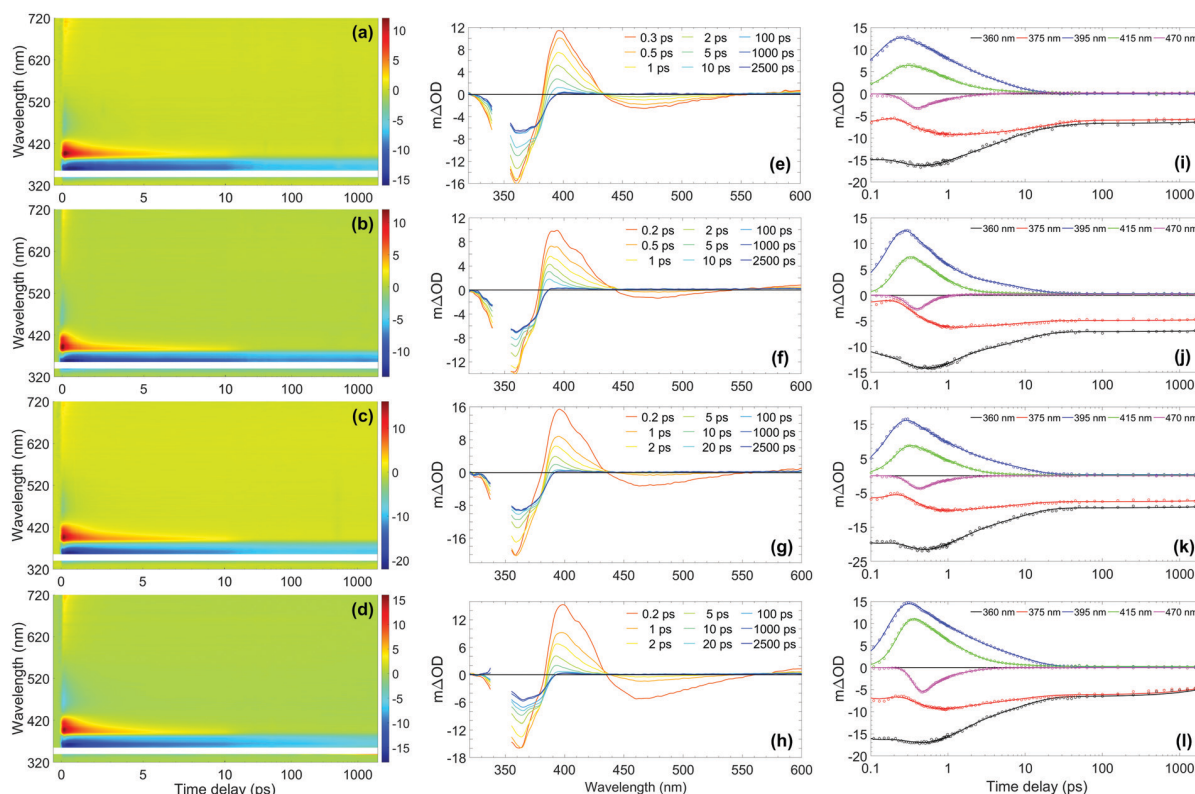


Fig. 2 (Left-hand column) Two-dimensional colour maps showing all transient absorption spectra (TAS) of ~10 mM avobenzone photoexcited at ~350 nm, with sample cell temperature set to 35 °C, in (a) ethanol, (b) cyclohexane, (c) diisopropyl adipate (DIA) and (d) lauryl lactate (LL). The region between 340–355 nm has been omitted due to oversaturation from the pump pulse. Zoomed-in false colour maps of the wavelength region > 400 nm can be found in the ESI† (Fig. S9). (Middle column) TAS at selected pump–probe time delays for avobenzone in (e) ethanol, (f) cyclohexane, (g) DIA and (h) LL. These plots are attained by taking vertical slices through the colour maps at the given time delay and are presented using the same mΔOD scale as the corresponding colour map, with the same wavelength region omitted. (Right-hand column) Lineouts to show spectral features at specific probe wavelengths in (i) ethanol, (j) cyclohexane, (k) DIA and (l) LL. The features at 360 nm and 375 nm are ground-state bleach features, 395 nm and 415 nm are excited-state absorption features, and 470 nm is stimulated emission. The circles denote the raw datapoints and the solid line in each case is the fit attained using a parallel model (time constants from fitting are presented in Table 1). The time delay axis is presented on a logarithmic scale. Time delays prior to 0.1 ps are presented on a linear scale in the ESI† (Fig. S6 for ethanol and cyclohexane, Fig. S7 for DIA and LL).

Table 1 Extracted TEAS time constants for four ~10 mM avobenzene solutions, following photoexcitation at ~350 nm and heating the sample to ~35 °C, obtained by using a parallel global kinetic fit model.⁴⁷ The error presented for τ_1 is the estimated instrument response (presented in Fig. S1 in the ESI for ethanol and cyclohexane); the errors presented for $\tau_{2,3}$ are those provided by the fitting software package. The quality of the fits is demonstrated in Fig. 2 and in the residual plots in Fig. S10 (ESI). The time constants for the room temperature TEAS measurements in ethanol and cyclohexane can be found in Table S3 of the ESI

Time constant	Ethanol	Cyclohexane	Diisopropyl adipate (DIA)	Lauryl lactate (LL)
τ_1 (fs)	150 ± 140	235 ± 80	165 ± 140	195 ± 140
τ_2 (ps)	1.2 ± 0.1	0.70 ± 0.08	1.0 ± 0.1	1.2 ± 0.1
τ_3 (ps)	8.2 ± 0.1	8.4 ± 0.1	7.7 ± 0.1	8.2 ± 0.1
τ_4 (ns)	> 2.5 ^a	> 2.5 ^a	> 2.5 ^a	> 2.5 ^a

^a Outside the time-window of the instrument.

follow. It is noted that the GSB region is partially obscured due to pump bleaching artefacts. Other significant spectral characteristics include an excited-state absorption (ESA) between 380 and 430 nm, and a short-lived stimulated emission (SE) between 450 and 550 nm. These ESA and SE features have been observed previously by Dunkelberger *et al.*²³ in TEAS measurements of avobenzene in methanol and cyclohexane, and also in the work of Verma *et al.*, who performed TEAS on avobenzene precursors: dibenzoylmethane (DBM) and benzoylacetone (BZA) in acetonitrile and hexane at room temperature.^{50,51} Combining the insights from these room-temperature studies^{23,50,51} with the results of our quantitative global kinetic fits using a parallel model, presented in Table 1 at skin surface temperature and in Table S3 (ESI[†]) at room temperature, informed our assignment of: spectral features (Fig. 2 and Fig. S2, ESI[†]), associated lifetimes τ_1 – τ_4 (Table 1), and the potential effect of the increased temperature. Also, for reference, the decay associated spectra (DAS) obtained from the global fits of avobenzene (in all four solvents) are presented in Fig. S4 of the ESI.[†] A sequential model, of the general form $A \xrightarrow{\tau_1} B \xrightarrow{\tau_2} \dots \xrightarrow{\tau_n} N$ was also considered for the extraction of spectral features, where n is the number of lifetimes required to describe the data. However, a parallel model was deemed appropriate considering the quality of the fits, reflected in the lineouts (Fig. 2) and the residuals (Fig. S10, ESI[†]). A parallel model could also prove more suitable if mixtures of UV filters were to be investigated using TEAS, as multiple molecular processes arising from different molecules would be induced simultaneously, at time zero ($\Delta t = 0$).

In all cases following photoexcitation, τ_1 represents the evolution of the chelated enol form of avobenzene from the Franck-Condon region. It is possible that there are additional ultrafast processes occurring within this time on a proportion of the excited molecules, such as excited-state intramolecular proton transfer, or rotation around the C–O single bond of the hydroxyl group to form non-chelated avobenzene species. These branching pathways have both been suggested in previous studies,^{12,51,52} although they cannot be confirmed from the evidence presented in this study as τ_1 is close to the instrument response timescale.

The lifetime assigned to τ_2 relates to the decay of the initially excited S_1 state of the chelated enol form of avobenzene via SE,

with the faster decay occurring in non-polar cyclohexane. The lineouts at 470 nm in Fig. 2(i) and (j) confirm that the SE does not persist much beyond 1–2 ps in either solvent. This was also observed both in the room temperature lineouts presented in Fig. S5 (ESI[†]) and also by Dunkelberger *et al.*²³ in their room temperature study of avobenzene, which is the first indication that the temperature increase has had little effect on photodynamics. The timescale of the SE is very short compared to the much longer timescales that would be expected for fluorescence. This indicates that long-lived radiative decay ($> ns$), which would be of concern for sunscreen applications, does not occur in avobenzene. However, a low intensity positive offset is present in the lineouts at 550 nm at both temperatures (Fig. S8, ESI[†]), which persists beyond the 2.5 ns timescale of our experiment. At 600 nm, following the decay of the initial ESA as observed in Fig. S8 and S9 (ESI[†]), a similar offset to that at 550 nm is present. These offsets are akin to similar data presented by Verma *et al.*⁵⁰ in DBM at 538 nm and could be attributed to the formation of a triplet state of enolic avobenzene. Such states have previously been proposed as an additional route to the formation of the diketo photoproduct of avobenzene and photodegradation of dibenzoylmethane compounds.^{50,53}

To investigate this possibility further, TD-DFT was used to calculate the energies of the singlet and triplet states of the chelated enol and diketo forms of avobenzene. Table S4 (ESI[†]) shows the optimised ground-state structures attained using DFT, alongside the calculated vertical excitation energies and state characters of the first five singlet and triplet states using TD-DFT. Table S5 shows the calculated triplet state energies using the Δ SCF method, which is generally considered to be more accurate for T_1 energy determination.⁵⁴ These calculations have returned values of between 460 and 500 nm for the absorption of the T_1 relative to the ground state. Furthermore, the $T_4(^3n\pi^*)$ state is close in energy to the $S_1(^1\pi\pi^*)$ state, further supporting the observation of fast intersystem crossing from the chelated enol form of avobenzene, in accordance with El Sayed's rule. The singlet-state energies calculated for the chelated enol form align well with experimental values (*e.g.* Fig. 1); moreover both the singlet and triplet state energies attained are comparable to those in previous computational studies.^{55,56}

To complete the assignment of the time constants given in Table 1, τ_3 is assigned to the lifetime of the vibrationally hot chelated enol form of avobenzene in the ground electronic state (S_0). In Fig. 2(e) and (f), a blue-shifting ESA peak with concurrent narrowing, a characteristic manifestation of vibrational cooling,⁵⁷ can be seen in the transients up to and including 10 ps. From the lineouts at 395 nm and 415 nm, the ESA has completely decayed after around 25 ps. The ESA decay coincides almost exactly with the maximum GSB recovery within the time delay limits of our experiments, in both the heated and room temperature models. Both in the case of avobenzene and DBM, these coincident recovery and decay rates are indicative of an intermediate species returning to its original, ground state form. Dunkelberger *et al.*²³ also suggest that, after UVA

photoexcitation, the vibrationally excited S_0 chelated enol form of avobenzone relaxes in the same timeframe as the GSB recovers. Verma *et al.*⁵⁰ also observed a concurrence between the decay of the GSB and the ESA for DBM in acetonitrile, where a complete recovery of the positive ESA feature at 385 nm is observed within 14 ps, leaving behind a constant (negative) GSB offset. The excess energy inducing vibrational motion in the ground electronic state, can then dissipate safely as heat into the surrounding environment, in this case the solvent. Such formation of a vibrationally excited species is considered a favourable relaxation pathway. The main difference, albeit relatively minor, between the two sample temperatures was the lifetime of τ_3 in ethanol, where a ~ 1 ps decrease in lifetime was observed under heating to skin surface temperature.

The negative offset at 360 and 375 nm, which remains constant from 25 ps up to the remaining time window of our experiments, reveals an incomplete GSB recovery, denoted by τ_4 (> 2.5 ns). The extent of GSB recovery is of significant interest for sunscreen applications. Ideally, a 100% GSB recovery would be observed within the TEAS time delay window, which would indicate that all excited-state molecules have recovered to their initial ground-state form. Thereafter, the molecule can reabsorb UV radiation and perform its role as a sunscreen filter. A close to full recovery (*i.e.* return to zero signal) is observed in UV filters such as octocrylene,²⁷ however, this is not the case with avobenzone, as previously evidenced. The most likely explanation for the incomplete GSB recovery in this instance is the formation of one or more photoproducts, such as long-lived photoisomers. Such isomers have been suggested in earlier laser flash photolysis experiments, with lifetimes on the order of milliseconds.^{3,12} A photoproduct cannot always be detected using TEAS as it may absorb outside the spectral window of the probe, or its appearance may manifest as a convolution of spectral features. For example, for the asymmetric molecule BZA, there was an observed increase in the ESA region with respect to time,⁵¹ which was assigned to the formation of further non-chelated enol species separate to that caused by hydroxyl bond torsion; a scenario that has also been suggested for avobenzone.²³ As such, in this instance, it is challenging to quantitatively determine GSB recovery percentage for avobenzone in our experiments, as there may be a convolution of signals from the formation of photoproducts in the GSB region. Furthermore, although not possible to determine an exact quantum yield, a small percentage of the photoexcited avobenzone molecules are likely to undergo intersystem crossing, given the proximity of $^1\pi\pi^*$ states to $^3n\pi^*$ states, as discussed earlier. It follows, therefore, that formation of triplet states is an additional contributing factor to the incomplete GSB recovery.

The effect of reducing the concentration of avobenzone 10-fold from 10 mM to 1 mM was also investigated at both temperatures (Fig. S3, ESI[†]). This concentration reduction had no qualitative effect on the dynamics observed for avobenzone, nor was there any significant effect observed when the temperature was increased at the lower concentration. It was not possible to test concentrations > 10 mM, as the optical density of the sample was too high at the 25 μm path length. In addition, owing to the similarities of the

TEAS spectra at both room (Fig. S2, ESI[†]) and skin surface temperature (Fig. 2), it can be confidently stated that the increase in temperature does not appear to have significant impact on the photoprotection mechanism of avobenzone, under these experimental conditions.

The knowledge gained on avobenzone (and comparable molecules) in ethanol and cyclohexane can now be used to interpret its behaviours in two emollients at skin surface temperature, representing a cosmetically more relevant system. The effect that emollients can have on sunscreen performance has been of recent experimental interest.⁵⁸ TEAS measurements at ~ 35 °C were performed in two emollients, DIA and LL. The measurements in emollient were conducted at surface skin temperature only, to determine any differences between the solvents in this closer to real-life model. The results are shown in the bottom two rows of Fig. 2, and the global fitting analysis results are shown alongside those for ethanol and cyclohexane in Table 1, to aid comparison. Both datasets reveal similar spectral features; these features, in turn, are also qualitatively comparable to those observed in ethanol and cyclohexane as discussed above. The slight quantitative differences in the time constants, are most likely due to minor variations in emollient polarity. Upon closer inspection of Fig. 2(l), showing the lineouts in LL, there appears to be the beginnings of a GSB recovery in the lineouts at 360 and 375 nm within the time window of our TEAS setup, in contrast to the three other solvents. This could indicate that, the relaxation of an intermediate species can occur faster in LL compared to the other solvents. Overall, the parallels between the TEAS measurements in Fig. 2 indicate that the way avobenzone dissipates excess UV energy on ultrafast timescales is mostly unaffected by the solvent environment, in agreement with the findings of Dunkelberger *et al.*²³ Furthermore, it can be deduced that the concentration of avobenzone does not appear to have a noticeable impact upon its ultrafast photodynamics within the 1–10 mM range.

To investigate the properties of avobenzone in emollients further, in keeping with a *bottom-up* approach, mixtures of UV filters including avobenzone were made and exposed to solar-simulated radiation for two hours. The results of the steady-state UV-visible spectroscopy used to track photodegradation (Fig. 3) suggest that ~ 4 $\mu\text{g mL}^{-1}$ avobenzone is photostable in DIA and LL, in mixtures where ethylhexyl methoxycinnamate (EHMC) and octocrylene are also present in low concentrations (~ 10 $\mu\text{g mL}^{-1}$ and ~ 13 $\mu\text{g mL}^{-1}$ respectively). This can be seen as the absorbance in the UVA region has remained constant for the duration of the irradiation time. It was not possible to observe whether the diketo photoproduct of avobenzone was being formed, due to saturation of the detector in the UV-visible spectrometer at wavelengths < 290 nm caused by emollient (solvent) absorption. The reduction in the absorption of these mixtures in the region of 290 – 320 nm is assigned to the *trans-cis* isomerization that is known to occur in EHMC.^{59–61} Although absorption of the UVB wavelengths is not affected by this isomerisation (*i.e.* there is no observed red or blue shift), the extinction coefficient of the *cis* species is markedly lower than the *trans* species, thus a reduction in absorption in the

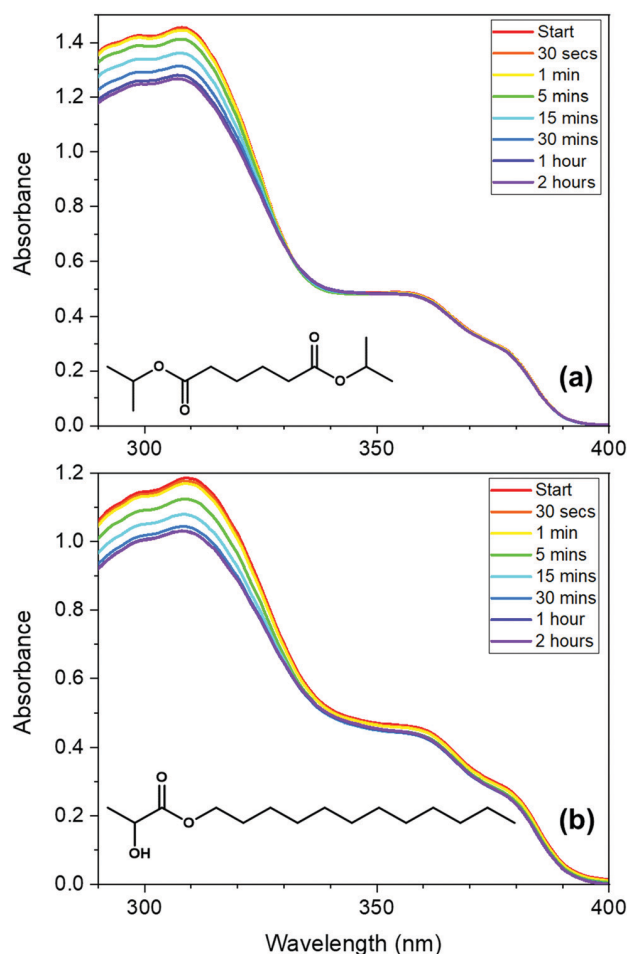


Fig. 3 UV-visible absorption spectra of low-concentration avobenzone, EHMC and octocrylene mixtures ($\sim 4 \mu\text{g mL}^{-1}$ of avobenzone, $\sim 10 \mu\text{g mL}^{-1}$ EHMC and $\sim 13 \mu\text{g mL}^{-1}$ octocrylene; 3:7.5:10 ratio), taken following irradiation using a solar simulator at regular intervals between 0 and 2 hours, in the following emollients: (a) diisopropyl adipate (DIA) and (b) lauryl lactate (LL). The molecular structure of the emollients is inset on the respective graphs. The spectra at each time point were measured three times consecutively, then averaged to attain the presented data. This was repeated twice on different days with new sample made with the same bulk ingredients, with similar results.

UVB region is observed.⁶¹ The concentrations used for the irradiation studies in Fig. 3 were markedly lower compared to a completed sunscreen formulation (around 10^4 times more dilute), however the concentrations were maximised to be suitable for this type of analysis.

Next, *in vitro* SPF and UVA-PF values were measured for the five oil phase samples (components detailed in Table S1, ESI[†]); the results are shown in Table 2. Samples 1–4 contain the same proportion of the three UV filters as the samples used to attain the results in Fig. 3, however SPF and UVA-PF protocols are designed for concentrations in line with those in a completed sunscreen formulation. By using these protocols, the effect of including additional UV filters in an avobenzone/emollient solution could be investigated at clinically relevant concentrations. The most concentrated samples (1 and 2) based upon DIA and LL respectively, demonstrate a similar performance overall, with

Table 2 Summary of the SPF and UVA-PF percentage changes attained for Samples 1 to 5 before and after irradiation at $\sim 550 \text{ W m}^{-2}$ over the 300–800 nm wavelength range for 3.6 hours. Values are an average of results from 3 different samples, which are in turn an average of readings from 3 different points on the sample plate. The negative values for percentage change denote a reduction in that parameter, with the errors equalling the standard deviation of the percentage changes. Sample numbers refer to the blend composition detailed in Table S1 (ESI)

Test	Sample	% Change SPF	% Change UVA-PF
Different emollients	1	-15.8 ± 2.2	-21.4 ± 1.6
	2	-14.9 ± 0.9	-20.3 ± 1.1
Different concentration of UV filters	3	-13.6 ± 1.6	-9.3 ± 1.2
	4	-9.7 ± 1.9	-3.7 ± 1.6
Different proportions of UV filters	5	-21.3 ± 1.3	-28.0 ± 1.4

the percentage decrease in SPF and UVA-PF following irradiation being slightly more favourable in Sample 2. However, upon comparison of Samples 1, 3 and 4, all of which have DIA as the base emollient, there appears to be some variation in performance when the concentrations of the UV filters are changed. Sample 1 has the active ingredients in the highest concentration, followed by Sample 3 (5-fold dilution compared to Sample 1), with Sample 4 having the lowest concentration (a 10-fold reduction compared to Sample 1). From the results in Table 2, it appears that the extent of degradation decreases as the concentration of filters is reduced. It is possible that the emollients are effective in dissipating excited-state energy from the UV filters via energy transfer (heating) from the filter to the solvent, thus minimising degradation. However, the more likely scenario is that there is added protection from a higher proportion of emollient due to spectral overlap, with the absorbance region of the emollients beginning at around 400 nm. This dependence may also explain why almost no degradation in the UVA region is observed in the UV-Vis spectra in Fig. 3, which measured the same ratio of filters in the lowest concentration.

To determine whether intermolecular interactions that can drive photodegradation occur in the bulk oil phase, Sample 1 and Sample 5 were compared. The amount of avobenzone is the same between each of these samples (equivalent to 2.2% w/w in an oil-in-water formulation, assuming 25% oil), but the proportions of EHMC and octocrylene have been reversed. It is known that EHMC adversely affects the photostability of avobenzone;^{62–64} conversely, octocrylene improves avobenzone's photostability via triplet-triplet energy state quenching.^{65–67} This is in line with observations between Sample 1 and Sample 5 (Table 2), whereby the percentage decrease in SPF and UVA-PF is larger for Sample 5 in both cases, which contains the greater proportion of EHMC. The study by Kikuchi *et al.*⁶² also concluded that the addition of EHMC to a mixture of avobenzone and octocrylene harms photostability. The results in Table 2 suggest that diffusion-limited energy transfer mechanisms between the UV filters in the mixture are likely have a role to play in the photostability of avobenzone, as previously investigated in the work of Yagi and co-workers,^{62,68–70} alongside the reduction in photodegradation due to spectral protection (solvent absorbing UV radiation rather than the UV filter).⁶⁷

It is noted that we opted not to study blends using TEAS for the present work, as a convolution of TEAS signals of all three UV filters may have masked avobenzone signals of interest. We aim, however, to further develop our TEAS setup in future experiments to assess the effect of these intermolecular energy transfer processes by: (1) extending the time-window of our measurements from fs through to ms; and (2) investigating higher concentration effects by minimising path length through the sample via model skin surface studies. The former could also be of great benefit for a more detailed assessment of the effect of GSB recovery on the long-term SPF and UVA-PF metrics.

This section is concluded by considering the TEAS measurements alongside the steady-state SPF and UVA-PF measurements. It is unsurprising that there is a notable reduction in SPF and UVA-PF of Samples 1–5, when one considers the incomplete GSB recovery seen in Fig. 2. Long-lived photoproducts of avobenzone (the presence of which is indicated by the incomplete recovery) not only reduce the UVA protection it provides; they also have the potential to disrupt the efficacy of sunscreen blends as photoproducts can undergo further light-induced processes. TEAS detects the early onset of photoproducts and the routes by which they are formed, which we suggest may offer an alternative tool for increasing emulsion photostability. For example, improvement could be realised by adding or changing functional groups within UV filters such as avobenzone⁷¹ towards increasing GSB recovery. Assuming there is no convolution of positive signals in the GSB region, this will indicate that the proportion of UV filter that returns to its electronic ground state has increased, thus reducing the drop in SPF and UVA-PF values. Encouraging evidence that this approach could be successful is indicated in the TEAS data and SPF/UVA-PF metrics for avobenzone in LL, whereby a marginal GSB recovery was observed towards the end of the TEAS spectral window, which is reflected in the slightly improved performance of LL in the SPF and UVA-PF tests compared to DIA.

Conclusions

In this work, the photoprotection mechanism of the UVA filter avobenzone has been studied using transient electronic absorption spectroscopy (TEAS), building upon prior research.²³ Specifically, we have tracked the excited state dynamics of avobenzone solutions at elevated temperatures, by heating the sample interaction region to skin surface temperature, thus aligning with closer-to-real-world sunscreen usage. The TEAS results have shown that upon UVA excitation, the excited-state relaxation mechanisms of avobenzone in ethanol, cyclohexane, diisopropyl adipate and lauryl lactate (the latter two being commercial emollients) are very similar. This observation holds whether these TEAS data are taken at skin surface temperature, room temperature and/or with a 10-fold reduction in concentration. In the future, it may be of interest to investigate whether larger deviations in temperature result in directly observable changes in intramolecular H-bond strength, or the decay rate of non-chelated enol photoproducts of avobenzone, as suggested in earlier publications.^{3,40}

The present study demonstrates that TEAS, supported here by DFT and steady-state irradiation methodologies, can be used as a complementary analysis tool alongside industry-standard techniques for evaluating sunscreen performance (SPF and UVA-PF testing). By garnering fundamental insight into the ultrafast photodynamics of sunscreen molecules, molecular design of optimal UV filters can be predicted; for example, maximising ground state bleach (GSB) recovery in TEAS measurements limits the potential photodegradation of the UV filter. It would be beneficial for future studies to monitor the evolution of the GSB beyond the nanosecond timescales possible here, to further affirm the link between ultrafast observations and long-term photostability. This, in turn, may lead to improved suncare formulations.

Author contributions

E. L. H. was responsible for preparing the manuscript, data curation, validation, formal analysis, investigation and visualization of the TEAS, steady-state and computational data. N. d. N. R. was responsible for data curation, investigation, formal analysis and validation of the SPF and UVA-PF data. J. C. provided resources, V. G. S. provided supervision and acquired funding. All authors contributed to the conceptualization of the study and reviewed the manuscript.

Conflicts of interest

There are no conflicts to declare.

Acknowledgements

E. L. H. thanks the Engineering and Physical Sciences Research Council (EPSRC) for a PhD studentship through the EPSRC Centre for Doctoral Training in Molecular Analytical Science, grant number EP/L015307/1; also, the Warwick Research Technology Platform for Scientific Computing and the HPC Midlands+ consortium (EPSRC grant number EP/P020232) for computational resources. N. d. N. R. acknowledges support and funding from the European Union's Horizon 2020 research and innovation programme under grant agreement number 844177—SUNNRL. V. G. S. thanks the Royal Society for a Royal Society Industry Fellowship and the EPSRC under Grant EP/N010825 for equipment funds (WCUS). The authors would also like to thank Dr Laurent Blasco for the expertise and enthusiasm he provided during helpful discussions, and Dr Claudio Ribeiro (Lubrizon) for conducting preliminary skin surface temperature measurements in São Paulo, Brazil. Finally, the authors thank Rod Wesson (University of Warwick) for building the temperature controller used in this work.

References

- 1 S. Q. Wang, P. R. Tanner, H. W. Lim and J. F. Nash, *Photochem. Photobiol. Sci.*, 2013, **12**, 197–202.
- 2 I. Andrae, A. Bringhen, F. Böhm, H. Gonzenbach, T. Hill, L. Mulroy and T. G. Truscott, *J. Photochem. Photobiol., B*, 1997, **37**, 147–150.

- 3 A. Cantrell and D. J. McGarvey, *J. Photochem. Photobiol., B*, 2001, **64**, 117–122.
- 4 J. B. Mancuso, R. Maruthi, S. Q. Wang and H. W. Lim, *Am. J. Clin. Dermatol.*, 2017, **18**, 643–650.
- 5 C. Paris, V. Lhiaubet-Vallet, O. Jimenez, C. Trullas and M. A. Miranda, *Photochem. Photobiol.*, 2009, **85**, 178–184.
- 6 S. Osseiran, E. M. Roider, H. Wang, Y. Suita, M. Murphy, D. E. Fisher and C. L. Evans, *J. Biomed. Opt.*, 2017, **22**, 125004.
- 7 S. Afonso, K. Horita, J. P. S. eSilva, I. F. Almeida, M. H. Amaral, P. A. Lobão, P. C. Costa, M. S. Miranda, J. C. G. E. da Silva and J. M. S. Lobo, *J. Photochem. Photobiol., B*, 2014, **140**, 36–40.
- 8 G. J. Mturi and B. S. Martincigh, *J. Photochem. Photobiol., A*, 2008, **200**, 410–420.
- 9 K. M. Hanson, M. Cutuli, T. Rivas, M. Antuna, J. Saoub, N. T. Tierce and C. J. Bardeen, *Photochem. Photobiol. Sci.*, 2020, **19**, 390–398.
- 10 J. J. Vallejo, M. Mesa and C. Gallardo, *Vitae*, 2011, **18**, 63–71.
- 11 A. R. Abid, B. Marciniak, T. Pędziński and M. Shahid, *J. Photochem. Photobiol., A*, 2017, **332**, 241–250.
- 12 M. Yamaji and M. Kida, *J. Phys. Chem. A*, 2013, **117**, 1946–1951.
- 13 B. P. Binks, P. D. Fletcher, A. J. Johnson, I. Marinopoulos, J. Crowther and M. A. Thompson, *J. Photochem. Photobiol., A*, 2017, **333**, 186–199.
- 14 S. Moi, B. Hosamani, K. Kumar, S. Gunaga, S. Raghothama and K. H. Gowd, *J. Photochem. Photobiol., A*, 2021, **420**, 113488.
- 15 N. A. Shaath, *Photochem. Photobiol. Sci.*, 2010, **9**, 464–469.
- 16 P. Govindu, B. Hosamani, S. Moi, D. Venkatachalam, S. Asha, V. John, V. Sandeep and K. Gowd, *Photochem. Photobiol. Sci.*, 2019, **18**, 198–207.
- 17 J. Kockler, S. Robertson, M. Oelgemöller, M. Davies, B. Bowden, H. G. Brittain and B. D. Glass, *Profiles of Drug Substances, Excipients and Related Methodology*, Elsevier, 2013, vol. 38, pp. 87–111.
- 18 S. Scalia and M. Mezzena, *AAPS PharmSciTech*, 2009, **10**, 384–390.
- 19 R. B. Murphy, J. Staton, A. Rawal and T. A. Darwish, *Photochem. Photobiol. Sci.*, 2020, **19**, 1410–1422.
- 20 I. Karlsson, L. Hillerström, A.-L. Stenfeldt, J. Mårtensson and A. Börje, *Chem. Res. Toxicol.*, 2009, **22**, 1881–1892.
- 21 W. Schwack and T. Rudolph, *J. Photochem. Photobiol., B*, 1995, **28**, 229–234.
- 22 J. A. Berenbeim, N. G. K. Wong, M. C. R. Cockett, G. Berden, J. Oomens, A. M. Rijs and C. E. H. Dessent, *J. Phys. Chem. A*, 2020, **124**, 2919–2930.
- 23 A. D. Dunkelberger, R. D. Kieda, B. M. Marsh and F. F. Crim, *J. Phys. Chem. A*, 2015, **119**, 6155–6161.
- 24 L. A. Baker, M. D. Horbury, S. E. Greenough, P. M. Coulter, T. N. V. Karsili, G. M. Roberts, A. J. Orr-Ewing, M. N. R. Ashfold and V. G. Stavros, *J. Phys. Chem. Lett.*, 2015, **6**, 1363–1368.
- 25 Y. Peperstraete, M. Staniforth, L. A. Baker, N. D. Rodrigues, N. C. Cole-Filipiak, W.-D. Quan and V. G. Stavros, *Phys. Chem. Chem. Phys.*, 2016, **18**, 28140–28149.
- 26 E. L. Holt, K. M. Krokidi, M. A. P. Turner, P. Mishra, T. S. Zwier, N. d. N. Rodrigues and V. G. Stavros, *Phys. Chem. Chem. Phys.*, 2020, **22**, 15509–15519.
- 27 L. A. Baker, M. D. Horbury and V. G. Stavros, *Opt. Express*, 2016, **24**, 10700–10709.
- 28 M.-H. Kao, R. K. Venkatraman, M. Sneha, M. Wilton and A. J. Orr-Ewing, *J. Phys. Chem. A*, 2021, **125**, 636–645.
- 29 N. d. N. Rodrigues, N. C. Cole-Filipiak, M. A. P. Turner, K. Krokidi, G. L. Thornton, G. W. Richings, N. D. M. Hine and V. G. Stavros, *Chem. Phys.*, 2018, **515**, 596–602.
- 30 L. A. Baker and V. G. Stavros, *Sci. Prog.*, 2016, **99**, 282–311.
- 31 E. L. Holt and V. G. Stavros, *Int. Rev. Phys. Chem.*, 2019, **38**, 243–285.
- 32 S. P. Huong, E. Rocher, J.-D. Fourneron, L. Charles, V. Monnier, H. Bun and V. Andrieu, *J. Photochem. Photobiol., A*, 2008, **196**, 106–112.
- 33 P. Trebse, O. Polyakova, M. Baranova, M. Kralj, D. Dolenc, M. Sakhra, A. Kutin and A. Lebedev, *Water Res.*, 2016, **101**, 95–102.
- 34 J. V. T. Gomes, A. C. P. da Silva, M. L. Bello, C. R. Rodrigues and B. A. M. C. Santos, *J. Mol. Model.*, 2019, **25**, 1–11.
- 35 C. T.-L. Chan, C. Ma, R. C.-T. Chan, H.-M. Ou, H.-X. Xie, A. K.-W. Wong, M.-L. Wang and W.-M. Kwok, *Phys. Chem. Chem. Phys.*, 2020, **22**, 8006–8020.
- 36 J. Wang, Y. Lei, Y. Guo, J. Wang and J. Ma, *Photochem. Photobiol. Sci.*, 2019, **18**, 3000–3007.
- 37 L. Ferrero, M. Pissavini and O. Doucet, *Photochem. Photobiol. Sci.*, 2010, **9**, 540–551.
- 38 J. Stanfield, U. Osterwalder and B. Herzog, *Photochem. Photobiol. Sci.*, 2010, **9**, 489–494.
- 39 A. Springsteen, R. Yurek, M. Frazier and K. F. Carr, *Anal. Chim. Acta*, 1999, **380**, 155–164.
- 40 E. V. Borisov, E. V. Skorodumov, V. M. Pachevskaya and P. E. Hansen, *Magn. Reson. Chem.*, 2005, **43**, 992–998.
- 41 M. D. Horbury, E. L. Holt, L. M. M. Mouterde, P. Balaguer, J. Cebrián, L. Blasco, F. Allais and V. G. Stavros, *Nat. Commun.*, 2019, **10**, 4748.
- 42 Y. Liu, X. Zhao, J. Luo and S. Yang, *J. Lumin.*, 2019, **206**, 469–473.
- 43 T. T. Abiola, N. d. N. Rodrigues, C. Ho, D. J. Coxon, M. D. Horbury, J. M. Toldo, M. T. do Casal, B. Rioux, C. Peyrot and M. M. Mention, *J. Phys. Chem. Lett.*, 2020, **12**, 337–344.
- 44 J. M. Woolley, M. Staniforth, M. D. Horbury, G. W. Richings, M. Wills and V. G. Stavros, *J. Phys. Chem. Lett.*, 2018, **9**, 3043–3048.
- 45 J. J. Snellenburg, S. P. Laptinok, R. Seger, K. M. Mullen and I. H. M. van Stokkum, *J. Stat. Softw.*, 2012, **49**, 1–22.
- 46 L. J. G. W. van Wilderen, C. N. Lincoln and J. J. van Thor, *PLoS One*, 2011, **6**, e17373.
- 47 J. Beckwith, C. Rumble and E. Vauthey, *Int. Rev. Phys. Chem.*, 2020, **39**, 135–216.
- 48 M. P. Grubb, A. J. Orr-Ewing and M. N. R. Ashfold, *Rev. Sci. Instrum.*, 2014, **85**, 064104.
- 49 G. Ni, G. Li, S. V. Boriskina, H. Li, W. Yang, T. Zhang and G. Chen, *Nat. Energy*, 2016, **1**, 1–7.
- 50 P. K. Verma, F. Koch, A. Steinbacher, P. Nuernberger and T. Brixner, *J. Am. Chem. Soc.*, 2014, **136**, 14981–14989.
- 51 P. K. Verma, A. Steinbacher, F. Koch, P. Nuernberger and T. Brixner, *Phys. Chem. Chem. Phys.*, 2015, **17**, 8459–8466.
- 52 S. Tobita, J. Ohba, K. Nakagawa and H. Shizuka, *J. Photochem. Photobiol., A*, 1995, **92**, 61–67.

- 53 A. Aspée, C. Aliaga and J. Scaiano, *Photochem. Photobiol.*, 2007, **83**, 481–485.
- 54 R. J. Charlton, R. M. Fogarty, S. Bogatko, T. J. Zuehlsdorff, N. D. M. Hine, M. Heeney, A. P. Horsfield and P. D. Haynes, *J. Chem. Phys.*, 2018, **148**, 104108.
- 55 M. Kojić, M. Petković and M. Etinski, *Phys. Chem. Chem. Phys.*, 2016, **18**, 22168–22178.
- 56 G. H. G. Trossini, V. G. Maltarollo, R. D. A. Garcia, C. A. S. O. Pinto, M. V. R. Velasco, K. M. Honorio and A. R. Baby, *J. Mol. Model.*, 2015, **21**, 319.
- 57 M. D. Horbury, W.-D. Quan, A. Flourat, F. Allais and V. G. Stavros, *Phys. Chem. Chem. Phys.*, 2017, **19**, 21127–21131.
- 58 M. Sohn, L. Amorós-Galicia, S. Krus, K. Martin and B. Herzog, *J. Photochem. Photobiol., B*, 2020, **205**, 111818.
- 59 L. R. Gaspar and P. M. Campos, *Int. J. Pharm.*, 2006, **307**, 123–128.
- 60 K. M. Hanson, S. Narayanan, V. M. Nichols and C. J. Bardeen, *Photochem. Photobiol. Sci.*, 2015, **14**, 1607–1616.
- 61 S. Pattanaargson, T. Munhapol, N. Hirunsupachot and P. Luangthongaram, *J. Photochem. Photobiol., A*, 2004, **161**, 269–274.
- 62 A. Kikuchi, Y. Nakabai, N. Oguchi-Fujiyama, K. Miyazawa and M. Yagi, *J. Lumin.*, 2015, **166**, 203–208.
- 63 R. M. Sayre, J. C. Dowdy, A. J. Gerwig, W. J. Shelds and R. V. Liloyd, *Photochem. Photobiol.*, 2005, **81**, 452–456.
- 64 D. Dondi, A. Albini and N. Serpone, *Photochem. Photobiol. Sci.*, 2006, **5**, 835–843.
- 65 V. Lhiaubet-Vallet, M. Marin, O. Jimenez, O. Gorchs, C. Trullas and M. A. Miranda, *Photochem. Photobiol. Sci.*, 2010, **9**, 552–558.
- 66 D. G. Beasley and T. A. Meyer, *Am. J. Clin. Dermatol.*, 2010, **11**, 413–421.
- 67 B. Herzog, J. Giesinger and V. Settels, *Photochem. Photobiol. Sci.*, 2020, **19**, 1636–1649.
- 68 S. Matsumoto, R. Kumasaka, M. Yagi and A. Kikuchi, *J. Photochem. Photobiol., A*, 2017, **346**, 396–400.
- 69 R. Kumasaka, A. Kikuchi and M. Yagi, *Photochem. Photobiol.*, 2014, **90**, 727–733.
- 70 A. Kikuchi and M. Yagi, *Chem. Phys. Lett.*, 2011, **513**, 63–66.
- 71 J. Zawadiak and M. Mrzyczek, *Spectrochim. Acta, Part A*, 2012, **96**, 815–819.

Electronic Supplementary Information

Determining the photostability of avobenzone in sunscreen formulation models using ultrafast spectroscopy

Supplementary Methods

(a) Instrument response

To estimate the instrument response function (IRF) of our TEAS setup, solvent-only scans of each solvent were taken under the same conditions as the sample, for time delays between -1 ps and 1 ps. A representative slice at ~ 380 nm was taken across all time delays and the resulting transients were fitted with a Gaussian function, shown in Equation 1. In this equation, A denotes the amplitude of the fitted curve; t_0 is the fitted time zero, indicating the centre of the curve where the peak amplitude occurs; σ is the standard deviation of the curve and finally, s is a variable that allows for any signal offset. In practice, t_0 is the exact time where the pump and probe meet the sample at the same time.

$$f(t) = A \exp\left(-\frac{(t-t_0)^2}{2\sigma^2}\right) + s \quad (1)$$

The value of σ is converted to the full width at half maximum (FWHM) value to extract the IRF, by multiplying by the scaling factor $2\sqrt{2\ln 2}$. After scaling, the extracted IRF lifetimes are ~ 140 fs in ethanol and ~ 80 fs in cyclohexane. The raw data and the fitted Gaussian function are shown in Fig. S1. At the selected wavelength, it was not possible to attain any signal from the solvent alone from either of the emollients, diisopropyl adipate and lauryl lactate. However, the upper bound of these lifetimes (140 fs) can be considered a good estimate for the IRF in emollient.

(b) Computational methods

All calculations were performed using the NWChem software package.¹ Density functional theory (DFT) geometry optimisations for the *chelated enol* and *diketo* structures of avobenzone (see Fig. 1) were carried out to determine the most stable, lowest energy conformations in the ground state. These calculations were conducted in implicitly modelled ethanol and cyclohexane, using the conductor-like screening model (COSMO, with SMD) built

into NWChem.^{2,3} The relaxation of the initial *enol* and *diketo* structures of avobenzene was initially carried out using DFT at the PBE/6-31g* level of theory. This initial structure was then further optimized either by improving the functional to PBE0 or improving the basis set to 6-311++g**, before arriving at the final structure, which was calculated at the PBE0/6-311++g** level of theory. Once these optimised structures were attained, time-dependent DFT (TD-DFT) was carried out to attain the vertical excitation energies of the singlet (S_n) and triplet (T_n) states of each species in both solvents using the same COSMO model. The vertical excitation energies of the five lowest energy singlet and triplet states were calculated using these optimised structures using TD-DFT at the PBE0/6-311++g** level of theory. The state characters were also calculated during these TD-DFT calculations and assigned manually. For additional confirmation of the T_1 state energy, a Δ SCF methodology was also used.⁴ The triplet single point energy for the Δ SCF method was calculated at the PBE0/6-311++g** level of theory. For this, the multiplicity was set to three on each of the optimised ground state structures; the single point energy was then compared to the ground state single point energy.

(c) SPF testing

The SPF and UVA-PF values for the five oil phase samples, prepared as described in the main manuscript were measured. Square poly(methyl methacrylate) (PMMA) plates of 5 cm by 5 cm (25 cm²), with a textured surface on one side and smooth on the other, were cleaned with deionized water and left to dry in a temperature controlled chamber at 25°C for at least two hours, until they were ready for use. Approximately 15 mg of sample was placed on the plates in a 3 x 3 square grid pattern. The samples were then applied by rubbing the samples onto each plate with a gloved finger (nitrile gloves), first in rotative motions and then with swift back and forth motions between opposite edges of the square plate, to achieve an even distribution of sample on the plate. After application, the sample coated PMMA plates were left to rest in the HD-Thermaster at 25°C for 30 minutes before testing. A blank plate was prepared in a similar fashion, using 15 mg of glycerin applied in a 3 x 3-point grid.

The SPF and UVA-PF studies were carried out using a LabSphere UV-2000 ultraviolet (UV) transmittance analyser (LabSphere, Inc.). The SPF and UVA-PF values for each plate are calculated based on an average of readings from 5 different points on the plate. The final values presented in Table 2 in the main manuscript are an average of 3 plates for each oil phase sample. Each plate was analysed before and after irradiation with a SUNTEST CPS+ (III) solar simulator (Atlas Material Testing Solutions). This solar simulator delivers 550 W/m² over

the 300 – 800 nm wavelength range, and the irradiation was carried out for 3 hours and 36 minutes, equating to a radiation dose of approximately 7130 kJ/m², comparable with that delivered for the photostability measurements presented in the main manuscript.

Supplementary Discussion

(a) Review on skin surface temperature

Skin surface temperature (SST) is affected by factors such as climate,^{5,6} humidity,⁷ exercise,^{8,9} and wound healing,¹⁰ all of which may affect the efficacy of a sunscreen. Commonly, determination of mean SST (T_s) requires the summation of a finite number (n) of local skin temperatures (t_i), multiplied by a weighting factor (w_i),^{11,12} which is usually the fraction of the total body area each local measurement accounts for.¹² This can be notated according to Equation 2.

$$T_s = \sum_{i=1}^n w_i \cdot t_i \quad (2)$$

However, establishing reliable parameters to substitute into Equation 2 presents challenges, and indicates that a range of temperatures could be recommended for simulating human SST during the collection of ultrafast spectra. One study investigating the effects of exercise on mean SST, by de Andrade Fernandes *et al.*,⁹ found that two methods of measuring t_i , (thermocouple and infrared thermography) offered statistically significant differences on the value of T_s . Furthermore, their results could have been dependent on factors including types of exercise, weather conditions and whether subjects are male or female.

In addition to ascertaining reliable t_i measurements, the optimum weighting factors for n sites ($3 \leq n \leq 17$) have also been investigated; an extensive review of these is provided by Liu *et al.*¹² The number and location of local measurement sites, including the corresponding w_i , are not standardised. This lack of standardisation creates a source of inconsistency between results found in mean SST studies. In the publication by Liu *et al.*,⁵ SST measurements were plotted individually for typical areas that sunscreen is applied to, such as the face and arms. On the face, the SST was between 35 and 38°C (in a climatic chamber at temperatures between 26 and 38°C), whereas on the arms, the range under equivalent conditions was 32 and 35°C. The mean SST found in this study (measured using thermocouples) was 33 to 36°C. Notably, the mean SST results from comparable ambient conditions (26, 30 and 34°C) between studies by

Liu et al.⁵ and Atmaca and Yigit⁷ are in close agreement with one another ($\pm 0.4^\circ\text{C}$), which increases confidence in the accuracy of this temperature range.

It is normal for SST to be below that of core body temperature ($\sim 37^\circ\text{C}$),¹³ however some studies have shown that this temperature can also be exceeded. González-Alonso *et al.*¹⁴ found that the maximum T_s when subjects performed exercise under very extreme conditions ($\sim 40^\circ\text{C}$) was 38°C . Local SSTs have also been found to exceed the human core body temperature; as mentioned previously, the local SST of facial skin peaked at 38°C in the study by Liu *et al.*⁵ Another scenario where localised increase in SST occurs is during the healing of a wound, which can cause the temperature of the skin surrounding it (the periwound) to increase beyond 37°C .^{10, 13}

In conclusion, the temperature of the CaF_2 substrate and sample mixture should be heated to above room temperature to be representative of human SST. Any temperature within the range 32 to 38°C is justifiable in the literature for sunscreen applications. If experiments were to be focused on one temperature alone, important effects of temperature on the photochemical properties of sunscreen molecules may be missed.

Supplementary Figures

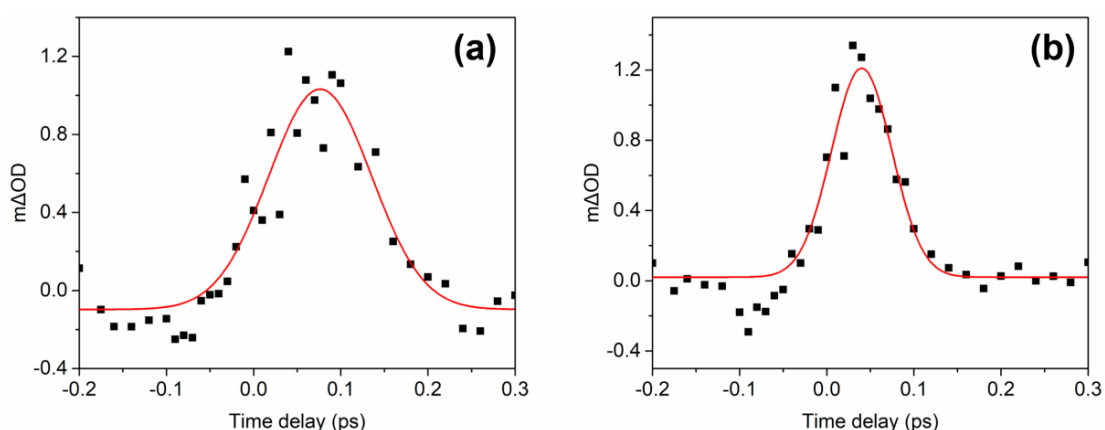


Figure S1: Instrument response functions in (a) ethanol (378 nm probe) and (b) cyclohexane (381 nm probe), when pumped at 350 nm, through 25 μm path length, without heating. The full-width half maximum was calculated to be ~ 140 fs in (a) and ~ 80 fs in (b).

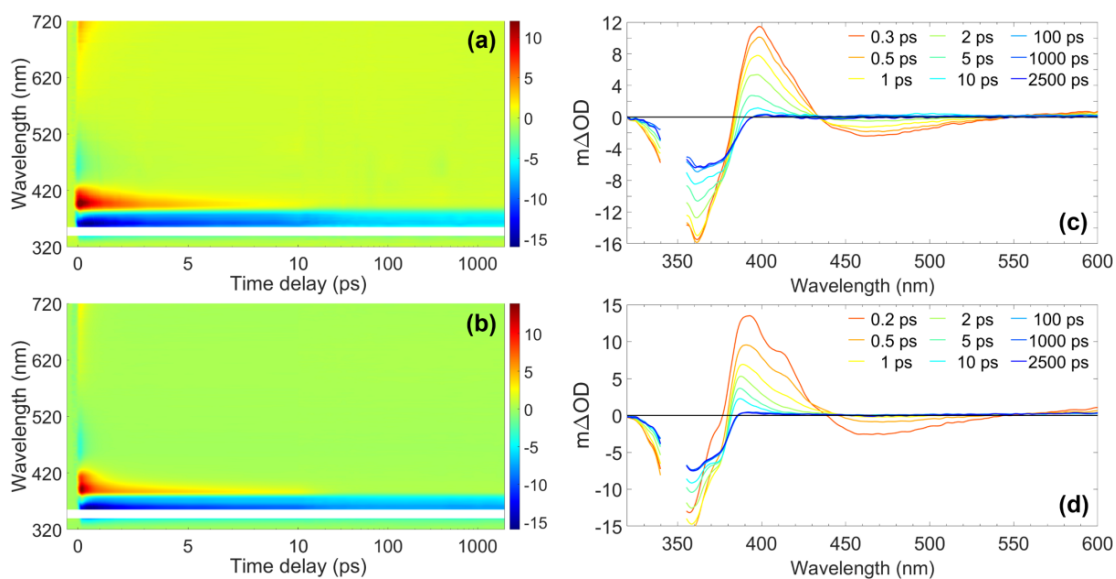


Figure S2: (Left) False colour heat maps showing all transient absorption spectra (TAS) of ~ 10 mM avobenzene photoexcited at approximately 350 nm in (a) ethanol and (b) cyclohexane with no heat applied. (Right) TAS at selected pump-probe time delays for avobenzene in (c) ethanol and (d) cyclohexane with no heat applied. These (right) plots are attained by taking vertical slices through the corresponding false colour heat maps at the given time delay and are presented using the same scale as the corresponding heat map. The region between 340 and 355 nm has been removed due to the pump laser pulse interfering with the data.

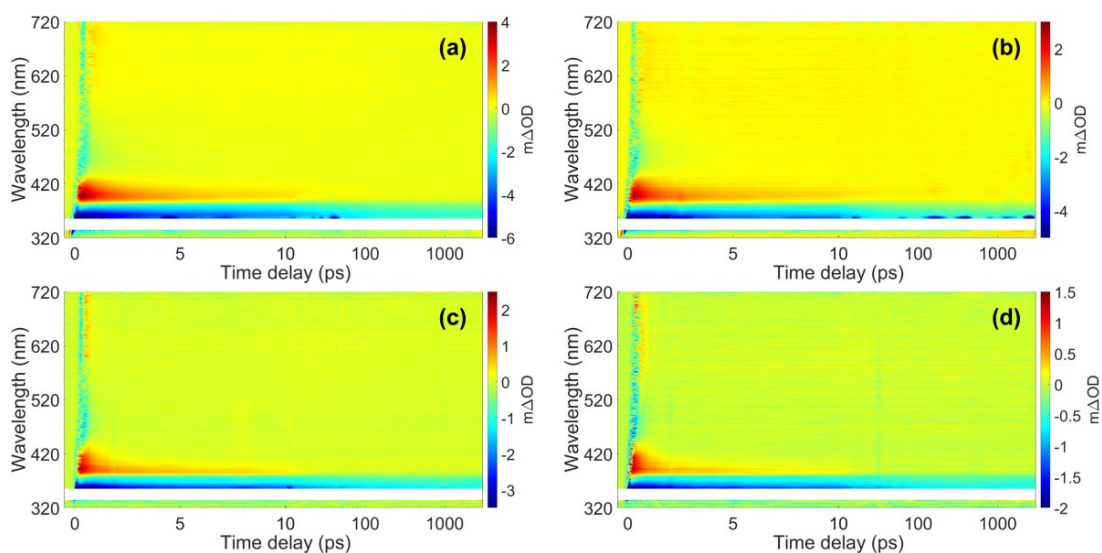


Figure S3: False colour heat maps (not chirp corrected) showing all transient absorption spectra (TAS) of ~ 1 mM avobenzene photoexcited at around 350 nm (a) in ethanol with no heat applied; (b) in ethanol with the sample cell heated to 35°C; (c) in cyclohexane with no heat applied and (d) in cyclohexane with the sample cell heated to 35°C. The region between 340 and 355 nm has been removed due to the pump laser pulse interfering with the data.

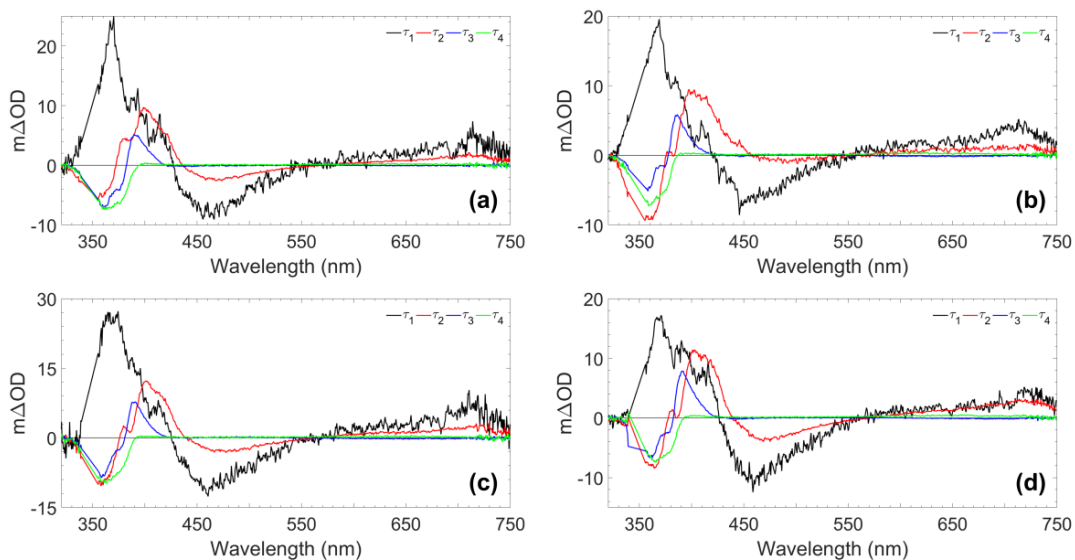


Figure S4: Decay associated spectra (DAS) for heated ~ 10 mM avobenzene solutions in (a) ethanol, (b) cyclohexane, (c) DIA and (d) LL, following photoexcitation at ~ 350 nm. These were obtained by using a parallel global kinetic fit model. The associated time constants can be found in Table 1 of the main manuscript. The values in the 340 – 355 nm region have been linearly interpolated.

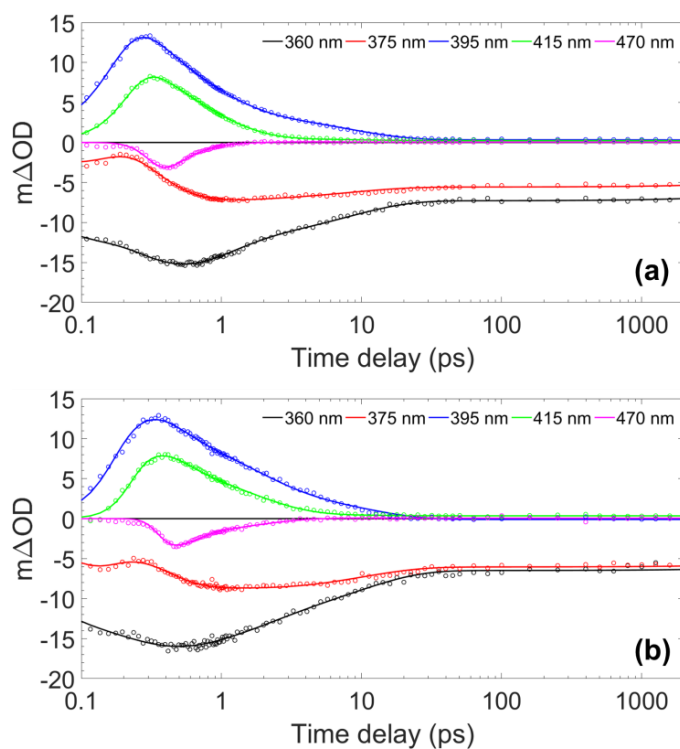


Figure S5: Lineouts to show spectral features at specific probe wavelengths for ~ 10 mM avobenzene in (a) cyclohexane and (b) ethanol with no heat applied. The circles denote the raw datapoints and the solid line in each case is the fit attained using a parallel kinetic model (time constants resulting from this fitting are shown in Table S3). The features at 360 nm and 375 nm are ground-state bleach features, 395 nm and 415 nm are excited-state absorption features and 470 nm is stimulated emission (see main manuscript for further details and discussion). The time delay axis is presented on a logarithmic scale. Time delays prior to 0.1 ps are presented on a linear scale in Fig. S6.

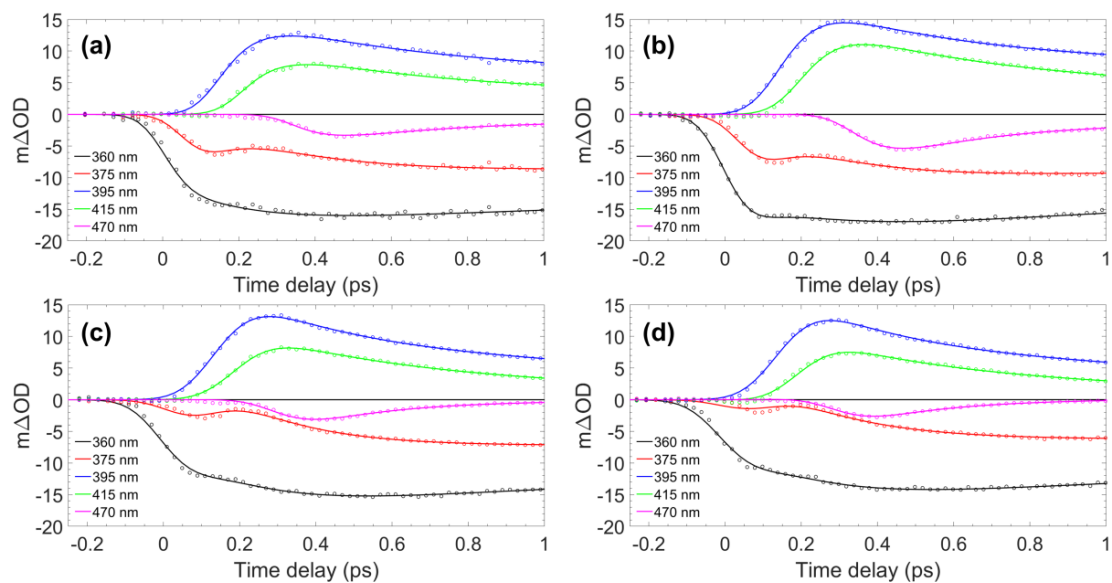


Figure S6: Lineouts prior to 1 ps showing spectral features at specific probe wavelengths for avobenzene photoexcited at around 350 nm (a) in ethanol with no heat applied; (b) in ethanol with the sample cell heated to 35°C; (c) in cyclohexane with no heat applied and (d) in cyclohexane with the sample cell heated to 35°C. The circles denote the raw datapoints and the solid line in each case is the fit attained using a parallel kinetic model.

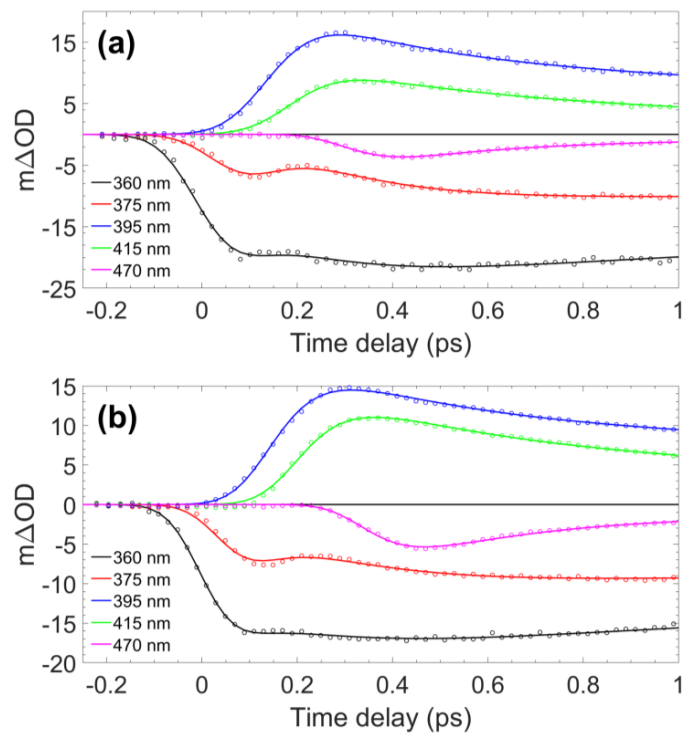


Figure S7: Lineouts prior to 1 ps showing spectral features at specific probe wavelengths for ~ 10 mM avobenzone photoexcited at around 350 nm and heated to $\sim 35^\circ\text{C}$ in (a) diisopropyl adipate (DIA) and (b) lauryl lactate (LL). The circles denote the raw datapoints and the solid line in each case is the fit attained using a parallel model.

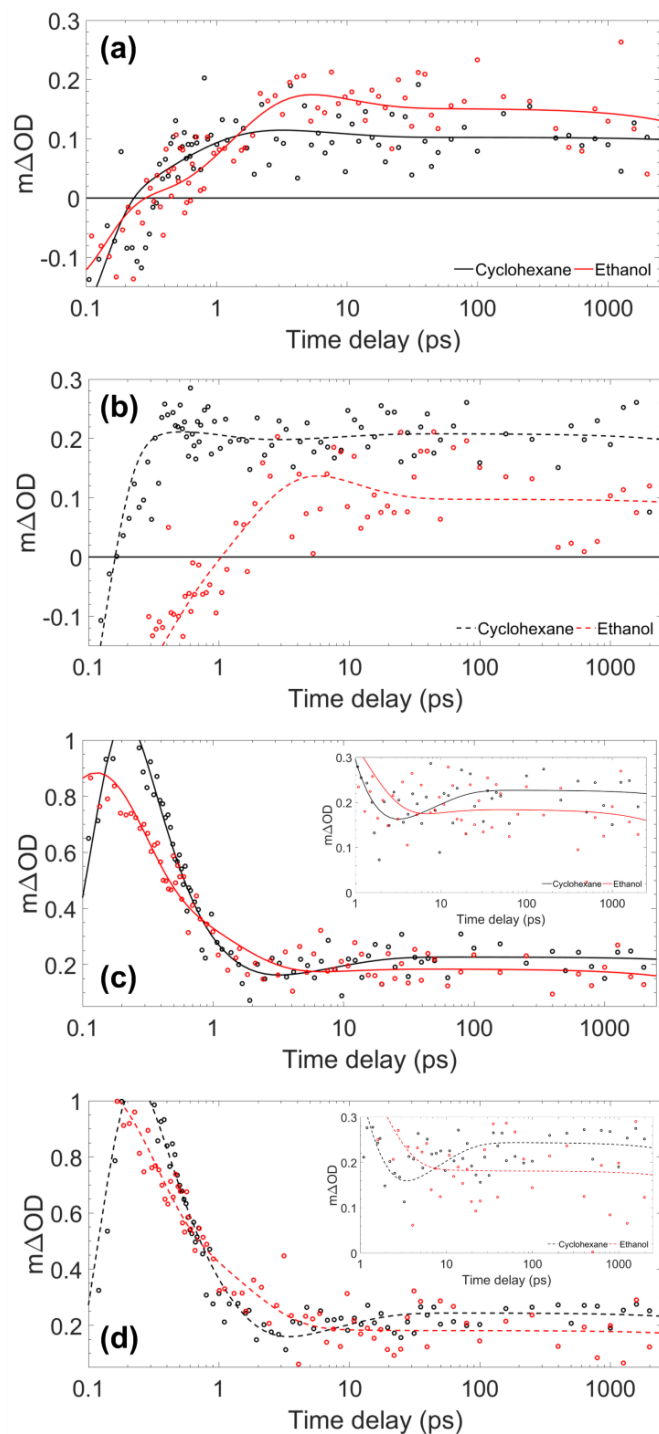


Figure S8: Lineouts to show offset feature at (a), (b) 550 nm and (c), (d) 600 nm for ~ 10 mM avobenzene in (red) ethanol and (black) cyclohexane photoexcited at 350 nm under heating to $\sim 35^\circ\text{C}$ (solid lines) and at room temperature (dotted lines). The circles denote the raw datapoints and the solid/dotted line in each case is the fit attained using a parallel model. The inset figure at 600 nm is a zoom-in of the data between the $m\Delta OD$ values of 0 and 0.3. The time delay axis is presented on a logarithmic scale.

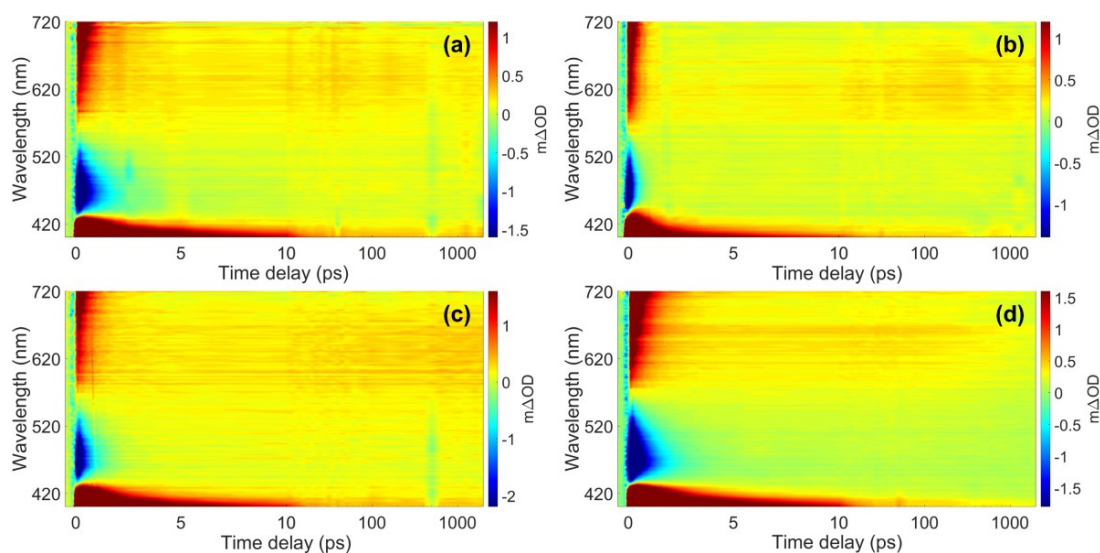


Figure S9: False colour heat maps showing all transient absorption spectra (TAS) of ~ 10 mM avobenzene photoexcited at approximately 350 nm heated to 35°C in (a) ethanol, (b) cyclohexane, (c) diisopropyl adipate (DIA) and (d) lauryl lactate (LL), between the probe wavelengths of 400 – 720 nm. The $m\Delta OD$ scale is 10-fold reduced compared to those presented in Fig. 2 in the main manuscript, to highlight the weaker features.

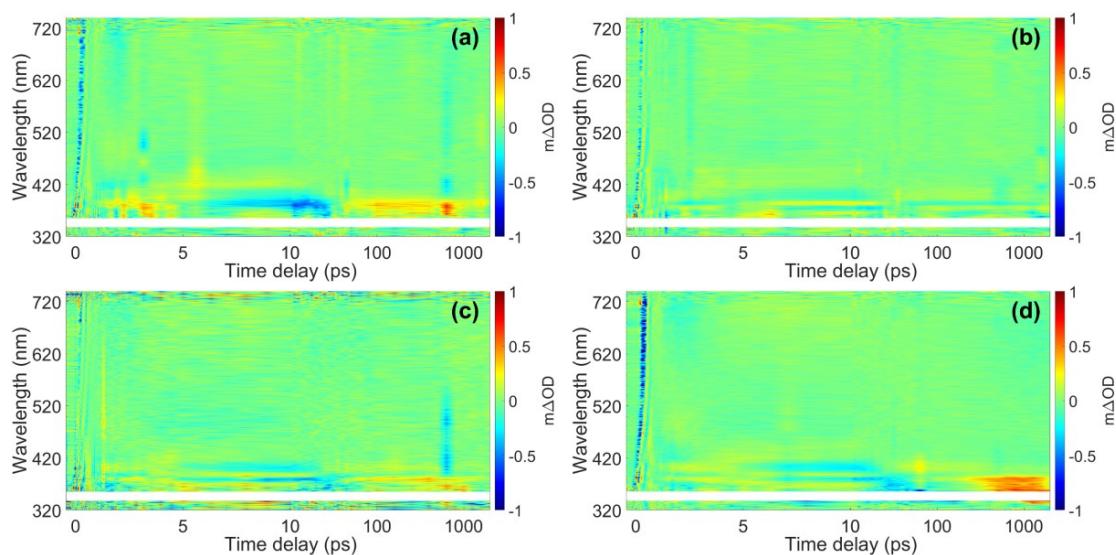


Figure S10: False colour heat maps showing the residuals attained from the parallel fitting procedure of ~ 10 mM avobenzene, photoexcited at approximately 350 nm and heated to 35°C in (a) ethanol, (b) cyclohexane, (c) diisopropyl adipate (DIA) and (d) lauryl lactate (LL).

Supplementary Tables

Table S1: Breakdown of the ingredients in the oil phases, per 25 g batch, tested for SPF and UVA-PF performance following irradiation.

Test	Raw Material	Sample 1	Sample 2
		Mass (g)	Mass (g)
Different emollients	Diisopropyl adipate	10	-
	Lauryl lactate	-	10
	Avobenzene	2.2	2.2
	Ethylhexyl methoxycinnamate	5.5	5.5
	Octocrylene	7.3	7.3
Different concentrations	Raw Material	Sample 3	Sample 4
		Mass (g)	Mass (g)
	Diisopropyl adipate	22	23.5
	Avobenzene	0.44	0.22
	Ethylhexyl methoxycinnamate	1.1	0.55
Octocrylene	1.46	0.73	
Different proportions	Raw Material	Sample 5	
		Mass (g)	
	Diisopropyl adipate	10	
	Avobenzene	2.2	
	Ethylhexyl methoxycinnamate	7.3	
Octocrylene	5.5		

Table S2: Amount of oil phase sample deposited onto each plate, along with amount after application and calculated final coverage for each PMMA plate analysed.

Sample	Plate number	Initial weight (mg)	Final weight (mg)	Final coverage (mg/cm ²)
1	1	14.8	9.6	0.384
	2	15.7	10.2	0.408
	3	15.6	9.3	0.372
Average		15.4	9.7	0.388
Standard Deviation		0.4	0.4	0.01
2	1	14.7	10.4	0.416
	2	14.8	9.6	0.384
	3	14.8	10.6	0.424
Average		14.8	10.2	0.408
Standard Deviation		0.05	0.4	0.02
3	1	15.3	10.3	0.412
	2	14.8	10.2	0.408
	3	14.9	10.9	0.436
Average		15.0	10.5	0.419
Standard Deviation		0.2	0.3	0.01
4	1	14.9	10.2	0.408
	2	15.2	10.6	0.424
	3	14.5	10.0	0.400
Average		14.9	10.3	0.411
Standard Deviation		0.3	0.3	0.01
5	1	14.4	10.7	0.428
	2	14.6	10.2	0.408
	3	15.0	10.2	0.408
Average		14.7	10.4	0.415
Standard Deviation		0.3	0.2	0.01

Table S3: Extracted TEAS time constants for two unheated ~10 mM avobenzene solutions, following photoexcitation at ~350 nm, obtained by using a parallel global kinetic fit model. The error presented for τ_1 is the estimated instrument response (presented in Fig. S1); the errors presented for $\tau_{2,3}$ are those provided by the software package. The quality of the fit is demonstrated in Fig. S5.

Time constant	Ethanol †	Cyclohexane
τ_1 (fs)	160 ± 140	210 ± 80
τ_2 (ps)	1.5 ± 0.1	0.74 ± 0.08
τ_3 (ps)	9.3 ± 0.1	8.0 ± 0.1
τ_4 (ns)	> 2.5*	> 2.5*

* Outside the time-window of the instrument

† During fitting τ_4 was arbitrarily fixed to 50 ns to aid convergence.

Table S4: Predicted singlet and triplet excited state vertical excitation energies (in nm) for the optimised ground-state geometry of avobenzene in its *chelated enol* and *diketo* forms. The energies, and state characters indicated in brackets, were calculated using TD-DFT at the PBE0/6-311++g** level of theory. The optimised ground-state structure, calculated using DFT using the methods detailed in the main manuscript, is also shown.

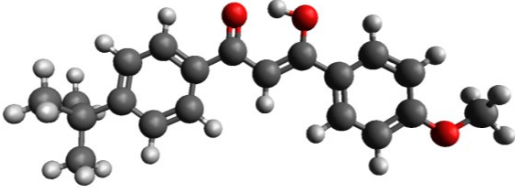
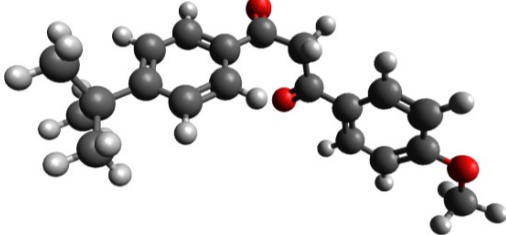
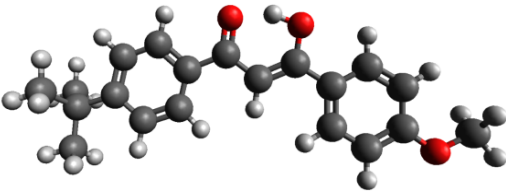
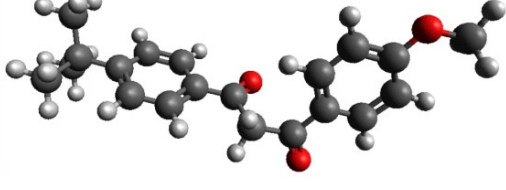
Ethanol				
<i>Chelated enol</i>	Singlets		Triplets	
	S ₁ ($\pi\pi^*$)	346	T ₁ ($\pi\pi^*$)	500
	S ₂ ($n\pi^*$)	309	T ₂ ($\pi\pi^*$)	390
	S ₃ ($\pi\pi^*$)	283	T ₃ ($\pi\pi^*$)	360
	S ₄ ($\pi\pi^*$)	281	T ₄ ($n\pi^*$)	337
	S ₅ ($\pi\pi^*$)	273	T ₅ ($\pi\pi^*$)	320
<i>Diketo</i>	Singlets		Triplets	
	S ₁ ($n\pi^*$)	313	T ₁ ($\pi\pi^*$)	404
	S ₂ ($n\pi^*$)	298	T ₂ ($\pi\pi^*$)	396
	S ₃ ($\pi\pi^*$)	284	T ₃ ($n\pi^*$)	360
	S ₄ ($\pi\pi^*$)	272	T ₄ ($n\pi^*$)	339
	S ₅ ($\pi\pi^*$)	266	T ₅ ($\pi\pi^*$)	317
Cyclohexane				
<i>Chelated enol</i>	Singlets		Triplets	
	S ₁ ($\pi\pi^*$)	337	T ₁ ($\pi\pi^*$)	490
	S ₂ ($n\pi^*$)	314	T ₂ ($\pi\pi^*$)	387
	S ₃ ($\pi\pi^*$)	276	T ₃ ($\pi\pi^*$)	359
	S ₄ ($\pi\pi^*$)	275	T ₄ ($n\pi^*$)	344
	S ₅ ($\pi\pi^*$)	267	T ₅ ($\pi\pi^*$)	313
<i>Diketo</i>	Singlets		Triplets	
	S ₁ ($n\pi^*$)	317	T ₁ ($\pi\pi^*$)	402
	S ₂ ($n\pi^*$)	315	T ₂ ($\pi\pi^*$)	386
	S ₃ ($\pi\pi^*$)	284	T ₃ ($n\pi^*$)	367
	S ₄ ($\pi\pi^*$)	266	T ₄ ($n\pi^*$)	365
	S ₅ ($n\pi^*$)	262	T ₅ ($\pi\pi^*$)	305

Table S5: Calculated Δ SCF values for the optimised ground-state geometries of avobenzene (*chelated enol* and *diketo* forms), calculated using DFT at the PBE0/6-311++g** level of theory. To model the triplet state, the ground state geometry was used with the multiplicity set to 3.

<i>Chelated enol</i>		
Solvent	Energy (eV)	Wavelength (nm)
Ethanol	2.6258	472
Cyclohexane	2.6924	460
<i>Diketo</i>		
Solvent	Energy (eV)	Wavelength (nm)
Ethanol	3.2439	382
Cyclohexane	3.3539	370

References

1. M. Valiev, E. J. Bylaska, N. Govind, K. Kowalski, T. P. Straatsma, H. J. Van Dam, D. Wang, J. Nieplocha, E. Apra and T. L. Windus, *Computer Physics Communications*, 2010, **181**, 1477-1489.
2. A. Klamt and G. Schüürmann, *Journal of the Chemical Society, Perkin Transactions 2*, 1993, 799-805.
3. A. V. Marenich, C. J. Cramer and D. G. Truhlar, *The Journal of Physical Chemistry B*, 2009, **113**, 6378-6396.
4. R. J. Charlton, R. M. Fogarty, S. Bogatko, T. J. Zuehlsdorff, N. D. M. Hine, M. Heeney, A. P. Horsfield and P. D. Haynes, *The Journal of Chemical Physics*, 2018, **148**, 104108.
5. Y. Liu, L. Wang, J. Liu and Y. Di, *Journal of Thermal Biology*, 2013, **38**, 440-448.
6. H. Liu, J. Liao, D. Yang, X. Du, P. Hu, Y. Yang and B. Li, *Building and Environment*, 2014, **73**, 232-238.
7. I. Atmaca and A. Yigit, *Journal of Thermal Biology*, 2006, **31**, 442-452.
8. G. Tanda, *Experimental Thermal and Fluid Science*, 2016, **71**, 103-113.
9. A. de Andrade Fernandes, P. R. dos Santos Amorim, C. J. Brito, A. G. de Moura, D. G. Moreira, C. M. A. Costa, M. Sillero-Quintana and J. C. B. Marins, *Physiological Measurement*, 2014, **35**, 189.
10. M. Fierheller and R. G. Sibbald, *Advances in Skin and Wound Care*, 2010, **23**, 369-379.

11. J. Choi, K. Miki, S. Sagawa and K. Shiraki, *International Journal of Biometeorology*, 1997, **41**, 68-75.
12. W. Liu, Z. Lian, Q. Deng and Y. Liu, *Building and Environment*, 2011, **46**, 478-488.
13. Ç. Yağmur, M. S. Engin and R. Ogawa, *Medical Hypotheses*, 2016, **97**, 4-6.
14. J. González-Alonso, C. Teller, S. L. Andersen, F. B. Jensen, T. Hyldig and B. Nielsen, *Journal of Applied Physiology*, 1999, **86**, 1032-1039.

Chapter 5

Conclusions and outlook

*“Suncare development is a pleasant
but difficult art”*

Laurent Blasco

This thesis employs a multitude of analytical techniques to examine the suitability of both current and potential UV filters for sunscreen use. The main research focus was to determine the photoprotection pathways afforded by these UV filters from the instant that radiation is absorbed, using femtosecond (10^{-15} s) transient electronic absorption spectroscopy (TEAS) to track the energy flow following photoexcitation. Moreover, the capabilities of TEAS have been extended to more closely mimic real-life conditions where a sunscreen would be used, towards predicting the efficacy of active ingredients when applied to the skin surface.

The first, introductory chapter is in three distinct sections. The first reflects upon overarching fundamental concepts, from the quantum principles governing the absorption of a photon by a molecule, to the various pathways via which this excess energy can be dissipated. The second section contains an in-depth review of the instrumentation, data collection and analysis methods involved in TEAS. Additional complementary techniques, including steady-state UV-visible and fluorescence spectroscopy, time-resolved ion yield, laser induced fluorescence, and computational methods are also detailed. The final section concerns the attributes of an ideal sunscreen and the metrics used to determine whether the required standards are met.

Chapter 2 explores the ultrafast decay mechanisms that occur in the salicylate family of sunscreen molecules: specifically, the worldwide-approved UVB filters homosalate and ethylhexyl salicylate (EHS), the latter to a lesser extent. Using both gas- and solution-phase experimental methodologies, in combination with computational studies, it was found that, akin to its smaller analogue methyl salicylate, homosalate undergoes barrierless excited-state intramolecular proton transfer

(ESIPT) upon photoexcitation. Then, a three-way branched decay mechanism was proposed. The fast ESIPT enables most of the photoexcited homosalate to relax non-radiatively, with only a small proportion following the alternative fluorescence or intersystem crossing pathways. Fluorescence measurements in solution revealed a large Stokes shift (> 100 nm) confirming the assignment of ESIPT, and a low quantum yield, corroborating the presence of a branched decay pathway. The same behaviours were also observed in the solution-phase only measurements of EHS. The mechanism proposed in Chapter 2 has since been supported by Chang *et al.* in their subsequent *in silico* study of methyl salicylate.¹ The laser-induced fluorescence results in Chapter 2 found that two excited-state conformers of homosalate were likely, whereby one of these conformers did not undergo ESIPT due to the presence of an energetic barrier. Overall, homosalate and EHS were considered to be effective options, at least from a photochemical perspective, for inclusion in sunscreen blends. However, it should be noted that concerns surrounding the endocrine disruption properties of homosalate have resulted in suggestions from the European Commission that its approved percentage by weight in a completed formulation be reduced from 10% to 0.5%;² demonstrating the importance of complementary biological tests.

In Chapter 3, the symmetrically-functionalised compound termed diethyl sinapate (DES), was studied as a candidate UVA filter to incorporate into a sunscreen formulation, for which current options are lacking. DES was designed in such a way that, should it undergo *cis-trans* isomerisation upon UV photoexcitation, the molecule retains the same structure, which is beneficial for long-term photostability. Furthermore, this design maintains the exemplary photochemical properties of UV filters found on the surface of plant leaves, from which the design of this molecule was inspired. It also alleviates concerns such as the genotoxicity and lower extinction coefficient of *cis*-isomers displayed by related cinnamates (*e.g.* EHMC). For the work in this chapter, the TEAS methodology took steps towards modelling close-to-real-life conditions. Measurements were conducted for the first time using a cosmetics grade emollient as the solvent, using a synthetic skin mimic as a substrate. It was found that the synthetic skin mimic slowed down relaxation to the ground state (assigned to the presence of a higher energetic barrier) compared to the molecule in bulk solution only. Differing behaviours were also found between polar and non-polar solvent environments, highlighting the importance of testing both different solvents and substrates. Overall, the TEAS results in solution were closely aligned to those that had been observed previously in the smaller, asymmetric molecule ethyl sinapate.³ In addition to encouraging spectroscopic properties, endocrine disruption assays indicated a favourable safety profile; finally, antioxidant assays also suggested positive

results (antioxidants are often added to cosmetic products to quench reactive oxygen species that may induce photoaging).⁴ Subsequently, a study on DES grafted on to cellulose nanocrystals has been carried out by Mendoza *et al.*,⁵ demonstrating how the functionality of these candidate UV filters can be extended to improve their cosmetic properties.

Chapter 4 presents a study on the effects of solvent, concentration and skin surface temperature on the widely-used UVA filter avobenzene, with an additional aim to link ultrafast photodynamics with the long-term photostability of more complex mixtures (formulation models). In contrast to earlier chapters, TEAS measurements were conducted at the typical temperature of the human skin surface, in both volatile solvents and cosmetic grade emollients, to assess whether the photodynamics were affected by the change in temperature. This was achieved by using a specialist sample cell, which had the ability to heat the sample region to the required temperature ($\sim 35^\circ\text{C}$). From the TEAS results presented, the alterations to the experimental conditions did not have a qualitative effect on the spectral features observed. The spectral features observed were also in line with those observed previously in TEAS measurements of avobenzene and related dibenzoylmethanes.^{6,7} Industry-standard SPF and UVA-PF testing protocols revealed that both the concentration and proportion of ingredients included in the oil phases of the formulations tested seemed to alter their performance. This was assigned as being most likely due to spectral overlap of the emollient with the UV region, however diffusion-limited intermolecular energy transfer processes are worthy of further investigation in the future. In addition, it is postulated that the long-term performance of avobenzene in the oil phases could be related to the ground-state bleach (GSB) recovery observed in the TEAS measurements, thus bridging the gap between the ultrafast and ultraslow dynamics. Future studies would benefit from a longer assessment of the evolution of the GSB, by extending the time delays beyond the 2.5 – 3 ns possible with the WCUS experimental setup at this time.

All three Chapters share the aim of determining optimum conditions for the action of UV filters within sunscreens. Although the specific focuses and motivations for each presented paper are altered, all benefit from following an experimental *bottom-up* approach. Chapter 3 built upon the gas-solution phase approach in Chapter 2 that used ethanol, cyclohexane and acetonitrile as solvents, by additionally testing in emollients, and on a synthetic skin substrate, towards a real-life model for TEAS. The importance of complementary biological studies, such as endocrine disruption characterisation in Chapter 3, is highlighted by the recently identified adverse properties of salicylate molecules,² as discussed prior. Together, Chapters 2

and 3 combine to show that, despite displaying very different spectral features, all three compounds demonstrate favourable spectroscopic properties in solution. From this, it can be inferred that there is no “perfect” TEAS spectrum for a UV filter, and each should be assessed on a case-by-case basis. For example, the GSB feature found in Chapter 4 for avobenzone, is an example of a less favourable spectral feature not identified in the preceding two Chapters. Chapter 4 also linked the new-found capabilities of ultrafast spectroscopy from Chapters 2 and 3, with the addition of measurements at elevated temperatures, to industry-standard *in vitro* SPF testing. The foundation for such a combination of industrially relevant metrics was made in Chapter 3, with the inclusion of the critical wavelength values for DES.

The experimental techniques used in this thesis, and combinations thereof, could be used to extend the repertoire of nature-based sunscreen filters, such as additional sinapate esters, or mycosporine-like amino-acids (MAAs), and work is continuing in this regard.^{8–13} Further to the earlier discussion of sinapate esters in relation to Chapter 3, MAAs are well-known for their UV protection properties in the systems from which they are extracted,¹⁴ including cyanobacteria, phytoplankton, plant-derived sources (*e.g.* algae), and fungal metabolites.^{15–22} As a result, they are also being regarded as potential new sunscreen ingredients and their use is being explored for cosmetic products in industry.^{23,24}

Looking to the future, the potential of ultrafast spectroscopy for sunscreen applications may not be limited to molecules that solely act as UV filters.²⁴ It has been found that the skin also suffers from deleterious effects caused by blue light exposure,²⁵ from sources such as mobile phones and computer screens. Studies thus far have focused upon the biological effects;^{26–28} however, there is potential for ultrafast spectroscopy techniques to be used to inform the design of blue light absorbers (and beyond), given their success at doing so for UV filters. Developing cosmetic ingredients that effectively protect the skin from visible and infrared light in addition to UV is of current industrial concern.²⁹ Emphasis is also being placed on developing multi-purpose cosmetic components, for example UV filters with antioxidant properties,^{17,30–33} as acknowledged in Chapter 3. Indeed, some MAAs, such as mycosporine-glycine, exhibit antioxidant properties along with a favourable photostability profile.^{17,33} Using the knowledge gained from experimental insights, ingredients could perhaps be tailor-made to satisfy client requirements; for example the addition of functional groups to a molecule to aid solubility, but maintaining all other functionalities. Opportunities also exist to extend the scope of ultrafast spectroscopy for cosmetic applications beyond sunscreens, *e.g.* for the testing of singlet oxygen quenchers that are currently being developed. Preferred characteristics

of excited-state dynamics of such molecules could be identified using the techniques discussed in this thesis.

References

- [1] X.-P. Chang, T.-S. Zhang, Y.-G. Fang and G. Cui, *J. Phys. Chem. A*, 2021, **125**, 1880–1891.
- [2] U. Bernauer, L. Bodin, Q. Chaudhry, P. Coenraads, M. Dusinska, J. Ezendam, E. Gaffet, C. Galli, B. Granum, E. Panteri *et al.*, *SCCS Opinion on Homosalate-SCCS/1622/20-Final Opinion*, 2021.
- [3] M. D. Horbury, A. L. Flourat, S. E. Greenough, F. Allais and V. G. Stavros, *Chem. Commun.*, 2018, **54**, 936.
- [4] H. Masaki, *J. Dermatol. Sci.*, 2010, **58**, 85.
- [5] D. J. Mendoza, M. Maliha, V. S. Raghuwanshi, C. Browne, L. M. Mouterde, G. P. Simon, F. Allais and G. Garnier, *Mater. Today Bio*, 2021, 100126.
- [6] A. D. Dunkelberger, R. D. Kieda, B. M. Marsh and F. Fleming Crim, *J. Phys. Chem. A*, 2015, **119**, 6155.
- [7] P. K. Verma, F. Koch, A. Steinbacher, P. Nuernberger and T. Brixner, *J. Am. Chem. Soc.*, 2014, **136**, 14981–14989.
- [8] L. A. Baker, M. Staniforth, A. L. Flourat, F. Allais and V. G. Stavros, *ChemPhysChem*, 2020, **21**, 2006–2011.
- [9] M. D. Horbury, M. A. Turner, J. S. Peters, M. Mention, A. L. Flourat, N. D. Hine, F. Allais and V. G. Stavros, *Front. Chem.*, 2020, **8**, 633.
- [10] A. L. Whittock, N. Auckloo, A. M. Cowden, M. A. Turner, J. M. Woolley, M. Wills, C. Corre and V. G. Stavros, *J. Phys. Chem. Lett.*, 2021, **12**, 3641–3646.
- [11] T. T. Abiola, N. d. N. Rodrigues, C. Ho, D. J. Coxon, M. D. Horbury, J. M. Toldo, M. T. do Casal, B. Rioux, C. Peyrot, M. M. Mention *et al.*, *J. Phys. Chem. Lett.*, 2020, **12**, 337–344.

- [12] T. T. Abiola, A. L. Whittock and V. G. Stavros, *Molecules*, 2020, **25**, 3945.
- [13] J. M. Toldo, M. T. do Casal and M. Barbatti, *J. Phys. Chem. A*, 2021, **125**, 5499–5508.
- [14] D. Karentz, F. S. McEuen, M. C. Land and W. C. Dunlap, *Mar. Biol.*, 1991, **108**, 157.
- [15] C. Roullier, M. Chollet-Krugler, E.-M. Pferschy-Wenzig, A. Maillard, G. N. Rechberger, B. Legouin-Gargadennec, R. Bauer and J. Boustie, *Phytochemistry*, 2011, **72**, 1348.
- [16] W. M. Bandaranayake, *Nat. Prod. Rep.*, 1998, **15**, 159.
- [17] S. Bhatia, A. Garg, K. Sharma, S. Kumar, A. Sharma and A. Purohit, *Pharmacogn. Rev.*, 2011, **5**, 138.
- [18] T. Řezanka, M. Temina, A. G. Tolstikov and V. M. Dembitsky, *Folia Microbiol.*, 2004, **49**, 339.
- [19] U. Karsten, T. Sawal, H. Dieter, K. Bischof, F. L. Figueroa, A. Flores-Moya and C. Wiencke, *Bot. Mar.*, 1998, **41**, 443.
- [20] E. P. Balskus and C. T. Walsh, *Science*, 2010, **329**, 1653.
- [21] R. P. Sinha, S. P. Singh and D.-P. Häder, *J. Photoch. Photobio. B*, 2007, **89**, 29.
- [22] J. M. Woolley and V. G. Stavros, *Sci. Prog.*, 2019, **102**, 287–303.
- [23] E. Chrapusta, A. Kaminski, K. Duchnik, B. Bober, M. Adamski and J. Bialczyk, *Mar. Drugs*, 2017, **15**, 326.
- [24] E. L. Holt and V. G. Stavros, *Int. Rev. Phys. Chem.*, 2019, **38**, 243–285.
- [25] B. H. Mahmoud, C. L. Hexsel, I. H. Hamzavi and H. W. Lim, *Photohem. Photobiol.*, 2008, **84**, 450.
- [26] J. Liebmann, M. Born and V. Kolb-Bachofen, *J. Invest. Dermatol.*, 2010, **130**, 259.
- [27] M. M. Kleinpenning, T. Smits, M. H. A. Frunt, P. E. J. Van Erp, P. C. M. Van De Kerkhof and R. M. J. P. Gerritsen, *Photodermatol. Photoimmunol. Photomed.*, 2010, **26**, 16.

- [28] K. P. Lawrence, T. Douki, R. P. Sarkany, S. Acker, B. Herzog and A. R. Young, *Sci. Rep.*, 2018, **8**, 12772.
- [29] S. Singer, S. Karrer and M. Berneburg, *Curr. Opin. Pharmacol.*, 2019, **46**, 24.
- [30] E. Gregoris, S. Fabris, M. Bertelle, L. Grassato and R. Stevanato, *Int. J. Pharm.*, 2011, **405**, 97.
- [31] G. Agati and M. Tattini, *New Phytol.*, 2010, **186**, 786.
- [32] S. Grether-Beck, A. Marini, T. Jaenicke and J. Krutmann, *Photodermatol. Photoimmunol. Photomed.*, 2014, **30**, 167–174.
- [33] A. Oren and N. Gunde-Cimerman, *FEMS Microbiol. Lett.*, 2007, **269**, 1.

Appendices

A1 Coding

The code presented below was written by myself using MATLAB, version R2017b. It has been implemented for much of the TEAS data presented in this thesis, hence its inclusion in the appendix. In the future, I hope that it can be used, modified and improved for the analysis of TEAS data.

Code for data averaging, baseline subtraction and plotting

```
%%DATA AVERAGING
%Read in files and truncate - csvread command up to 2.5 ns.
%If different final time delay, increase 4th number in vector to the
%number of columns of data in the excel file.
%Once row and column is set for one dataset, the others will be the same.
%Row and columns numbers start from 0, not 1.

%Read in location and file name string
    file_name = 'C:\Users\emily\OneDrive\Documents\PhD\...\transients_Scan_';
%Set number of filled columns and rows that you wish to read in
    colsNum = 122; %Time delays
    rowsNum = 740; %Wavelengths
%Read in each dataset individually (csv format)
%Manually adjust depending on how many datasets you have
%There are three in this case to save space! (normally at least five)
    number_of_datasets = 3;
    set1=csvread(strcat(file_name,'1.csv'),1,0,[1,0,rowsNum,colsNum]);
    set2=csvread(strcat(file_name,'2.csv'),1,0,[1,0,rowsNum,colsNum]);
    set3=csvread(strcat(file_name,'3.csv'),1,0,[1,0,rowsNum,colsNum]);
    format long %Inserted to ensure no rounding errors
    wavelength = set1(:,1); %Creates vector of wavelengths
%Read in time delay values from the csv file
    timed = csvread(strcat(file_name,'1.csv'),0,1,[0,1,0,colsNum]);
    timedelay = timed./1000; %convert from fs to ps
%Separately convert data from OD to mOD
    newset1 = set1(:, 2:end).*1000;
```

```

        newset2 = set2(:, 2:end).*1000;
        newset3 = set3(:, 2:end).*1000;
%Average all datasets (optical density only)
        avgdata = (newset1 + newset2 + newset3)./number_of_datasets;
%Prepare a matrix that can be filled with baseline subtracted data
        [m,n] = size(avgdata);
%Set first column (first time delay of -1 ps) of the averaged data
%as the baseline
        baseline=avgdata(:,1);
        for i = 1:n %For every column, this loop subtracts the baseline
            avgdata(:,i) = avgdata(:,i) - baseline;
        end
%Export csv file of averaged data
%Removes -1 ps column as it is now a zero vector
        avgdata2=[wavelength, avgdata(:,2:end)];
        timedelay2=[0,timedelay(2:end)];
        avgdatax = [timedelay2;avgdata2];
        csvwrite(strcat(file_name,'averaged.csv'),avgdatax);
% avgdata3 = transpose(avgdatax); used if needed
% csvwrite(strcat(file_name,'averaged_transposed.csv'), avgdata3);

%%PLOTTING HEAT MAPS PART 1 - AVERAGED DATA
%Plotting heat maps, where up to 10 ps is presented on a linear scale
%and logarithmic thereafter
        f1 = find(timedelay <= 10);
        f2 = find(timedelay >= 10);
%Loop used to remove pump scatter that cannot be effectively subtracted
%from the dataset
        pump_range_index = find(wavelength>=335 & wavelength <=355);
        for i=min(pump_range_index):max(pump_range_index)
            avgdata(i,2:end) = NaN;
        end
%Sets up grids for linear and logarithmic halves of plot
        [x1,y1]= meshgrid(timedelay(2:length(f1)), wavelength);
        [x2,y2]= meshgrid(timedelay(length(f1):end), wavelength);
        figure(1)
        colormap('jet(256)'); %set colormap
        ax1 = subplot(121);
        contourf(x1, y1, avgdata(:, f1(2:end))), 100, 'LineStyle', 'none')
        xlabel('Time delay (ps)')
        xlabelh = get(gca,'xlabel');
        set(xlabelh,'Position',get(xlabelh,'Position') + [5.25 -10 0])
        ylabel('Wavelength (nm)')
%Uncomment below to automatically set colorbar limits to the maximum
%and minimum values of the data, not always appropriate
        %caxis([min(min(avgdata(:, [f1(2:end),f2(2:end)])))

```

```

    %max(max(avgdata(:, [f1(2:end), f2(2:end)]))))
    caxis([-m n]) %Set colourbar limits manually
    set(gca, 'FontSize', 36, 'XMinorTick', 'on', 'YMinorTick', 'on')
    hold on %Ensures both halves of heatmap (linear and logarithmic) appear on the same plot
    ax2 = subplot(122);
    contourf(x2, y2, avgdata(:, f2), 100, 'LineStyle', 'none')
    %Axis position set so this plot is directly next to the linear plot
    set(ax1, 'position', [0.1 0.175 0.4 0.8]);
    set(ax2, 'position', [0.5 0.175 0.4 0.8]);
    set(ax2, 'xscale', 'log', 'xlim', [10 2000]); %Time delay axis (10 - 2000 ps)
    set(ax2, 'axislocation', 'right')
    xticklabels(ax2, {'10', '100', '1000'})
    %Set wavelength axis limits
    set([ax1 ax2], 'ylim', [320 720], 'ytick', 320:100:720, 'box', 'off');
    uistack(ax2, 'top');
    %Create colourbar scale
    c = colorbar;
    ylabel(c, 'm\DeltaOD', 'FontSize', 40)
    %Ensure colourbar limits are the same between the two plots, (un)comment accordingly
    %caxis([min(min(avgdata(:, [f1(2:end), f2(2:end)]))))
    %max(max(avgdata(:, [f1(2:end), f2(2:end)]))))
    caxis([-m n])
    %Set design of colour bar
    set(gca, 'FontSize', 36)
    set(gca, 'YTickLabelMode', 'Manual', 'YMinorTick', 'on')
    set(gca, 'YTick', [])

%%PLOTTING HEAT MAPS PART 2 - CHIRP CORRECTED DATA
%Plot chirp corrected version (exported from KOALA package)
cc_data=csvread('C:\Users\emily\OneDrive\Documents\PhD\
..._transients_Scan_averagedCC.csv', 1, 0, [1, 0, rowsNum, colsNum-1]);
%Prepare the two halves of the new plot
f1 = find(timedelay <= 10);
f2 = find(timedelay >= 10);
%As before, remove all data affected by pump scatter
pump_range_index_cc = find(wavelength>=340 & wavelength <=355);
for i=min(pump_range_index_cc):max(pump_range_index_cc)
    cc_data(i, 2:end) = NaN;
end
%Prepare the grids to input chirp corrected data plots
[x1, y1] = meshgrid(timedelay(2:length(f1)), wavelength);
[x2, y2] = meshgrid(timedelay(length(f1):end), wavelength);
figure(2)
colormap('jet(256)'); %set colormap
ax1 = subplot(121);
contourf(x1, y1, cc_data(:, f1(2:end))), 500, 'LineStyle', 'none')

```

```

xlabel('Time delay (ps)')
xlabh = get(gca,'xlabel');
set(xlabh,'Position',get(xlabh,'Position') + [5.25 -10 0])
%set(ax1, 'xtick', 0:2:10) %Change if desired
ylabel('Wavelength (nm)')
%caxis([min(min(cc_data(:, [f1(2:end),f2(2:end)])))
%max(max(cc_data(:, [f1(2:end),f2(2:end)])))])
caxis([-m2 n2])
set(gca, 'FontSize', 36, 'XMinorTick', 'on')
hold on
ax2 = subplot(122);
contourf(ax2, y2, cc_data(:, f2), 500, 'LineStyle', 'none')
set(ax1,'position',[0.1 0.175 0.4 0.8]);
set(ax2,'position',[0.5 0.175 0.4 0.8]);
set(ax2,'xscale','log','xlim',[10 2000]);
set(ax2,'yaxislocation', 'right')
xticklabels(ax2, {'10', '100', '1000'})
set([ax1 ax2], 'ylim', [320 720], 'ytick', 320:100:720, 'box', 'off');
uistack(ax2, 'top');
%Prepare chirp corrected data colourbar
c = colorbar;
ylabel(c, 'm\DeltaOD', 'FontSize', 40)
%caxis([min(min(cc_data(:, [f1(2:end),f2(2:end)])))
%max(max(cc_data(:, [f1(2:end),f2(2:end)])))])
caxis([-m2 n2])
%Parameters can be set in the same way as the average data heat map

%%PART 3 - PLOT VERTICAL SLICES TO SHOW TRANSIENTS AT SPECIFIC TIME DELAYS
%Select the time delays that you would like to present and list them
times_toplot = [0.4; 1; 2; 5; 10; 50; 100; 1000; 2000; 3000];
len = length(times_toplot);
TD = zeros(len,1);
figure(3)
linecolors=(jet(len));
is_nan = find(isnan(cc_data)==1);
for index = 1:length(is_nan)
    cc_data(is_nan(index))=0;
end
for i=1:len
    hold on
%Step 1 of loop: find the actual time delay closest to the one you selected
%and plot them
    TD(i) = find(abs(timedelay-times_toplot(i)) ==
    min(abs(timedelay - times_toplot(i))));
    plot(wavelength, smooth(cc_data(:, TD(i))), 'LineWidth', 2, 'color',

```

```

%Change colour of each plotted line
    linecolors((len+1)-i,:), 'HandleVisibility', 'off')
    if i == numel(times_toplot)
        hold off
    end
end
end
%This loop rounds the time delay values in the legend
actual_times = zeros(length(times_toplot));
for i = 1:length(times_toplot)
    if times_toplot(i) <= 20
        actual_times(i) = round(timedelay(TD(i)),1);
    else
        actual_times(i) = round(timedelay(TD(i)),-1);
    end
end
end
hold on
%Plots the line y=0 for reference
plot(wavelength,zeros(length(wavelength)), 'color', 'black',
'LineWidth', 2, 'HandleVisibility', 'off')
hold off
%These parameters can be changed depending on your requirements and design preferences
set(gca,'FontSize', 36, 'box', 'on')
%Set wavelength range and increments for the x-axis labels
set(gca, 'xlim', [320 600], 'xtick', 350:50:600, 'xminortick', 'on')
%Set wavelength range and increments for the y-axis labels
set(gca, 'ylim', [-5 3], 'ytick',-4:2:4)
%Automate creation of legend
ledge = legend(strcat(num2str(actual_times(:)), ' ps'),
'location','southeast');
set(ledge, 'FontSize', 18)
legend('boxoff')
%Set axis labels
xlabel('Wavelength (nm)', 'FontSize', 36)
ylabel('m\DeltaOD','FontSize', 40)

```

A2 Declaration of contributions

Chapter 2 In the first paper, presented in Chapter 2 (Holt *et al.*, *Phys. Chem. Chem. Phys.*, 2020, **22**, 15509), the research was conducted collaboratively. Theoretical results were obtained predominantly by M. A. P. Turner, with assistance from the author and K. M. Krokidi. Ultrafast time-resolved gas-phase measurements were conducted by K. M. Krokidi with some laboratory assistance from N. d. N. Rodrigues, in the laboratory of V. G. Stavros. Frequency-resolved gas-phase results were conducted by P. Mishra under the supervision of T. S. Zwier. The writing of the paper was conducted primarily by the author, with contributions from M. A. P. Turner, K. M. Krokidi, and N. d. N. Rodrigues. V. G. Stavros provided advisory help and an overall critique of the manuscript.

Chapter 3 For the second paper presented in Chapter 3 (Horbury *et al.*, *Nat. Commun.*, 2019, **10**, 4748), author contributions are noted in the published manuscript, and are reproduced with more details here. The molecule studied in this Chapter was synthesised by L. M. M. Mouterde under the supervision of F. Allais. P. Balaguer conducted the endocrine disruption measurements and the DPPH assays to determine antioxidant activity. The author and M. D. Horbury collected and analysed the time-resolved and steady-state spectroscopy data with equal contributions, in the laboratory of V. G. Stavros. M. D. Horbury wrote the manuscript with contributions from the author, L. M. M. Mouterde, P. Balaguer and F. Allais. Advice regarding the use of the synthetic skin mimic was provided by L. Blasco and J. Cebrián. Supervisory guidance was provided throughout the preparation of the manuscript by L. Blasco, J. Cebrián and V. G. Stavros.

Chapter 4 In the third paper, presented in Chapter 4 (Holt *et al.*, *Phys. Chem. Chem. Phys.*, 2021, **23**, 24439), the making of the oil phases, and the subsequent SPF testing and analysis, was conducted by N. d. N. Rodrigues, under the guidance of J. Cebrián. Supervisory help and guidance was provided throughout the preparation of the manuscript by J. Cebrián and V. G. Stavros. All authors have proof-read and critiqued the manuscript.

A3 Bibliography

Full lists of references can be found at the end of each Chapter. However, I wanted to acknowledge the following resources, which have been invaluable for reference during the preparation of this thesis and used for general reference throughout:

- P. W. Atkins, *Physical Chemistry* (Fifth Edition), Oxford University Press, Oxford, 1994; also *Physical Chemistry* (Sixth Edition), Oxford University Press, 1999.
- B. Wardle, *Principles and Applications of Photochemistry*, John Wiley and Sons, 2009.
- R. P. Wayne, *Principles and Applications of Photochemistry*, Oxford University Press, 1999.
- D. C. Harris and M. D. Bertolucci, *Symmetry and Spectroscopy: an introduction to vibrational and electronic spectroscopy*, Dover Publications, 1989
- The PhD theses of previous members of the Stavros Group at the University of Warwick: Michael D. Horbury (2016), Lewis A. Baker (2017), Natércia das Neves Rodrigues (2018), Matthew A. P. Turner (2020), Jack M. Woolley (2020), S. Ed Greenough (2014).